NONLINEAR DIFFUSION ACCELERATION IN VOIDS FOR THE LEAST-SQUARES TRANSPORT EQUATION

A Dissertation

by

HANS RÜDIGER HAMMER

Submitted to the Office of Graduate and Professional Studies of
Texas A&M University
in partial fulfillment of the requirements for the degree of

DOCTOR OF PHILOSOPHY

Chair of Committee,	Jim E. Morel
Committee Members,	Jean-Luc Guermond
	Ryan G. McClarren
	Jean C. Ragusa
Head of Department,	Yassin A. Hassan

August 2017

Major Subject: Nuclear Engineering

ABSTRACT

In this dissertation we present advances to the nonlinear diffusion acceleration for void regions using second order forms of the transport equation. We consider the weighted least-squares and the self-adjoint angular flux transport equations. We show that these two equations are closely related through the definition of the weight function and how the nonlinear diffusion acceleration can be extended to hold in void regions. Using a Fourier analysis we show the convergence properties of our method for homogeneous and heterogeneous problems. We use several problems to study the numerical behavior and the influence of different discretization schemes.

Second order forms of the transport equation allow the use of continuous finite elements (CFEM). CFEM discretization is computationally cheaper and easier to implement on unstructured meshes, allowing more detailed geometries. The self-adjoint transport operators result normally in symmetric positive-definite matrices which allow the use of efficient linear algebra solvers with an enormous advantage in memory usage. In this dissertation we study the weighted least-squares and compare to the self-adjoint angular flux transport equations with void treatment, both well defined in voids.

The nonlinear diffusion acceleration (NDA) is an effective scheme to increase convergence for highly diffusive problems, but can also ensure conservation for non-conservative transport schemes. However, for second order transport equations, the scheme was not yet defined in voids. In this dissertation we derived modifications to the NDA to handle problems containing void regions. A Fourier analysis showed that the newly developed modifications accelerates unconditionally for scattering ratios smaller than one. Extensive testing on various parameters was performed to ensure

that the modifications are stable and efficient.

Numerical tests with Reed's problem showed that the NDA scheme results in a non-constant flux shape in the void regions. Further investigations revealed that this coarse mesh problem is caused by the interface coupling between void and material regions. The separation of the low-order equation at the interface ameliorates these problems. We give a proof-of-concept for a high-order CFEM/low-order DFEM scheme as well as for an artificial diffusion scheme to restore causality and obtain an improved scalar flux solution in the void.

The NDA void modifications were then tested on a modified C5G7 problem, a challenging reactor physics benchmark. The results were compared to first order transport and the self-adjoint angular flux equation with void treatment. The results indicated that the weighted least-squares equations give adequate results while maintaining a symmetric positive-definite matrix.

DEDICATION

To my parents, my sister and Andreea. To all the people who walked with me on my path and helped me to achieve this goal.

ACKNOWLEDGMENTS

I want to thank Prof. Morel for supporting and guiding me towards this dissertation. I also want to thank the other professors on my committee for there help in discussions about this dissertation.

This dissertation was also greatly supported by INL's Reactor Physics Modeling and Simulation Group. I want to thank Javier Ortensi, Yaqi Wang, Sebastian Schunert and Mard DeHart, who gave me the possibility to work with them and providing help and support.

Finally I want to thank my fellow graduate students for a supportive and friendly work environment. I want especially thank Carolyn McGraw for providing PDT results as comparison, and Tarek Ghaddar for many more and many less useful discussions.

CONTRIBUTORS AND FUNDING SOURCES

Contributors

This work was supported by a dissertation committee consisting of Professor Morel as advisor and Professors McClarren and Ragusa of the Department of Nuclear Engineering and Professor Guermond of the Department of Mathematics.

The initial implementation of the unweighted Least-Squares transport scheme in Rattlesnake was done by Jacob Peterson. Both SAAF schemes were implemented by Yaqi Wang, INL, the main author of Rattlesnake. Sebastian Schunert, INL, implemented initially the non-local diffusion coefficient in Rattlesnake. The PDT reference solution for the modified C5G7 benchmark was created by Carolyn McGraw with graphite cross sections provided by Andrew Till, LANL.

All other work conducted for the dissertation was completed by the student independently.

Funding Sources

This material is based upon work supported by the Department of Energy, Battelle Energy Alliance, LLC, under Award Number DE-AC07-05ID14517.

NOMENCLATURE

Abbreviations

AD	Artificial Diffusion Coefficient
AMG	Algebraic-multigrid
AVG	Average pin power error
C5G7	Reactor physics benchmark with seven energy groups
CFEM	Continuous finite element method
DFEM	Discontinuous finite element method
DSA	Diffusion Synthetic Acceleration
HTGR	High Temperature Gas-cooled Reactor
INL	Idaho National Laboratory
LS	Least-squares equation
MOOSE	Finite element framework developed by INL
MRE	Mean relative pin power errors
NDA	Nonlinear diffusion acceleration
NDA LS	NDA using a unweighted LS transport solve
NDA SAAF	NDA using a SAAF transport solve
NDA SAAFτ	NDA using a SAAFτ transport solve
NDA WLS	NDA using a WLS transport solve
NDA 1	NDA using a WLS transport solve and SAAFτ drift vector
NDA 2	NDA using a SAAFτ transport solve and WLS drift vector

pcm	Percent Millirho - unit for reactivity
PJFNK	Preconditioned Jacobian-Free Newton Krylov
PP1	Relative error for the maximal pin power
PP2	Relative error for the minimal pin power
RMS	Root-means square of the pin power error
SAAF	Self-adjoint angular flux equation
SAAFτ	Self-adjoint angular flux equation with void treatment
S_N	Method of discrete ordinances
SI	Source iterations
SPD	symmetric positive-definite
TREAT	Transient Reactor Test facility
WLS	Weighted least-squares equation
XML	Extended markup language

Symbols (with default units, as appropriate)

$\mathbf{A}$		Discretized streaming and collision matrix
$\mathbf{B}$		Discretized scattering matrix
c	[-]	Scattering ratio
$\mathbf{C}$		Discretized diffusion matrix
D	[cm]	Diffusion coefficient
$\underline{\underline{\mathrm{D}}}$	[cm]	Nonlocal diffusion tensor
$\mathrm{D}_{\max}$	[cm]	Maximal value for the diffusion coefficient
D_{ϵ}	[cm]	Artificial NDA diffusion coefficient
$\mathcal{D}$		Moments to discrete operator
$\mathcal{D}$		Problem domain

$\partial\mathcal{D}$		Boundary of the domain
$\partial\mathcal{D}^+$		Outgoing boundary $\vec{\Omega}\cdot\vec{n}>0$
$\partial\mathcal{D}^-$		Incoming boundary $\vec{\Omega}\cdot\vec{n}<0$
$\partial\mathcal{D}_{\mathrm{R}}$		Reflective part of the boundary
$\partial\mathcal{D}_{\mathrm{V}}$		Vacuum part of the boundary
e	[-]	Relative error in scalar flux
E	[eV]	Energy
E	[-]	Eddington factor
$\mathbf{E}$		Discretized zeroth moment drift matrix
E_n	[-]	Exponential-Integral function
f	$[\frac{1}{\mathrm{cm}}]$	Weight for WLS optional boundary condition
f	[cm]	Solution to nonlocal diffusion auxiliary transport system
$\mathcal{F}$		Fission source operator
f^-		DFEM quantity f on the left side of an interface
f^+		DFEM quantity f on the right side of an interface
$\mathbf{F}$		Discretized first moment drift matrix
$\mathbf{G}$		Discretized second moment drift matrix
h	[cm]	Spatial mesh cell thickness
$\hat{\imath}$	[-]	Imaginary number
$\vec{J}$	$[\frac{1}{\mathrm{cm}^2\mathrm{s}}]$	Neutron current
$\tilde{J}$	[-]	Upwind NDA correction factor
$\hat{J}$	[-]	Fourier magnitude for current
$\hat{\jmath}^{\mathrm{in}}$	$[\frac{1}{\mathrm{cm}^2\mathrm{s}}]$	Partial current into the domain or cell across a surface

$\hat{j}^{\text{out}}$	$[\frac{1}{\text{cm}^2\text{s}}]$	Partial current out of the domain or cell across a surface
$\hat{j}^{+}$	$[\frac{1}{\text{cm}^2\text{s}}]$	Partial current in direction of surface normal
$\hat{j}^{-}$	$[\frac{1}{\text{cm}^2\text{s}}]$	Partial current in opposite direction of surface normal
k_{eff}	[-]	Neutron multiplication factor
ℓ	[cm]	Distance to boundary in direction $\vec{\Omega}$
$\mathcal{L}$		Streaming and collision operator
$\mathcal{L}^{\dagger}$		Adjoint of the streaming and collision operator
$\mathbb{N}_0$		Natural numbers including zero
$\mathcal{M}$		Discrete to moment operator
$\vec{n}$	[-]	Normal vector of a face
P_l	[-]	Legendre polynomial of the lth order
q	$[\frac{\text{n}}{\text{s}}]$	Distributed external source
$\mathcal{Q}$		Distributed source operator
p	[cm]	Weight for Eddington current in generalized current formulation
$\tilde{p}$	[cm]	Weight for classical current in generalized current formulation
$\mathbb{R}^{+}$		Space of positive real numbers
$\mathcal{S}$		Scattering source operator
t	[s]	Time
u	$[\frac{\text{m}}{\text{s}}]$	Velocity
v	$[\frac{\text{m}}{\text{s}}]$	Neutron speed
w	[cm]	Weight for WLS equation
$W_{\mathcal{D}}$		Trial function space for FEM domain

$\mathbf{W_l}$	[-]	Angular quadrature matrix for lth moment
$w_{\max}$	[cm]	Limit of WLS weight function
Y_l^p	[-]	Spherical harmonics
x	[cm]	Spatial coordinate
$\vec{x}$	[cm]	Spatial coordinate vector
x_{b}	[cm]	Spatial coordinate on the boundary
x_{I}	[cm]	Material interface coordinate in two region problem
x_{L}	[cm]	Left boundary coordinate in two region problem
x_{R}	[cm]	Right boundary coordinate in two region problem
$\hat{\alpha}$	[-]	NDA drift vector
β	[-]	NDA generalized Marshak boundary factor
$\hat{\gamma}$	[-]	DFEM NDA face correction factor
Γ		Interior mesh interface for the DFEM discretization
δf	[-]	Error in quantity f
ϵ	[-]	Asymptotic scaling factor
ϵ	[-]	Artificial diffusion coefficient
ζ	[-]	Threshold for SAAFτ stabilization
$\hat{\zeta}$	[-]	Threshold for WLS NDA current formulations
ζ_{D}	[-]	Threshold parameter for joined diffusion coefficient
κ	[-]	NDA boundary correction factor
$\hat{\kappa}$	[-]	Internal penalty factor for DFEM diffusion

λ	[-]	Frequency of the Fourier mode
μ	[-]	Cosine of direction
$\bar{\nu}$	$[\frac{\mathrm{n}}{\mathrm{s}}]$	Average number of neutrons released per fission
ξ	[-]	Second moment drift term
$\hat{\xi}$	[-]	Fourier magnitude for second moment
ρ	[-]	Spectral radius
σ_{a}	$[\frac{1}{\mathrm{cm}}]$	Macroscopic absorption cross section
σ_{f}	$[\frac{1}{\mathrm{cm}}]$	Macroscopic fission cross section
σ_l	$[\frac{1}{\mathrm{cm}}]$	Macroscopic scattering cross section moments
σ_{s}	$[\frac{1}{\mathrm{cm}}]$	Macroscopic scattering cross section
σ_{t}	$[\frac{1}{\mathrm{cm}}]$	Macroscopic total cross section
σ_{tr}	$[\frac{1}{\mathrm{cm}}]$	Macroscopic transport cross section
τ	[cm]	SAAFτ stabilization parameter
τ		Continuous mesh element for the DFEM discretization
$\hat{\tau}$	[cm]	Weight for WLS generalized current formulation
ϕ	$[\frac{1}{\mathrm{cm}^2\mathrm{s}}]$	Scalar flux
$\hat{\phi}$	[-]	Fourier magnitude for scalar flux
ϕ^{inc}	$[\frac{1}{\mathrm{cm}^2\mathrm{s}}]$	Incoming isotropic flux
χ	[-]	Fission spectrum
ψ	$[\frac{1}{\mathrm{cm}^2\mathrm{s}\cdot\mathrm{st}}]$	Angular flux
$\hat{\psi}$	[-]	Fourier magnitude for angular flux
ψ^{inc}	$[\frac{1}{\mathrm{cm}^2\mathrm{s}\cdot\mathrm{st}}]$	Incoming angular flux
$\vec{\Omega}$	[-]	Direction of particle movement
ω_m	[-]	Angular quadrature set weight

Indices

g	Energy group index
i	Spatial cell index, half indices indicate mesh vertices
l	Scattering moment index
k	NDA iteration index
m	Discrete angle index
G	Number of energy groups
L	Number of scattering moments
N	Number of spatial cells
N_{A}	Number of azimuthal angles
M	Number of angles in quadrature set

Mathematical Operators

$\vec{\nabla} f$	Gradient of f
$\vec{\nabla} \cdot f$	Divergence of f
$(\cdot\,,\cdot)_{\mathcal{D}}$	Inner product over the domain interior
$\langle \cdot\,,\cdot \rangle_{\partial\mathcal{D}}$	Inner product over the domain boundary
$\langle \cdot\,,\cdot \rangle_{\Gamma}$	Inner product over the interior interface
$\|\cdot\|_{L_2}$	L_2-norm of a vector
ψ^*	Angular test function
ϕ^*	Isotropic test function
$[\![\cdot]\!]$	DFEM jump operator
$\{\!\{\cdot\}\!\}$	DFEM average operator
$O(\cdot)$	Smaller than the order

TABLE OF CONTENTS

Page

LIST OF FIGURES

FIGURE Page

LIST OF TABLES

TABLE Page

1. INTRODUCTION AND LITERATURE REVIEW

1.1 Purpose

The linear Boltzmann-transport equation describes the movements and interactions of uncharged particles in a background media. Solving the transport equation is of high interest in many fields in science and engineering, including nuclear reactor physics, fusion technology, thermal radiation transport and astrophysics. It describes the transport problem in a high dimensional phase space which requires discretization not only in space but also in angle and energy. Therefore only very simple problems can be solved analytically and numerical methods are required for most practical purposes. Even with rapid development of computational resources, solving the transport equation is still a challenge even on large super computers. Recent development in simulation techniques also fashion more detailed approaches and a reduction in simplifications. This results in a further increase of the computational cost. Efficient ways to invert the transport operator are therefore still needed.

The use of the discrete ordinance methods [10] with source iterations is a common and well proven method to solve the linear Boltzmann transport equation [5]. Over the years researchers developed many improvements to this simple solution process. Many addressed the slow iterative convergence of the source iterations for highly diffusive media, for example the diffusion synthetic acceleration or the nonlinear diffusion acceleration. Still, up to now, no attempt to use diffusion acceleration in problems containing a void could be found in the literature. The low order diffusion equation becomes singular in these regions. The need for void regions rose with recent reduction in simplifications in calculations for advanced reactor designs e.g. High Temperature Gas-cooled Reactors (HTGR) or other gas cooled reactors e.g. the Transient Reactor

Test (TREAT) facility [14] containing voids. In addition these reactors are graphite moderated. The high scattering ratio renders the standard source iteration technique inefficient. Detailed simulations hence need efficient acceleration schemes compatible with voids.

The transport equation is a first order partial-differential equation. The standard solution technique is a sweeping algorithm. Recent research showed that this can be done efficiently and highly scalable on orthogonal meshes [6, 7, 24]. On unstructured meshes the sweeping is more complex [30, 52], but these type of meshes offer a more detailed representation of the problem geometry. Transforming the transport equation into a second order equation offers discretization that results in symmetric positive-definite systems [19]. These can than be solved by highly efficient linear algebra solvers [57], an advantage on unstructured meshes. However most second order forms become singular in voids. Exceptions are the self-adjoint angular flux equation with void treatment (SAAFτ) [76] and the least-squares (LS) equation compatible with voids [23]. The ability for detailed meshing with the ability to solve void regions makes these two equations very interesting for simulations.

In this dissertation we present advances to the nonlinear diffusion acceleration for void regions using second order forms of the transport equation. We consider the weighted least-squares and the self-adjoint angular flux transport equations. We show that these two equations a closely related through the definition of the weight function and how the nonlinear diffusion acceleration can be extended to hold in void regions. Using a Fourier analysis we show the convergence properties of our method for homogeneous and heterogeneous problems. We use several problems to study the numerical behavior and the influence of different discretization schemes.

1.2 Background

Deterministic transport methods are divided into two major groups regarding their angular discretization. Both methods, S_N [10, Chp. 1] and P_N [67, Chp. 9.6 - 9.7], have advantages and disadvantages. The S_N method shows ray effects, artifacts for low scattering problems with localized sources [36, 37, 45, 48]. The P_N method is rotationally invariant and hence does not produce ray-effects, but it gives inaccurate solutions whenever the S_N solutions exhibit ray effects. One major advantage of the S_N method is the decoupling of the directions in the streaming and collision operator. This enables the use of iterative solution techniques for the scattering source [5].

The simplest iterative method is source iterations. It requires the inversion of the streaming and collision operator. Traditionally this first order operator is inverted by sweeping algorithms [52]. Adams [6, 7] and Hawkins [24] showed that this can be done highly efficient and scalable to a large number of processors. Their research is limited to orthogonal meshes. Most sweep algorithms use discontinuous finite elements (DFEM) to discretize space since it is able to robustly handle the streaming of particles across material interfaces [74].

Sweeping algorithms become more difficult to implement on unstructured meshes [52] and the complexity and scalability is not as easy achieved as for structured meshes. Unstructured meshes allow the modeling of complex geometry with less cells, thus reducing the number of unknowns drastically compared to structured meshes.

Several forms of second order equations were introduced throughout the years. The first and most commonly used are the even and odd parity forms [16, 54, 70]. The largest advantage of this form, as listed by Morel and Ghee [47] is the use of continuous finite elements (CFEM). This form of finite elements offers easier and more straight forward discretization on unstructured meshes [19]. It also reduces the

number of unknown needed per cell for the same order of shape functions compared to discontinuous finite elements. The resulting matrix equations are in general symmetric positive definite. This is a highly desirable property, which allows the usage of special, highly efficient solvers, e.g. conjugate gradient [57, Chp. 6.7]. The conjugate gradient algorithm only requires the storage of three solutions vectors, which is a huge advantage compared the general GMRES algorithm. One disadvantage is that the matrix is not a block lower triangular matrix, thus it is not solvable by sweeping techniques. This causes the number of iterations required for convergence to increase with an increasing number of unknowns, whereas it saturates for sweeps. Thus unless a multigrid preconditioner is used, second order methods lose to sweeps with enough unknowns. Recently the self-adjoint angular flux equation (SAAF) equation [47] started to become of interest in the computational community [58, 72, 76]. This second order form has the same advantages as the even-odd parity equations. However it solves for the full angular flux itself, hence some of the disadvantages, e.g. the implicit coupling of reflective boundary conditions, can be avoided [47]. The scheme is used as the main solver in Rattlesnake [75, 76], Idaho National Laboratory's transport code within the MOOSE framework [17].

One of the larger problems with second order forms is the fact, that most of them are unbound in voids. Both the even-odd parity and the SAAF equation contain the total cross section in the denominator [3, 47]. Several ways of dealing with the void problem can be found in literature. De Olivera et al. [12] used ray-tracing across void regions with a second order scheme in optical thicker regions. Ackroyd [3] et al. proposed two methods for the even-odd parity equation, a best approximation method and absorption and reemitting method. Wang [76] extended the SAAF formulation with a void treatment. This introduces a first order derivative but makes the matrix non-symmetric. Hansen at el. [23] developed a second order least-squares form that

is both compatible with voids and the solution technique of source iterations. The later is not given for the standard least-squares form [15]. A similar method using a least-squares functional was introduced by Hai-Tao Ju at al. [22]. Lewis [38] showed that mixed finite elements for the diffusion equation result in a nonsingular response in void regions.

In practical problems the regions of the spatial mesh can have cells that are optical thick and highly diffusive. These problems require discretizations that posses the thick diffusion limit [33]. It has been shown that the second order form have this property [4, 23, 46, 47]. A second necessary property is causality. The definition of causality in this context is that particles are only influenced by upstream information. Given a point $\vec{x}$ and a direction, $\vec{\Omega}$, the associated "upstream" points in an infinite medium are defined by

$$\vec{x}_{\text{upstream}} = \vec{x} - s\vec{\Omega} \qquad \forall s \in \mathcal{R}^{+}. \tag{1.1}$$

Second order forms however might be influenced by downstream information or information ahead. Problems with causality of this formulations occur at material interfaces from optical thin into optical thick material regions. A weight function ameliorates the problems with causality of the least-squares formulation [80]. However the proposed weight function is singular in voids which renders the equation singular in voids with zero cross sections.

Least-squares methods are inherently non-conservative. Peterson et al. [53] used a conservative low order form in the nonlinear diffusion acceleration to enforce particle conservation, thus the NDA algorithm offers advantages also in problems with low or no scattering. However, the resulting system of equations is not consistent. Consistency in this context means that the transport and the drift-diffusion solution

converge to the same answer.

1.3 The transport equation

The derivation of the linear Boltzman transport can be found in many textbooks [39, 56, 67]. It is an integro-differential equation with a first order partial derivative and describes the balance of neutron sources and sinks. It has up to seven independent variables and hence requires not only discretization in space but also in angle and energy. This dissertation focuses on the neutron transport equations since our main applications are reactor physics and eigenvalue calculations. On an arbitrary domain $\mathcal{D}$ the transport equation is

$$\frac{1}{v}\frac{\partial}{\partial t}\psi + \vec{\Omega}\cdot\vec{\nabla}\psi + \sigma_{\mathrm{t}}\psi = \int_0^\infty \int_{4\pi} \sigma_{\mathrm{s}}\left(\vec{\Omega}\cdot\vec{\Omega}', E' \to E\right)\psi\left(\vec{\Omega}', E'\right)\, d\vec{\Omega}'\, dE' + \frac{\chi}{4\pi}\int_0^\infty \int_{4\pi} \bar{\nu}\sigma_{\mathrm{f}}\left(E'\right)\psi\left(\vec{\Omega}', E'\right)\, d\vec{\Omega}'\, dE' + \frac{q}{4\pi} \quad (1.2)$$

with the associated Dirichlet boundary condition on the non-reentry boundary $\partial\mathcal{D}$ with outwards normal $\vec{n}$

$$\psi\left(\vec{x}_b,\vec{\Omega},E\right) = \psi^{inc}\left(\vec{x}_b,\vec{\Omega},E\right), \qquad \forall \vec{x}_b \in \partial\mathcal{D}, \quad \vec{\Omega}\cdot\vec{n}\left(\vec{x}_b\right) < 0, \quad E \in \mathbb{R}^+. \quad (1.3)$$

To keep the equation short, most variable dependencies were omitted and only the ones necessary were included. The used symbols are standard in most textbooks. $\psi\left(\vec{x},\vec{\Omega},E\right)$ is the angular flux at position $\vec{x} \in \mathcal{D}$ in direction $\vec{\Omega}$ with energy E and velocity v. The macroscopic total cross section is denoted by $\sigma_{\mathrm{t}}\left(\vec{x},E\right)$, $\sigma_{\mathrm{s}}\left(\vec{\Omega}\cdot\vec{\Omega}', E' \to E\right)$ is the scattering and $\sigma_{\mathrm{f}}\left(\vec{x},E\right)$ the fission macroscopic cross section. The average number of neutrons released by fission is $\bar{\nu}\left(\vec{x}\right)$ and $\chi\left(\vec{x},E\right)$ is the resulting fission spectrum. The distributed source is denoted by $q\left(\vec{x},E\right)$.

We define two auxiliary variables which are of great importance in transport

problems. The scalar flux is obtain by integration over all angles

$$\phi \equiv \int_{4\pi} \psi \, d\vec{\Omega}. \tag{1.4}$$

It is used to calculate reaction rates including energy release from fission and is in most cases the main quantity of interest in reactor physics calculations. The neutron current

$$\vec{J} \equiv \int_{4\pi} \vec{\Omega}\psi \, d\vec{\Omega} \tag{1.5}$$

relates to the net movement of neutrons, which is important to determine the leakage of a system.

In this dissertation only two types of steady-state cases were considered, source and eigenvalue calculations, thus the time derivative vanishes. We also express the scattering term with a spherical moments expansion

$$\vec{\Omega} \cdot \vec{\nabla}\psi + \sigma_{\mathrm{t}}\psi = \int_0^\infty \sum_{l=0}^{\infty} \sum_{p=-l}^{l} \frac{2l+1}{4\pi} \mathrm{Y}_l^p \left(\vec{\Omega}\right) \sigma_l \left(E' \to E\right) \phi_l^p \left(E'\right) \, dE' + \frac{\chi}{4\pi} \int_0^\infty \bar{\nu}\sigma_{\mathrm{f}} \left(E'\right) \phi \left(E'\right) \, dE' + \frac{q}{4\pi} \tag{1.6}$$

with the angular flux moments

$$\phi_l^p \equiv \int_{4\pi} \mathrm{Y}_l^p \left(\vec{\Omega}\right) \psi \, d\vec{\Omega} \tag{1.7}$$

and the scattering moments

$$\sigma_l \left(E' \to E\right) \equiv 2\pi \int_{-1}^{1} \sigma_{\mathrm{s}} \left(E' \to E, \mu\right) P_l \left(\mu\right) \, d\mu \tag{1.8}$$

In this expansion Y_l^p denotes the spherical harmonics function and P_l is the Legendre polynomial of lth order. This expansion is exact for an infinite number of terms, in practice however, the scattering expansion is truncated at a sufficient large L.

For the S_N method the angular flux is evaluated along discrete directions with the angular quadrature $\left\{\vec{\Omega}_m, \omega_m\right\}_{m=1}^{M}$ [10, Ch. 1]

$$\vec{\Omega}_m \cdot \vec{\nabla}\psi_m + \sigma_\mathrm{t}\psi_m = \int_0^\infty \sum_{l=0}^{\infty}\sum_{p=-l}^{l} \frac{2l+1}{4\pi}\mathrm{Y}_l^p\left(\vec{\Omega}_m\right)\sigma_l\left(E' \to E\right)\phi_l^p\left(E'\right)\,dE' + \frac{\chi}{4\pi}\int_0^\infty \bar{\nu}\sigma_\mathrm{f}\left(E'\right)\phi\left(E'\right)\,dE' + \frac{q}{4\pi} \quad (1.9)$$

The S_N methods decouples the direction on the left hand side of the transport equation. The directions are only coupled by the scattering and fission operators. This allows to invert the streaming and collision operator independently and makes iterative techniques possible.

The energy is treated with the multi-group approximation [20, 27]. The energy range is divided into finite groups and the values are averaged over these groups. The transport equation then becomes

$$\vec{\Omega}_m \cdot \vec{\nabla}\psi_{m,g} + \sigma_\mathrm{t}\psi_{m,g} = \sum_{g'=1}^{G}\sum_{l=0}^{L}\sum_{p=-l}^{l} \frac{2l+1}{4\pi}\mathrm{Y}_l^p\left(\vec{\Omega}_m\right)\sigma_{l,g'\to g}\phi_{l,g'}^p + \frac{\chi_g}{4\pi}\sum_{g'=1}^{G}\bar{\nu}\sigma_{\mathrm{f},g'}\phi_{g'} + \frac{q_g}{4\pi} \quad (1.10)$$

Of special interest in reactor physics are criticality problems. The largest eigenvalue k_eff is called the neutron multiplication factor. It determines the behavior of the neutron population over times. Corresponding to the eigenvalue is the eigenmode, the

spatial distribution of the flux. The fission source is renormalized with $\frac{1}{k_{\text{eff}}}$ to obtain

$$\vec{\Omega}_m \cdot \vec{\nabla}\psi_{m,g} + \sigma_{\text{t}}\psi_{g,m} = \sum_{g'=1}^{G}\sum_{l=0}^{L}\sum_{p=-l}^{l} \frac{2l+1}{4\pi} \mathrm{Y}_l^p\left(\vec{\Omega}_m\right) \sigma_{l,g'\to g}\phi_{l,g'}^p + \frac{1}{k_{\text{eff}}}\frac{\chi_g}{4\pi}\sum_{g'=1}^{G}\bar{\nu}\sigma_{\text{f},g'}\phi_{g'} + \frac{q_g}{4\pi} \quad (1.11)$$

For most of this dissertation it is sufficient to consider the mono-energetic transport equation. The acceleration techniques that we will discuss are not dependent on energy. This makes the derivations easier to understand, the extension to multi-groups is a minor complexity. If necessary, complications for the multi-group approximation will be discussed, since the multi-group approximation will be needed for the C5G7 benchmark. The transport equation simplifies for one energy group to

$$\vec{\Omega} \cdot \vec{\nabla}\psi_m + \sigma_{\text{t}}\psi_m = \sum_{l=0}^{L}\sum_{p=-l}^{l} \frac{2l+1}{4\pi} \mathrm{Y}_l^p\left(\vec{\Omega}_m\right) \sigma_l\phi_l^p + \frac{\bar{\nu}\sigma_{\text{f}}}{4\pi}\phi + \frac{q}{4\pi} \quad (1.12)$$

and the corresponding mono-energetic eigenvalue problem is

$$\vec{\Omega} \cdot \vec{\nabla}\psi_m + \sigma_{\text{t}}\psi_m = \sum_{l=0}^{L}\sum_{p=-l}^{l} \frac{2l+1}{4\pi} \mathrm{Y}_l^p\left(\vec{\Omega}_m\right) \sigma_l\phi_l^p + \frac{1}{k_{\text{eff}}}\frac{\bar{\nu}\sigma_{\text{f}}}{4\pi}\phi + \frac{q}{4\pi} \quad (1.13)$$

Most multi-group transport problems are solved by solving mono-energetic transport problems with cross-group scattering and fission treated as external sources. Hence the one-group transport equation is the heart of every more complex problem and the efficient inversion of it is the foundation of all S_N transport codes.

In some cases it is of advantage to express the transport equation in operator form. We will make use of this expression in the derivation of the least-squares form. The equation is

$$\mathcal{L}\psi = \mathcal{S}\psi + \mathcal{F}\psi + \mathcal{Q} \quad (1.14a)$$

where

$$\mathcal{L} \equiv \vec{\Omega} \cdot \vec{\nabla} + \sigma_{\mathrm{t}} \tag{1.14b}$$

is the streaming and collision operator,

$$\mathcal{S} \equiv \int_0^\infty dE' \int_{4\pi} d\vec{\Omega}' \, \sigma_{\mathrm{s}} \left(\vec{\Omega} \cdot \vec{\Omega}', E' \to E \right) \tag{1.14c}$$

the scattering operator and

$$\mathcal{F} \equiv \frac{\chi}{4\pi} \int_0^\infty dE' \int_{4\pi} d\vec{\Omega}' \, \bar{\nu}\sigma_{\mathrm{f}} \left(\vec{\Omega}', E' \right) \tag{1.14d}$$

the fission source operator. The distributed source is denoted with $\mathcal{Q}$. The moments operator

$$\mathcal{M} \equiv \int_{4\pi} d\vec{\Omega} \mathrm{Y}_l^p \left(\vec{\Omega} \right), \qquad l = 0 \ldots L, \quad p = -l \ldots l \tag{1.15}$$

converts the angular flux into the flux moments and the operator $\mathcal{D}$ calculates the angular flux from the flux moments. The eigenvalue equation in operator is written as

$$\mathcal{L}\psi \equiv \mathcal{S}\psi + \frac{1}{k_{\mathrm{eff}}} \mathcal{F}\psi + \mathcal{Q} \tag{1.16}$$

1.4 Acceleration

The most basic iteration scheme for the mono-energetic transport Eq. (1.12) is the source iteration (SI) [5]. For easier understanding only the scattering source is considered and the fission source is neglect. The efficient solve of this problem is essential for more complex problems e.g. multi-group and eigenvalue problems. Equation (1.12) is coupled between the directions only by the scattering source. By using a lagged estimate for the flux moments (Eq. (1.7)) the directions decouple and it is possible to solve them independently. The SI scheme for the $k+1$st iteration

given an iterate of the flux moments at k is

$$\vec{\Omega}_m \cdot \vec{\nabla}\psi_m^{k+\frac{1}{2}} + \sigma_{\mathrm{t}}\psi_m^{k+\frac{1}{2}} = \sum_{l=0}^{L}\sum_{p=-l}^{l} \frac{2l+1}{4\pi} \mathrm{Y}_l^p\left(\vec{\Omega}_m\right)\sigma_l\phi_l^{p,k} + \frac{q}{4\pi} \tag{1.17a}$$

$$\phi_l^{p,k+1} = \sum_{m=1}^{M} \omega_m \mathrm{Y}_l^p\left(\vec{\Omega}_m\right)\psi_m^{k+\frac{1}{2}} \tag{1.17b}$$

At the beginning of each iteration the old estimate for the angular flux is used to calculate the flux moments and the scattering source. Equation (1.17a) is solve for a new estimate of the angular flux $\psi^{k+\frac{1}{2}}$. Base on the new estimate Eq. (1.17b) is used to calculate the new moments of the scalar flux. Using the operator notation we can express the source iterations as

$$\phi^{k+1} = \mathcal{M}\left(\mathcal{L}^{-1}\mathcal{S}\mathcal{D}\phi^k + \mathcal{L}^{-1}\mathcal{Q}\right) \tag{1.18}$$

For a zero initial guess of the scattering source the SI scheme produces at iteration k the flux of particles that have scattered at most $k-1$ times. We can see easily that for small systems with low scattering this scheme converges rapidly. But for diffusive systems with low absorption and almost no leakage SI converges slowly, hence is inefficient and expensive.

A measure of the efficiency of an iteration scheme is the error reduction per iteration. For the analysis of the convergence behavior we consider the isotropic case in an infinite homogeneous medium. Since SI iterates on the scattering source the error in the scalar flux determines the error in the angular fluxes. Given the exact scalar flux solution ϕ the error is obtained by

$$\delta\phi^k \equiv \phi^k - \phi. \tag{1.19}$$

where $\delta\phi^k$ denotes the scalar flux error at the kth iteration. The error reduction can be expressed as

$$\rho \equiv \frac{\delta\phi^{k+1}}{\delta\phi^k} \tag{1.20}$$

with ρ the spectral radius. ρ is the eigenvalue with the largest magnitude of the operator $\mathcal{ML}^{-1}\mathcal{SD}$ from Eq. (1.18). A negative eigenvalue implies oscillations of the numerical value around the exact solution.

For the infinite homogeneous problem with the total cross section σ_t and the isotropic scattering cross section σ_s, the convergence behavior can be analyzed with a Fourier analysis. The spectral radius of the SI scheme is $\rho = c$, where c denotes the scattering ratio

$$c \equiv \frac{\sigma_\mathrm{s}}{\sigma_\mathrm{t}} \tag{1.21}$$

This results confirms the physical interpretation discussed earlier. Hence for an infinite pure scatterer, SI never converges. This underlines the need of acceleration techniques in materials with a high scattering ratio c.

One of the most efficient acceleration techniques for the SI process is the diffusion-synthetic acceleration (DSA). The concept of synthetic acceleration was first introduced by Kopp [29]. The basic idea is to use an additive correction to the SI scheme. An estimate for the error in the scalar flux is obtained by solving a low-order diffusion equation. The scheme can be considered as a preconditioned Richardson iteration. Gelberd and Hageman [18] explored as an alternative to the diffusion equation the use of the S_2-equation as low order equation. Reed [55] showed that the DSA scheme is only conditionally stable using diamond-differenced S_N with cell-centered differenced diffusion. Alcouffe [8] resolved this by showing that DSA requires a consistent spatial discretization. His result showed that it is possible to use DSA in an stable and efficient manner even for optical thick cells given consistency. However a consistent

discretization is not easily achieved. Starting from there, a lot of research was performed to extend and improve the DSA scheme. A detailed description is given in the review article by Adams and Larsen [5]. The major drawback of the DSA methods is, that the extension for eigenvalue problems is difficult [69, Chp. VII]. This limits the use of this method in reactor physics calculations.

A second type of accelerations methods are the nonlinear methods. The group of methods are not preconditioned Richardson schemes, since they normally obtain a different transport solution than the unaccelerated SI scheme. The first method, Quasidiffusion, was developed by Gol'din [21]. It uses the Eddington tensor, informed from a transport solve, in a diffusion equation. For a linearly anisotropic angular flux the Quasidiffusion method reduces to the normal diffusion equation [44, 43]. As a nonlinear method it is also applicable to eigenvalue problems [9], a fact that is especially of interest in reactor calculations.

Related to the Quasidiffusion method is the nonlinear diffusion acceleration (NDA) method first introduced by Smith [65]. This method corrects the diffusion equation by introducing a drift term with the drift vector calculated from a high-order solution. Further research by Willen et al. [77, 78] describe how to accelerate problems with anisotropic scattering, while Park et al. [51] used NDA for criticality problems. Since the nonlinear acceleration techniques solve for the scalar flux instead of a correction, implementation of eigenvalue problems is straight forward. This makes the NDA method interesting where DSA struggles. Schunert et al. [61, 62, 63] analyzed the NDA scheme for first order transport with DFEM discretization, while Wang et al. [72, 76] use NDA in combination with the second order SAAF equation. Peterson et al. [53] utilize a non-consistent NDA to ensure particle conservation for the non-conservative LS equation, a technique we will also use in this dissertation.

However, both Quasidiffusion and NDA are not defined in voids without modifica-

tion. Schunert et al. [59] used a directional, nonlocal diffusion coefficient proposed by Morel [50]. This diffusion coefficient is well defined in finite voids. Schunert showed that using this directional diffusion tensor improved the convergence for heterogeneous problems, but did not consider pure void regions. Wang [76] introduced a void treatment for the SAAF equation, but still uses the classical diffusion coefficient, which is singular in voids.

1.5 Structure

This dissertation first introduces in Chapter 2 the second order forms of the transport equation, the weighted least squares (WLS) equation and the self-adjoint angular flux equation (SAAF) and the SAAFτ equation, which includes a void treatment. We will discuss how the WLS and SAAF equations are related by a weight function and how to optimize the weight function in voids.

Chapter 3 derives the NDA for the second order transport equation. With the help of a Fourier analysis, the NDA scheme is extended for geometries with void regions using a nonlocal definition of the diffusion coefficient and a combination of neutron current formulations. These modifications are then extensively studied for convergence properties in heterogeneous problems, including problems with voids.

Numerical results are presented in Chapter 4. We first analyze simple one-dimensional problems before we move on to a more complex reactor physics problem, a modified version of the C5G7 benchmark. To overcome an extended solution space of the drift-diffusion equation in voids, several discretization schemes for the low-order equation were tested additionally to the non-local diffusion coefficient as proof of concepts. The use of a discontinuous scheme restores partially the causality and improves significantly the results for coarse meshes. An artificial diffusion coefficient also showed better results in voids than the non-local diffusion coefficient.

In the final chapter we put the accomplishments of this dissertation into context and give some ideas for further work.

2. SECOND ORDER FORMS OF THE TRANSPORT EQUATION*

2.1 Self-Adjoint Angular Flux Equation

The self-adjoint angular flux (SAAF) equation was first introduced by Pomraning and Clark [54]. They derived the SAAF equation by the means of a purely algebraic equation. However, their derivation necessitated the assumption of a spatially constant cross section. Ackroyed [2] derived the full three dimensional SAAF equation without any assumptions. He showed that the SAAF equation is the Euler-Lagrange equation for a certain generalized least-squares functional. A simpler purely algebraic derivation was presented by Morel and McGhee [47].

The SAAF equation solves for the full range angular flux instead of either the even or odd-parity components of the classical self-adjoint methods. Incoming and outgoing directions couple in the same manner as in the first order transport equation Eq. (1.2). This leads to a simpler implementation of reflective boundary conditions.

We will derive the steady-state mono-energetic SAAF equation for simplicity. The extension to multi-group is straight forward. The derivation starts with the first order steady state transport Eq. (1.14a) and replace the streaming and collision operator Eq. (1.14b)

$$\vec{\Omega} \cdot \psi + \sigma_{\mathrm{t}} \psi = \mathcal{S}\psi + \mathcal{F}\psi + \mathcal{Q} \tag{2.1}$$

We solve Eq. (2.1) for the angular flux

$$\psi = -\frac{1}{\sigma_{\mathrm{t}}} \vec{\Omega} \cdot \vec{\nabla}\psi + \frac{1}{\sigma_{\mathrm{t}}} \mathcal{S}\psi + \frac{1}{\sigma_{\mathrm{t}}} \mathcal{F}\psi + \frac{1}{\sigma_{\mathrm{t}}} \mathcal{Q} \tag{2.2}$$

*Part of the data reported in this chapter is reprinted with permission from *Nonlinear Diffusion Acceleration in Voids for the Weighted Least-Square Transport Equation* by Hans R. Hammer, Jim E. Morel, and Yaqi Wang. M&C 2017 - International Conference on Mathematics & Computational Methods Applied to Nuclear Science & Engineering, 16-20 April 2017.

and substitute this into the streaming term in Eq. (2.1) to obtain the SAAF equation

$$-\vec{\Omega}\cdot\vec{\nabla}\left[\frac{1}{\sigma_{\mathrm{t}}}\vec{\Omega}\cdot\vec{\nabla}\psi\right]+\sigma_{\mathrm{t}}\psi=\mathcal{S}\psi+\mathcal{F}\psi+\mathcal{Q}-\vec{\Omega}\cdot\vec{\nabla}\left[\frac{1}{\sigma_{\mathrm{t}}}\mathcal{S}\psi+\frac{1}{\sigma_{\mathrm{t}}}\mathcal{F}\psi+\frac{1}{\sigma_{\mathrm{t}}}\mathcal{Q}\right] \quad (2.3a)$$

with the boundary conditions

$$\psi\left(\vec{x}_b,\vec{\Omega}\right)=\psi^{\mathrm{inc}}\left(\vec{x}_b,\vec{\Omega}\right), \qquad \forall\vec{x}_b\in\partial\mathcal{D}, \quad \vec{\Omega}\cdot\vec{n}<0 \quad (2.3b)$$

$$\vec{\Omega}\cdot\vec{\nabla}\psi\left(\vec{x}_b\right)+\sigma_{\mathrm{t}}\psi\left(\vec{x}_b\right)=\mathcal{S}\psi\left(\vec{x}_b\right)+\mathcal{F}\psi\left(\vec{x}_b\right)+\mathcal{Q}\psi\left(\vec{x}_b\right), \qquad \vec{\Omega}\cdot\vec{n}>0 \quad (2.3c)$$

With the definitions for the scattering and fission operators Eqs. (1.14c) and (1.14d) the multi-group SAAF equation becomes

$$\begin{aligned}-\vec{\Omega}\cdot\vec{\nabla}\left[\frac{1}{\sigma_{\mathrm{t},g}}\vec{\Omega}\cdot\vec{\nabla}\psi_g\right]+\sigma_{\mathrm{t},g}\psi_g=&\sum_{g'=1}^{G}\sum_{l=0}^{L}\sum_{p=-l}^{l}\frac{2l+1}{4\pi}\mathrm{Y}_l^p\left(\vec{\Omega}\right)\sigma_{l,g'\to g}\phi_{l,g'}^p\\&+\frac{\chi_g}{4\pi}\sum_{g'=1}^{G}\bar{\nu}\sigma_{\mathrm{f},g'}\phi_{g'}+\frac{q_g}{4\pi}-\vec{\Omega}\cdot\vec{\nabla}\left[\frac{1}{\sigma_{\mathrm{t},g}}\sum_{g'=1}^{G}\sum_{l=0}^{L}\sum_{p=-l}^{l}\frac{2l+1}{4\pi}\mathrm{Y}_l^p\left(\vec{\Omega}\right)\sigma_{l,g'\to g}\phi_{l,g'}^p\right.\\&\left.+\frac{1}{\sigma_{\mathrm{t},g}}\frac{\chi_g}{4\pi}\sum_{g'=1}^{G}\bar{\nu}\sigma_{\mathrm{f},g'}\phi_{g'}+\frac{1}{\sigma_{\mathrm{t},g}}\frac{q_g}{4\pi}\right] \quad (2.4)\end{aligned}$$

and the mono-energetic steady state SAAF equation simplifies to

$$\begin{aligned}-\vec{\Omega}\cdot\vec{\nabla}\left[\frac{1}{\sigma_{\mathrm{t}}}\vec{\Omega}\cdot\vec{\nabla}\psi\right]+\sigma_{\mathrm{t}}\psi=&\sum_{l=0}^{L}\sum_{p=-l}^{l}\frac{2l+1}{4\pi}\mathrm{Y}_l^p\left(\vec{\Omega}\right)\sigma_l\phi_l^p+\frac{1}{4\pi}\bar{\nu}\sigma_{\mathrm{f}}\phi+\frac{q}{4\pi}\\&-\vec{\Omega}\cdot\vec{\nabla}\left[\frac{1}{\sigma_{\mathrm{t}}}\sum_{l=0}^{L}\sum_{p=-l}^{l}\frac{2l+1}{4\pi}\mathrm{Y}_l^p\left(\vec{\Omega}\right)\sigma_l\phi_l^p+\frac{1}{\sigma_{\mathrm{t}}}\frac{1}{4\pi}\bar{\nu}\sigma_{\mathrm{f}}\phi+\frac{q}{4\pi\sigma_{\mathrm{t}}}\right] \quad (2.5)\end{aligned}$$

Equation (2.5) can be solved using the spherical harmonics (P_N) [32] or the discrete

ordinance (S_N) [72] method. We will concentrate on the S_N method, since this method is compatible with source iterations and corresponding acceleration. Given a quadrature $\{\psi_m, \omega_m\}$, the angular flux can be expressed along the direction $\vec{\Omega}_m$ and we obtain the S_N SAAF equation. To derive the weak form we first multiply Eq. (2.15) by a test function ψ_m^* and integrate over the whole domain. Using integration by parts on all terms containing a derivative we obtain for a specific direction $m = 1 \dots M$

$$\begin{aligned}
&\left(\frac{1}{\sigma_\mathrm{t}}\vec{\Omega}\cdot\vec{\nabla}\psi_m, \vec{\Omega}\cdot\vec{\nabla}\psi_m^*\right)_{\mathcal{D}} + \left(\sigma_\mathrm{t}\psi_m, \psi_m^*\right)_{\mathcal{D}} - \left\langle \vec{\Omega}\cdot\vec{\nabla}\psi_m, \frac{1}{\sigma_\mathrm{t}}\left(\vec{\Omega}\cdot\vec{n}\right)\psi_m^* \right\rangle_{\partial\mathcal{D}} \\
&\qquad = \left(\sum_{l=0}^{L}\sum_{p=-l}^{l}\frac{2l+1}{4\pi}\mathrm{Y}_l^p\left(\vec{\Omega}_m\right)\sigma_l\phi_l^p, \frac{1}{\sigma_\mathrm{t}}\vec{\Omega}\cdot\vec{\nabla}\psi_m^* + \psi_m^*\right)_{\mathcal{D}} \\
&\qquad + \left(\frac{\bar{\nu}\sigma_\mathrm{f}}{4\pi}\phi, \frac{1}{\sigma_\mathrm{t}}\vec{\Omega}\cdot\vec{\nabla}\psi_m^* + \psi_m^*\right)_{\mathcal{D}} + \left(\frac{q}{4\pi}, \frac{1}{\sigma_\mathrm{t}}\vec{\Omega}\cdot\vec{\nabla}\psi_m^* + \psi_m^*\right)_{\mathcal{D}} \\
&\qquad - \left\langle \sum_{l=0}^{L}\sum_{p=-l}^{l}\frac{2l+1}{4\pi}\mathrm{Y}_l^p\left(\vec{\Omega}_m\right)\sigma_l\phi_l^p + \frac{\bar{\nu}\sigma_\mathrm{f}}{4\pi}\phi + \frac{q}{4\pi}, \frac{1}{\sigma_\mathrm{t}}\left(\vec{\Omega}\cdot\vec{n}\right)\psi_m^* \right\rangle_{\partial\mathcal{D}}
\end{aligned} \tag{2.6}$$

where

$$\left(\cdot,\cdot\right)_{\mathcal{D}} \equiv \int_{\mathcal{D}} dV \tag{2.7}$$

is the standard spatial inner product and

$$\left\langle\cdot,\cdot\right\rangle_{\partial\mathcal{D}} \equiv \oint_{\partial\mathcal{D}} dA \tag{2.8}$$

is the corresponding surface integral. Using Eq. (2.2) on the boundary we can simplify the boundary integrals and obtain the weak form of the SAAF equation: Given a trial space $W_{\mathcal{D}}$, consisting of continuous basis functions, the weak form for a specific

direction $m = 1 \dots M$ is as follows: find $\psi_m \in W_{\mathcal{D}}$ such that

$$\begin{aligned}\left(\frac{1}{\sigma_{\mathrm{t}}}\vec{\Omega}\cdot\vec{\nabla}\psi_m, \vec{\Omega}\cdot\vec{\nabla}\psi_m^*\right)_{\mathcal{D}} + \left(\sigma_{\mathrm{t}}\psi_m, \psi_m^*\right)_{\mathcal{D}} + \left\langle \psi_m, \left(\vec{\Omega}\cdot\vec{n}\right)\psi_m^*\right\rangle_{\partial\mathcal{D}} \\ = \left(\sum_{l=0}^{L}\sum_{p=-l}^{l}\frac{2l+1}{4\pi}\mathrm{Y}_l^p\left(\vec{\Omega}_m\right)\sigma_l\phi_l^p, \frac{1}{\sigma_{\mathrm{t}}}\vec{\Omega}\cdot\vec{\nabla}\psi_m^* + \psi_m^*\right)_{\mathcal{D}} \\ + \left(\frac{\bar{\nu}\sigma_{\mathrm{f}}}{4\pi}\phi, \frac{1}{\sigma_{\mathrm{t}}}\vec{\Omega}\cdot\vec{\nabla}\psi_m^* + \psi_m^*\right)_{\mathcal{D}} + \left(\frac{q}{4\pi}, \frac{1}{\sigma_{\mathrm{t}}}\vec{\Omega}\cdot\vec{\nabla}\psi_m^* + \psi_m^*\right)_{\mathcal{D}} \quad (2.9)\end{aligned}$$

The discretization of the SAAF generates in general a sparse symmetric positive-definite matrix and not a lower triangular matrix as the first order equation with DFEM sweeping algorithm normally does. While a symmetric positive-definite matrix allows the use of efficient numerical solution techniques, it prevent the use of sweeping methods traditionally employed for the first order transport equation. The total cross sections appears in Eq. (2.2) in the denominator, hence also in the SAAF equation. Therefore the SAAF equation is not defined in voids. Derivation of the multi-group and eigenvalue equations is similar and straight forward.

2.2 Self-Adjoint Angular Flux Equation with void treatment

The standard SAAF equation is not defined in voids. Wang et al. [76] proposed a modified version of the SAAF equation that is well defined in voids. Here we shall give a short derivation of the self-adjoint angular-flux equation with void treatment (SAAFτ). Further details are described in the paper by Wang.

We first define the stabilization parameter τ as a function of a cell's optical thickness

$$\tau \equiv \begin{cases} \frac{1}{\sigma_{\mathrm{t}}}, & \sigma_{\mathrm{t}}h \geq \zeta \\ \frac{h}{\zeta}, & \sigma_{\mathrm{t}}h < \zeta \end{cases} \quad (2.10)$$

with ζ the stabilization threshold, normally set to 0.5 as described in the reference [76]. We subtract and add $\tau\sigma_{\mathrm{t}}\psi$ to ψ to obtain

$$\psi = (1 - \tau\sigma_{\mathrm{t}})\,\psi + \tau\sigma_{\mathrm{t}}\psi \tag{2.11}$$

Next we substitute Eq. (2.2) into the last term of Eq. (2.11) to get

$$\psi = (1 - \tau\sigma_{\mathrm{t}})\,\psi + \tau\left(-\vec{\Omega}\cdot\vec{\nabla}\psi + \mathcal{S}\psi + \mathcal{F}\psi + \mathcal{Q}\right) \tag{2.12}$$

Substituting from Eq. (2.12) into the streaming term of the transport Eq. (2.1) we get the SAAFτ equation

$$\begin{aligned} &-\vec{\Omega}\cdot\vec{\nabla}\left[\tau\vec{\Omega}\cdot\vec{\nabla}\psi\right] + \vec{\Omega}\cdot\vec{\nabla}\left[(1-\sigma_{\mathrm{t}}\tau)\,\psi\right] + \sigma_{\mathrm{t}}\psi \\ &\qquad = \mathcal{S}\psi + \mathcal{F}\psi + \mathcal{Q} - \vec{\Omega}\cdot\vec{\nabla}\left[\tau\mathcal{S}\psi + \tau\mathcal{F}\psi + \tau\mathcal{Q}\right] \end{aligned} \tag{2.13a}$$

with the boundary conditions

$$\psi\left(\vec{x}_b, \vec{\Omega}\right) = \psi^{\mathrm{inc}}\left(\vec{x}_b, \vec{\Omega}\right), \qquad \forall \vec{x}_b \in \partial\mathcal{D}, \quad \vec{\Omega}\cdot\vec{n} < 0 \tag{2.13b}$$

$$\vec{\Omega}\cdot\vec{\nabla}\psi\left(\vec{x}_b\right) + \sigma_{\mathrm{t}}\psi\left(\vec{x}_b\right) = \mathcal{S}\psi\left(\vec{x}_b\right) + \mathcal{F}\psi\left(\vec{x}_b\right) + \mathcal{Q}\psi\left(\vec{x}_b\right), \qquad \vec{\Omega}\cdot\vec{n} > 0 \tag{2.13c}$$

The multi-group SAAFτ equation

$$\begin{aligned} &-\vec{\Omega}\cdot\vec{\nabla}\left[\tau_g\vec{\Omega}\cdot\vec{\nabla}\psi_g\right] + \vec{\Omega}\cdot\vec{\nabla}\left[(1-\sigma_{\mathrm{t},g}\tau_g)\,\psi_g\right] + \sigma_{\mathrm{t},g}\psi_g \\ &\qquad = \sum_{g'=1}^{G}\sum_{l=0}^{L}\sum_{p=-l}^{l}\frac{2l+1}{4\pi}\mathrm{Y}_l^p\left(\vec{\Omega}\right)\sigma_{l,g'\to g}\phi_{l,g'}^p + \frac{\chi_g}{4\pi}\sum_{g'=1}^{G}\bar{\nu}\sigma_{\mathrm{f},g'}\phi_{g'} + \frac{q_g}{4\pi} \\ &-\vec{\Omega}\cdot\vec{\nabla}\left[\tau_g\sum_{g'=1}^{G}\sum_{l=0}^{L}\sum_{p=-l}^{l}\frac{2l+1}{4\pi}\mathrm{Y}_l^p\left(\vec{\Omega}\right)\sigma_{l,g'\to g}\phi_{l,g'}^p + \frac{\tau_g\chi_g}{4\pi}\sum_{g'=1}^{G}\bar{\nu}\sigma_{\mathrm{f},g'}\phi_{g'} + \frac{\tau_g q_g}{4\pi}\right] \end{aligned} \tag{2.14}$$

is similar to the SAAF form Eq. (2.4) expect for a first order term in case of optical thin cells. Simplifying to one group gives

$$-\vec{\Omega}\cdot\vec{\nabla}\left[\tau\vec{\Omega}\cdot\vec{\nabla}\psi\right]+\vec{\Omega}\cdot\vec{\nabla}\left[\left(1-\sigma_{\mathrm{t}}\tau\right)\psi\right]+\sigma_{\mathrm{t}}\psi=\sum_{l=0}^{L}\sum_{p=-l}^{l}\frac{2l+1}{4\pi}\mathrm{Y}_{l}^{p}\left(\vec{\Omega}_{m}\right)\sigma_{l}\phi_{l}^{p}$$
$$+\frac{1}{4\pi}\bar{\nu}\sigma_{\mathrm{f}}\phi+\frac{q}{4\pi}-\vec{\Omega}\cdot\vec{\nabla}\left[\tau\sum_{l=0}^{L}\sum_{p=-l}^{l}\frac{2l+1}{4\pi}\mathrm{Y}_{l}^{p}\left(\vec{\Omega}\right)\sigma_{l}\phi_{l}^{p}+\tau\frac{\bar{\nu}\sigma_{\mathrm{f}}}{4\pi}\phi+\tau\frac{q}{4\pi}\right] \quad (2.15)$$

The weak form can be derived as shown in Section 2.1. The resulting weak form for the S_N SAAFτ is: Given a trial space $W_{\mathcal{D}}$, consisting of continuous basis functions, the weak form for a specific direction $m = 1 \dots M$ is as follows: find $\psi_m \in W_{\mathcal{D}}$ such that

$$\left(\tau\vec{\Omega}\cdot\vec{\nabla}\psi_{m},\vec{\Omega}\cdot\vec{\nabla}\psi_{m}^{*}\right)_{\mathcal{D}}+\left(\left(1-\sigma_{\mathrm{t}}\tau\right)\psi_{m},\vec{\Omega}\cdot\vec{\nabla}\psi_{m}^{*}\right)_{\mathcal{D}}+\left(\sigma_{\mathrm{t}}\psi_{m},\psi_{m}^{*}\right)_{\mathcal{D}}$$
$$+\left\langle\psi_{m},\left(\vec{\Omega}\cdot\vec{n}\right)\psi_{m}^{*}\right\rangle_{\partial\mathcal{D}}=\left(\sum_{l=0}^{L}\sum_{p=-l}^{l}\frac{2l+1}{4\pi}\mathrm{Y}_{l}^{p}\left(\vec{\Omega}_{m}\right)\sigma_{l}\phi_{l}^{p},\tau\vec{\Omega}\cdot\vec{\nabla}\psi_{m}^{*}+\psi_{m}^{*}\right)_{\mathcal{D}}$$
$$+\left(\frac{\bar{\nu}\sigma_{\mathrm{f}}}{4\pi}\phi,\tau\vec{\Omega}\cdot\vec{\nabla}\psi_{m}^{*}+\psi_{m}^{*}\right)_{\mathcal{D}}+\left(\frac{q}{4\pi},\tau\vec{\Omega}\cdot\vec{\nabla}\psi_{m}^{*}+\psi_{m}^{*}\right)_{\mathcal{D}} \quad (2.16)$$

These equation are compatible with voids, however the system matrix is not symmetric anymore due to the first derivative. For $\zeta = 0$ the stabilization parameter Eq. (2.10) is $\tau = \frac{1}{\sigma_{\mathrm{t}}}$ and Eq. (2.16) is equivalent to the simple SAAF weak form Eq. (2.9). The derivation of the multi-group and eigenvalue equations is again left to the reader since they do not pose a major difficulty.

2.3 Least-Squares Equation

The standard least-squares (LS) form of the transport equation [15]

$$\left(\mathcal{L}-\mathcal{S}\right)^{\dagger}\left(\mathcal{L}-\mathcal{S}\right)\psi=\left(\mathcal{L}-\mathcal{S}\right)^{\dagger}q \quad (2.17)$$

is not compatible with source iterations since the left hand side of the equation remains coupled in all directions. The Least-Squares Equation derived by Hansen et al. [23] is a second order transport equation that is compatible with voids. In contrast to traditional least-squares forms this equation is also usable with iterative solutions techniques e.g. source iterations with or without acceleration.

We start from the first order transport equation in operator form Eq. (1.14a)

$$\mathcal{L}\psi = \mathcal{S}\psi + \mathcal{F}\psi + \mathcal{Q} \tag{2.18}$$

Under the standard inner product

$$\Big(\cdot \, , \cdot \Big) \equiv \int_{\mathcal{D}} \int_{4\pi} \int_{0}^{\infty} \, dE \, d\Omega \, dV. \tag{2.19}$$

the adjoint of the streaming and collision operator is

$$\mathcal{L}^{\dagger} \equiv -\vec{\Omega} \cdot \vec{\nabla} + \sigma_{\mathrm{t}}. \tag{2.20}$$

Note that we only use the adjoint of the streaming and collision operator, and not the full adjoint to the transport equation. This gives us the ability to use source iterations. We multiply the transport equation with the adjoint operator

$$\mathcal{L}^{\dagger}\mathcal{L}\psi = \mathcal{L}^{\dagger}\mathcal{S}\psi + \mathcal{L}^{\dagger}\mathcal{F}\psi + \mathcal{L}^{\dagger}\mathcal{Q}. \tag{2.21}$$

The mono-energetic LS equation can be written as

$$-\vec{\Omega}\cdot\vec{\nabla}\left[\vec{\Omega}\cdot\vec{\nabla}\psi\right]-\vec{\Omega}\cdot\psi\vec{\nabla}\sigma_{\mathrm{t}}+\sigma_{\mathrm{t}}^{2}\psi=-\vec{\Omega}\cdot\vec{\nabla}\left[\sum_{l=0}^{L}\sum_{p=-l}^{l}\frac{2l+1}{4\pi}\mathrm{Y}_{l}^{p}\left(\vec{\Omega}\right)\sigma_{l}\phi_{l}^{p}+\frac{\bar{\nu}\sigma_{\mathrm{f}}}{4\pi}\phi+\frac{q}{4\pi}\right]$$
$$+\sigma_{\mathrm{t}}\sum_{l=0}^{L}\sum_{p=-l}^{l}\frac{2l+1}{4\pi}\mathrm{Y}_{l}^{p}\left(\vec{\Omega}\right)\sigma_{l}\phi_{l}^{p}+\frac{\sigma_{\mathrm{t}}\bar{\nu}\sigma_{\mathrm{f}}}{4\pi}\phi+\frac{q\sigma_{\mathrm{t}}}{4\pi} \quad (2.22a)$$

and the corresponding boundary condition is

$$\psi\left(\vec{x}_{b},\vec{\Omega}\right)=\psi^{\mathrm{inc}}\left(\vec{x}_{b},\vec{\Omega}\right),\qquad\forall\vec{x}_{b}\in\partial\mathcal{D},\quad\vec{\Omega}\cdot\vec{n}<0 \quad (2.22b)$$

$$\vec{\Omega}\cdot\vec{\nabla}\psi\left(\vec{x}_{b}\right)+\sigma_{\mathrm{t}}\psi\left(\vec{x}_{b}\right)=\mathcal{S}\psi\left(\vec{x}_{b}\right)+\mathcal{F}\psi\left(\vec{x}_{b}\right)+\mathcal{Q}\psi\left(\vec{x}_{b}\right),\qquad\vec{\Omega}\cdot\vec{n}>0 \quad (2.22c)$$

We utilize the S_N method and derive the weak form by multiplying Eq. (2.22a) with a test function ψ_m^* and integrate over the spatial domain $\mathcal{D}$. We apply integration by parts to all terms containing a derivative and obtain

$$\left(\vec{\Omega}_{m}\cdot\vec{\nabla}\psi_{m},\vec{\Omega}_{m}\cdot\vec{\nabla}\psi_{m}^{*}+\sigma_{\mathrm{t}}\psi_{m}^{*}\right)_{\mathcal{D}}+\left(\sigma_{\mathrm{t}}\psi_{m},\vec{\Omega}_{m}\cdot\vec{\nabla}\psi_{m}^{*}+\sigma_{\mathrm{t}}\psi_{m}^{*}\right)_{\mathcal{D}}$$
$$=\left(\sum_{l=0}^{L}\sum_{p=-l}^{l}\frac{2l+1}{4\pi}\sigma_{l}\phi_{l}^{p}\mathrm{Y}_{l}^{p}\left(\vec{\Omega}_{m}\right),\vec{\Omega}_{m}\cdot\vec{\nabla}\psi_{m}^{*}+\sigma_{\mathrm{t}}\psi_{m}^{*}\right)_{\mathcal{D}}+\left(\frac{\nu\sigma_{\mathrm{f}}}{4\pi}\phi,\vec{\Omega}_{m}\cdot\vec{\nabla}\psi_{m}^{*}+\sigma_{\mathrm{t}}\psi_{m}^{*}\right)_{\mathcal{D}}$$
$$+\left(\frac{q}{4\pi},\vec{\Omega}_{m}\cdot\vec{\nabla}\psi_{m}^{*}+\sigma_{\mathrm{t}}\psi_{m}^{*}\right)_{\mathcal{D}}+\left\langle\vec{\Omega}_{m}\cdot\vec{\nabla}\psi_{m}+\sigma_{\mathrm{t}}\psi_{m},\left(\vec{\Omega}_{m}\cdot\vec{n}\right)\psi_{m}^{*}\right\rangle_{\partial\mathcal{D}}$$
$$-\left\langle\sum_{l=0}^{L}\sum_{p=-l}^{l}\frac{2l+1}{4\pi}\sigma_{l}\mathrm{Y}_{l}^{p}\left(\vec{\Omega}_{m}\right)\phi_{l}^{p}+\frac{\nu\sigma_{\mathrm{f}}}{4\pi}\phi+\frac{q}{4\pi},\left(\vec{\Omega}_{m}\cdot\vec{n}\right)\psi_{m}^{*}\right\rangle_{\partial\mathcal{D}} \quad (2.23)$$

With the assumption that the first-order multi-group S_N transport Eq. (1.9) is exactly met on the boundary $\partial\mathcal{D}$, all of the boundary terms cancel. An additional motivation for making this assumption is that it renders our Galerkin method for the second-order least-squares equation equivalent to the least-squares finite-element method for the first-order form of the S_N equations using the same trial space.

The natural boundary condition of Eq. (2.28) is a Dirichlet boundary condition. However this is difficult to implement in numerical codes, since it is ambiguous at boundary corners and edges. We chose to use the optional weak boundary condition

$$\left\langle f_m \left(\psi_m - \psi_m^{inc}\right), \psi_m^* \right\rangle_{\partial\mathcal{D}^-} \tag{2.24}$$

instead, where $\partial\mathcal{D}^-$ is the portion of the boundary for which $\vec{\Omega}_m \cdot \vec{n} < 0$.

We define

$$f_m \equiv \sigma_t \left|\vec{\Omega} \cdot \vec{n}\right| \tag{2.25}$$

based on the SAAF boundary condition [31]. However, the SAAF boundary conditions are defined over the whole boundary, while the optional LS boundary condition is only defined on the incoming boundary. For near void problems

$$f_m \equiv \max\left(\sigma_t, \frac{1}{h}\right) \left|\vec{\Omega} \cdot \vec{n}\right| \tag{2.26}$$

gives a more accurate and better conditioned version. Here h denotes a characteristic length constant of the boundary cell. Another boundary condition, which shows often better results, is based on a diffusion limit analysis

$$f_m \equiv \frac{4}{h} \left|\vec{\Omega} \cdot \vec{n}\right| + \sigma_t \left(3 \left|\vec{\Omega} \cdot \vec{n}\right|^2 + 2 \left|\vec{\Omega} \cdot \vec{n}\right|\right) \tag{2.27}$$

and is well defined in voids.

By adding the boundary condition Eq. (2.24) to Eq. (2.28) we obtain the LS weak formulation: Given a trial space $W_{\mathcal{D}}$, consisting of continuous basis functions, the

weak form for a specific direction $m = 1 \dots M$ is as follows: find $\psi_m^* \in W_{\mathcal{D}}$ such that

$$\begin{aligned}
&\left(\vec{\Omega}_m \cdot \vec{\nabla}\psi_m, \vec{\Omega}_m \cdot \vec{\nabla}\psi_m^* + \sigma_{\mathrm{t}}\psi_m^*\right)_{\mathcal{D}} + \left(\sigma_{\mathrm{t}}\psi_m, \vec{\Omega}_m \cdot \vec{\nabla}\psi_m^* + \sigma_{\mathrm{t}}\psi_m^*\right)_{\mathcal{D}} \\
&+ \left\langle f_m\left(\psi_m - \psi_m^{\mathrm{inc}}\right), \psi_m^* \right\rangle_{\partial\mathcal{D}^-} = \left(\sum_{l=0}^{L}\sum_{p=-l}^{l} \frac{2l+1}{4\pi}\sigma_l \phi_l^p \mathrm{Y}_l^p\left(\vec{\Omega}_m\right), \vec{\Omega}_m \cdot \vec{\nabla}\psi_m^* + \sigma_{\mathrm{t}}\psi_m^*\right)_{\mathcal{D}} \\
&\qquad + \left(\frac{\nu\sigma_{\mathrm{f}}}{4\pi}\phi, \vec{\Omega}_m \cdot \vec{\nabla}\psi_m^* + \sigma_{\mathrm{t}}\psi_m^*\right)_{\mathcal{D}} + \left(\frac{q}{4\pi}, \vec{\Omega}_m \cdot \vec{\nabla}\psi_m^* + \sigma_{\mathrm{t}}\psi_m^*\right)_{\mathcal{D}} \quad (2.28)
\end{aligned}$$

However, all least squares methods are inherently non-conservative. Conservation is normally considered essential in reactor physics. Peterson et al. [53] showed that this drawback can be overcome by the use of a conservative low order equation for the nonlinear diffusion acceleration. In this dissertation we will use the same approach. We will also show that the influence of conservation on source calculations is small, however for criticality calculations it introduces a large error.

2.4 Weighted Least-Squares Method

The weighted least-squares transport equation addresses some issues of the unweighted LS equation across material interfaces and in voids. Due to the second order nature of the LS equation, downstream information can influence the upstream solution. An optically thick material further downstream in the direction of flow reduces the flux in the unweighted LS equation. This is a coarse mesh problem that decreases with increasing refinement of the mesh. The introduction of a weight function reduces this problem significantly [80].

Multiplying Eq. (2.18) with a weight function $\mathcal{W}$ and the adjoint operator Eq. (2.20) gives the weighted least-squares equation compatible with source iteration.

$$\mathcal{L}^\dagger \mathcal{W} \mathcal{L}\psi = \mathcal{L}^\dagger \mathcal{W} \mathcal{S}\psi + \mathcal{L}^\dagger \mathcal{W} \mathcal{F}\psi + \mathcal{L}^\dagger \mathcal{W} \mathcal{Q} \quad (2.29)$$

The mono-energetic WLS equation can be written as

$$
\begin{aligned}
&-\vec{\Omega}\cdot\vec{\nabla}\left[w\vec{\Omega}\cdot\vec{\nabla}\psi\right]-\vec{\Omega}\cdot\psi\vec{\nabla}\left[w\sigma_{\mathrm{t}}\right]+w\sigma_{\mathrm{t}}^{2}\psi \\
&\qquad=-\vec{\Omega}\cdot\vec{\nabla}\left[w\sum_{l=0}^{L}\sum_{p=-l}^{l}\frac{2l+1}{4\pi}\mathrm{Y}_{l}^{p}\left(\vec{\Omega}\right)\sigma_{l}\phi_{l}^{p}+w\frac{\bar{\nu}\sigma_{\mathrm{f}}}{4\pi}\phi+w\frac{q}{4\pi}\right] \\
&\qquad\quad+w\sigma_{\mathrm{t}}\sum_{l=0}^{L}\sum_{p=-l}^{l}\frac{2l+1}{4\pi}\mathrm{Y}_{l}^{p}\left(\vec{\Omega}\right)\sigma_{l}\phi_{l}^{p}+w\frac{\sigma_{\mathrm{t}}\bar{\nu}\sigma_{\mathrm{f}}}{4\pi}\phi+w\frac{q\sigma_{\mathrm{t}}}{4\pi}
\end{aligned}
\tag{2.30a}
$$

where w denotes a weight function. The corresponding boundary condition is

$$
\psi\left(\vec{x}_{b},\vec{\Omega}\right)=\psi^{\mathrm{inc}}\left(\vec{x}_{b},\vec{\Omega}\right),\qquad\forall\vec{x}_{b}\in\partial\mathcal{D},\quad\vec{\Omega}\cdot\vec{n}<0 \tag{2.30b}
$$

$$
\vec{\Omega}\cdot\vec{\nabla}\psi\left(\vec{x}_{b}\right)+\sigma_{\mathrm{t}}\psi\left(\vec{x}_{b}\right)=\mathcal{S}\psi\left(\vec{x}_{b}\right)+\mathcal{F}\psi\left(\vec{x}_{b}\right)+\mathcal{Q}\psi\left(\vec{x}_{b}\right),\qquad\vec{\Omega}\cdot\vec{n}>0 \tag{2.30c}
$$

Using the same derivation as described in Section 2.3 we derive the weak form of the WLS equation. Given a trial space $W_{\mathcal{D}}$, consisting of continuous basis functions, the weak form for a specific direction $m=1\ldots M$ is as follows: Find $\psi_{m}^{*}\in W_{\mathcal{D}}$ such that

$$
\begin{aligned}
&\left(w\vec{\Omega}_{m}\cdot\vec{\nabla}\psi_{m},\vec{\Omega}_{m}\cdot\vec{\nabla}\psi_{m}^{*}+\sigma_{\mathrm{t}}\psi_{m}^{*}\right)_{\mathcal{D}}+\left(w\sigma_{\mathrm{t}}\psi_{m},\vec{\Omega}_{m}\cdot\vec{\nabla}\psi_{m}^{*}+\sigma_{\mathrm{t}}\psi_{m}^{*}\right)_{\mathcal{D}} \\
&\qquad=\left(w\sum_{l=0}^{L}\sum_{p=-l}^{l}\frac{2l+1}{4\pi}\mathrm{Y}_{l}^{p}\left(\vec{\Omega}_{m}\right)\sigma_{l}\phi_{l}^{p},\vec{\Omega}_{m}\cdot\vec{\nabla}\psi_{m}^{*}+\sigma_{\mathrm{t}}\psi_{m}^{*}\right)_{\mathcal{D}} \\
&\qquad\quad+\left(w\frac{\nu\sigma_{\mathrm{f}}}{4\pi}\phi,\vec{\Omega}_{m}\cdot\vec{\nabla}\psi_{m}^{*}+\sigma_{\mathrm{t}}\psi_{m}^{*}\right)_{\mathcal{D}}+\left(w\frac{q}{4\pi},\vec{\Omega}_{m}\cdot\vec{\nabla}\psi_{m}^{*}+\sigma_{\mathrm{t}}\psi_{m}^{*}\right)_{\mathcal{D}}
\end{aligned}
\tag{2.31}
$$

The following weight function

$$
w\equiv\frac{1}{\sigma_{\mathrm{t}}} \tag{2.32}
$$

improves the causality and makes our equations equivalent to the SAAF equation

(Eq. (2.9)). To show this we use the left hand side of Eq. (2.31) and use integration by parts on the first order derivatives

$$\begin{aligned}
&\left(w\vec{\Omega}_m \cdot \vec{\nabla}\psi_m, \vec{\Omega}_m \cdot \vec{\nabla}\psi_m^* + \sigma_{\mathrm{t}}\psi_m^*\right)_{\mathcal{D}} + \left(w\sigma_{\mathrm{t}}\psi_m, \vec{\Omega}_m \cdot \vec{\nabla}\psi_m^* + \sigma_{\mathrm{t}}\psi_m^*\right)_{\mathcal{D}} \\
&\quad = \left(w\vec{\Omega}_m \cdot \vec{\nabla}\psi_m, \vec{\Omega}_m \cdot \vec{\nabla}\psi_m^*\right)_{\mathcal{D}} + \left(w\vec{\Omega}_m \cdot \vec{\nabla}\psi_m, \sigma_{\mathrm{t}}\psi_m^*\right)_{\mathcal{D}} \\
&\qquad + \left(w\sigma_{\mathrm{t}}\psi_m, \vec{\Omega}_m \cdot \vec{\nabla}\psi_m^*\right)_{\mathcal{D}} + \left(w\sigma_{\mathrm{t}}\psi_m, \sigma_{\mathrm{t}}\psi_m^*\right)_{\mathcal{D}} \\
&\quad = \left(w\vec{\Omega}_m \cdot \vec{\nabla}\psi_m, \vec{\Omega}_m \cdot \vec{\nabla}\psi_m^*\right)_{\mathcal{D}} + \left(\psi_m, \vec{\Omega} \cdot \vec{\nabla}\left[w\sigma_{\mathrm{t}}\right]\psi_m^*\right)_{\mathcal{D}} \\
&\qquad + \left(w\sigma_{\mathrm{t}}\psi_m, \sigma_{\mathrm{t}}\psi_m^*\right)_{\mathcal{D}} + \left\langle w\sigma_{\mathrm{t}}\psi, \left(\vec{\Omega} \cdot \vec{n}\right)\psi_m^*\right\rangle_{\partial\mathcal{D}}
\end{aligned} \tag{2.33}$$

Using Eq. (2.32) in Eq. (2.33) eliminates the first order derivative term. Substituting Eq. (2.33) and Eq. (2.32) into Eq. (2.31) will reduce the equation to Eq. (2.9). However, the weight function Eq. (2.32) is not defined in voids. To compensate for this we redefine the weight function to

$$w \equiv \min\left(\frac{1}{\sigma_{\mathrm{t}}}, w_{\max}\right) \tag{2.34}$$

where $w_{\max}$ denotes a maximum value for the weight function. This definition will make the WLS equation well defined in voids and maintain the symmetric positive-definite properties of the resulting discretized matrix. However, the WLS equation is the same as the SAAF equation only for sufficient large total cross section σ_{t}. $w\sigma_{\mathrm{t}}$ jumps at material interfaces with at least one material with $\sigma_{\mathrm{t}} < {w_{\max}}^{-1}$ thus the derivative is infinite. Therefore we decided to use Eq. (2.31) and add the same optional boundary conditions described in Section 2.3

$$\left\langle w f_m\left(\psi_m - \psi_m^{\mathrm{inc}}\right), \psi^*\right\rangle_{\partial\mathcal{D}^-} \tag{2.35}$$

with f_m described in Eqs. (2.26) and (2.27).

For Eq. (2.25) and $\sigma_{\mathrm{t}} \geq 1/w_{\max}$ the WLS equation with optional boundary condition is still equivalent to the SAAF equation. To show this we, use Eq. (2.33) and add the optional boundary condition Eq. (2.24) to get the equation

$$\begin{aligned}\left(\frac{1}{\sigma_{\mathrm{t}}}\vec{\Omega}_m \cdot \vec{\nabla}\psi_m, \vec{\Omega}_m \cdot \vec{\nabla}\psi_m^*\right)_{\mathcal{D}} + \left(\sigma_{\mathrm{t}}\psi_m, \psi_m^*\right)_{\mathcal{D}} \\ + \left\langle \psi_m, \left(\vec{\Omega}_m \cdot \vec{n}\right)\psi_m^* \right\rangle_{\partial\mathcal{D}} + \left\langle \left(\psi_m - \psi_m^{inc}\right), \left|\vec{\Omega}_m \cdot \vec{n}\right| \psi_m^* \right\rangle_{\partial\mathcal{D}^-} = 0 \quad (2.36)\end{aligned}$$

The weight function Eq. (2.32) and optional boundary factor Eq. (2.25) are already substituted in. The boundary terms can now be separated and the absolute value replaces to obtain

$$\begin{aligned}\left\langle \psi_m, \left(\vec{\Omega}_m \cdot \vec{n}\right)\psi_m^* \right\rangle_{\partial\mathcal{D}} + \left\langle \left(\psi_m - \psi_m^{inc}\right), \left|\vec{\Omega}_m \cdot \vec{n}\right| \psi_m^* \right\rangle_{\partial\mathcal{D}^-} \\ = \left\langle \psi_m, \left(\vec{\Omega}_m \cdot \vec{n}\right)\psi_m^* \right\rangle_{\partial\mathcal{D}^+} + \left\langle \psi_m, \left(\vec{\Omega}_m \cdot \vec{n}\right)\psi_m^* \right\rangle_{\partial\mathcal{D}^-} \\ - \left\langle \psi_m, \left(\vec{\Omega}_m \cdot \vec{n}\right)\psi_m^* \right\rangle_{\partial\mathcal{D}^-} + \left\langle \psi_m^{inc}, \left(\vec{\Omega}_m \cdot \vec{n}\right)\psi_m^* \right\rangle_{\partial\mathcal{D}^-} \\ = \left\langle \psi_m, \left(\vec{\Omega}_m \cdot \vec{n}\right)\psi_m^* \right\rangle_{\partial\mathcal{D}^+} + \left\langle \psi_m^{inc}, \left(\vec{\Omega}_m \cdot \vec{n}\right)\psi_m^* \right\rangle_{\partial\mathcal{D}^-} \quad (2.37)\end{aligned}$$

This is the SAAF boundary condition as stated in Eq. (2.9). Thus even with optional boundary condition the WLS equation is equivalent to the SAAF equation. However, only for Eq. (2.25), but not for Eqs. (2.26) and (2.27).

The resulting mono-energetic WLS equation used in this dissertation is defined as follows: Given a trial space $W_{\mathcal{D}}$, consisting of continuous basis functions, the weak

form for a specific direction $m = 1 \dots M$ is as follows: Find $\psi_m^* \in W_{\mathcal{D}}$ such that

$$\begin{aligned}
&\left(w\vec{\Omega}_m \cdot \vec{\nabla}\psi_m, \vec{\Omega}_m \cdot \vec{\nabla}\psi_m^* + \sigma_{\mathrm{t}}\psi_m^*\right)_{\mathcal{D}} + \left(w\sigma_{\mathrm{t}}\psi_m, \vec{\Omega}_m \cdot \vec{\nabla}\psi_m^* + \sigma_{\mathrm{t}}\psi_m^*\right)_{\mathcal{D}} \\
+&\left\langle w f_m \left(\psi_m - \psi_m^{\mathrm{inc}}\right), \psi^* \right\rangle_{\partial\mathcal{D}^-} = \left(w \sum_{l=0}^{L} \sum_{p=-l}^{l} \frac{2l+1}{4\pi} \mathrm{Y}_l^p\left(\vec{\Omega}_m\right) \sigma_l \phi_l^p, \vec{\Omega}_m \cdot \vec{\nabla}\psi_m^* + \sigma_{\mathrm{t}}\psi_m^*\right)_{\mathcal{D}} \\
&\qquad + \left(w\frac{\nu\sigma_{\mathrm{f}}}{4\pi}\phi, \vec{\Omega}_m \cdot \vec{\nabla}\psi_m^* + \sigma_{\mathrm{t}}\psi_m^*\right)_{\mathcal{D}} + \left(w\frac{q}{4\pi}, \vec{\Omega}_m \cdot \vec{\nabla}\psi_m^* + \sigma_{\mathrm{t}}\psi_m^*\right)_{\mathcal{D}} \quad (2.38)
\end{aligned}$$

with the weight function as described in Eq. (2.34) and the boundary functions as described in Eq. (2.26) or Eq. (2.27). Note that for $w = 1$ the WLS equation reduces to the unweighted LS scheme Eq. (2.28).

2.5 Numerical results for weighted least-squares transport

To test the effect of the weighting on the LS equation, consider a one dimensional problem with two material regions. The left region contains a weak absorber ($\sigma_{\mathrm{t},1} = 0.1\,\frac{1}{\mathrm{cm}}$), while the right region has a strong absorber ($\sigma_{\mathrm{t},2} = 10\,\frac{1}{\mathrm{cm}}$). Each region is 1 cm thick and the problem is surrounded by vacuum. A constant source of $q = 1\,\frac{\mathrm{n}}{\mathrm{s}}$ is added in both regions. We compared the unweighted LS to the weighted LS and the SAAFτ formulation. LS and WLS formulations used the boundary condition Eqs. (2.26) and (2.26) and and all calculations employed a S_8 Gauss quadrature.

Figure 2.1 shows the results for the scalar flux. The LS result in the left half of the problem was strongly influenced by the thick material in the right half. The boundary condition had only an effect on the left boundary with Eq. (2.27) (LS 2) closer to the reference boundary value as Eq. (2.26) (LS 1). The introduction of the weight function for the WLS ameliorated this problem. The result for the WLS scheme was strongly dependent on the choice of optional boundary condition. The boundary condition Eq. (2.26) (WLS 1) gave the same result as the SAAF calculations. Both schemes were far off the reference solution with the left boundary value well below

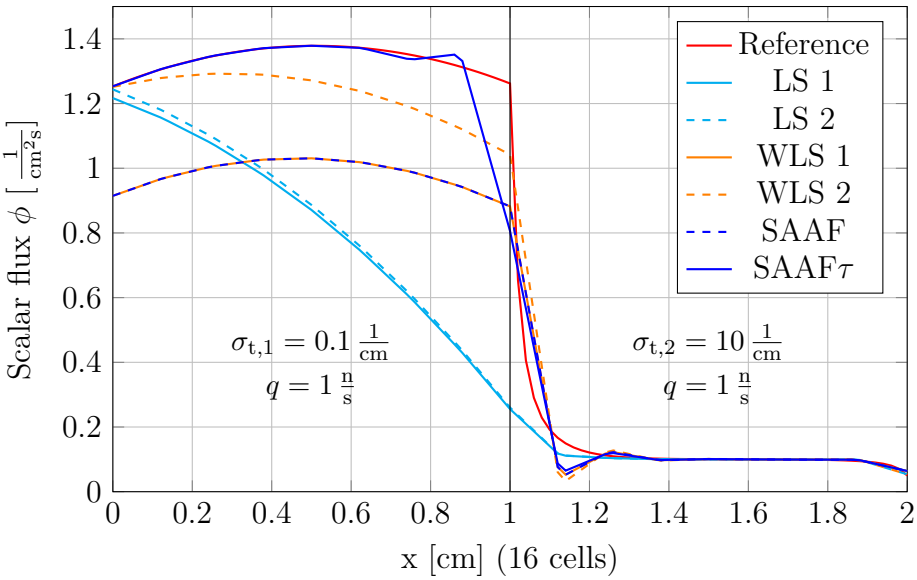

Figure 2.1 Comparison of the scalar flux results for the two absorber problem with a source using several transport schemes.

the reference boundary value. The boundary condition Eq. (2.27) improves the left boundary value, however the result showed still a decrease of the scalar flux towards the thick material. The SAAFτ scheme was closest to the reference solution, but it had a strong decrease in the cell next to the material interface and oscillations left of that cell.

2.5.1 Angular dependent weight function

The results for the angular fluxes showed that the error for the WLS scheme is strongly dependent on the angle. For more perpendicular directions the error was larger (Fig. 2.2) than for μ closer to one. This implies that an angular dependent weight function might further ameliorate the error of the WLS scheme. A simple,

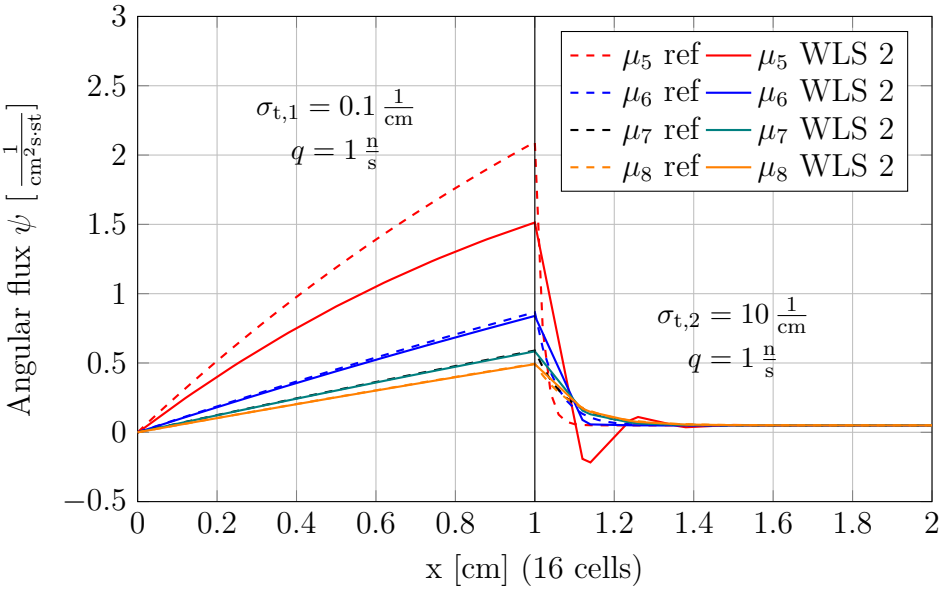

Figure 2.2 Comparison of the angular flux for positive angles between the WLS solution with boundary condition Eq. (2.27) and the reference solution ($0 < \mu_1 < \mu_2 < \mu_3 < \mu_4 < 1$).

angular dependent weight function is

$$w_m \equiv \frac{1}{\mu_m \sigma_\mathrm{t}}. \tag{2.39}$$

Calculations showed, that this modification has no effect on the result. The problem is, that a full row of the matrix is weighted by the same μ. The weight function however, changes the strength of the link between cells across the interface within the matrix. Strong absorber influences adjacent material regions more weakly. Within a material region, no difference is made, since the weight function is constant. This is also the reason, why the simple angular weight function Eq. (2.39) has no effect. The whole direction has the same weighting and the relative strength of the matrix links remain constant.

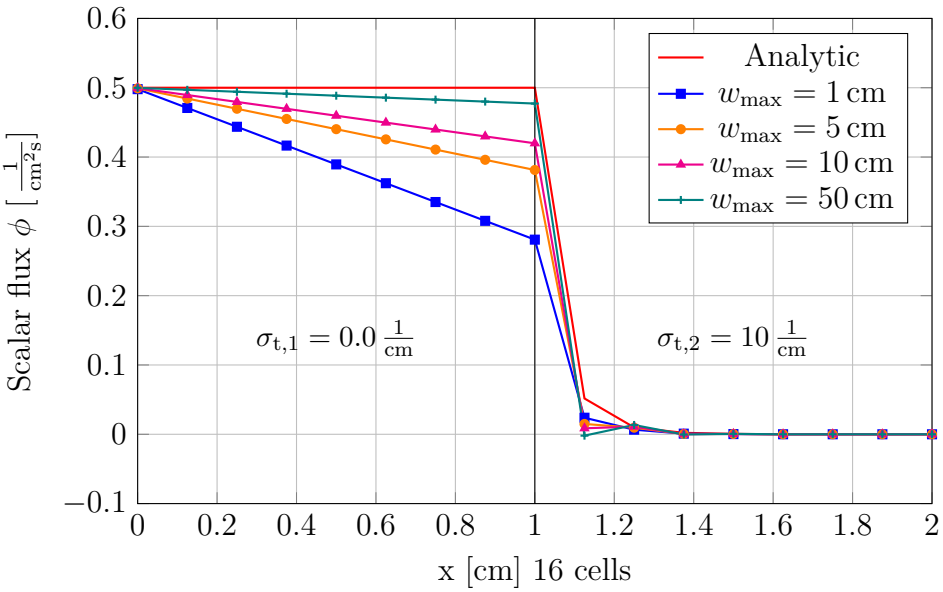

Figure 2.3 Scalar fluxes using the WLS transport scheme for different weight function limit $w_{\max}$ for the two region void problem with left inflow.

2.5.2 Weight function in voids

As stated in Section 2.4, the weight function must be limited to be defined in void regions. We further studied the influence of the maximal weight $w_{\max}$ on the accuracy of the WLS implementation. The test problem is a two region slab with a void ($\sigma_{t,1} = 0\,\frac{1}{\text{cm}}$) on the left side and a strong absorber ($\sigma_{t,2} = 10\,\frac{1}{\text{cm}}$) on the right side. Two subcases with an isotropic flux of $\phi^{\text{inc}} = 1\,\frac{1}{\text{cm}^2\text{s}}$ on the left or the right boundary respectively demonstrate the directionality of the problem. For all WLS calculations boundary condition Eq. (2.27) with S_8 were used.

Figure 2.3 shows the scalar flux results for the left inflow case. The increase of the maximal weight improved the slope of the scalar flux significantly in the void region. However, the increased resulted in a stronger dip after the material interface. The

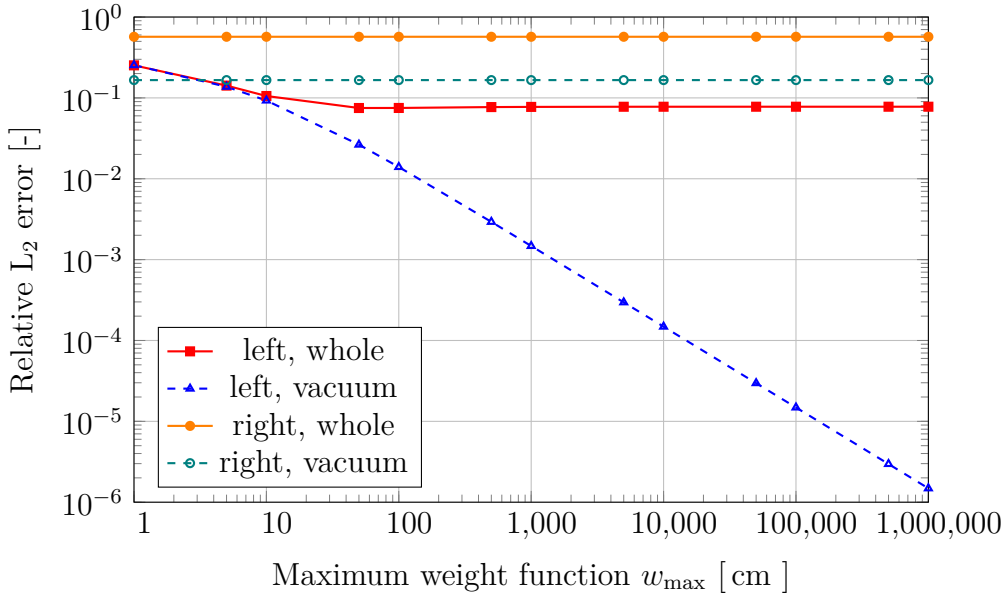

Figure 2.4 Error convergence with increasing weight function limit $w_{\max}$ for the two region void problem with left or right inflow for the whole problem and the vacuum region separately.

reduction in the relative error

$$e \equiv \frac{\|\phi(x) - \phi_{\text{exact}}(x)\|_{L_2}}{\|\phi_{\text{exact}}(x)\|_{L_2}} \tag{2.40}$$

with increasing $w_{\max}$ is shown in Fig. 2.4. The convergence is shown for the error of the whole domain and for the void part separately. We can see that for the left inflow case the error in the void converged with first order. For $w_{\max} < 10\,\text{cm}$ the error in the void region dominated the error for the whole problem, however for larger $w_{\max}$ the error in the material region dominated and hence no further error reduction can be seen. From this we concluded that a $w_{\max}$ in the range between 100 cm and 1000 cm is sufficient. These values are however problem dependent and a function of the mesh. Hence we run a study on the effects of mesh refinement on the optimal

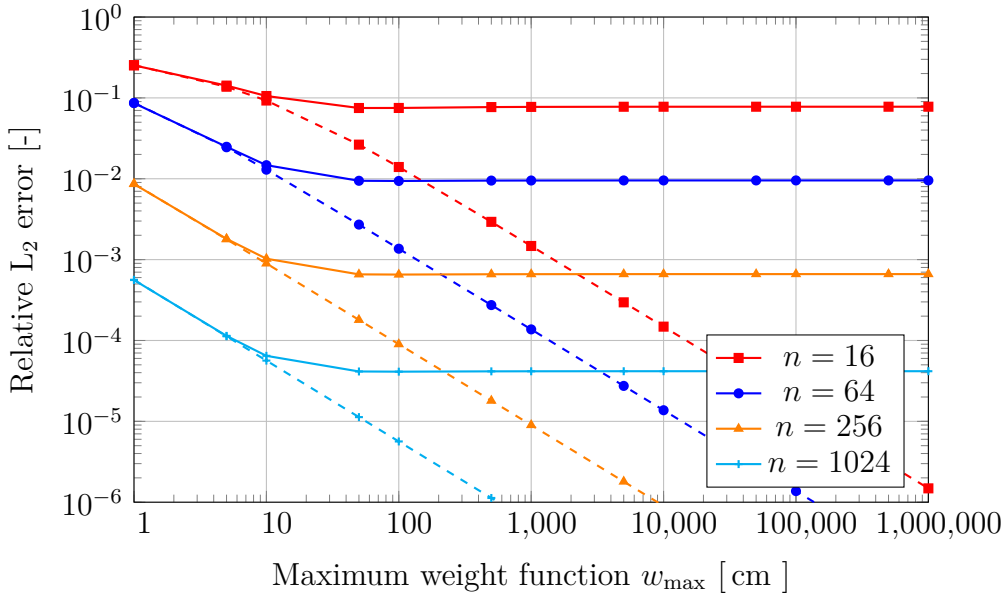

Figure 2.5 Effect of mesh refinement on the error convergence with increasing weight function limit $w_{\max}$ for the two region void problem with left inflow (solid line for the whole problem, dashed for the vacuum region separately).

limit of the weight function. Our results showed that the optimal weight limit is independent from the mesh refinement as shown in Fig. 2.5. In the figure, the solid lines show the error for the whole problem, the dashed lines for the vacuum part of the problem. All refinements showed that at approx. $w_{\max} = 100\,\text{cm}$ the error in the void is negligible.

For the right inflow problem Fig. 2.6 shows that $w_{\max}$ had no effect whatsoever on the error in both the whole domain as for void region. This clearly demonstrates the directionality of the causality problem.

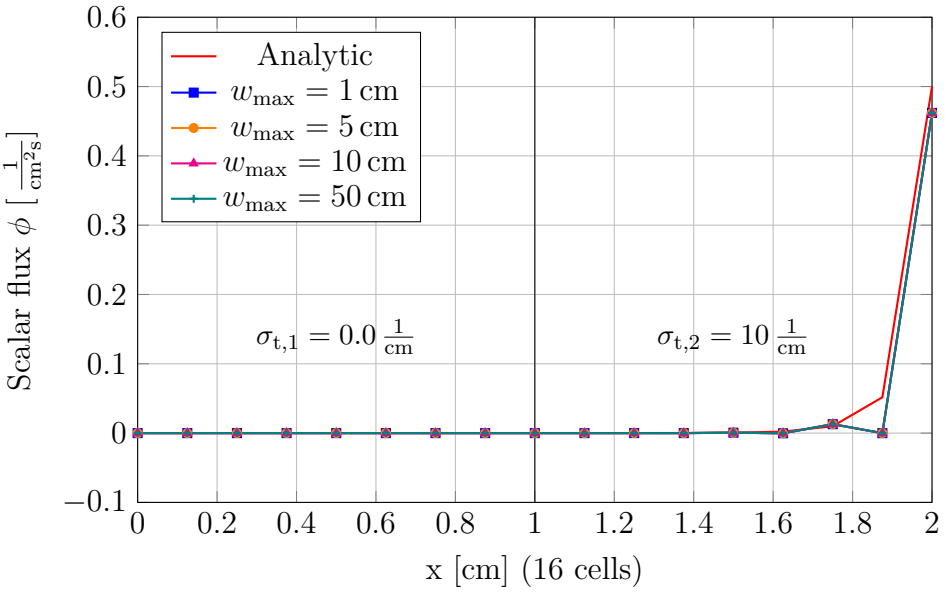

Figure 2.6 WLS scalar fluxes results for different weight function limit $w_{\max}$ for the two region void problem with right inflow.

3. NONLINEAR DIFFUSION ACCELERATION*

3.1 Derivation of the Nonlinear Diffusion Acceleration

We start with the mono-energetic steady-state neutron transport Eq. (1.12). Integrating over all directions gives the balance equation

$$\vec{\nabla} \cdot \vec{J} + \sigma_{\mathrm{t}}\phi = \sigma_{\mathrm{s}}\phi + \bar{\nu}\sigma_{\mathrm{f}}\phi + q. \tag{3.1}$$

This equation has two unknowns, the scalar flux ϕ and the current $\vec{J}$. To close this equation we need an additional equation. Multiplying Eq. (1.12) by $\vec{\Omega}$ and integrating over all directions obtains the first moment equation

$$\vec{\nabla} \cdot \int_{4\pi} \vec{\Omega}\vec{\Omega}\psi \, d\vec{\Omega} + \sigma_{\mathrm{t}}\vec{J} = \sigma_1\vec{J}. \tag{3.2}$$

Solving equation Eq. (3.2) for $\vec{J}$ gives

$$\vec{J} = -\frac{1}{\sigma_{\mathrm{tr}}}\vec{\nabla}[E\phi] \tag{3.3}$$

where E denotes the Eddington factor

$$E \equiv \frac{1}{\phi}\int_{4\pi} \vec{\Omega}\vec{\Omega}\psi \, d\vec{\Omega}. \tag{3.4}$$

*Part of the data reported in this chapter is reprinted with permission from *Nonlinear Diffusion Acceleration in Voids for the Weighted Least-Square Transport Equation* by Hans R. Hammer, Jim E. Morel, and Yaqi Wang. M&C 2017 - International Conference on Mathematics & Computational Methods Applied to Nuclear Science & Engineering, 16-20 April 2017.

and the transport cross section is defined as

$$\sigma_{\mathrm{tr}} \equiv \sigma_{\mathrm{t}} - \sigma_1. \tag{3.5}$$

Substituting Eq. (3.3) into the balance equation Eq. (3.1) gives the quasi-diffusion equation

$$-\vec{\nabla} \cdot \left[\frac{1}{\sigma_{\mathrm{tr}}}\vec{\nabla}[E\phi]\right] + \sigma_{\mathrm{a}}\phi = \bar{\nu}\sigma_{\mathrm{f}}\phi + q \tag{3.6}$$

For the linear anisotropic case the Eddington E factor reduces to a $1/3$ and Eq. (3.6) becomes the classical diffusion equation. For non-linear anisotropic cases, the Eddington factor E can be evaluated using the angular fluxes from a transport solution. This scheme is called the quasi-diffusion methods and was first developed by Gol'din [21] in 1964. In multi-dimensional problems the Eddington factor becomes a symmetric positive-definite tensor. This results in an asymmetric diffusion equation, which is more complicated to solve. Miften and Larsen present an algorithm to derive a symmetric method [43]. It however requires the solve of two equations.

To derive the Nonlinear Diffusion Acceleration, the diffusion term of Eq. (3.6) is separated using the product rule

$$-\vec{\nabla} \cdot \left[\frac{1}{\sigma_{\mathrm{tr}}}E\vec{\nabla}\phi\right] - \vec{\nabla} \cdot \left[\frac{1}{\sigma_{\mathrm{tr}}}\phi\vec{\nabla}E\right] + \sigma_{\mathrm{a}}\phi = \bar{\nu}\sigma_{\mathrm{f}}\phi + q \tag{3.7}$$

This is a drift-diffusion equation, with a second order diffusion term and a first order correction term, the drift vector. The diffusion coefficient is

$$\mathrm{D} \equiv \frac{1}{\sigma_{\mathrm{tr}}}E \tag{3.8}$$

which again simplifies to the classical coefficient

$$\mathrm{D} = \frac{1}{3\sigma_{\mathrm{tr}}} \tag{3.9}$$

for the linear anisotropic case. The drift vector is further expanded by

$$\begin{aligned}
\hat{\alpha} &\equiv \frac{1}{\sigma_{\mathrm{tr}}} \vec{\nabla} E \\
&= \frac{1}{\sigma_{\mathrm{tr}}} \frac{\int_{4\pi} \vec{\Omega}\vec{\Omega} \cdot \vec{\nabla}\psi \, d\vec{\Omega}}{\phi} - \frac{1}{\sigma_{\mathrm{tr}}} \frac{\int_{4\pi} \vec{\Omega}\vec{\Omega}\psi \, d\vec{\Omega}}{\phi^2} \vec{\nabla}\phi \\
&= \frac{1}{\sigma_{\mathrm{tr}}} \frac{\int_{4\pi} \vec{\Omega}\vec{\Omega} \cdot \vec{\nabla}\psi \, d\vec{\Omega}}{\phi} - \frac{\mathrm{D}\vec{\nabla}\phi}{\phi}
\end{aligned} \tag{3.10}$$

This gives the NDA drift-diffusion equation

$$-\vec{\nabla} \cdot \left[\mathrm{D}\vec{\nabla}\phi\right] - \vec{\nabla} \cdot [\hat{\alpha}\phi] + \sigma_{\mathrm{a}}\phi = q \tag{3.11}$$

From Eqs. (3.10) and (3.11) we can see that the diffusion terms cancel in the case, that high-order and low-order solution converge to the same solution, which is the case for consistent schemes. However, Lebedev [41, Chapter XI.10] and Schubert et al. [59] showed that the choice of the diffusion coefficient influences the spectral radius of problems. For simplicity and good iterative properties, Eq. (3.9) is commonly chosen in the NDA algorithm.

While reflective boundary conditions are natural to diffusion equations, the vacuum boundary condition requires an explicit expression. Let us separate the boundary $\partial\mathcal{D}$ into the reflective part $\partial\mathcal{D}_{\mathrm{R}}$ and the vacuum boundary $\partial\mathcal{D}_{\mathrm{V}}$. The reflective boundary condition is the natural boundary condition of the drift-diffusion equation, thus the vacuum condition must be defined. Miften and Larsen [44] proposed a general

Marshak boundary condition. With the partial currents for inflow

$$\hat{\jmath}^{\,\mathrm{in}}\left(\vec{x}_b\right) \equiv \int_{\vec{n}\cdot\vec{\Omega}<0} \left|\vec{\Omega}\cdot\vec{n}\right| \psi\left(\vec{x}_b,\vec{\Omega}\right)\, d\vec{\Omega}, \qquad \vec{x}_b \in \partial\mathcal{D}_{\mathrm{V}} \tag{3.12}$$

and outflow

$$\hat{\jmath}^{\,\mathrm{out}}\left(\vec{x}_b\right) \equiv \int_{\vec{n}\cdot\vec{\Omega}>0} \left|\vec{\Omega}\cdot\vec{n}\right| \psi\left(\vec{x}_b,\vec{\Omega}\right)\, d\vec{\Omega}, \qquad \vec{x}_b \in \partial\mathcal{D}_{\mathrm{V}} \tag{3.13}$$

the current across the boundary can be described as

$$\vec{J}\cdot\vec{n} = \hat{\jmath}^{\,\mathrm{out}} - \hat{\jmath}^{\,\mathrm{in}} \tag{3.14}$$

Adding and subtracting the incoming partial current $\hat{\jmath}^{\,\mathrm{in}}$ gives

$$\begin{aligned} \vec{J}\cdot\vec{n} &= \int_{4\pi} \left|\vec{\Omega}\cdot\vec{n}\right| \psi\left(\vec{\Omega}\right)\, d\vec{\Omega} - 2\hat{\jmath}^{\,\mathrm{in}} \\ &= \beta\phi - 2\hat{\jmath}^{\,\mathrm{in}} \end{aligned} \tag{3.15}$$

with

$$\beta \equiv \frac{1}{\phi}\int_{4\pi} \left|\vec{\Omega}\cdot\vec{n}\right| \psi\left(\vec{\Omega}\right)\, d\vec{\Omega}. \tag{3.16}$$

the vacuum boundary factor, which can be easily computed given the angular fluxes.

We can show that in the isotropic case this is equal to the familiar Marshak boundary condition. Both partial currents become in the isotropic case

$$\hat{\jmath}^{\,\mathrm{in}} = \hat{\jmath}^{\,\mathrm{out}} = \frac{\phi}{4} \tag{3.17}$$

and the boundary factor becomes $\beta = \frac{1}{2}$. Substituting this in Eq. (3.15) gives

$$\frac{\phi}{4} - \frac{\vec{J} \cdot \vec{n}}{2} = \hat{j}^{\text{in}}. \tag{3.18}$$

3.1.1 Derivation of the Nonlinear Diffusion Acceleration for the self-adjoint angular flux equation with void treatment

The NDA SAAFτ is a consistent scheme. This means that the low order equation is derived from the SAAFτ high order equation Eq. (2.15) as shown by Wang [76]. The P_0 projection of Eq. (2.15) is

$$-\int_{4\pi} \vec{\Omega} \cdot \vec{\nabla}\Big[\tau\vec{\Omega} \cdot \vec{\nabla}\psi\Big]\, d\vec{\Omega} + \vec{\nabla} \cdot \Big[(1-\tau\sigma_{\text{t}})\vec{J}\Big] + \sigma_{\text{t}}\phi \\ = \sigma_{\text{s}}\phi + \bar{\nu}\sigma_{\text{f}}\phi + q - \vec{\nabla}\Big[\tau\sigma_1\vec{J}\Big] \tag{3.19}$$

Using the same technique as described above, we can divide and multiply the angular flux withing the integral term by the scalar flux to obtain an equivalent of the Eddington factor Eq. (3.4). The integral is then divided into a diffusion term and a correction term using the product rule. The correction term is then combined with the first order neutron current terms into the SAAFτ drift vector

$$\hat{\alpha} \equiv \frac{1}{\phi}\left(\int_{4\pi} \vec{\Omega} \cdot \tau\vec{\Omega} \cdot \vec{\nabla}\psi\, d\vec{\Omega} - \Big[(1-\tau\sigma_{\text{tr}})\vec{J}\Big] - \text{D}\vec{\nabla}\phi\right). \tag{3.20}$$

which is different from Eq. (3.10). This gives the drift-diffusion equation

$$-\vec{\nabla}\text{D}\vec{\nabla}\phi - \vec{\nabla}[\hat{\alpha}\phi] + \sigma_{\text{a}}\phi = \bar{\nu}\sigma_{\text{f}}\phi + q \tag{3.21}$$

with the diffusion coefficient

$$\mathrm{D} \equiv \frac{\tau}{\phi} \int_{4\pi} \vec{\Omega}\vec{\Omega}\psi \, d\vec{\Omega}. \tag{3.22}$$

It is only different from Eq. (3.8) in the case of optical thin cells as defined in Eq. (2.10) or anisotropic scattering. For simplicity, Wang decided to use the classical diffusion coefficient Eq. (3.9) instead of Eq. (3.22).

The boundary condition are derived differently for the SAAFτ NDA. Based on Eq. (3.14) Wang defined

$$\vec{J} \cdot \vec{n} = \frac{\kappa}{4}\phi - \hat{\jmath}^{\,\mathrm{in}} \tag{3.23}$$

with the SAAFτ vacuum boundary coefficient

$$\begin{aligned} \kappa\left(\vec{x}_b\right) &\equiv \frac{4}{\phi}\hat{\jmath}^{\,\mathrm{out}}\left(\vec{x}_b\right) \\ &= \frac{4}{\phi}\int_{\vec{n}\cdot\vec{\Omega}>0} \left|\vec{\Omega}\cdot\vec{n}\right| \psi\left(\vec{x}_b, \vec{\Omega}\right) \, d\vec{\Omega}, \qquad \forall \vec{x}_b \in \partial\mathcal{D}_{\mathrm{V}} \end{aligned} \tag{3.24}$$

The weak form of the low order equation is derived by multiplying Eq. (3.21) with a test function ϕ^* and integrating over the whole domain $\mathcal{D}$. Integrating the diffusion and the drift term by parts gives

$$\begin{aligned} \left(\mathrm{D}\vec{\nabla}\phi, \vec{\nabla}\phi^*\right)_{\mathcal{D}} + \left(\hat{\alpha}\phi, \vec{\nabla}\phi^*\right)_{\mathcal{D}} + \left(\sigma_{\mathrm{a}}\phi, \phi^*\right)_{\mathcal{D}} + \left\langle \frac{\kappa}{4}\phi - \hat{\jmath}^{\,\mathrm{in}}, \phi^* \right\rangle_{\partial\mathcal{D}_{\mathrm{V}}} \\ = \left(\bar{\nu}\sigma_{\mathrm{f}}\phi, \phi^*\right)_{\mathcal{D}} + \left(q, \phi^*\right)_{\mathcal{D}} \end{aligned} \tag{3.25}$$

For a given iteration k the SAAFτ NDA scheme is defined as follows:

1. Solve the SAAFτ transport equation for $m = 1 \dots M$

$$\left(\tau\vec{\Omega}\cdot\vec{\nabla}\psi_m^{k+\frac{1}{2}},\vec{\Omega}\cdot\vec{\nabla}\psi_m^*\right)_{\mathcal{D}} + \left(\left(1-\sigma_{\mathrm{t}}\tau\right)\psi_m^{k+\frac{1}{2}},\vec{\Omega}\cdot\vec{\nabla}\psi_m^*\right)_{\mathcal{D}} + \left(\sigma_{\mathrm{t}}\psi_m^{k+\frac{1}{2}},\psi_m^*\right)_{\mathcal{D}} + \left\langle\psi_m^{k+\frac{1}{2}},\left(\vec{\Omega}\cdot\vec{n}\right)\psi_m^*\right\rangle_{\partial\mathcal{D}} = \left(\sum_{l=0}^{L}\sum_{p=-l}^{l}\frac{2l+1}{4\pi}\mathrm{Y}_l^p\left(\vec{\Omega}_m\right)\sigma_l\phi_l^{p,k},\tau\vec{\Omega}\cdot\vec{\nabla}\psi_m^*+\psi_m^*\right)_{\mathcal{D}} + \left(\frac{1}{4\pi}\bar{\nu}\sigma_{\mathrm{f}}\phi^k+\frac{q}{4\pi},\tau\vec{\Omega}\cdot\vec{\nabla}\psi_m^*+\psi_m^*\right)_{\mathcal{D}} \quad (3.26a)$$

2. Calculate the correction terms for the drift-diffusion equation

$$\kappa^{k+\frac{1}{2}} = \frac{4}{\phi}\sum_{\vec{n}\cdot\vec{\Omega}_m>0}\omega_m\left|\vec{n}\cdot\vec{\Omega}_m\right|\psi_m^{k+\frac{1}{2}} \quad (3.26b)$$

$$\hat{\alpha}^{k+\frac{1}{2}} = \frac{1}{\phi^{k+\frac{1}{2}}}\left(\tau\sum_{m=1}^{M}\vec{\Omega}_m\left(\vec{\Omega}_m\cdot\vec{\nabla}\psi_m^{k+\frac{1}{2}}\right) - \left[\left(1-\tau\sigma_{\mathrm{tr}}\right)\vec{J}^{k+\frac{1}{2}}\right] - \mathrm{D}\vec{\nabla}\phi^{k+\frac{1}{2}}\right) \quad (3.26c)$$

3. Solve the drift-diffusion equation

$$-\left(\mathrm{D}\vec{\nabla}\phi^{k+1},\vec{\nabla}\phi^*\right)_{\mathcal{D}} - \left(\hat{\alpha}^{k+\frac{1}{2}}\phi^{k+1},\vec{\nabla}\phi^*\right)_{\mathcal{D}} + \left(\sigma_{\mathrm{a}}\phi^{k+1},\phi^*\right)_{\mathcal{D}} + \left\langle\frac{\kappa^{k+\frac{1}{2}}}{4}\phi^{k+1}-\hat{j}^{\mathrm{in}},\phi^*\right\rangle_{\partial\mathcal{D}_{\mathrm{V}}} = \left(\bar{\nu}\sigma_{\mathrm{f}}\phi^{k+1},\phi^*\right)_{\mathcal{D}} + \left(q,\phi^*\right)_{\mathcal{D}} \quad (3.26d)$$

4. Check convergence

$$\frac{\|\phi^{k+1}-\phi^{k+\frac{1}{2}}\|_{L_2}}{\|\phi^{k+\frac{1}{2}}\|_{L_2}} < \mathrm{tol} \quad (3.26e)$$

5. Update the scattering source

3.1.2 Derivation of the Nonlinear Diffusion Acceleration for the weighted least-squares equation

It is also possible to derive a consistent form of the NDA for the WLS equation. However, this form would be non-conservative as the WLS scheme. Hence we derive a non-consistent, but conservative low order equation as shown by Peterson [53]. Non-consistent means that both equations, high-order and NDA low order equation, converge to the same solution only in the limit as the mesh is increasingly refined. However, for sufficient large cross sections, the NDA WLS scheme becomes consistent even for the inconsistently derived low order equation.

The derivation follows the outlined procedure in Section 3.1. Multiplying Eq. (3.11) by a test function ϕ^* and integrating over the domain gives the corresponding weak form. All derivative terms are integrated by parts. However, to be consistent with the SAAFτ implementation, the boundary condition as described in Section 3.1.1 will be used. This makes it possible, to use the same low-order implementation for NDA SAAFτ and NDA WLS.

$$-\left(\mathrm{D}\vec{\nabla}\phi,\vec{\nabla}\phi^*\right)_{\mathcal{D}}-\left(\hat{\alpha}\phi,\vec{\nabla}\phi^*\right)_{\mathcal{D}}+\left(\sigma_{\mathrm{a}}\phi,\phi^*\right)_{\mathcal{D}}+\left\langle\frac{\kappa}{4}\phi^{k+1}-\hat{j}^{\mathrm{in}},\phi^*\right\rangle_{\partial\mathcal{D}} = \left(\bar{\nu}\sigma_{\mathrm{f}}\phi,\phi^*\right)_{\mathcal{D}}+\left(q,\phi^*\right)_{\mathcal{D}}. \quad (3.27)$$

Clearly this equation is the same drift-diffusion equation as for the NDA SAAFτ (Eq. (3.21)). This allows an easy implementation and comparison of both methods.

For a given iteration k the WLS NDA scheme is defined as follows:

1. Solve the WLS transport equation for $m = 1 \dots M$

$$\begin{aligned}\left(w\vec{\Omega}_m \cdot \vec{\nabla}\psi_m^{k+\frac{1}{2}} + w\sigma_{\mathrm{t}}\psi_m^{k+\frac{1}{2}}, \vec{\Omega}_m \cdot \vec{\nabla}\psi_m^* + \sigma_{\mathrm{t}}\psi_m^*\right)_{\mathcal{D}} \\ + \left\langle wf_m\left(\psi_m^{k+\frac{1}{2}} - \psi_m^{\mathrm{inc}}\right), \psi_m^*\right\rangle_{\partial\mathcal{D}^-} \\ = \left(w\sum_{l=0}^{L}\sum_{p=-l}^{l}\frac{2l+1}{4\pi}\mathrm{Y}_l^p\left(\vec{\Omega}_m\right)\sigma_l\phi_l^{p,k}, \vec{\Omega}_m \cdot \vec{\nabla}\psi_m^* + \sigma_{\mathrm{t}}\psi_m^*\right)_{\mathcal{D}} \\ + \left(w\bar{\nu}\sigma_{\mathrm{f}}\phi^k, \vec{\Omega}_m \cdot \vec{\nabla}\psi_m^* + \sigma_{\mathrm{t}}\psi_m^*\right)_{\mathcal{D}} + \left(wq_m, \vec{\Omega}_m \cdot \vec{\nabla}\psi_m^* + \sigma_{\mathrm{t}}\psi_m^*\right)_{\mathcal{D}} \quad (3.28a)\end{aligned}$$

2. Calculate the correction terms for the diffusion equation

$$\kappa^{k+\frac{1}{2}} = \frac{4}{\phi}\sum_{\vec{n}\cdot\vec{\Omega}_m>0}\omega_m\left|\vec{n}\cdot\vec{\Omega}_m\right|\psi_m^{k+\frac{1}{2}} \quad (3.28b)$$

$$\hat{\alpha}^{k+\frac{1}{2}} = \frac{1}{\phi^{k+\frac{1}{2}}}\left(\frac{1}{\sigma_{\mathrm{tr}}}\sum_{m=1}^{M}\omega_m\vec{\Omega}_m\left(\vec{\Omega}_m \cdot \vec{\nabla}\psi_m^{k+\frac{1}{2}}\right) - \mathrm{D}\vec{\nabla}\phi^{k+\frac{1}{2}}\right) \quad (3.28c)$$

3. Solve the diffusion equation

$$\begin{aligned}-\left(\mathrm{D}\vec{\nabla}\phi^{k+1}, \vec{\nabla}\phi^*\right)_{\mathcal{D}} - \left(\hat{\alpha}^{k+\frac{1}{2}}\phi^{k+1}, \vec{\nabla}\phi^*\right)_{\mathcal{D}} + \left(\sigma_{\mathrm{a}}\phi^{k+1}, \phi^*\right)_{\mathcal{D}} \\ + \left\langle\frac{\kappa^{k+\frac{1}{2}}}{4}\phi^{k+1} - \hat{j}^{\mathrm{in}}, \phi^*\right\rangle_{\partial\mathcal{D}_{\mathrm{V}}} = \left(\bar{\nu}\sigma_{\mathrm{f}}\phi^{k+1}, \phi^*\right)_{\mathcal{D}} + \left(q, \phi^*\right)_{\mathcal{D}} \quad (3.28d)\end{aligned}$$

4. Check convergence

$$\frac{\|\phi^{k+1} - \phi^k\|_{L_2}}{\|\phi^k\|_{L_2}} < \mathrm{tol} \quad (3.28e)$$

5. Update the scattering source

The difference in between the NDA for SAAFτ and WLS lays in the drift vector and

the check for the convergence. As a non-consistent scheme the transport and diffusion solution do not converge to the same solution. Therefore it is required to use two consecutive diffusion solution to obtain the error.

The iteration scheme for the NDA starts with a low order solve of Eq. (3.28d) assuming $\hat{\alpha}^{\frac{1}{2}} = 0$ and $\kappa^{\frac{1}{2}} = 1$. The scalar flux is transferred to the high order system and used for the scattering and fission source. The new angular flux is obtained and the drift vector and boundary coefficient calculated. These are then used for the next low order diffusion solve. This iteration continues until convergence of the low order and high order solutions.

The derivation of the multi-group equations is similar and we leave it to the reader to do so. The only thing to be consider are the cross group scattering terms in the drift vector

$$\hat{\alpha}_g^{k+\frac{1}{2}} \equiv \frac{1}{\phi_g^{k+\frac{1}{2}}} \left(\frac{1}{\sigma_{\mathrm{tr},g}} \sum_{m=1}^{M} \omega_m \vec{\Omega}_m \left(\vec{\Omega}_m \cdot \vec{\nabla} \psi_{m,g}^{k+\frac{1}{2}} \right) - \frac{1}{\sigma_{\mathrm{tr},g}} \sum_{\substack{g'=1 \\ g' \neq g}}^{G} \sigma_{1,g' \to g} \vec{J}_{g'}^{k+\frac{1}{2}} - \mathrm{D}_g \vec{\nabla} \phi_g^{k+\frac{1}{2}} \right). \quad (3.29)$$

and the drift-diffusion equation

$$\begin{aligned} &- \left(\mathrm{D}_g \vec{\nabla} \phi_g^{k+1}, \vec{\nabla} \phi_g^* \right)_{\mathcal{D}} - \left(\hat{\alpha}_g^{k+\frac{1}{2}} \phi_g^{k+1}, \vec{\nabla} \phi_g^* \right)_{\mathcal{D}} + \left(\sigma_{\mathrm{a},g} \phi_g^{k+1}, \phi_g^* \right)_{\mathcal{D}} + \left\langle \frac{\kappa_g^{k+\frac{1}{2}}}{4} \phi_g^{k+1}, \phi_g^* \right\rangle_{\partial \mathcal{D}_{\mathrm{V}}} \\ &\quad = \left(\sum_{\substack{g'=1 \\ g' \neq g}}^{G} \sigma_{\mathrm{s},g' \to g} \phi_{g'}^{k+1}, \phi_g^* \right)_{\mathcal{D}} + \left(\sum_{g'=1}^{G} \bar{\nu} \sigma_{\mathrm{f},g'} \phi_{g'}^{k+1}, \phi_g^* \right)_{\mathcal{D}} + \left(q_g, \phi_g^* \right)_{\mathcal{D}} + \left\langle \hat{\jmath}_g^{\mathrm{in}}, \phi_g^* \right\rangle_{\partial \mathcal{D}_{\mathrm{V}}} \end{aligned} \quad (3.30)$$

3.2 Fourier Analysis

The drift vector Eq. (3.10) and the diffusion coefficient Eq. (3.9) are not defined in void regions. To be able to analyze changes to the NDA when changing the drift vector we use a Fourier Analysis. This tool uses a Fourier transformation to determine the spectral radius for an iterative technique. Since the discretization can change the spectral radius, especially for a non-consistent acceleration formulation [5], we study the one-dimensional discretized equations.

3.2.1 High-order equation

First we consider the high order equation to be able to derive the NDA correction terms. The one-dimensional NDA equation for WLS Eq. (3.28a) in the weak form with the iteration index k is

$$\left(w\mu\frac{\partial}{\partial x}\psi^{k+\frac{1}{2}},\mu\frac{\partial}{\partial x}\psi^{*}+\sigma_{\mathrm{t}}\psi^{*}\right)_{\mathcal{D}}+\left(w\sigma_{\mathrm{t}}\psi^{k+\frac{1}{2}},\mu\frac{\partial}{\partial x}\psi^{*}+\sigma_{\mathrm{t}}\psi^{*}\right)_{\mathcal{D}} = \left(w\frac{c\sigma_{\mathrm{t}}}{2}\phi^{k},\mu\frac{\partial}{\partial x}\psi^{*}+\sigma_{\mathrm{t}}\psi^{*}\right)_{\mathcal{D}}+\left(w\frac{q}{2},\mu\frac{\partial}{\partial x}\psi^{*}+\sigma_{\mathrm{t}}\psi^{*}\right)_{\mathcal{D}} \tag{3.31}$$

with the scattering cross section

$$\sigma_{\mathrm{s}}=c\sigma_{\mathrm{t}} \tag{3.32}$$

Using the problem's exact solution ψ with

$$\psi=\psi^{k}+\delta\psi^{k} \tag{3.33}$$

where $\delta\psi^k$ is the error in the kth iteration and subtracting it from Eq. (3.31) gives the WLS equation for the error

$$\left(w\mu\frac{\partial}{\partial x}\delta\psi^{k+\frac{1}{2}},\mu\frac{\partial}{\partial x}\psi^*\right)_{\mathcal{D}}+\left(w\mu\frac{\partial}{\partial x}\delta\psi^{k+\frac{1}{2}},\sigma_{\mathrm{t}}\psi^*\right)_{\mathcal{D}}+\left(w\sigma_{\mathrm{t}}\delta\psi^{k+\frac{1}{2}},\mu\frac{\partial}{\partial x}\psi^*\right)_{\mathcal{D}}$$
$$+\left(w\sigma_{\mathrm{t}}\delta\psi^{k+\frac{1}{2}},\sigma_{\mathrm{t}}\psi^*\right)_{\mathcal{D}}=\left(w\frac{c\sigma_{\mathrm{t}}}{2}\delta\phi^k,\mu\frac{\partial}{\partial x}\psi^*\right)_{\mathcal{D}}+\left(w\frac{c\sigma_{\mathrm{t}}}{2}\delta\phi^k,\sigma_{\mathrm{t}}\psi^*\right)_{\mathcal{D}}. \quad (3.34)$$

We apply first order continuous finite elements with the cell index i, where integer indices indicate the interior of a cell, while half indices denote the mesh vertices

$$\begin{aligned}&\frac{w\mu^2}{h}\left(2\delta\psi_{i+\frac{1}{2}}^{k+\frac{1}{2}}-\delta\psi_{i-\frac{1}{2}}^{k+\frac{1}{2}}-\delta\psi_{i+\frac{3}{2}}^{k+\frac{1}{2}}\right)+\frac{w\mu\sigma_{\mathrm{t}}}{2}\left(\delta\psi_{i+\frac{3}{2}}^{k+\frac{1}{2}}-\delta\psi_{i-\frac{1}{2}}^{k+\frac{1}{2}}\right)\\ -&\frac{w\mu\sigma_{\mathrm{t}}}{2}\left(\delta\psi_{i+\frac{3}{2}}^{k+\frac{1}{2}}-\delta\psi_{i-\frac{1}{2}}^{k+\frac{1}{2}}\right)+\frac{wh\sigma_{\mathrm{t}}^2}{2}\left(\frac{4}{3}\delta\psi_{i+\frac{1}{2}}^{k+\frac{1}{2}}+\frac{1}{3}\delta\psi_{i-\frac{1}{2}}^{k+\frac{1}{2}}+\frac{1}{3}\delta\psi_{i+\frac{3}{2}}^{k+\frac{1}{2}}\right)\\ =&\frac{w\mu c\sigma_{\mathrm{t}}}{4}\left(\delta\phi_{i-\frac{1}{2}}^{k}-\delta\phi_{i+\frac{3}{2}}^{k}\right)+\frac{wc\sigma_{\mathrm{t}}^2h}{4}\left(\frac{4}{3}\delta\phi_{i+\frac{1}{2}}^{k}+\frac{1}{3}\delta\phi_{i-\frac{1}{2}}^{k}+\frac{1}{3}\delta\phi_{i+\frac{3}{2}}^{k}\right)\end{aligned} \quad (3.35)$$

and note that the two first order terms cancel. Additionally the equation can be divided by the weight function w. Hence the spectral radius for an infinite medium is independent of the weight function. The Fourier Ansatz

$$\delta\psi\left(x,\mu\right)=\int_0^\infty\hat{\psi}\left(\lambda,\mu\right)\mathrm{e}^{\hat{\imath}\lambda\sigma_{\mathrm{t}}x}\,d\lambda \quad (3.36)$$

gives for the error of the flux moments

$$\begin{aligned}
\delta\phi(x) &= \int_{-1}^{1}\int_{0}^{\infty} \hat{\psi}(\lambda,\mu)\, \mathrm{e}^{\hat{\imath}\lambda\sigma_\mathrm{t}x}\, d\lambda\, d\mu \\
&= \int_{0}^{\infty} \hat{\phi}(\lambda)\, \mathrm{e}^{\hat{\imath}\lambda\sigma_\mathrm{t}x}\, d\lambda \qquad (3.37)\\
\delta J(x) &= \int_{-1}^{1} \mu \int_{0}^{\infty} \hat{\psi}(\lambda,\mu)\, \mathrm{e}^{\hat{\imath}\lambda\sigma_\mathrm{t}x}\, d\lambda\, d\mu \\
&= \int_{0}^{\infty} \hat{J}(\lambda)\, \mathrm{e}^{\hat{\imath}\lambda\sigma_\mathrm{t}x}\, d\lambda \qquad (3.38)\\
\delta\xi(x) &= \int_{-1}^{1} \mu^2 \int_{0}^{\infty} \hat{\psi}(\lambda,\mu)\, \mathrm{e}^{\hat{\imath}\lambda\sigma_\mathrm{t}x}\, d\lambda\, d\mu \\
&= \int_{0}^{\infty} \hat{\xi}(\lambda)\, \mathrm{e}^{\hat{\imath}\lambda\sigma_\mathrm{t}x}\, d\lambda \qquad (3.39)
\end{aligned}$$

Substituting the Ansatz into Eq. (3.35) gives an equation for a specific frequency λ. Substituting the exponential function by trigonometric functions gives

$$\begin{aligned}
&2\mu^2\left(1-\cos\left(\lambda\sigma_\mathrm{t}h\right)\right)\hat{\psi}^{k+\frac{1}{2}} + \frac{\sigma_\mathrm{t}^2h^2}{3}\left(2+\cos\left(\lambda\sigma_\mathrm{t}h\right)\right)\hat{\psi}^{k+\frac{1}{2}} \\
&\qquad = -\frac{\mu c\sigma_\mathrm{t}h}{2}\hat{\imath}\sin\left(\lambda\sigma_\mathrm{t}h\right)\hat{\phi}^{k} + \frac{c\sigma_\mathrm{t}^2h^2}{6}\left(2+\cos\left(\lambda\sigma_\mathrm{t}h\right)\right)\hat{\phi}^{k} \qquad (3.40)
\end{aligned}$$

This equation is solved for the angular flux at iteration $k+\frac{1}{2}$

$$\hat{\psi}^{k+\frac{1}{2}} = \frac{-\frac{\mu c\sigma_\mathrm{t}h}{2}\hat{\imath}\sin\left(\lambda\sigma_\mathrm{t}h\right) + \frac{c\sigma_\mathrm{t}^2h^2}{6}\left(2+\cos\left(\lambda\sigma_\mathrm{t}h\right)\right)}{2\mu^2\left(1-\cos\left(\lambda\sigma_\mathrm{t}h\right)\right) + \frac{\sigma_\mathrm{t}^2h^2}{3}\left(2+\cos\left(\lambda\sigma_\mathrm{t}h\right)\right)}\hat{\phi}^{k} \qquad (3.41)$$

and is dependent on the scalar flux at the kth iteration, the frequency λ and geometric parameters. Note that the solution has an even and an odd part in μ. This fact simplifies the angular integration of the flux moments Eqs. (3.37) to (3.39). These

are for the step $k+\frac{1}{2}$ based on the angular flux

$$\begin{aligned}\hat{\phi}^{k+\frac{1}{2}}(\lambda) &= \int_{-1}^{1} \hat{\psi}^{k+\frac{1}{2}}(\lambda)\, d\mu \\ &= \hat{\phi}^{l} \cdot \frac{c\sigma_{\mathrm{t}}h}{3}\left(2+\cos\left(\lambda\sigma_{\mathrm{t}}h\right)\right) \frac{\tan^{-1}\left(\frac{\sqrt{6(1-\cos(\lambda\sigma_{\mathrm{t}}h))}}{\sigma_{\mathrm{t}}h\sqrt{2+\cos(\lambda\sigma_{\mathrm{t}}h)}}\right)}{\sqrt{\frac{2}{3}\left(1-\cos\left(\lambda\sigma_{\mathrm{t}}h\right)\right)\left(2+\cos\left(\lambda\sigma_{\mathrm{t}}h\right)\right)}}\end{aligned} \tag{3.42}$$

$$\begin{aligned}\hat{J}^{k+\frac{1}{2}}(\lambda) &= \int_{-1}^{1} \mu\hat{\psi}^{k+\frac{1}{2}}(\lambda)\, d\mu \\ &= -\hat{\phi}^{l} \cdot \frac{c\sigma_{\mathrm{t}}h}{2}\hat{\imath}\sin\left(\lambda\sigma_{\mathrm{t}}h\right) \\ &\quad \cdot \left(\frac{1}{\left(1-\cos\left(\lambda\sigma_{\mathrm{t}}h\right)\right)} - 2 \cdot \frac{\sigma_{\mathrm{t}}h\sqrt{\frac{2+\cos(\lambda\sigma_{\mathrm{t}}h)}{3}}\tan^{-1}\left(\frac{\sqrt{6(1-\cos(\lambda\sigma_{\mathrm{t}}h))}}{\sigma_{\mathrm{t}}h\sqrt{2+\cos(\lambda\sigma_{\mathrm{t}}h)}}\right)}{\sqrt{2\left(1-\cos\left(\lambda\sigma_{\mathrm{t}}h\right)\right)}^{3}} \right)\end{aligned} \tag{3.43}$$

and

$$\begin{aligned}\hat{\xi}^{k+\frac{1}{2}}(\lambda) &= \int_{-1}^{1} \mu^{2}\hat{\psi}^{k+\frac{1}{2}}(\lambda)\, d\mu \\ &= \hat{\phi}^{l} \cdot \frac{c\sigma_{\mathrm{t}}^{2}h^{2}}{6}\left(2+\cos\left(\lambda\sigma_{\mathrm{t}}h\right)\right) \\ &\quad \cdot \left(\frac{1}{\left(1-\cos\left(\lambda\sigma_{\mathrm{t}}h\right)\right)} - 2 \cdot \frac{\sigma_{\mathrm{t}}h\sqrt{\frac{2+\cos(\lambda\sigma_{\mathrm{t}}h)}{3}}\tan^{-1}\left(\frac{\sqrt{6(1-\cos(\lambda\sigma_{\mathrm{t}}h))}}{\sigma_{\mathrm{t}}h\sqrt{2+\cos(\lambda\sigma_{\mathrm{t}}h)}}\right)}{\sqrt{2\left(1-\cos\left(\lambda\sigma_{\mathrm{t}}h\right)\right)}^{3}} \right)\end{aligned} \tag{3.44}$$

3.2.2 Eddington NDA formulation

As shown in Section 3.1, different NDA methods results in the same low-order drift equation with different closure terms (Eqs. (3.26c) and (3.28c)). Using the found expression for the flux moments Eqs. (3.42) to (3.44) allows to study the effect of

these drift vector closures on the convergence. First, we study the standard closure Eq. (3.28c). We will refer to this scheme further on as Eddington scheme. This drift term is not defined in voids.

By subtracting the exact scalar flux solution ϕ from the one dimensional low-order equation

$$\left(\mathrm{D}\frac{\partial}{\partial x}\phi^{k+1},\frac{\partial}{\partial x}\phi^{*}\right)_{\mathcal{D}}+\left(\hat{\alpha}^{k+\frac{1}{2}}\phi^{k+1},\frac{\partial}{\partial x}\phi^{*}\right)_{\mathcal{D}}+\left((1-c)\,\sigma_{\mathrm{t}}\phi^{k+1},\phi^{*}\right)_{\mathcal{D}} = (q,\phi^{*})_{\mathcal{D}} \quad (3.45)$$

we obtain an equation for the error $\delta\phi$. The drift vector term needs to be linearized

$$\begin{aligned}\hat{\alpha}\phi^{k+1} &= \frac{\frac{1}{\sigma_{\mathrm{t}}}\frac{\partial}{\partial x}\xi^{k+\frac{1}{2}}-\mathrm{D}\frac{\partial}{\partial x}\phi^{k+\frac{1}{2}}}{\phi^{k+\frac{1}{2}}}\phi^{k+1}\\ &= \frac{1}{\sigma_{\mathrm{t}}}\frac{\partial}{\partial x}\delta\xi^{k+\frac{1}{2}}-\mathrm{D}\frac{\partial}{\partial x}\delta\phi^{k+\frac{1}{2}}\end{aligned} \quad (3.46)$$

and substituted into the error equation to obtain

$$\left(\mathrm{D}\frac{\partial}{\partial x}\delta\phi^{k+1},\frac{\partial}{\partial x}\phi^{*}\right)_{\mathcal{D}}+\left(\frac{1}{\sigma_{\mathrm{t}}}\frac{\partial}{\partial x}\delta\xi^{k+\frac{1}{2}},\frac{\partial}{\partial x}\phi^{*}\right)_{\mathcal{D}}-\left(\mathrm{D}\frac{\partial}{\partial x}\delta\phi^{k+\frac{1}{2}},\frac{\partial}{\partial x}\phi^{*}\right)_{\mathcal{D}}+\left((1-c)\,\sigma_{\mathrm{t}}\delta\phi^{k+1},\phi^{*}\right)_{\mathcal{D}}=0 \quad (3.47)$$

This equation is discretized by applying the inner products using first order continuous finite elements

$$\begin{aligned}&\frac{\mathrm{D}}{h}\left(2\delta\phi_{i+\frac{1}{2}}^{k+1}-\delta\phi_{i-\frac{1}{2}}^{k+1}-\delta\phi_{i+\frac{3}{2}}^{k+1}\right)+\frac{\sigma_{\mathrm{t}}h}{2}(1-c)\left(\frac{4}{3}\delta\phi_{i+\frac{1}{2}}^{k+1}+\frac{1}{3}\delta\phi_{i-\frac{1}{2}}^{k+1}+\frac{1}{3}\delta\phi_{i+\frac{3}{2}}^{k+1}\right)\\ &\quad=-\frac{1}{\sigma_{\mathrm{t}}h}\left(2\delta\xi_{i+\frac{1}{2}}^{k+\frac{1}{2}}-\delta\xi_{i-\frac{1}{2}}^{k+\frac{1}{2}}-\delta\xi_{i+\frac{3}{2}}^{k+\frac{1}{2}}\right)+\frac{\mathrm{D}}{h}\left(2\delta\phi_{i+\frac{1}{2}}^{k+\frac{1}{2}}-\delta\phi_{i-\frac{1}{2}}^{k+\frac{1}{2}}-\delta\phi_{i+\frac{3}{2}}^{k+\frac{1}{2}}\right)\end{aligned} \quad (3.48)$$

Substituting the Fourier definitions Eqs. (3.37) and (3.39) into the discretized equation we obtain a frequency equation. The exponential function is expressed by trigonometric functions and the low-order equation can be solved for

$$\hat{\phi}^{k+1} = \frac{\frac{2\mathrm{D}}{h}\left(1-\cos\left(\lambda\sigma_{\mathrm{t}}h\right)\right)\hat{\phi}^{k+\frac{1}{2}} - \frac{2}{\sigma_{\mathrm{t}}h}\left(1-\cos\left(\lambda\sigma_{\mathrm{t}}h\right)\right)\hat{\xi}^{k+\frac{1}{2}}}{\frac{2\mathrm{D}}{h}\left(1-\cos\left(\lambda\sigma_{\mathrm{t}}h\right)\right) + \frac{\sigma_{\mathrm{t}}h}{3}\left(1-c\right)\left(2+\cos\left(\lambda\sigma_{\mathrm{t}}h\right)\right)} \tag{3.49}$$

The $k+1$st iteration scalar flux is only defined by the flux moments from the $k+\frac{1}{2}$ iteration. These are known from the high-order equation. Substituting Eqs. (3.42) and (3.44) into Eq. (3.49) and using the classical diffusion coefficient Eq. (3.9) gives the expression for the spectral radius Eq. (1.20)

$$\begin{aligned}\rho\left(\lambda,\sigma_{\mathrm{t}}h\right) = {} & \frac{c\sigma_{\mathrm{t}}h\left(1-\cos\left(\lambda\sigma_{\mathrm{t}}h\right)\right)\left(2+\cos\left(\lambda\sigma_{\mathrm{t}}h\right)\right)}{\frac{2}{\sigma_{\mathrm{t}}h}\left(1-\cos\left(\lambda\sigma_{\mathrm{t}}h\right)\right) + \sigma_{\mathrm{t}}h\left(1-c\right)\left(2+\cos\left(\lambda\sigma_{\mathrm{t}}h\right)\right)} \\ & \cdot\left(\frac{2}{3}\frac{\tan^{-1}\left(\frac{\sqrt{6(1-\cos(\lambda\sigma_{\mathrm{t}}h))}}{\sigma_{\mathrm{t}}h\sqrt{2+\cos(\lambda\sigma_{\mathrm{t}}h)}}\right)}{\sigma_{\mathrm{t}}h\sqrt{\frac{2}{3}\left(1-\cos\left(\lambda\sigma_{\mathrm{t}}h\right)\right)\left(2+\cos\left(\lambda\sigma_{\mathrm{t}}h\right)\right)}}\right. \\ & \left. -\frac{1}{\left(1-\cos\left(\lambda\sigma_{\mathrm{t}}h\right)\right)} + 2\frac{\sigma_{\mathrm{t}}h\tan^{-1}\left(\frac{\sqrt{6(1-\cos(\lambda\sigma_{\mathrm{t}}h))}}{\sigma_{\mathrm{t}}h\sqrt{2+\cos(\lambda\sigma_{\mathrm{t}}h)}}\right)}{\sqrt{2\left(1-\cos\left(\lambda\sigma_{\mathrm{t}}h\right)\right)^{3}}}\right)\end{aligned} \tag{3.50}$$

The maximum spectral radius is found to be 0.22466 for $c = 1.0$, which is very close to the analytical value found by Adams [5]. As Fig. 3.1 shows, the spectral radius reaches it maximum for thin cells. For thick cells, the spectral radius decreases exponentially. This shows that the scheme is always highly efficient, even though it is can be inconsistent for small optical thicknesses.

One parameter, that influences the convergence, is the used diffusion coefficient. Since the classical diffusion coefficient (Eq. (3.9)) is unbound in voids, we will have to modify it to be compatible with voids. For this it is important to know how the

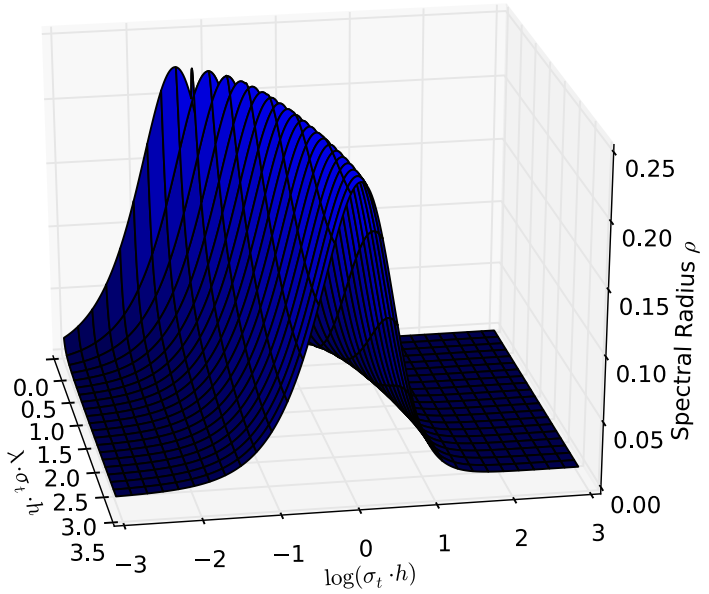

Figure 3.1 Spectral radius for the Eddington NDA formulation in an infinite homogeneous medium as a function of optical cell thickness and frequency for $c = 1$.

diffusion coefficient influences the convergence behavior. For this reason we varied the factor 1/3 of the diffusion coefficient and calculated the corresponding spectral radius. For a few selected factors the results are shown in Fig. 3.2. In this plot, dotted lines indicate the absolute value of a negative eigenvalues is the spectral radius, which means the error (Eq. (1.19)) oscillates around the exact solution. The classical diffusion coefficient is optimal for optical thick cells ($\sigma_t h \gg 1$), reducing the spectral radius exponentially towards zero. However, for optical thin cells ($\sigma_t h \leq 1$), a slightly smaller diffusion coefficient gave a better convergence. For $D \approx 0.285\sigma_t^{-1}$ the spectral radius is $\rho \approx 0.1893$ at $\sigma_t h = 0.1$ compared to $\rho \approx 0.2247$ for the classical diffusion coefficient.

This can be better seen in Fig. 3.3 that shows the spectral radius as a function of the diffusion coefficient. The plot shows an optical thin and an optical thick case.

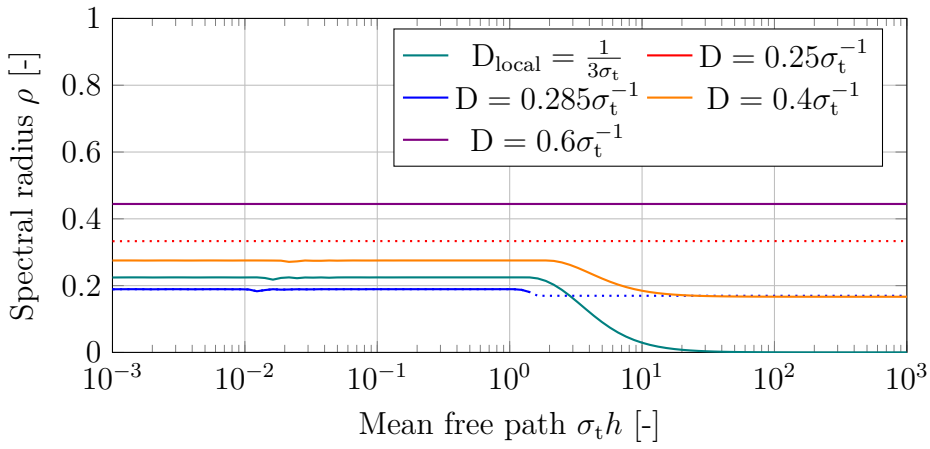

Figure 3.2 Spectral radius for $c = 1$ as function of the optical cell thickness for different diffusion coefficient in an infinite homogeneous medium (a dotted line indicates a negative value).

The result showed that diffusion coefficients larger than the local diffusion coefficient slowly increase the spectral radius. For smaller diffusion coefficients the increase of the spectral radius is rapid with small variations from the optimal value. Optical thin and thick cases have the same behavior except for values around the local diffusion coefficient. For smaller coefficient than the optimal ones, both cases jump to negative eigenvalue of maximum magnitude. Therefore the diffusion coefficient must be close to this minimum to obtain a good iterative convergence.

3.2.3 Current NDA formulation

A different way of closing the low-order equation is by substituting the classical neutron current Eq. (1.5) for the Eddington factor using Eq. (3.3). The drift vector becomes

$$\hat{\alpha}^{k+\frac{1}{2}} = \frac{1}{\phi^{k+\frac{1}{2}}}\left(-\vec{J}^{k+\frac{1}{2}} - \mathrm{D}\vec{\nabla}\phi^{k+\frac{1}{2}}\right) \tag{3.51}$$

with the one dimensional linearization

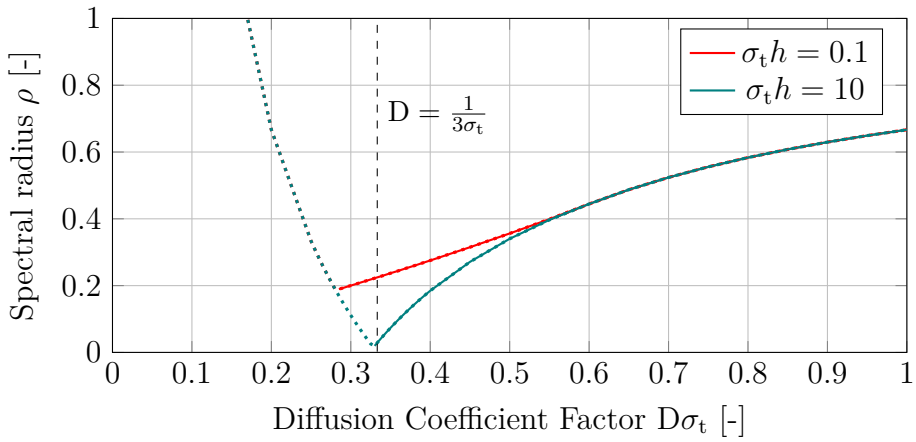

Figure 3.3 Spectral radius for $c = 1$ as function of the diffusion coefficient factor in an infinite homogeneous medium for two optical thicknesses (a dotted line indicates a negative eigenvalue).

$$\hat{\alpha}^{k+\frac{1}{2}}\phi^{k+1} = -\delta J^{k+\frac{1}{2}} - \mathrm{D}\frac{\partial}{\partial x}\delta\phi^{k+\frac{1}{2}} \tag{3.52}$$

This drift vector is defined even with zero total cross section. Substituting this drift vector into the low-order error equation gives

$$\left(\mathrm{D}\frac{\partial}{\partial x}\delta\phi^{k+1}, \frac{\partial}{\partial x}\phi^*\right)_{\mathcal{D}} - \left(\delta J^{k+\frac{1}{2}}, \frac{\partial}{\partial x}\phi^*\right)_{\mathcal{D}} - \left(\mathrm{D}\frac{\partial}{\partial x}\delta\phi^{k+\frac{1}{2}}, \frac{\partial}{\partial x}\phi^*\right)_{\mathcal{D}} + \left((1-c)\,\sigma_\mathrm{t}\delta\phi^{k+1}, \phi^*\right)_{\mathcal{D}} = 0 \tag{3.53}$$

The discretized equation is then

$$\frac{\mathrm{D}}{h}\left(2\delta\phi_{i+\frac{1}{2}}^{k+1} - \delta\phi_{i-\frac{1}{2}}^{k+1} - \delta\phi_{i+\frac{3}{2}}^{k+1}\right) + \frac{\sigma_\mathrm{t}h}{2}(1-c)\left(\frac{4}{3}\delta\phi_{i+\frac{1}{2}}^{k+1} + \frac{1}{3}\delta\phi_{i-\frac{1}{2}}^{k+1} + \frac{1}{3}\delta\phi_{i+\frac{3}{2}}^{k+1}\right) = \frac{1}{2}\left(\delta J_{i-\frac{1}{2}}^{k+\frac{1}{2}} - \delta J_{i+\frac{3}{2}}^{k+\frac{1}{2}}\right) + \frac{\mathrm{D}}{h}\left(2\delta\phi_{i+\frac{1}{2}}^{k+\frac{1}{2}} - \delta\phi_{i-\frac{1}{2}}^{k+\frac{1}{2}} - \delta\phi_{i+\frac{3}{2}}^{k+\frac{1}{2}}\right) \tag{3.54}$$

Using the same method as above and substitute the Fourier Ansatz Eqs. (3.37) and (3.38) we obtain the scalar flux at $k+1$ as

$$\hat{\phi}^{k+1} = \frac{\frac{2\mathrm{D}}{h}\left(1-\cos\left(\lambda\sigma_{\mathrm{t}}h\right)\right)\hat{\phi}^{k+\frac{1}{2}} - \hat{\imath}\sin\left(\lambda\sigma_{\mathrm{t}}h\right)\hat{J}^{k+\frac{1}{2}}}{\frac{2\mathrm{D}}{h}\left(1-\cos\left(\lambda\sigma_{\mathrm{t}}h\right)\right) + \frac{\sigma_{\mathrm{t}}h}{3}\left(1-c\right)\left(2+\cos\left(\lambda\sigma_{\mathrm{t}}h\right)\right)} \tag{3.55}$$

With the diffusion coefficient and the expression for the high order scalar flux Eq. (3.42) and neutron current Eq. (3.43) we obtain

$$\begin{aligned}\rho\left(\lambda,\sigma_{\mathrm{t}}h\right) = {} & \frac{3}{\frac{2}{\sigma_{\mathrm{t}}h}\left(1-\cos\left(\lambda\sigma_{\mathrm{t}}h\right)\right) + \sigma_{\mathrm{t}}h\left(1-c\right)\left(2+\cos\left(\lambda\sigma_{\mathrm{t}}h\right)\right)} \\ & \cdot\left(\frac{2}{9}c\left(1-\cos\left(\lambda\sigma_{\mathrm{t}}h\right)\right)\left(2+\cos\left(\lambda\sigma_{\mathrm{t}}h\right)\right)\right. \\ & \quad \cdot\frac{\tan^{-1}\left(\frac{\sqrt{6\left(1-\cos\left(\lambda\sigma_{\mathrm{t}}h\right)\right)}}{\sigma_{\mathrm{t}}h\sqrt{2+\cos\left(\lambda\sigma_{\mathrm{t}}h\right)}}\right)}{\sqrt{\frac{2}{3}\left(1-\cos\left(\lambda\sigma_{\mathrm{t}}h\right)\right)\left(2+\cos\left(\lambda\sigma_{\mathrm{t}}h\right)\right)}} - \frac{c\sigma_{\mathrm{t}}h\sin^2\left(\lambda\sigma_{\mathrm{t}}h\right)}{2\left(1-\cos\left(\lambda\sigma_{\mathrm{t}}h\right)\right)} \\ & \quad \left.+\sin^2\left(\lambda\sigma_{\mathrm{t}}h\right)\frac{c\sigma_{\mathrm{t}}^2h^2\sqrt{\frac{2+\cos\left(\lambda\sigma_{\mathrm{t}}h\right)}{3}}\tan^{-1}\left(\frac{\sqrt{6\left(1-\cos\left(\lambda\sigma_{\mathrm{t}}h\right)\right)}}{\sigma_{\mathrm{t}}h\sqrt{2+\cos\left(\lambda\sigma_{\mathrm{t}}h\right)}}\right)}{\sqrt{2\left(1-\cos\left(\lambda\sigma_{\mathrm{t}}h\right)\right)^3}}\right)\end{aligned} \tag{3.56}$$

While for thin cells in a pure scatter ($c=1$), the results are the same as for the Eddington formulation, for thick cells the spectral radius approaches asymptotically 1 for high frequencies as shown in Fig. 3.4.

To better understand the reason for the loss of efficiency for the current formulation we compare the results. Looking at Eqs. (3.49) and (3.55) we see that the only difference is in the term containing $\hat{J}$ respectively $\hat{\xi}$. All other terms are the same in both equations. Figure 3.5 shows that for high frequencies the contribution of the current term is reduced to zero. The reason for this behavior can be found in Eq. (3.54). The discretization of the current term originating in the drift vector is a badly behaved central difference two point approximation skipping the center node.

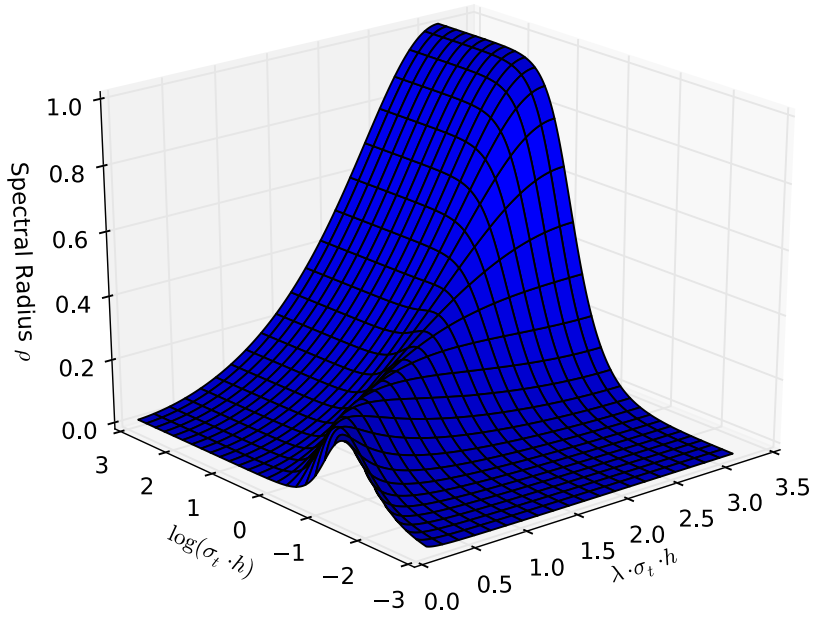

Figure 3.4 Spectral radius for the Current NDA formulation in an infinite homogeneous medium as a function of optical cell thickness and frequency.

This type of discretization cannot represent high frequencies. For the highest possible frequency on a mesh, alternating between every node, this term becomes zero for all cases. The error cannot be reduced and hence the scheme will never converge on this frequency. This leads then to a spectral radius of one.

3.3 Modifications for Voids

3.3.1 Diffusion coefficient in voids

The classical formulation of the diffusion coefficient (Eq. (3.9)) is unbounded in voids. However, if we consider Eq. (3.11), we see that in the case of spatial and iterative convergence the diffusion terms cancel, however the diffusion coefficient has a strong influence on the spectral radius as shown in Figs. 3.2 and 3.3. We chose to use a non-local definition of the diffusion coefficient, which is close to the local diffusion

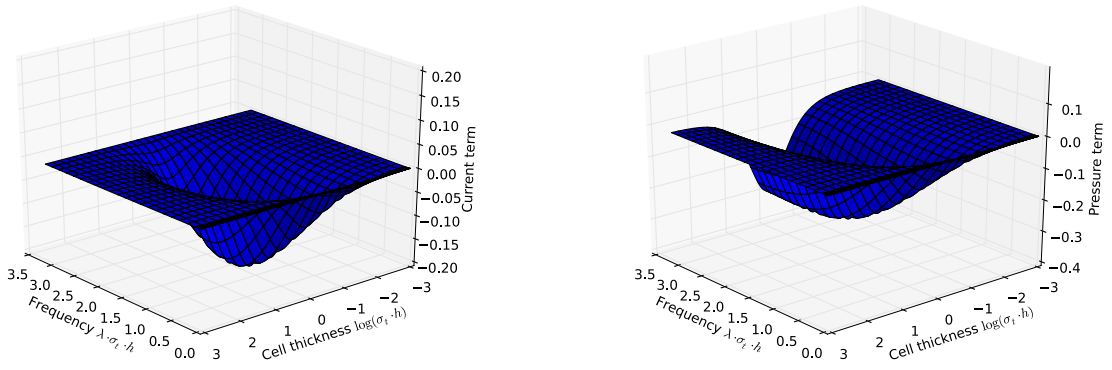

(a) Current (b) Eddington

Figure 3.5 Comparison of the terms in the current and the Eddington formulation, that shows clearly the reduction to zero for the current term at high frequencies for $c = 1$.

coefficient in optical thick cells and well limited in optical thin cells. The derivation was first proposed by Morel [50, 49] and later studied by Larsen and Trahan [35, 68] and Schunert [59]. Larsen and Morel [34] extended the theory recently to anisotropic scattering. We will use the last paper to show the derivation here, however we limit it to the isotropic case.

We consider the isotropic, mono-energetic transport equation Eq. (1.12)

$$\vec{\Omega} \cdot \vec{\nabla}\psi_m + \sigma_\mathrm{t}\psi_m = \frac{1}{4\pi}\sigma_\mathrm{s}\phi + \frac{\bar{\nu}\sigma_\mathrm{f}}{4\pi}\phi + \frac{q}{4\pi}. \tag{3.57}$$

Integrating over all angles gives the balance equation Eq. (3.1). If we consider a linear anisotropic angular flux

$$\psi_m = \frac{\phi}{4\pi} + \frac{3\vec{\Omega}_m \cdot \vec{J}}{4\pi} \tag{3.58}$$

the first moment Eq. (3.2) reduces to

$$\frac{1}{3}\vec{\nabla}\phi + \sigma_{\mathrm{t}}\vec{J} = 0. \tag{3.59}$$

This gives the diffusion approximation

$$\vec{J} = -\mathrm{D}\vec{\nabla}\phi \tag{3.60}$$

with the classical diffusion coefficient Eq. (3.9). The same result can be derived by an asymptotic expansion with a small parameter ϵ, in which

$$\phi = O\left(1\right) \tag{3.61a}$$

$$\vec{J} = O\left(\epsilon\right) \tag{3.61b}$$

$$\vec{\nabla} = O\left(\epsilon\right) \tag{3.61c}$$

The method proposed by Larsen and Morel does not require ψ to be linear in angle, however it does assume Eq. (3.61) to hold.

The analysis continues by solving the balance Eq. (3.1) for the scattering term

$$\sigma_{\mathrm{s}}\phi = \vec{\nabla}\cdot\vec{J} + \sigma_{\mathrm{t}}\phi - \bar{\nu}\sigma_{\mathrm{f}}\phi - q \tag{3.62}$$

and substitute this into the transport Eq. (3.57) to obtain

$$\vec{\Omega}\cdot\vec{\nabla}\psi_m + \sigma_{\mathrm{t}}\psi_m = \frac{1}{4\pi}\left(\vec{\nabla}\cdot\vec{J} + \sigma_{\mathrm{t}}\phi\right). \tag{3.63}$$

The solution to Eq. (3.63) is

$$\begin{aligned}\psi\left(x,\vec{\Omega}\right) &= \frac{1}{4\pi}\left(\vec{\Omega}\cdot\vec{\nabla}+\sigma_{\mathrm{t}}\right)^{-1}\left[\vec{\nabla}\cdot\vec{J}+\sigma_{\mathrm{t}}\phi\right] \\ &= \frac{1}{4\pi}\left(\vec{\Omega}\cdot\vec{\nabla}+\sigma_{\mathrm{t}}\right)^{-1}\left[\left(\vec{\Omega}\cdot\vec{\nabla}+\sigma_{\mathrm{t}}\right)\phi+\vec{\nabla}\cdot\vec{J}-\vec{\Omega}\cdot\vec{\nabla}\phi\right] \\ &= \frac{1}{4\pi}\left(\vec{\Omega}\cdot\vec{\nabla}+\sigma_{\mathrm{t}}\right)^{-1}\left(\vec{\Omega}\cdot\vec{\nabla}+\sigma_{\mathrm{t}}\right)\phi+\frac{1}{4\pi}\left(\vec{\Omega}\cdot\vec{\nabla}+\sigma_{\mathrm{t}}\right)^{-1}\vec{\nabla}\cdot\vec{J} \\ &\quad -\frac{1}{4\pi}\left(\vec{\Omega}\cdot\vec{\nabla}+\sigma_{\mathrm{t}}\right)^{-1}\vec{\Omega}\cdot\vec{\nabla}\phi. \end{aligned} \tag{3.64}$$

Multiplying Eq. (3.64) with $\vec{\Omega}$ and integrating over all angles gives us an expression for the current

$$\begin{aligned}\vec{J} = \frac{1}{4\pi}\int_{4\pi}\vec{\Omega}\left(\vec{\Omega}\cdot\vec{\nabla}+\sigma_{\mathrm{t}}\right)^{-1}\left(\vec{\Omega}\cdot\vec{\nabla}+\sigma_{\mathrm{t}}\right)\phi\,d\vec{\Omega} \\ +\frac{1}{4\pi}\int_{4\pi}\vec{\Omega}\left(\vec{\Omega}\cdot\vec{\nabla}+\sigma_{\mathrm{t}}\right)^{-1}\vec{\nabla}\cdot\vec{J}\,d\vec{\Omega} \\ -\frac{1}{4\pi}\int_{4\pi}\vec{\Omega}\left(\vec{\Omega}\cdot\vec{\nabla}+\sigma_{\mathrm{t}}\right)^{-1}\vec{\Omega}\cdot\vec{\nabla}\phi\,d\vec{\Omega}.\end{aligned} \tag{3.65}$$

The line integral operator $\left(\vec{\Omega}\cdot\vec{\nabla}+\sigma_{\mathrm{t}}\right)^{-1}$ can be found using the method of characteristics as

$$\left(\vec{\Omega}\cdot\vec{\nabla}+\sigma_{\mathrm{t}}\right)^{-1}g\left(x,\vec{\Omega}\right) = \int_0^{\ell\left(x,-\vec{\Omega}\right)}\mathrm{e}^{-\int_0^s\sigma_{\mathrm{t}}\left(x-s'\vec{\Omega}\right)ds'}g\left(x-s\vec{\Omega}\right)\,ds \tag{3.66}$$

where ℓ is the distance to the boundary in direction $\vec{\Omega}$ and g is an arbitrary function.

We can use this to analyze Eq. (3.65) term by term. The first term gives

$$\begin{aligned}
\vec{J}_1 &= \frac{1}{4\pi}\int_{4\pi}\vec{\Omega}\left(\vec{\Omega}\cdot\vec{\nabla}+\sigma_{\mathrm{t}}\right)^{-1}\left(\vec{\Omega}\cdot\vec{\nabla}+\sigma_{\mathrm{t}}\right)\phi\,d\vec{\Omega} \\
&= \frac{1}{4\pi}\int_{4\pi}\vec{\Omega}\int_0^{l\left(x,-\vec{\Omega}\right)}\mathrm{e}^{-\int_0^s\sigma_{\mathrm{t}}\left(x-s'\vec{\Omega}\right)ds'}\left(-\frac{\partial}{\partial s}+\sigma_{\mathrm{t}}\left(x-\sigma_{\mathrm{t}}\vec{\Omega}\right)\right)\phi\left(x-s\vec{\Omega}\right)\,ds\,d\vec{\Omega} \\
&= -\frac{1}{4\pi}\int_{4\pi}\vec{\Omega}\int_0^{l\left(x,-\vec{\Omega}\right)}\frac{\partial}{\partial s}\left[\mathrm{e}^{-\int_0^s\sigma_{\mathrm{t}}\left(x-s'\vec{\Omega}\right)ds'}\phi\left(x-s\vec{\Omega}\right)\right]\,ds\,d\vec{\Omega} \\
&= -\frac{1}{4\pi}\int_{4\pi}\vec{\Omega}\left[\mathrm{e}^{-\int_0^s\sigma_{\mathrm{t}}\left(x-s'\vec{\Omega}\right)ds'}\phi\left(x-s\vec{\Omega}\right)\right]_0^{\ell\left(x,-\vec{\Omega}\right)}\,d\vec{\Omega} \\
&= \frac{1}{4\pi}\int_{4\pi}\vec{\Omega}\phi\,d\vec{\Omega}-\frac{1}{4\pi}\int_{4\pi}\vec{\Omega}\mathrm{e}^{-\int_0^s\sigma_{\mathrm{t}}\left(x-s'\vec{\Omega}\right)ds'}\phi\left(x-\ell\left(x,-\vec{\Omega}\right)\vec{\Omega}\right)\,d\vec{\Omega}
\end{aligned} \tag{3.67}$$

The first integral is odd in angle and hence cancels. The second integral is an integral over the incoming boundary $\partial\mathcal{D}_{\mathrm{V}}^{-}$. Since ψ satisfies a vacuum boundary condition and most values get exponentially attenuated from the boundary to the point of interest, Larsen and Morel chose to ignore this term:

$$\vec{J}_1 \approx 0. \tag{3.68}$$

The second integral in Eq. (3.65) becomes with Eq. (3.61)

$$\begin{aligned}
\vec{J}_2 &= \frac{1}{4\pi}\int_{4\pi}\vec{\Omega}\left(\vec{\Omega}\cdot\vec{\nabla}+\sigma_{\mathrm{t}}\right)^{-1}\vec{\nabla}\cdot\vec{J}\,d\vec{\Omega} \\
&= O\left(\epsilon^2\right)
\end{aligned} \tag{3.69}$$

and hence can be neglected. Using Eq. (3.61) on the third integral in Eq. (3.65) we

get

$$\begin{aligned}\vec{J}_3 &= -\frac{1}{4\pi}\int_{4\pi}\vec{\Omega}\int_0^{\ell\left(x,-\vec{\Omega}\right)} \mathrm{e}^{-\int_0^s \sigma_\mathrm{t}\left(x-s'\vec{\Omega}\right)ds'}\vec{\Omega}\cdot\vec{\nabla}\phi\left(x-s\vec{\Omega}\right)\,ds\,d\vec{\Omega} \\ &\approx -\frac{1}{4\pi}\int_{4\pi}\vec{\Omega}\int_0^{\ell\left(x,-\vec{\Omega}\right)} \mathrm{e}^{-\int_0^s \sigma_\mathrm{t}\left(x-s'\vec{\Omega}\right)ds'}\vec{\Omega}\cdot\vec{\nabla}\phi\left(x\right)\,d\vec{\Omega} \\ &= -\frac{1}{4\pi}\int_{4\pi}\vec{\Omega}\int_0^{\ell\left(x,-\vec{\Omega}\right)} \mathrm{e}^{-\int_0^s \sigma_\mathrm{t}\left(x-s'\vec{\Omega}\right)ds'}\vec{\Omega}\,d\vec{\Omega}\cdot\vec{\nabla}\phi \end{aligned} \tag{3.70}$$

with

$$\vec{\nabla}\phi\left(x-s\vec{\Omega}\right) = \vec{\nabla}\phi\left(x\right) + O\left(\epsilon^2 s\right) \tag{3.71}$$

Eqs. (3.68) to (3.70) gives for the current Eq. (3.65)

$$\begin{aligned} J &= -\frac{1}{4\pi}\int_{4\pi}\vec{\Omega}\int_0^{\ell\left(x,-\vec{\Omega}\right)} \mathrm{e}^{-\int_0^s \sigma_\mathrm{t}\left(x-s'\vec{\Omega}\right)ds'}\vec{\Omega}\,d\vec{\Omega}\cdot\vec{\nabla}\phi \\ &= -\underline{\underline{\mathrm{D}}}\vec{\nabla}\phi \end{aligned} \tag{3.72}$$

where the non-local diffusion coefficient

$$\underline{\underline{\mathrm{D}}} \equiv \frac{1}{4\pi}\int_{4\pi}\vec{\Omega}\int_0^{\ell\left(x,-\vec{\Omega}\right)} \mathrm{e}^{-\int_0^s \sigma_\mathrm{t}\left(x-s'\vec{\Omega}\right)ds'}\vec{\Omega}\,d\vec{\Omega} \tag{3.73}$$

is a 3×3 tensor. With Eq. (3.66) this can be expressed as

$$D_{ij} \equiv \frac{1}{4\pi}\int_{4\pi}\left(\vec{\Omega}\cdot\vec{e}_i\right)\left(\vec{\Omega}\cdot\vec{e}_j\right) f\left(\vec{\Omega}\right)\,d\vec{\Omega} \tag{3.74}$$

where $f\left(\vec{\Omega}\right)$ is the solution to an auxiliary transport problem

$$\vec{\Omega}\cdot\vec{\nabla}f + \sigma_\mathrm{t} f = 1 \tag{3.75a}$$

with the vacuum and reflective boundary conditions ($\vec{\Omega}_{\mathrm{R}}$ is the reflected angle for $\vec{\Omega}$)

$$f\left(x_b, \vec{\Omega}\right) = 0, \qquad \forall x_b \in \partial\mathcal{D}_{\mathrm{V}}, \quad \vec{\Omega} \cdot \vec{n} < 0 \tag{3.75b}$$

$$f\left(x_b, \vec{\Omega}\right) = f\left(x_b, \vec{\Omega}_{\mathrm{R}}\right), \qquad \forall x_b \in \partial\mathcal{D}_{\mathrm{R}}, \quad \vec{\Omega} \cdot \vec{n} < 0. \tag{3.75c}$$

This equation can be easily solved using any technique to solve a transport equation. In this study we obtain the non-local diffusion tensor from a WLS solve. Morel proposed originally reflective boundary conditions for the whole problem, however in this dissertation the actual boundary conditions of the problem were used. Note that the equation does not have a scattering source, therefore no source iterations are necessary. The result is well defined in finite voids. Schunert at el. [59] showed that this diffusion coefficient can improve convergence properties of the NDA in problems with discontinuous material properties.

For an infinite homogeneous medium, the non-local diffusion coefficient reduced to the classical local diffusion coefficient. This can easily be shown by using the equilibrium solution

$$f = \frac{1}{\sigma_{\mathrm{t}}} \tag{3.76}$$

in Eq. (3.74). The result is a matrix with the local diffusion coefficient on the main diagonal and all other entries zero.

An example for the non-local diffusion coefficient is shown in Fig. 3.6. The non-local diffusion coefficient is well limited in voids, but the actual value is dependent on the adjacent material regions. If the regions next to a void are optical thin, the value is larger than next to optical thick regions. For optical thick regions the non-local diffusion coefficient settles fast to the value of the local coefficient. In optical thin regions, this equilibrium is not reached.

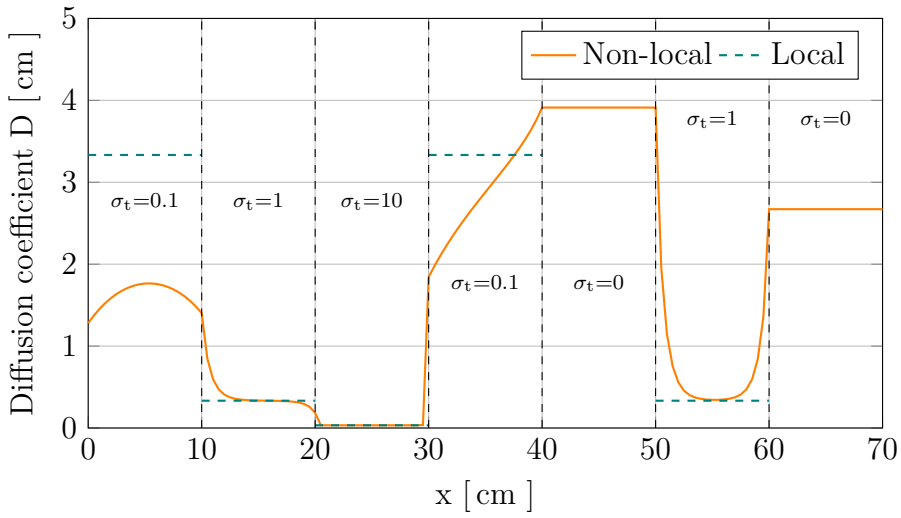

Figure 3.6 Non-local diffusion coefficient for a problem with several material regions (cross sections in $\frac{1}{\text{cm}}$) in comparison to the local diffusion coefficient.

3.3.2 Drift vector formulation

In addition to the diffusion coefficient, the Eddington form of the current in the drift vector formulation Eq. (3.10) becomes singular in voids. The alternative drift vector using the classical neutron current loses efficiency for optical thick cells, but is well defined in voids. Hence we must find a formulation for the drift vector, which is both well defined in voids and efficient for optical thick cells. Consider the general form of the drift vector

$$\hat{\alpha} = \frac{-\vec{J} - \mathrm{D}\vec{\nabla}\phi}{\phi}. \tag{3.77}$$

The diffusion term is well defined given a diffusion coefficient, which is defined in voids such as the non-local diffusion tensor proposed above. The current can be expressed

either by using the Eddington formulation for the current used in Eq. (3.10)

$$\vec{J}_{\text{Eddington}} = -\frac{1}{\sigma_{\text{tr}}} \sum_{m=1}^{M} \omega_m \vec{\Omega}_m \Big(\vec{\Omega}_m \cdot \vec{\nabla} \psi_m \Big), \tag{3.78}$$

or by the alternative of the direct or first moment representation

$$\vec{J}_{\text{Current}} = \sum_{m=1}^{M} \omega_m \vec{\Omega}_m \psi_m, \tag{3.79}$$

or a combination of both formulation to achieve stability in voids and unconditional efficiency.

The first possibility is a simple switch between the two formulations for the current depending on the optical thickness of the cell. For thin cells the direct formulation Eq. (3.79) is used while for thick cells the Eddington formulation Eq. (3.78) ensures a high convergence rate. The combined formulation is obtained as

$$\vec{J} \equiv \begin{cases} \frac{1}{\sigma_{\text{tr}}} \sum\limits_{m=1}^{M} \omega_m \vec{\Omega} \left(\vec{\Omega}_m \cdot \vec{\nabla} \psi_m \right) & \sigma_{\text{tr}} h \geq \hat{\zeta} \\ \sum\limits_{m=1}^{M} \omega_m \vec{\Omega}_m \psi_m & \sigma_{\text{tr}} h < \hat{\zeta} \end{cases} \tag{3.80}$$

where $\hat{\zeta}$ is a threshold value for the optical thickness to switch between the two formulations and h is a characteristic length of the cell. Taking Fig. 3.7 into account $\hat{\zeta} = 0.01$ should provide good convergence for all optical thicknesses. A Fourier analysis for an infinite material reduces to a combination of Eqs. (3.50) and (3.56) and hence has the same convergence properties for a homogeneous material as the Eddington formulation.

Even though the NDA schemes for WLS and SAAFτ were derived differently, the resulting low order equation is identical. However, the drift vector is different

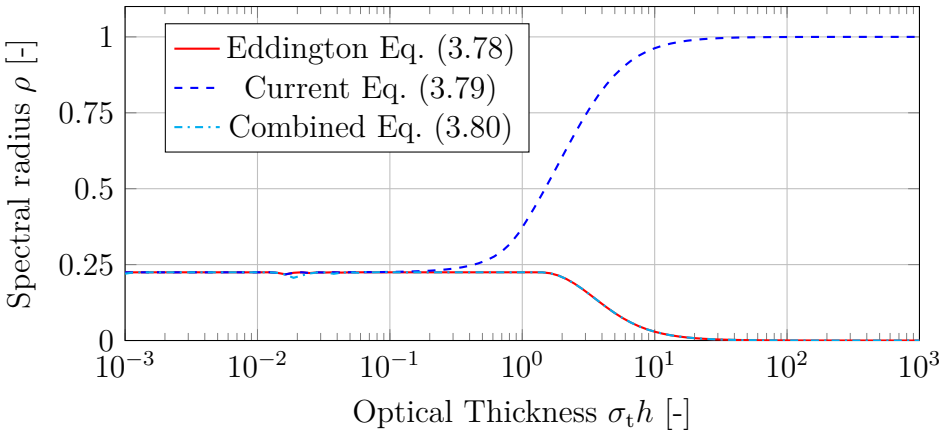

Figure 3.7 Spectral radius for $c = 1$ as function of the optical cell thickness for the Eddington, Current and Combined NDA formulations in an infinite homogeneous material.

between both schemes. The SAAFτ offers for thin cells an additive combination of Eddington and Current formulations. With the definition of τ in Eq. (2.10) the SAAFτ drift vector is well defined in void. The Eddington formulation for the current is limited by τ and corrected by the direct formulation of the current. This results into a formulation where the Eddington and direct current are weighted by τ

$$\vec{J} = \tau\sigma_t \vec{J}_{\text{Eddington}} + (1 - \tau\sigma_t)\, \vec{J}_{\text{Current}}. \tag{3.81}$$

This drift vector can also be used with the WLS transport equation and this NDA scheme is denoted by the τ scheme. The linearization of Eq. (3.26c) is

$$\hat{\alpha}_\tau^{k+\frac{1}{2}} \phi^{k+1} = \tau\delta\xi^{k+\frac{1}{2}} - (1 - \tau\sigma_t)\, \delta J^{k+\frac{1}{2}} - \mathrm{D}\frac{\partial}{\partial x}\delta\phi^{k+\frac{1}{2}}. \tag{3.82}$$

To perform a Fourier analysis Eqs. (3.49) and (3.55) are used to find the scalar flux

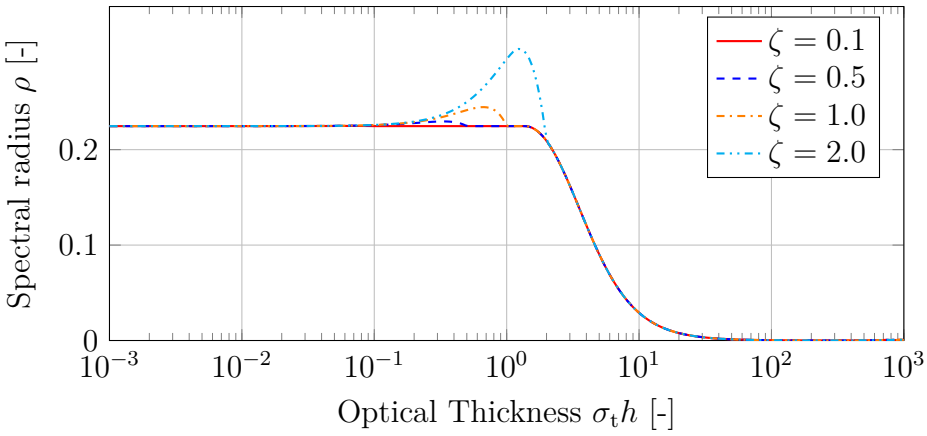

Figure 3.8 Spectral radius for $c = 1$ as function of the optical cell thickness and the threshold parameter ζ for the τ formulation in an infinite homogeneous material.

at iteration $k+1$ to

$$\hat{\phi}^{k+1} = \sigma_t \tau \hat{\phi}^{k+1}_{\text{Eddington}} + (1 - \tau\sigma_t)\, \hat{\phi}^{k+1}_{\text{Current}}$$

and hence the spectral radius for the τ drift vector as

$$\begin{aligned}
\rho(\lambda, \sigma_t h) = {} & \frac{3}{\frac{2}{\sigma_t h}(1 - \cos(\lambda\sigma_t h)) + \sigma_t h\,(1-c)\,(2 + \cos(\lambda\sigma_t h))} \\
& \cdot \left(\frac{2}{9} c\,(1 - \cos(\lambda\sigma_t h))\,(2 + \cos(\lambda\sigma_t h)) \cdot \frac{\tan^{-1}\left(\frac{\sqrt{6(1-\cos(\lambda\sigma_t h))}}{\sigma_t h \sqrt{2+\cos(\lambda\sigma_t h)}} \right)}{\sigma_t h \sqrt{\frac{2}{3}(1 - \cos(\lambda\sigma_t h))\,(2 + \cos(\lambda\sigma_t h))}} \right. \\
& - \left(\frac{c\tau h \sigma_t^2}{3}(2 + \cos(\lambda\sigma_t h))\,(1 - \cos(\lambda\sigma_t h)) + (1 - \tau\sigma_t)\frac{c\sigma_t h}{2}\sin^2(\lambda\sigma_t h) \right) \\
& \left. \left(\frac{1}{2(1 - \cos(\lambda\sigma_t h))} + 2\frac{\sigma_t h \sqrt{\frac{2+\cos(\lambda\sigma_t h)}{3}} \tan^{-1}\left(\frac{\sqrt{6(1-\cos(\lambda\sigma_t h))}}{\sigma_t h \sqrt{2+\cos(\lambda\sigma_t h)}} \right)}{\sqrt{2(1 - \cos(\lambda\sigma_t h))}^3} \right) \right).
\end{aligned} \tag{3.83}$$

The spectral radius is a function of the stabilization parameter and hence of the threshold parameter ζ. Figure 3.8 shows the spectral radius of the NDA algorithm

using a WLS transport equation and the τ drift vector. It can be seen, that for optimal convergence the threshold parameter should be $\zeta \leq 0.1$. Then the same convergence as for the combined formulation Eq. (3.80) is achieved.

3.4 Heterogeneous Fourier Analysis

To further investigate the convergence properties of the modified scheme we need to be able to handle multiple material regions, including void regions. The homogeneous Fourier Analysis performed in Section 3.2 allows only one material. Therefore we derive a numerical Fourier Analysis with multiple regions. We assume an infinite periodic mesh with no assumptions regarding the periodicity of the solution. Figure 3.9 shows a mesh for a problem with two material regions and 2 cells per region. The mesh extends infinitely beyond the section shown, repeating the same structure. Nevertheless we do not assume the solution is periodic. The solution has the form of a vector, i.e. four variable types, multiplied by a complex exponential depending on the position on the whole, infinite mesh.

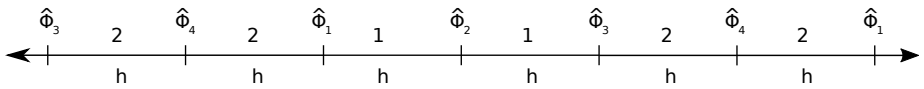

Figure 3.9 Section of an infinite mesh for the Fourier analysis with 2 regions and 4 periodic cells.

3.4.1 High order equation

Starting from the WLS error Eq. (3.34) we discretize using linear CFEM but with multiple regions

$$\begin{aligned}
&\left(\mu^2\left(\frac{w_i}{h_i}+\frac{w_{i+1}}{h_{i+1}}\right)+\mu\left(w_i\sigma_{\mathrm{t},i}-w_{i+1}\sigma_{\mathrm{t},i+1}\right)+\frac{w_i\sigma_{\mathrm{t},i}^2h_i}{3}+\frac{w_{i+1}\sigma_{\mathrm{t},i+1}^2h_{i+1}}{3}\right)\psi_{i+\frac{1}{2}}^{k+\frac{1}{2}}\\
&\quad+\left(-\frac{\mu^2w_i}{h_i}+\frac{w_i\sigma_{\mathrm{t},i}^2h_i}{6}\right)\psi_{1-\frac{1}{2}}^{k+\frac{1}{2}}+\left(-\frac{\mu^2w_{i+1}}{h_{i+1}}+\frac{w_{i+1}\sigma_{\mathrm{t},i+1}^2h_{i+1}}{6}\right)\psi_{1+\frac{3}{2}}^{k+\frac{1}{2}}\\
&=\left(\mu\frac{w_ic_i\sigma_{\mathrm{t},i}}{4}+\frac{w_ic_i\sigma_{\mathrm{t},i}^2h_i}{12}\right)\phi_{i-\frac{1}{2}}^{k}+\left(-\mu\frac{w_{i+1}c_{i+1}\sigma_{\mathrm{t},i+1}}{4}+\frac{w_{i+1}c_{i+1}\sigma_{\mathrm{t},i+1}^2h_{i+1}}{12}\right)\phi_{i+\frac{3}{2}}^{k}\\
&\quad+\left(\mu\frac{w_ic_i\sigma_{\mathrm{t},i}-w_{i+1}c_{i+1}\sigma_{\mathrm{t},i+1}}{4}+\frac{w_ic_i\sigma_{\mathrm{t},i}^2h_i}{6}+\frac{w_{i+1}c_{i+1}\sigma_{\mathrm{t},i+1}^2h_{i+1}}{6}\right)\phi_{i+\frac{1}{2}}^{k}
\end{aligned}\tag{3.84}$$

The weight function is dependent on the cell, and therefore it does not cancel for the multi-region analysis as in the homogeneous Fourier Analysis. Based on Eq. (3.36) we use the following Ansatz

$$\psi_{i+\frac{1}{2}}^{k}=\int_0^\infty\hat{\psi}_{i+\frac{1}{2}}^{k}\left(\lambda,\mu\right)\mathrm{e}^{\hat{\imath}\lambda x_{i+\frac{1}{2}}}\,d\lambda \tag{3.85}$$

and the corresponding flux moments

$$\hat{\phi}_{i+\frac{1}{2}}^{k}\left(\lambda\right)=\int_{-1}^{1}\hat{\psi}_{i+\frac{1}{2}}^{k}\left(\lambda,\mu\right)\,d\mu \tag{3.86}$$

$$\hat{J}_{i+\frac{1}{2}}^{k}\left(\lambda\right)=\int_{-1}^{1}\mu\hat{\psi}_{i+\frac{1}{2}}^{k}\left(\lambda,\mu\right)\,d\mu \tag{3.87}$$

$$\hat{\xi}_{i+\frac{1}{2}}^{k}\left(\lambda\right)=\int_{-1}^{1}\mu^2\hat{\psi}_{i+\frac{1}{2}}^{k}\left(\lambda,\mu\right)\,d\mu \tag{3.88}$$

The periodic geometry gives

$$\hat{\psi}_{i+\frac{1}{2}}^{k}\left(\lambda,\mu\right)=\hat{\psi}_{i+\frac{1}{2}+N}^{k}\left(\lambda,\mu\right) \tag{3.89}$$

where N denotes the number of cells after which the geometry is repeated. This condition does not require the solution for a specific frequency λ to be periodic within N cells. The S_N angular discretization gives for the scalar flux Eq. (3.86)

$$\hat{\phi}^k_{i+\frac{1}{2}} = \sum_{m=1}^{M} \omega_m \hat{\psi}^k_{i+\frac{1}{2},m} \tag{3.90}$$

and written in vector form

$$\vec{\hat{\phi}}^k = \mathbf{W_0} \vec{\hat{\psi}}^k \tag{3.91}$$

where $\mathbf{W_0}$ is the zeroth moment angular quadrature matrix. Accordingly the neutron current Eq. (3.87) is

$$\vec{\hat{J}}^k = \mathbf{W_1} \vec{\hat{\psi}}^k \tag{3.92}$$

and the second moment Eq. (3.88) is

$$\vec{\hat{\xi}}^k = \mathbf{W_2} \vec{\hat{\psi}}^k \tag{3.93}$$

with $\mathbf{W_1}$ and $\mathbf{W_2}$ the first respectively the second moment angular quadrature matrices. Using these definitions, Eq. (3.84) can be written as matrix equation

$$\mathbf{A} \vec{\hat{\psi}}^{k+\frac{1}{2}} = \mathbf{B} \vec{\hat{\phi}}^k \tag{3.94}$$

where $\mathbf{A}$ is the streaming and collision matrix with the entries for $i = 1 \dots N, m = 1 \dots M$ (index $s_i = m \cdot N + (i \mod N)$)

$$a_{s_i s_{i-1}} = w_i \left(-\frac{\mu_m^2}{h_i} + \frac{\sigma_{\mathrm{t},i}^2 h_i}{6} \right) \mathrm{e}^{-\hat{\imath}\lambda h_i} \tag{3.95a}$$

$$a_{s_i s_i} = w_i \left(\frac{\mu_m^2}{h_i} + \sigma_{\mathrm{t},i}\mu_m + \frac{\sigma_{\mathrm{t},i}^2 h_i}{3} \right) + w_{i+1} \left(\frac{\mu_m^2}{h_{i+1}} - \mu_m \sigma_{\mathrm{t},i+1} + \frac{\sigma_{\mathrm{t},i+1}^2 h_{i+1}}{3} \right) \tag{3.95b}$$

$$a_{s_i s_{i+1}} = w_{i+1} \left(-\frac{\mu_m^2}{h_{i+1}} + \frac{\sigma_{\mathrm{t},i+1}^2 h_{i+1}}{6} \right) \mathrm{e}^{\hat{\imath}\lambda h_{i+1}} \tag{3.95c}$$

and $\mathbf{B}$ the scattering matrix for $i = 1 \dots N, m = 1 \dots M$ (with the indices $s_i = m \cdot I + i$ and $t_i = (i \mod N)$)

$$b_{s_i t_{i-1}} = w_i \left(\mu_m \frac{c_i \sigma_{\mathrm{t},i}}{4} + \frac{c_i \sigma_{\mathrm{t},i}^2 h_i}{12} \right) \mathrm{e}^{-\hat{\imath}\lambda h_i} \tag{3.96a}$$

$$b_{s_i t_i} = w_i c_i \sigma_{\mathrm{t},i} \left(\frac{\mu_m}{4} + \frac{\sigma_{\mathrm{t},i} h_i}{6} \right) + w_{i+1} c_{i+1} \sigma_{\mathrm{t},i+1} \left(-\frac{\mu_m}{4} + \frac{\sigma_{\mathrm{t},i+1} h_{i+1}}{6} \right) \tag{3.96b}$$

$$b_{s_i t_{i+1}} = w_{i+1} \left(-\mu_m \frac{c_{i+1} \sigma_{\mathrm{t},i+1}}{4} + \frac{c_{i+1} \sigma_{\mathrm{t},i+1}^2 h_{i+1}}{12} \right) \mathrm{e}^{\hat{\imath}\lambda h_{i+1}} \tag{3.96c}$$

Solving Eq. (3.94) gives

$$\vec{\hat{\psi}}^{k+\frac{1}{2}} = \mathbf{A}^{-1} \mathbf{B} \vec{\hat{\phi}}^{k} \tag{3.97}$$

and from that follows with Eq. (3.91)

$$\vec{\hat{\phi}}^{k+\frac{1}{2}} = \mathbf{W_0} \mathbf{A}^{-1} \mathbf{B} \vec{\hat{\phi}}^{k} \tag{3.98}$$

The spectral radius for source iterations with WLS transport is the absolute value of the eigenvalue with the largest magnitude of the systems matrix in Eq. (3.91) with $\phi^{k+1} = \phi^{k+\frac{1}{2}}$. It can be easily found using numerical libraries such as SciPy [26].

Table 3.1 Input cases 1 for the periodic two region Fourier analysis with different total cross section, each region has 2 cells.

#		Region 1		Region 2	
1	a	$\sigma_{t,1} = 1.0 \frac{1}{cm}$	$c_1 = 1.0$	$\sigma_{t,2} = 1.0 \frac{1}{cm}$	$c_2 = 1.0$
	b	$\sigma_{t,1} = 1.0 \frac{1}{cm}$	$c_1 = 1.0$	$\sigma_{t,2} = 2.0 \frac{1}{cm}$	$c_2 = 1.0$
	c	$\sigma_{t,1} = 1.0 \frac{1}{cm}$	$c_1 = 1.0$	$\sigma_{t,2} = 5.0 \frac{1}{cm}$	$c_2 = 1.0$
	d	$\sigma_{t,1} = 1.0 \frac{1}{cm}$	$c_1 = 1.0$	$\sigma_{t,2} = 10.0 \frac{1}{cm}$	$c_2 = 1.0$

3.4.2 Analysis of heterogeneous test problems for WLS transport

First we study the effect of the weight function on the convergence rate of the linearized acceleration scheme. As discussed in Section 3.2.1 the weight function can be neglected for homogeneous media. However for heterogeneous media it can affect the spectral radius. To study the effects of heterogeneous media several test cases were considered as shown in Tables 3.1 to 3.4. Cases 1 (Table 3.1) used different cross sections, but the same scattering ration. Cases 2 (Table 3.2) and 3 (Table 3.3) used materials with different cross sections and scattering ratios. Cases 4 (Table 3.4) were test problems containing a void and varying scattering ratio. For all test cases, the cell size h was varied in a range from 10^{-3} cm to 10^3 cm. All test cases used periodic boundary conditions. Note that the spectral radius is a function of the mean free path $\sigma_t h$. In our test cases we used h to influence the optical thickness of the problem while σ_t defines the ratio in the optical thickness between the two regions. All results for the selected test cases can be reproduced by other choices of h and σ_t given the same optical thickness.

The results for test cases 1 show that the spectral radius was not influenced by materials with different optical thickness as long as the scattering ratio is the same

Table 3.2 Input cases 2 for the periodic two region Fourier analysis with different scattering ratios, each region has 2 cells.

#		Region 1		Region 2	
2	a	$\sigma_{t,1} = 1.0\,\frac{1}{\text{cm}}$	$c_1 = 1.0$	$\sigma_{t,2} = 1.0\,\frac{1}{\text{cm}}$	$c_2 = 0.5$
	b	$\sigma_{t,1} = 1.0\,\frac{1}{\text{cm}}$	$c_1 = 1.0$	$\sigma_{t,2} = 2.0\,\frac{1}{\text{cm}}$	$c_2 = 0.5$
	c	$\sigma_{t,1} = 1.0\,\frac{1}{\text{cm}}$	$c_1 = 1.0$	$\sigma_{t,2} = 5.0\,\frac{1}{\text{cm}}$	$c_2 = 0.5$
	d	$\sigma_{t,1} = 1.0\,\frac{1}{\text{cm}}$	$c_1 = 1.0$	$\sigma_{t,2} = 10.0\,\frac{1}{\text{cm}}$	$c_2 = 0.5$

Table 3.3 Input cases 3 with different scattering rations and the higher c in the thick material for the periodic two region Fourier analysis, each region has 2 cells.

#		Region 1		Region 2	
3	a	$\sigma_{t,1} = 1.0\,\frac{1}{\text{cm}}$	$c_1 = 1.0$	$\sigma_{t,2} = 1.0\,\frac{1}{\text{cm}}$	$c_2 = 0.5$
	b	$\sigma_{t,1} = 2.0\,\frac{1}{\text{cm}}$	$c_1 = 1.0$	$\sigma_{t,2} = 1.0\,\frac{1}{\text{cm}}$	$c_2 = 0.5$
	c	$\sigma_{t,1} = 5.0\,\frac{1}{\text{cm}}$	$c_1 = 1.0$	$\sigma_{t,2} = 1.0\,\frac{1}{\text{cm}}$	$c_2 = 0.5$
	d	$\sigma_{t,1} = 10.0\,\frac{1}{\text{cm}}$	$c_1 = 1.0$	$\sigma_{t,2} = 1.0\,\frac{1}{\text{cm}}$	$c_2 = 0.5$

Table 3.4 Void test cases (Cases 4) for the periodic two region Fourier analysis, each region uses 2 cells.

#		Region 1		Region 2	
4	a	$\sigma_{t,1} = 1.0\,\frac{1}{\text{cm}}$	$c_1 = 1.0$	$\sigma_{t,2} = 0.0\,\frac{1}{\text{cm}}$	$c_2 = 0.0$
	b	$\sigma_{t,1} = 1.0\,\frac{1}{\text{cm}}$	$c_1 = 0.9999$	$\sigma_{t,2} = 0.0\,\frac{1}{\text{cm}}$	$c_2 = 0.0$
	c	$\sigma_{t,1} = 1.0\,\frac{1}{\text{cm}}$	$c_1 = 0.99$	$\sigma_{t,2} = 0.0\,\frac{1}{\text{cm}}$	$c_2 = 0.0$
	d	$\sigma_{t,1} = 1.0\,\frac{1}{\text{cm}}$	$c_1 = 0.9$	$\sigma_{t,2} = 0.0\,\frac{1}{\text{cm}}$	$c_2 = 0.0$

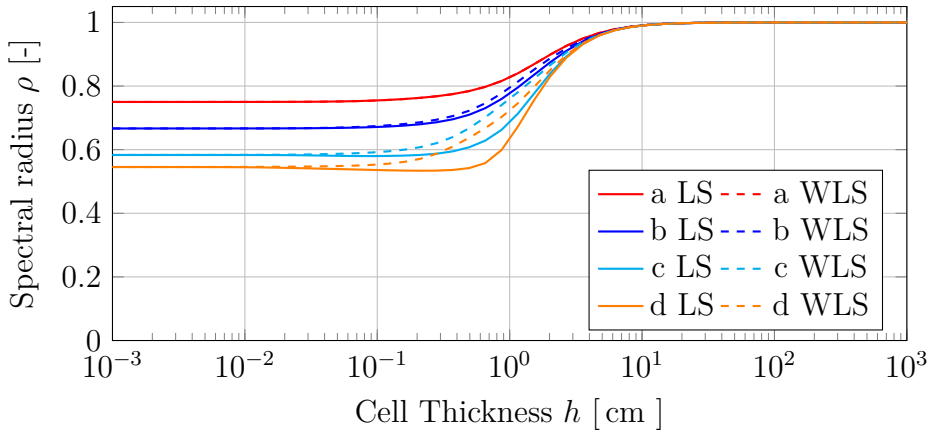

Figure 3.10 Comparison of the spectral radii for source iterations for the test cases 2 (Table 3.2) using the LS and WLS equations.

between both materials. For problems with different scattering ratios, the spectral radius for thin cells was a cross section weighted average between both scattering ratios as shown in Fig. 3.10. For thick cells the higher scattering ratio dominated the spectral radius, since the cell was too thick for neutrons to leak into the other region. Additionally, the LS and WLS scheme (weight function Eq. (2.34)) showed a different spectral radius in the transition zone between these two limits. In these cases the WLS showed a larger spectral radius than the LS scheme, and the difference was larger for larger cross sections in the second region. For cases 3 the WLS scheme showed a smaller spectral radius in the transition zone as can be seen in Fig. 3.11. The same behavior as discussed for cases 2 applied to the cases 3, for thin cells the spectral radius was a cross section weighted average of the materials' c and for thick cells the maximum c. For the void cases the spectral radius was the scattering ratio of the material region.

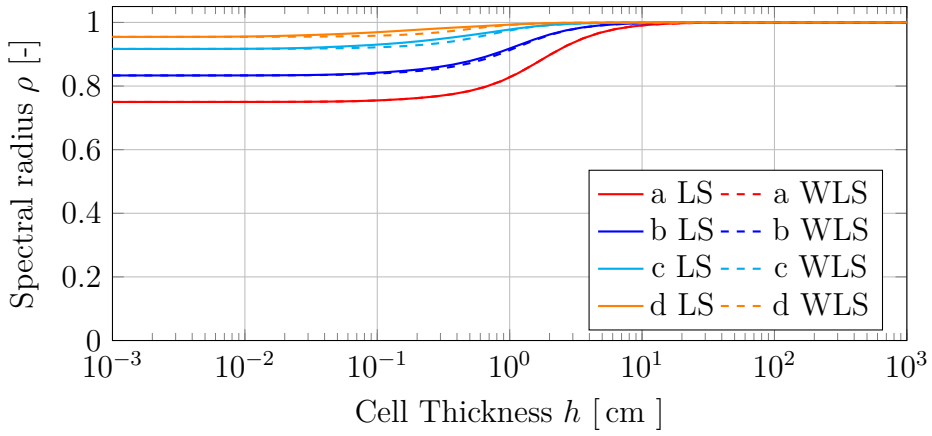

Figure 3.11 Comparison of the spectral radii for source iterations for the test cases 3 (Table 3.3) for using LS and WLS equations.

3.4.3 Low order equation

All the different formulation that were considered can be expressed by a general linearized drift vector

$$\hat{\alpha}^{k+\frac{1}{2}}\phi^{k+1} = \frac{p}{\sigma_{\mathrm{t}}}\xi^{k+\frac{1}{2}} - \tilde{p}J^{k+\frac{1}{2}} - \mathrm{D}\frac{\partial}{\partial x}\phi^{k+\frac{1}{2}} \tag{3.99}$$

where p and $\tilde{p}$ are weights depending on the formulation as shown in Table 3.5 with

$$\hat{\tau} \equiv \begin{cases} 1, & \sigma_{\mathrm{t}}h \geq \hat{\zeta} \\ 0, & \sigma_{\mathrm{t}}h < \hat{\zeta} \end{cases} \tag{3.100}$$

Table 3.5 Weight factors for the different current formulations for the general drift vector.

Formulation	p	$\tilde{p}$
Eddington	1	0
Current	0	1
Combined	$\hat{\tau}$	$1-\hat{\tau}$
τ	$\sigma_{\mathrm{t}}\tau$	$1-\sigma_{\mathrm{t}}\tau$

based on Eq. (3.80) and τ defined in Eq. (2.10). Based on Eqs. (3.47) and (3.53) the general low-order error equation becomes

$$\begin{aligned}
&\left(\mathrm{D}\frac{\partial}{\partial x}\delta\phi^{k+1},\frac{\partial}{\partial x}\phi^{*}\right)_{\mathcal{D}}+\left((1-c)\,\sigma_{\mathrm{t}}\delta\phi^{k+1},\phi^{*}\right)_{\mathcal{D}}\\
&=-\left(\frac{p}{\sigma_{\mathrm{t}}}\frac{\partial}{\partial x}\delta\xi^{k+\frac{1}{2}},\frac{\partial}{\partial x}\phi^{*}\right)_{\mathcal{D}}+\left(\tilde{p}\delta J^{k+\frac{1}{2}},\frac{\partial}{\partial x}\phi^{*}\right)_{\mathcal{D}}+\left(\mathrm{D}\frac{\partial}{\partial x}\delta\phi^{k+\frac{1}{2}},\frac{\partial}{\partial x}\phi^{*}\right)_{\mathcal{D}}
\end{aligned}\tag{3.101}$$

with the discretization

$$\begin{aligned}
&\left(\frac{\mathrm{D}_i}{h_i}+\frac{\mathrm{D}_{i+1}}{h_{i+1}}+\frac{(1-c_i)\,\sigma_{\mathrm{t},i}h_i}{3}+\frac{(1-c_{i+1})\,\sigma_{\mathrm{t},i+1}h_{i+1}}{3}\right)\phi_{i+\frac{1}{2}}^{k+1}\\
&\quad+\left(-\frac{D_i}{h_i}+\frac{(1-c_i)\,\sigma_{\mathrm{t},i}h_i}{6}\right)\phi_{i-\frac{1}{2}}^{k+1}+\left(-\frac{D_{i+1}}{h_{i+1}}+\frac{(1-c_{i+1})\,\sigma_{\mathrm{t},i+1}h_{i+1}}{6}\right)\phi_{i+\frac{3}{2}}^{k+1}\\
&=-\left(\left(\frac{p_i}{\sigma_{\mathrm{t},i}h_i}+\frac{p_{i+1}}{\sigma_{\mathrm{t},i+1}h_i}\right)\xi_{i+\frac{1}{2}}^{k+\frac{1}{2}}-\frac{p_i}{\sigma_{\mathrm{t},i}h_i}\xi_{i-\frac{1}{2}}^{k+\frac{1}{2}}-\frac{p_{i+1}}{\sigma_{\mathrm{t},i+1}h_{i+1}}\xi_{i+\frac{3}{2}}^{k+\frac{1}{2}}\right)+\frac{\tilde{p}_i}{2}\left(\delta J_{i-\frac{1}{2}}^{k+\frac{1}{2}}+\delta J_{i+\frac{1}{2}}^{k+\frac{1}{2}}\right)\\
&-\frac{\tilde{p}_{i+1}}{2}\left(\delta J_{i+\frac{1}{2}}^{k+\frac{1}{2}}+\delta J_{i+\frac{3}{2}}^{k+\frac{1}{2}}\right)+\left(\left(\frac{\mathrm{D}_i}{h_i}+\frac{\mathrm{D}_{i+1}}{h_{i+1}}\right)\phi_{i+\frac{1}{2}}^{k+\frac{1}{2}}-\frac{\mathrm{D}_i}{h_i}\phi_{i-\frac{1}{2}}^{k+\frac{1}{2}}-\frac{\mathrm{D}_{i+1}}{h_{i+1}}\phi_{i+\frac{3}{2}}^{k+\frac{1}{2}}\right).
\end{aligned}\tag{3.102}$$

With the Fourier Ansatz Eqs. (3.39), (3.86) and (3.87) we can write this as vector equation

$$\mathbf{C}\vec{\hat{\phi}}^{k+1}=\mathbf{E}\,(p)\,\vec{\hat{\xi}}^{k+\frac{1}{2}}+\mathbf{F}\,(\tilde{p})\,\vec{\hat{J}}^{k+\frac{1}{2}}+\mathbf{G}\vec{\hat{\phi}}^{k+\frac{1}{2}}\tag{3.103}$$

with the entries of the diffusion matrix $\mathbf{C}$ for $i = 1 \ldots N$

$$c_{ii-1} = \left(-\frac{D_i}{h_i} + \frac{(1 - c_i)\,\sigma_{\mathrm{t},i} h_i}{6} \right) \mathrm{e}^{-\hat{\imath}\lambda h_i} \tag{3.104a}$$

$$c_{ii} = \frac{\mathrm{D}_i}{h_i} + \frac{\mathrm{D}_{i+1}}{h_{i+1}} + \frac{(1 - c_i)\,\sigma_{\mathrm{t},i} h_i}{3} + \frac{(1 - c_{i+1})\,\sigma_{\mathrm{t},i+1} h_{i+1}}{3} \tag{3.104b}$$

$$c_{ii+1} = \left(-\frac{D_{i+1}}{h_{i+1}} + \frac{(1 - c_{i+1})\,\sigma_{\mathrm{t},i+1} h_{i+1}}{6} \right) \mathrm{e}^{\hat{\imath}\lambda h_{i+1}}, \tag{3.104c}$$

for the zeroth moment drift matrix $\mathbf{E}$

$$e_{ii-1} = \frac{p_i}{\sigma_{\mathrm{t},i} h_i} \mathrm{e}^{-\hat{\imath}\lambda h_i} \tag{3.105a}$$

$$e_{ii} = -\frac{p_i}{\sigma_{\mathrm{t},i} h_i} - \frac{p_{i+1}}{\sigma_{\mathrm{t},i+1} h_{i+1}} \tag{3.105b}$$

$$e_{ii+1} = \frac{p_{i+1}}{\sigma_{\mathrm{t},i+1} h_{i+1}} \mathrm{e}^{\hat{\imath}\lambda h_{i+1}} \tag{3.105c}$$

and for the first moment drift matrix $\mathbf{F}$

$$f_{ii-1} = \frac{\tilde{p}_i}{2} \mathrm{e}^{-\hat{\imath}\lambda h_i} \tag{3.106a}$$

$$f_{ii} = \frac{\tilde{p}_i}{2} - \frac{\tilde{p}_{i+1}}{2} \tag{3.106b}$$

$$f_{ii+1} = -\frac{\tilde{p}_{i+1}}{2} \mathrm{e}^{\hat{\imath}\lambda h_{i+1}}. \tag{3.106c}$$

Finally we get for the second moment drift matrix $\mathbf{G}$

$$g_{ii-1} = -\frac{\mathrm{D}_i}{h_i} \mathrm{e}^{-\hat{\imath}\lambda h_i} \tag{3.107a}$$

$$g_{ii} = \frac{\mathrm{D}_i}{h_i} + \frac{\mathrm{D}_{i+1}}{h_{i+1}} \tag{3.107b}$$

$$g_{ii+1} = -\frac{\mathrm{D}_{i+1}}{h_{i+1}} \mathrm{e}^{\hat{\imath}\lambda h_{i+1}} \tag{3.107c}$$

Substituting Eqs. (3.91) to (3.93) into Eq. (3.103) gives with the high order solution

for the angular flux Eq. (3.97)

$$\vec{\hat{\phi}}^{k+1} = \mathbf{C}^{-1}\Big(\mathbf{E}\mathbf{W_0} + \mathbf{F}\left(\tilde{p}\right)\mathbf{W_1} + \mathbf{G}\left(p\right)\mathbf{W_2}\Big)\mathbf{A}^{-1}\mathbf{B}\vec{\hat{\phi}}^{k} \tag{3.108}$$

The spectral radius of the acceleration scheme can be found as the eigenvalue with the largest magnitude of the system matrix in Eq. (3.108).

3.4.4 Analysis of heterogeneous test problems for NDA schemes

We used the same method as described in Section 3.4.2 to obtain the spectral radii for the test cases in Tables 3.1 to 3.4.

First we studied the effect of the weight function Eq. (2.34) on the spectral radius of the different NDA schemes. Figure A.1 shows the effect of WLS on the spectral radius for the test cases with different material but the same scattering ratio (Table 3.1). It can be seen that the use of a weight function in the transport solver in cases with different materials (b-d) decreased the maximal spectral radius for all schemes but the current scheme as shown in Table 3.6. While for thin and thick cells the results were the same as for the infinite study, in the intermediate range the NDA using unweighted LS showed increased spectral radii. The NDA using WLS showed an increase for the spectral radius at least a magnitude smaller. The maximal spectral radius for the current formulation remained 1, but for cases 1c and 1d the spectral radius in the intermediate range was larger for the LS case as shown in Fig. A.1b.

For test cases 2 (Table 3.2) Fig. A.2 shows small differences for the Eddington formulation, the combined formulation and the τ formulation. In this case, the NDA using WLS had a slightly higher spectral radius locally in the intermediate h range, but the maximal spectral radius for the WLS scheme was slightly smaller than for the LS scheme as shown in Table 3.6. For the current formulation the impact of the weight function was much larger. The maximal spectral radius for thick cells was

Table 3.6 Eigenvalues with the largest magnitude for the different NDA formulations using LS and WLS high order solvers.

#		Eddington		Current		Combined		τ	
		LS	WLS	LS	WLS	LS	WLS	LS	WLS
1	a	0.2247	0.2247	1.0000	1.0000	0.2257	0.2257	0.2248	0.2248
	b	0.2291	0.2247	1.0000	1.0000	0.2291	0.2256	0.2291	0.2248
	c	0.2399	0.2247	1.0000	1.0000	0.2399	0.2256	0.2399	0.2248
	d	0.2489	0.2247	1.0000	1.0000	0.3774	0.2262	0.2583	0.2249
2	a	0.2174	0.2174	0.6250	0.6250	0.2174	0.2174	0.2174	0.2174
	b	0.2112	0.2085	0.8500	0.7500	0.2112	0.2085	0.2112	0.2085
	c	0.2244	0.2207	0.9712	0.8750	0.2244	0.2207	0.2244	0.2207
	d	0.2250	0.2233	0.9926	0.9318	0.2250	0.2233	0.2250	0.2233
3	a	0.2174	0.2174	0.6250	0.6250	0.2174	0.2174	0.2174	0.2174
	b	0.2247	0.2230	0.5171	0.5498	0.2247	0.2230	0.2247	0.2230
	c	0.2370	0.2244	0.6161	0.5488	0.2370	0.2244	0.2370	0.2244
	d	0.2460	0.2244	0.7815	0.6000	0.3718	0.2248	0.2557	0.2244

decreased significantly for the scheme using WLS and with different cross sections (cases b-d).

For cases 3 the results were similar for the Eddington, combined and τ formulations as shown in Fig. A.3. The unweighted LS scheme gave spectral radii higher in the intermediate h range for all formulations. But for the current formulation the NDA WLS scheme gave significant higher results in the thick cell range, nevertheless only for case b the maximal spectral radius was larger for the WLS case as shown in Table 3.6.

These results showed that the use of WLS gives in most cases better convergence for the linearized analysis. Especially for the current formulation, the improvement of the convergence is significant. The reason for this is probably that the WLS transport scheme is consistent with the NDA formulation in non-voids.

Table 3.7 Eigenvalues with the largest magnitude for the different NDA formulations using local and non-local (nlc) diffusion coefficients with the WLS high-order solve.

#		Eddington		Current		Combined		τ	
		local	nlc	local	nlc	local	nlc	local	nlc
1	a	0.2247	0.2247	1.0000	1.0000	0.2257	0.2257	0.2248	0.2248
	b	0.2247	0.2904	1.0000	1.0000	0.2256	0.2904	0.2248	0.2904
	c	0.2247	-0.4040	1.0000	1.0000	0.2256	-0.4040	0.2248	-0.4040
	d	0.2247	-0.8932	1.0000	1.0000	0.2262	-0.8932	0.2249	-0.8932
2	a	0.2174	0.2174	0.6250	0.6250	0.2174	0.2174	0.2174	0.2174
	b	0.2085	0.2153	0.7500	0.7273	0.2085	0.2153	0.2085	0.2153
	c	0.2207	0.2074	0.8750	0.8500	0.2207	0.2074	0.2207	0.2074
	d	0.2233	-0.2579	0.9318	0.9143	0.2233	-0.2579	0.2233	-0.2579
3	a	0.2174	0.2174	0.6250	0.6250	0.2174	0.2174	0.2174	0.2174
	b	0.2230	0.2706	0.5498	0.5799	0.2230	0.2706	0.2230	0.2706
	c	0.2244	0.3467	0.5488	0.6187	0.2244	0.3467	0.2244	0.3467
	d	0.2244	-0.5907	0.6000	0.6613	0.2248	-0.5907	0.2244	-0.5907

The second parameter to consider is the non-local diffusion coefficient and its effect on the convergence rate. Figures A.4 to A.6 show the results for cases 1 to 3. In the plots a dotted line indicates the absolute value of a negative eigenvalue is the spectral radius. Eddington, combined and τ scheme showed very similar behavior hence only the Eddington formulation is shown. These schemes became oscillatory for test cases 1 and 3c and 3d. The LS formulation was unstable for test case 1d and 3d. No WLS test cases showed a spectral radius larger than one. Additionally the spectral radius does not go towards zero for large h as for the local diffusion coefficient.

These results clearly indicated the large impact of the diffusion coefficient on the spectral radius. Table 3.7 shows the comparison of local and non-local diffusion coefficient for the NDA WLS. In most cases the non-local diffusion coefficient results in

Table 3.8 Eigenvalues with the largest magnitude for the void test cases for the NDA formulations (Table 3.4) using the non-local diffusion coefficient and LS and WLS transport solvers.

#		c	Current		Combined		τ	
			LS	WLS	LS	WLS	LS	WLS
4	a	1.0000	1.0000	0.9947	1.0000	0.9939	-9999.0000	-9910.0000
	b	0.9999	0.9900	0.9357	0.9734	0.6468	-352.9000	-313.1000
	c	0.99	0.8793	0.8540	0.7863	0.4625	-33.8700	-11.3900
	d	0.9	0.6463	0.6159	0.5589	0.3658	-8.4860	-1.2360

a spectral radius with a larger magnitude than the local diffusion coefficient. However, the non-local diffusion coefficient is limited in optical thin and void cells, whereas the local diffusion coefficient goes to infinity in these cases. Nevertheless for thick cell the local diffusion coefficient is well defined and the results indicate it gives a better convergence than the non-local counter part. The definition of the joined diffusion coefficient

$$\mathrm{D} \equiv \begin{cases} \mathrm{D}_{\mathrm{local}} & \sigma_{\mathrm{t}} h \geq \zeta_{\mathrm{D}} \\ \mathrm{D}_{\mathrm{nonlocal}} & \sigma_{\mathrm{t}} h < \zeta_{\mathrm{D}} \end{cases} \tag{3.109}$$

tries to combine both advantages. The results for some test cases using the combined scheme are shown in Fig. A.7. It shows that the switch introduced an intermediate region where the spectral radius differed from both, local and non-local diffusion coefficient. This region might show a larger spectral radius than the two other formulations and also can introduce oscillations. The behavior of this intermediate region strongly depended on the problem and the choice of ζ_{D}.

The results so far gave a better understanding on the influence of parameters on the

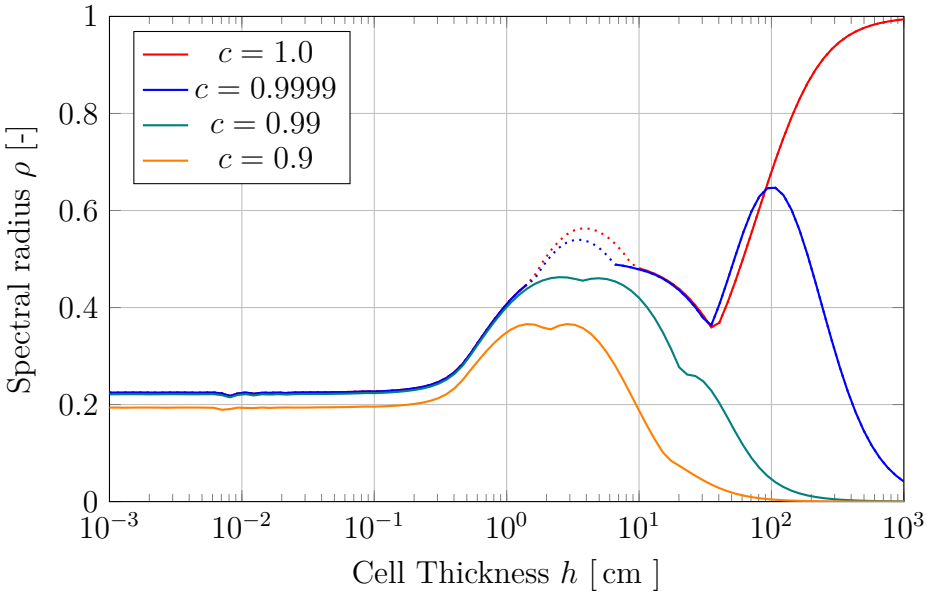

Figure 3.12 Spectral radius for the void test cases (Table 3.4) for the combined NDA scheme using WLS (dotted for negative eigenvalues).

spectral radius. This is now used to study the effects of void regions on the convergence and stability of the NDA algorithm. Only the current, combined and τ schemes hold in voids. The results for all void cases (Table 3.4) using the combined scheme are shown in Fig. 3.12. The other schemes are shown in Fig. A.8. The dotted part of the plot indicate negative eigenvalues. Even though the combined scheme showed for all non-void cases a spectral radius $\rho < 1$, it goes to one for large h and $c = 1$. However, reducing the scattering ratio only to $c = 0.9999$ reduced the maximum spectral radius significantly as shown in Table 3.8. For all $c < 1$ the combined formulation gave better acceleration than the current formulation (Fig. A.8a). Figure A.8b shows that the use of WLS instead of LS improved the convergence significantly. The τ scheme using a LS or WLS transport solution was not unconditionally stable as shown in Fig. A.8c. Based on these results, the combined current formulation is the best choice for the

Table 3.9 Comparison of the eigenvalues with the largest magnitude for the void test cases with the combined NDA WLS formulation (Table 3.4) using the non-local, joined and limited diffusion coefficients with different parameters.

#	c	Non-Local		Limited local			
		$\zeta_D = \infty$	10^{-3}	$D_{max} = 1\,cm$	$10\,cm$	$100\,cm$	$1000\,cm$
a	1.0000	0.9939	0.9939	-1.0270	0.9988	0.9990	0.9990
b	0.9999	0.6468	-0.6660	-0.9521	0.8947	0.9644	0.9885
c	0.99	0.4625	-0.5354	-0.6572	0.4491	0.7223	0.8870
d	0.9	0.3658	-0.3267	-0.3301	0.1944	0.4092	0.6564

NDA WLS in voids. It provides unconditionally stable and efficient acceleration for all physical relevant problems.

The non-local diffusion coefficient gave mixed results for test cases 1 to 3. Hence it is of interest how it compares in voids. The alternative is the joined coefficient Eq. (3.109). We chose $\zeta_D < 10^{-3}$ so this case is the limit since the void always uses the non-local and the material region always uses the local diffusion coefficient. All larger ζ_D would give a combination of the this case and the pure non-local case ($\zeta_D = \infty$). The third option is to limit the local diffusion coefficient Eq. (3.9) by

$$D = \min\left(\frac{1}{3\sigma_t}, D_{max}\right) \tag{3.110}$$

where D_{max} is a constant. The effects of the magnitude of D_{max} up to 1000 were also studied.

Figure A.9 shows the spectral radii for the different diffusion coefficients in the void test cases (Table 3.4). For pure scatterers, the purely non-local diffusion coefficient did better than the combined and the limited with $D_{max} = 1$. The higher limited coefficients had a lower spectral radius in the intermediate h range, but increased

toward one earlier than the non-local coefficient. For $c = 0.9999$ the non-local coefficient was better than all other schemes, and especially better than the two schemes ($D_{max} \geq 10$) that were comparable for $c = 1$. However for $c \leq 0.9$ the other schemes started to perform better or equal than the pure non-local coefficient as can be seen in Table 3.9.

For optical thick cells and pure scatterers the modified NDA scheme looses effectiveness. This is caused by an interface between an optically very thick cell and a very thin cell. To improve convergence we studied the effect of introducing cells of intermediate optical thickness. The last interface cells in the material are increasingly refined towards the void, creating a series of cells with decreasing optical thickness towards the void region. Every level of feathering means that the cells next to the void is divided by two, hence a level three feathering produces an interface with cells of $\frac{\sigma_t h}{2}$, $\frac{\sigma_t h}{4}$ and two with $\frac{\sigma_t h}{8}$ thickness. In this study we modified the cross section to maintain a regular mesh. Figure 3.13 shows that this procedure moved the practical optical thickness, for which the scheme lost effectiveness to optically thicker cells. This, however, came with the price of having more spatial cells in the problem. The implemented feathering scheme was only intended for a test and is by no means optimal.

Nevertheless, the test showed that the use of the non-local diffusion coefficient can lead to unstable systems (Fig. 3.13a) if it was calculated with a mesh that is not fine enough. This happens if the cell thickness becomes to large. Using the WLS transport equation resulted in oscillations at the void-material interface in the diffusion coefficient for unresolved thick cells, which became negative for thicknesses between 10 and 100, degrading the convergence rate. Using the joined diffusion coefficient (Eq. (3.109)), these oscillations can be eliminated and the scheme converges again as can be seen in Fig. 3.13b. This shows the importance to obtain a good approximation

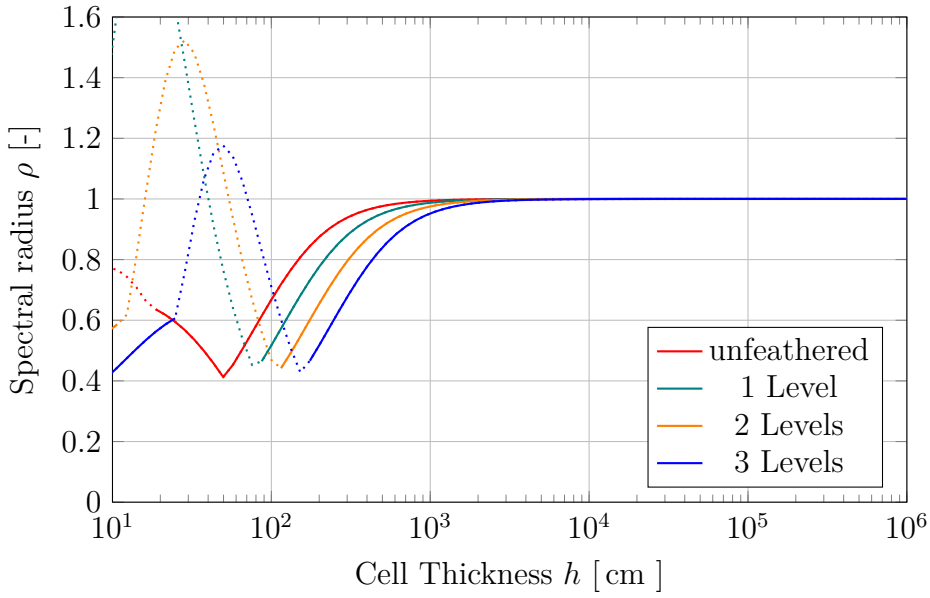

(a) Non-local diffusion coefficient

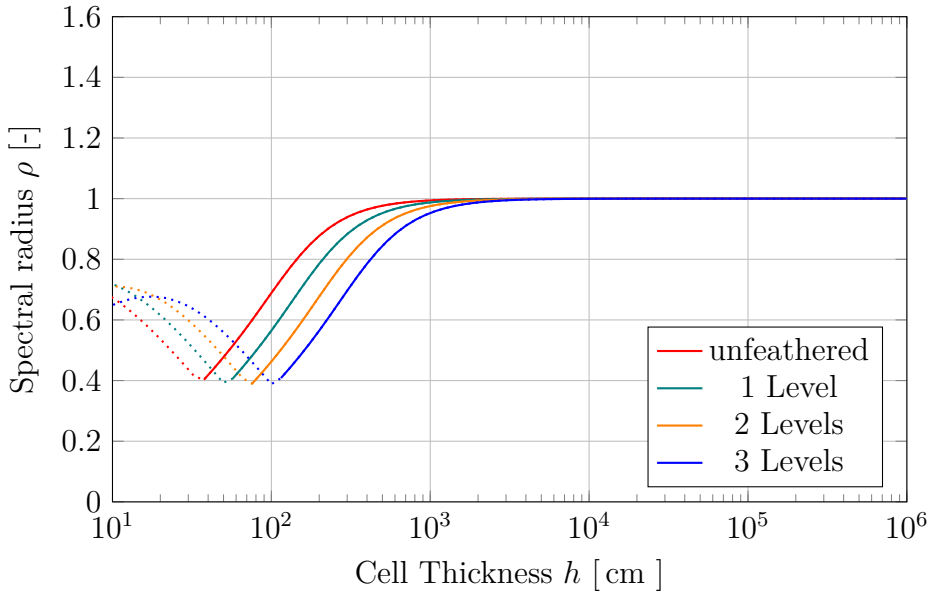

(b) Joined diffusion coefficient

Figure 3.13 Spectral radius for $c = 1$ as function of the cell thickness for different levels of feathering using the nonlocal and the joined diffusion coefficient (dotted line indicates negative eigenvalues).

of the non-local diffusion coefficient.

The better performance of the non-local diffusion coefficient in cases with high scattering ratios and the difficulties to define a problem dependent D_{max} convinced us to continue to use the non-local diffusion coefficient. It offers a method to limit the diffusion coefficient in voids automatically problem dependent. A wrong guess for D_{max} can strongly influence the convergence or make the problem even unstable. The use of the non-local diffusion coefficient in non-voids can however lead to an unstable convergence, if the mesh of the non-local diffusion coefficient calculation is unresolved, which can be avoided with the joined diffusion coefficient.

3.5 Numerical Fourier Analysis

To verify our finding we use a numerical code to obtain the spectral radii and compare it to the values obtained from the Fourier analysis. Since the NDA method is a non-linear method, it is not possible to use the traditional method to converge against a zero solution. Hence we introduce a source $q = \sigma_a$ to obtain a constant solution $\phi = 1$ everywhere in the problem. This limits the number of iterations we can perform before having problems with machine accuracy. especially for small spectral radii. The calculations were randomly initialized with values uniformly distributed between 0 and 10 to cover all frequencies. Of interest were the number of iterations after which the error was reduced by a factor of 10^{-6} to the initial random guess and the spectral radius, which was obtained as the ratio of the errors of the last iteration to the previous iteration. We ran 10 samples and took the average over these for the spectral radii and the number of iterations to limit the influence of a specific initial guess.

The periodic boundary condition requires that on a mesh with N cells the scalar

flux satisfies the condition

$$\phi_0 = \phi_{N+1}. \tag{3.111}$$

This limits the frequencies a mesh with the regular size h can support, since for all frequencies λ must then hold

$$\begin{aligned} \phi_0 &= \phi_{N+1} \mathrm{e}^{\hat{\imath}\lambda N h} \\ &= \phi_0 \mathrm{e}^{\hat{\imath}\lambda N h} \end{aligned} \tag{3.112}$$

which is only true if

$$\lambda = \frac{k\pi}{Nh} \qquad k \in \mathbb{N}_0. \tag{3.113}$$

Therefore a mesh with N cells has only discrete frequencies, but the analytic Fourier analysis gives the spectral radius over all frequencies. To obtain a better comparison between the analytic and the numerical Fourier analysis, we restricted the frequencies in the analytic Fourier analysis to the frequencies supported by the selected mesh. Table 3.10 shows the comparison of the spectral radii from the analytic Fourier analysis with all frequencies (Analytic) to the restricted analytic and the average computational spectral radii for several mean free path on two different meshes. The results show a good agreement between the restricted spectral radii and the observed ones for both meshes. Furthermore the fine mesh with 1000 cells agrees well with the analytic Fourier Analysis except for the smallest h. The coarser mesh has larger differences for small cell thicknesses $h \leq 0.01$. The reason that the restricted and numerical spectral radii for small h is smaller than the predicted is that the eigenvalue peak for these cases is limited to a small range of frequencies as shown in Section 3.5. The discrete frequencies cannot resolve these small peaks.

Table 3.10 Average computational spectral radii using the Eddington formulation for the infinite Fourier Analysis with $c = 0.9999$ compared to the analytical Fourier Analysis with all frequencies (Analytic) and with frequencies restricted to the supported ones on the corresponding mesh (Restricted).

Cell Thickness	Analytic	100 Mesh Cells		1000 Mesh Cells	
		Restricted	Numerical	Restricted	Numerical
0.001	0.2236	0.0066	0.0063	0.1649	0.1634
0.01	0.2246	0.1631	0.1566	0.2246	0.2144
0.1	0.2246	0.2246	0.2124	0.2246	0.2135
1	0.2246	0.2246	0.2189	0.2246	0.2193
10	0.0289	0.0289	0.0255	0.0289	0.0260
100	0.0003	0.0003	0.0002	0.0003	0.0002
1000	< 0.0001	< 0.0001	< 0.0001	< 0.0001	< 0.0001

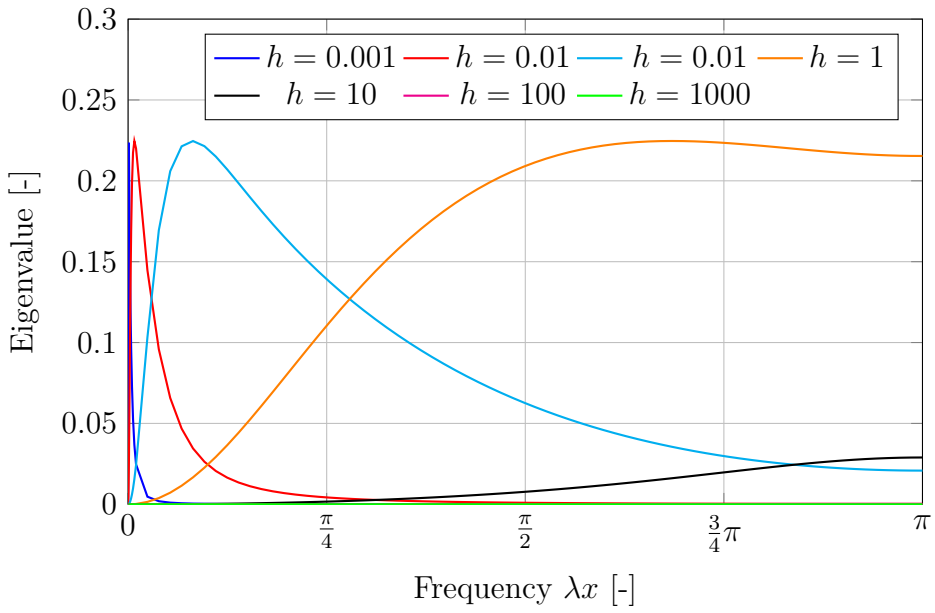

Figure 3.14 Distribution of the eigenvalues as a function of the frequency for all cell thicknesses.

Table 3.11 Average computational spectral radii and average number of NDA iterations for the infinite Fourier Analysis with $c = 0.9999$ compared to the analytical Fourier Analysis for the Eddington and Current Formulation on a mesh with 1000 Cells.

Cell	Eddington			Current		
Thickness	Analytic	Numerical	Iterations	Analytic	Numerical	Iterations
0.001	0.2236	0.1634	4.6	0.2236	0.1630	4.5
0.01	0.2246	0.2144	6.0	0.2246	0.2123	5.9
0.1	0.2246	0.2135	6.3	0.2259	0.2143	6.2
1	0.2246	0.2193	7.0	0.3723	0.3651	10.0
10	0.0289	0.0260	3.0	0.9602	0.9590	202.6
100	0.0003	0.0002	2.0	0.7996	0.7943	39.1
1000	< 0.0001	< 0.0001	1.0	0.0385	0.0346	3.0

The comparison between of the spectral radii and average number of iterations for the Eddington and Current formulation, using the fine mesh with 1000 cells, can be seen in Table 3.11. The numerical analysis clearly showed the predicted increase of the spectral radius for optical thick cells for the Current formulation. Note that for $c = 0.9999$ the spectral radius of the Current formulation does not go asymptotically towards one as it does for $c = 1$, but peaks at approx. $h = 10$ and goes to zero for optical very thick cells. The results demonstrates that this increase in the spectral radius causes the a number of required iterations to be two magnitudes larger than for the Eddington formulation.

We performed the same calculations for test case 4b (Table 3.4), a void case with a scattering region with $c = 0.9999$ using the Combined Formulation with the non-local diffusion coefficient. We used 2000 cells for the periodic problem, 2 cells per region as we did for the analytic Fourier Analysis and repeated this 500 times to obtain a decent sized mesh. Again we ran 10 samples and took the average. The results as shown in Table 3.12 showed good agreement to the predicted spectral radii except for

Table 3.12 Average computational spectral radii and average number of NDA iterations for the two region void problem with $c = 0.9999$ (Case 4b, Table 3.4) for Combined Formulation using the non-local and the joined diffusion coefficient compared to the corresponding analytical Fourier Analysis.

Cell	Non-local Coefficient			Joined Coefficient		
Thickness	Analytic	Numerical	Iterations	Analytic	Numerical	Iterations
0.001	0.2233	0.1769	4.3	0.4777	0.1258	3.7
0.01	0.2245	0.2119	5.8	0.4781	0.3277	6.6
0.1	0.2268	0.2142	6.0	0.4799	0.4671	10.8
1	0.4070	0.4267	11.3	0.5751	0.5661	18.0
10	0.4785	0.4531	14.1	0.5452	0.5379	16.6
100	0.6484	0.7867	29.1	0.6377	0.6297	21.0
1000	0.0413	0.0339	4.0	0.0413	0.0340	4.0

$h = 100$. At this thickness the numerical spectral radius was significantly higher than the analytical, which cannot be explained by the limitation of frequencies. However the cells are too thick for a reliable calculations of the non-local diffusion coefficient, which gave negative results in the material region, causing a degrading of convergence. To prove this, the diffusion coefficient was switched to the joined diffusion coefficient (Eq. (3.109)) with $\zeta_D = 10^{-3}$. This used the local diffusion coefficient in the material region and hence avoids the increase in the spectral radius as can be seen in the right half of Table 3.12. Since the non-local diffusion coefficient is constant in the void region, the result in the void can be used without problems.

The numerical Fourier Analysis confirmed that the void modifications are an unconditionally stable and efficient scheme. However they also showed that the calculation of the non-local diffusion coefficient can strongly influence the convergence rate, if the mesh for this calculations is unresolved and the non-local diffusion coefficient shows oscillations and negativities. Furthermore, the calculations of the non-local diffusion coefficient transforms any problem into a pure absorber problem, thus if a

mesh is refined enough for a diffusive problem, it might not for the calculation of the non-local diffusion coefficient. Hence the non-local diffusion coefficient requires careful treatment to avoid instabilities in the NDA algorithm.

4.1 Reed's Problem

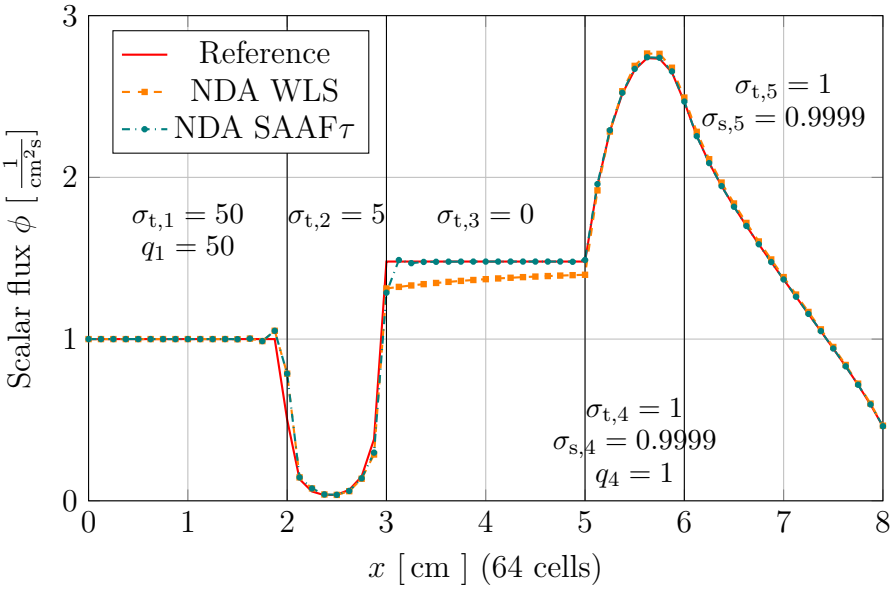

Figure 4.1 Solution for the modified Reed's problem with NDA SAAFτ and NDA WLS. Comparison to a highly refined WLS reference solution. (Cross sections in $\frac{1}{\text{cm}}$and source strengths in $\frac{\text{n}}{\text{s}}$).

To test the void NDA modifications, we used a slightly modified version of Reed's problem, a well know test problem containing a void region and a highly diffusive region. The calculations used both NDA schemes, the NDA WLS Eq. (3.28) and the NDA SAAFτ Eq. (3.26). The results are shown in Fig. 4.1 and the relative error in

*Part of the data reported in this chapter is reprinted with permission from *Nonlinear Diffusion Acceleration in Voids for the Weighted Least-Square Transport Equation* by Hans R. Hammer, Jim E. Morel, and Yaqi Wang. M&C 2017 - International Conference on Mathematics & Computational Methods Applied to Nuclear Science & Engineering, 16-20 April 2017.

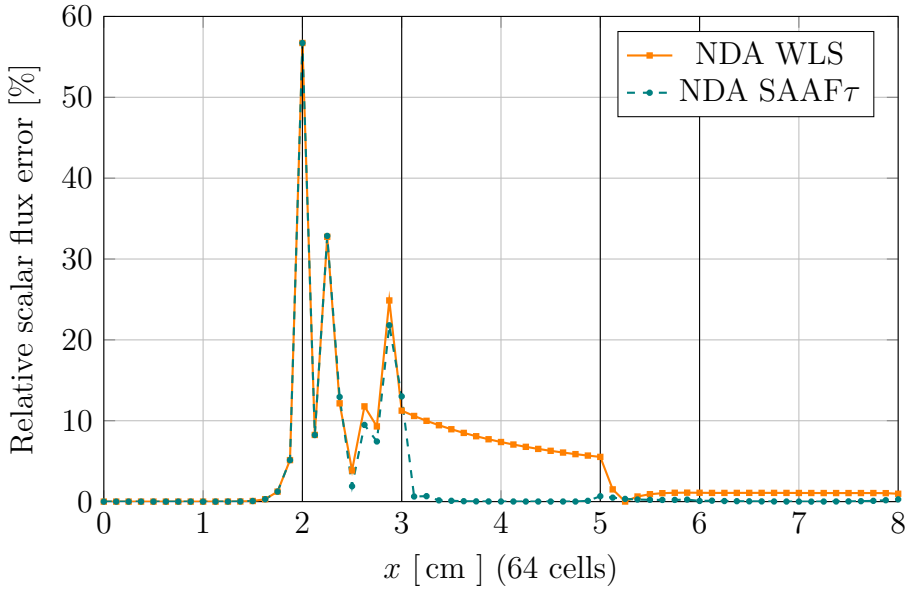

Figure 4.2 Relative error for the modified Reed's problem with NDA SAAFτ and NDA WLS to the WLS reference solution.

the scalar flux can be seen in Fig. 4.2. Both schemes have large errors in the absorber region. These are mainly caused by the low magnitude of the scalar flux in that region. In the void region the NDA WLS solution shows a non-constant flux and a wrong magnitude. This affects the adjacent scattering region. The NDA SAAFτ solution showed small oscillations at the void's left boundary and a decrease in the scalar flux only in the leftmost cell in the void. These inaccuracies in both NDA WLS and NDA SAAFτ disappear with increasing mesh refinement.

Both schemes needed 16 iterations to reduce the error between two consecutive low order solutions (Eq. (3.28e)) below the error tolerance of 10^{-10}. The NDA SAAFτ scheme is consistent, hence the difference between high-order and low order solution (Eq. (3.26e)) can also be used as measurement for the error. It took only 14 iterations to reduce the iterative error below the tolerance. The NDA WLS scheme is

inconsistent and therefore the high-order and low-order solutions only converge in the limit of spatial refinement.

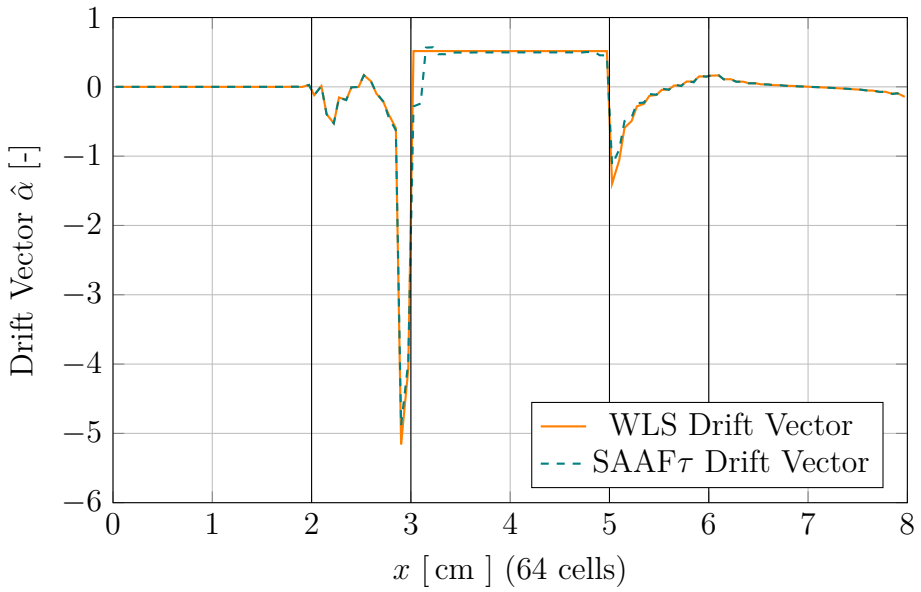

Figure 4.3 Drift vectors from the WLS and SAAF transport calculation for the modified Reed's problem.

The drift vectors from both WLS and SAAFτ agree well as can be seen in Fig. 4.3, except for the left cells in the void region. The SAAFτ drift vector has oscillation on the left side of the void region. The WLS drift vector is constant throughout the void region.

4.2 Two region problem with void

To further investigate the non-constant flux of the NDA WLS solution in the void region as shown in Fig. 4.1 we simplified the problem to an one dimensional two region problem. The left half of the problem contains a void ($\sigma_{\mathrm{t},1} = 0\,\frac{1}{\mathrm{cm}}$), while

the right side contains a strong absorber ($\sigma_{\mathrm{t},2} = 10\,\frac{1}{\mathrm{cm}}$). On the left boundary is an incident isotropic flux $\phi^{\mathrm{inc}} = 1.0\,\frac{1}{\mathrm{cm^2 s}}$. The problem is 2 cm wide with x_{L} the left boundary, x_{R} the right boundary and $x_{\mathrm{I}} = 1\,\mathrm{cm}$ the interface between the void and the absorber. We study this pure absorber problem even though no NDA iterations or acceleration are required to obtain the solution. However, the low-order equation also ensures conservation for the WLS scheme, so it is reasonable to use it in the case of zero or small scattering ratios.

4.2.1 Analytical solution

It is easy to obtain an analytic solution to this simple problem as show in Appendix B. The analytical solution in the void with an isotropic incoming flux on the left boundary is given by

$$\phi_1(x) = \frac{\phi^{\mathrm{inc}}}{2} \tag{4.1a}$$

and for the absorption region

$$\phi_2(x) = \frac{\phi^{\mathrm{inc}}}{2}\mathrm{E}_2\left(\sigma_{\mathrm{t}}\left(x - x_{\mathrm{I}}\right)\right) \tag{4.1b}$$

with E_n the exponential-integral function

$$\mathrm{E}_n(x) \equiv \int_1^\infty \frac{\mathrm{e}^{-xt}}{t^n}\,dt. \tag{4.2}$$

In Appendix B.1.2 we also derive the analytic S_N solution. This solution is needed as reference for the transport solutions and the corresponding NDA solutions. It employs a Gauss-quadrature to integrate over the angle. We will refer to this solution as the S_N analytic solution.

With the analytic solution it is possible to calculate the drift vector $\hat{\alpha}$ analytically.

In the void region the drift vector $\hat{\alpha}_1 = -0.5$ is constant (Eq. (B.8a), and so is the non-local diffusion coefficient D_1 (Eq. (B.19a)). Therefore the drift-diffusion equation Eq. (3.11) simplifies in the void region to

$$-\mathrm{D}_1 \frac{\partial^2}{\partial x^2}\phi_1 - \hat{\alpha}_1 \frac{\partial}{\partial x}\phi_1 = 0 \tag{4.3}$$

where the subscript 1 stands for the left half of the problem. The analytical solution to Eq. (4.3) is

$$\phi_1(x) = A_1 + B_1 \mathrm{e}^{-\frac{\hat{\alpha}_1}{\mathrm{D}_1}x} \tag{4.4}$$

with A_1 and B_1 constants to be determined by the boundary and interface conditions. As we can see, the constant solution is part of the solution space of Eq. (4.4) but not the exclusive one. For a nonzero constant B_1 the solution can also be exponential.

The solution Eq. (4.4) in the void region is conservative. This can be easily shown using Eq. (3.77) and solve for the drift current

$$J = -\mathrm{D}\frac{\partial}{\partial x}\phi - \hat{\alpha}\phi. \tag{4.5}$$

Substituting the current with the solution Eq. (4.4) into the balance equation Eq. (3.1) shows conservation.

4.2.2 Numerical results

The problem does not feature scattering, hence no iteration process is required to obtain the solution. This allowed us to compare the transport solution and the solutions to the drift-diffusion equation using different drift vectors. These drift vectors were obtained from the analytical solution (Eq. (B.8)) and from the WLS and SAAFτ transport solve.

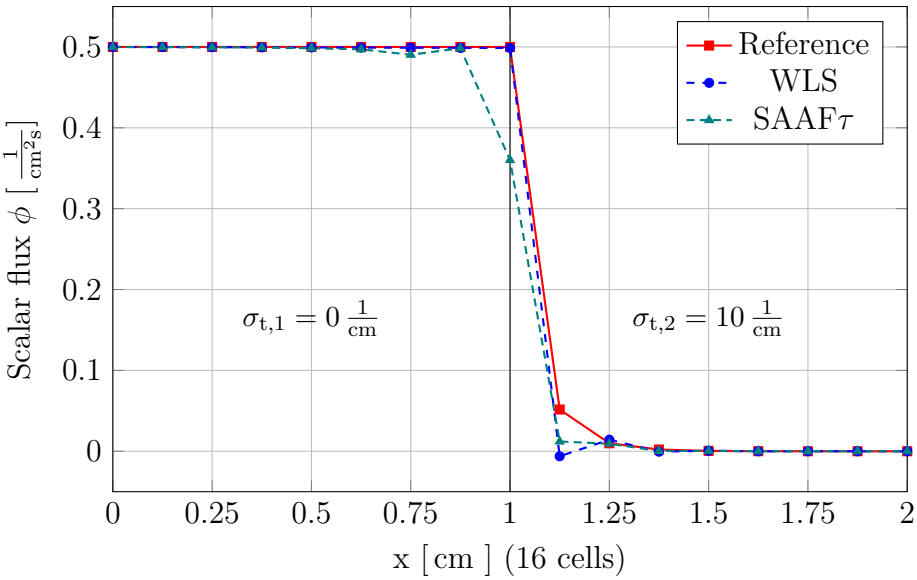

Figure 4.4 WLS and SAAFτ transport solutions for the two region problem with a void and an incident isotropic flux on the left side compared to an analytic reference solution.

Figure 4.4 shows the solution to the problem using the WLS and SAAFτ transport solvers in comparison to the analytic S_N solution (Eq. (B.9) for S_8 quadrature). The WLS used a weight function limit of $w_{\max} = 1000\,\text{cm}$ and the SAAFτ used $\zeta = 0.5$. These parameters were also used for the remaining results in this section. The result of the WLS scheme showed a constant flux in the void region. The SAAFτ scheme started oscillating towards the right side of the void region and dropped significantly in the last cell before the material interface. Both schemes had a dip after the interface in the material half and continuing oscillations into the material region, which is a typical behavior on material interfaces of second order equations. Due to the higher value of the WLS solution on the interface, the dip for it was lower than for the SAAFτ solution.

Now that the angular fluxes of the transport solutions were known, we were able

to calculate all correction terms for the NDA. In addition we calculated drift vectors and boundary coefficient (Eq. (3.24)) from the analytic (Eq. (B.8)) and S_N analytic solution (Eq. (B.14)). As mentioned before, with the correction terms the low order drift-diffusion solution can be obtained without any further transport solve. Hence we can compare the results for the different drift vectors without any feedback from the drift-diffusion solution, which we would have, if we were required to iterate.

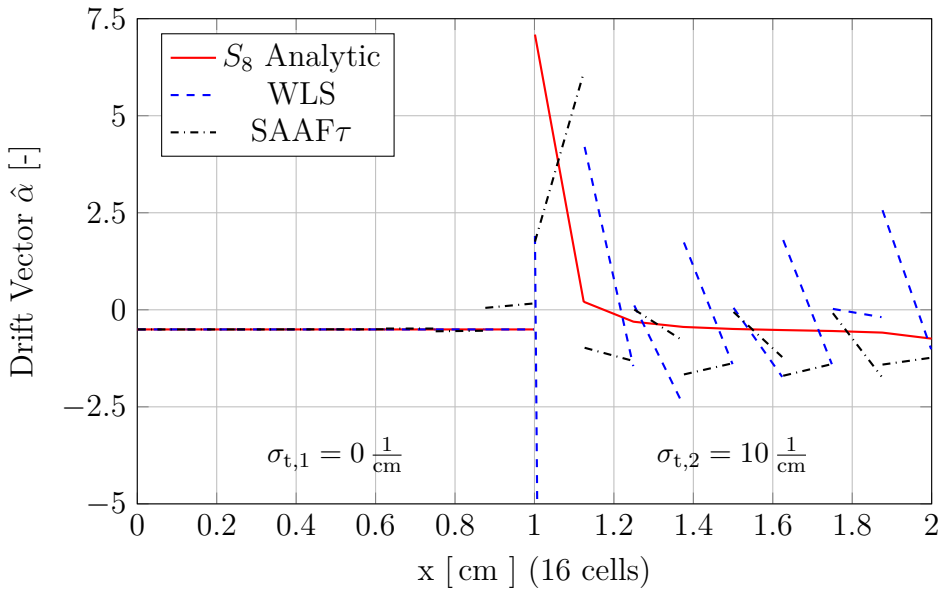

Figure 4.5 Analytic and numerical drift vectors for the two region problem.

Figure 4.5 shows the drift vectors. All drift vectors were negative and constant in the void except the SAAFτ. It started oscillating towards the material interface and was positive in the last void cell before the interface. We can find this behavior reflected in the SAAFτ transport solution shown in Fig. 4.4. The other drift vectors are very close to the S_N analytical drift vector. In the material region the drift vector results were far off the reference. The transport solutions oscillated and the

low magnitude of the scalar flux ϕ made the drift vector ill-conditions. Since the derivative of the scalar fluxes were discontinuous, so were the drift vectors.

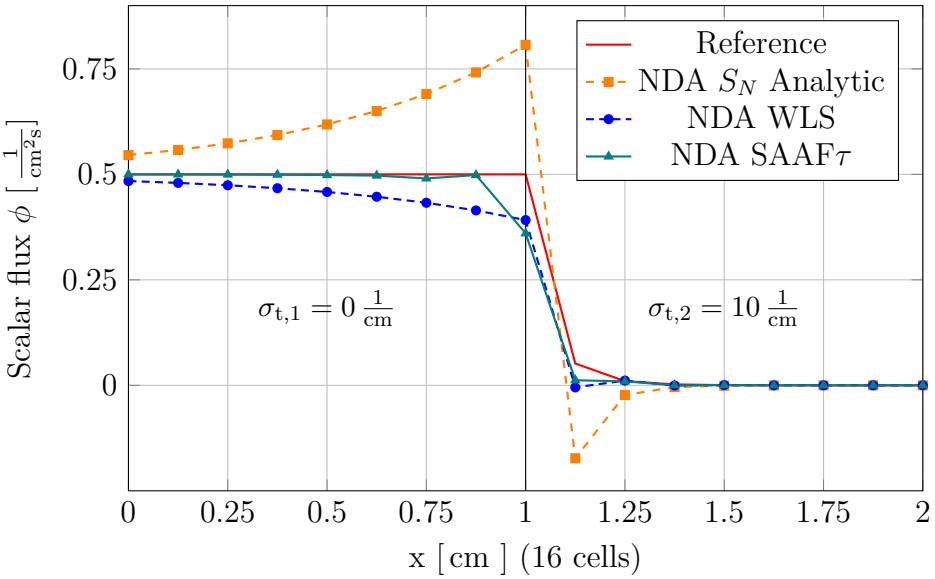

Figure 4.6 NDA solutions to the two region problem with a void and an incident isotropic flux on the left side using different drift vectors.

If we use the drift vectors discussed above we obtain the NDA solutions shown in Fig. 4.6. All calculation used an analytic expression for the non-local diffusion coefficient Eq. (B.19). The WLS drift vector produced an exponentially decreasing flux in the void regions. As we have shown earlier, this is part of the solution space of the drift-diffusion equation. Surprisingly the analytic drift vector gave the worst result. The scalar flux in the void region was exponentially increasing towards the material interface. The results show that a more accurate drift vector does not necessarily increase the accuracy of the NDA solution. The interface and boundary conditions of the void region determine the shape of the scalar flux within the void. The SAAFτ

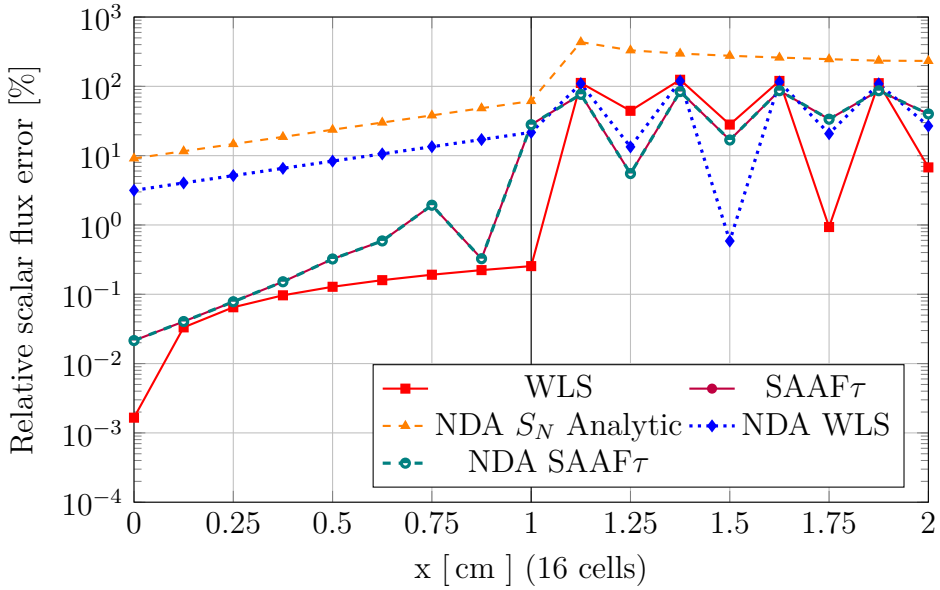

Figure 4.7 Relative error in the scalar flux of the transport and NDA solutions for the two region problem with a void, the NDA solutions use different drift vector vectors.

was constant in the left part of the void region. In the last cell before the interface it decreased strongly. Since the SAAFτ drift vector is not constant in voids, Eqs. (4.3) and (4.4) are not valid. The oscillations of the transport solution forced the NDA solution to be consistent.

The relative error in the scalar flux is shown in Fig. 4.7. The largest error showed the NDA with the analytic drift vector. In the void region the WLS transport solution had the least error. The SAAFτ transport and the NDA using the SAAFτ drift vector had the same error. All numerical schemes showed approximately the same error in the material region with strong oscillations.

The NDA SAAFτ uses a different formulation of the drift vector (Eq. (3.26c)) then the NDA WLS (Eq. (3.28c)). To measure the influence of the drift vector formulation and ensure that the large deviation is not caused by the drift vector,

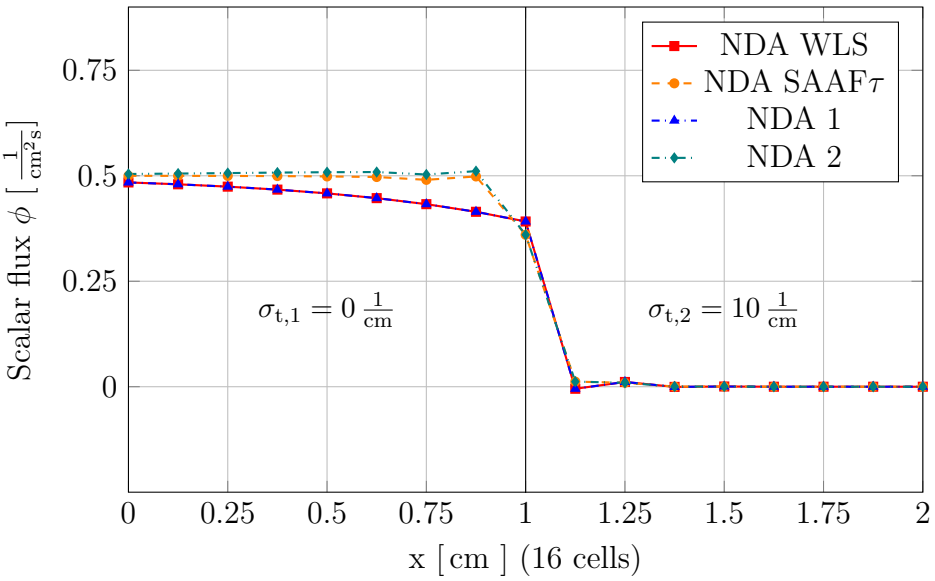

Figure 4.8 Comparison of the NDA solutions for the two region problem with switched drift vectors.

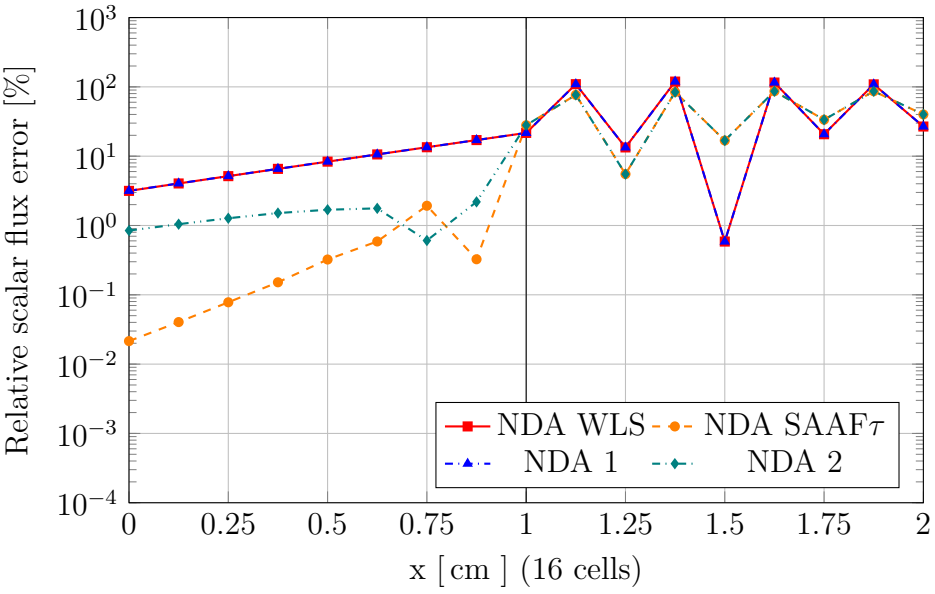

Figure 4.9 Relative error in the scalar flux of the NDA solutions for the two region problem with switched drift vectors.

the formulations were used with the other transport scheme. Hence Eq. (3.26c) used the transport solution from Eq. (3.28a) (WLS transport with τ-scheme, labeled with NDA 1) and respectively Eq. (3.28c) the solution from Eq. (3.26a) (SAAFτ transport with combined scheme, labeled with NDA 2). The low-order drift diffusion and the boundary conditions were the same for both formulations. Figure 4.8 shows the comparison of the switched drift vectors with the original schemes. The corresponding relative errors are shown in Fig. 4.9. The drift vector formulation switch affected the solutions only in the void part of the problem. The NDA WLS scheme error was comparable to the NDA 1 scheme. For NDA SAAFτ the consistent schemes showed significant lower error than the NDA 2 scheme using the same transport solution. However, the NDA 2 solution still has a lower error than any solution using the WLS transport solution. This is particular interesting, since the WLS transport solution showed a smaller error in the void than the SAAFτ solution (Fig. 4.7). This shows that the formulation of the drift vector was not the cause of the large deviations for the WLS scheme but the interface conditions.

The described error in the void is a coarse mesh problem. Increasing refinement of the mesh reduced the error as shown in Fig. 4.10. All schemes converged spatially with second order. So did the schemes using the switched formulation of the drift vector (not shown to keep the plot simple). The convergence for NDA 1 was similar to the NDA WLS scheme and the convergence of NDA 2 was similar to the NDA SAAFτ.

We also studied the spatial convergence if we kept the number of cells in the void constant (8 cells). Since void regions normally do not hold many details, refinement might be a waste of computational resources. The results showed, that the spatial convergence is second order to the number of cells in the material region. This indicates again, that the error in the void region is caused by the error on the material

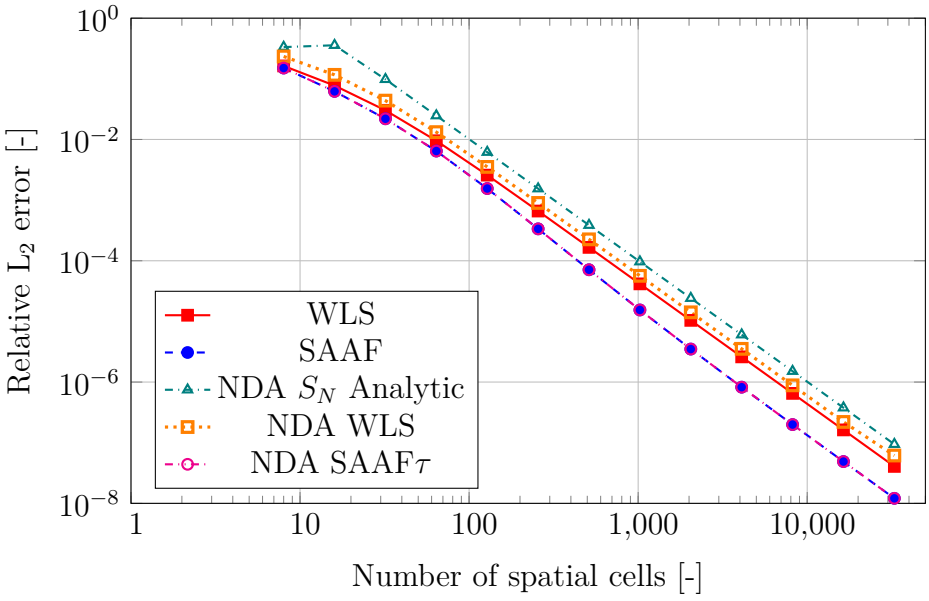

Figure 4.10 Convergence of the error with mesh refinement for the two region problem for transport and NDA solutions.

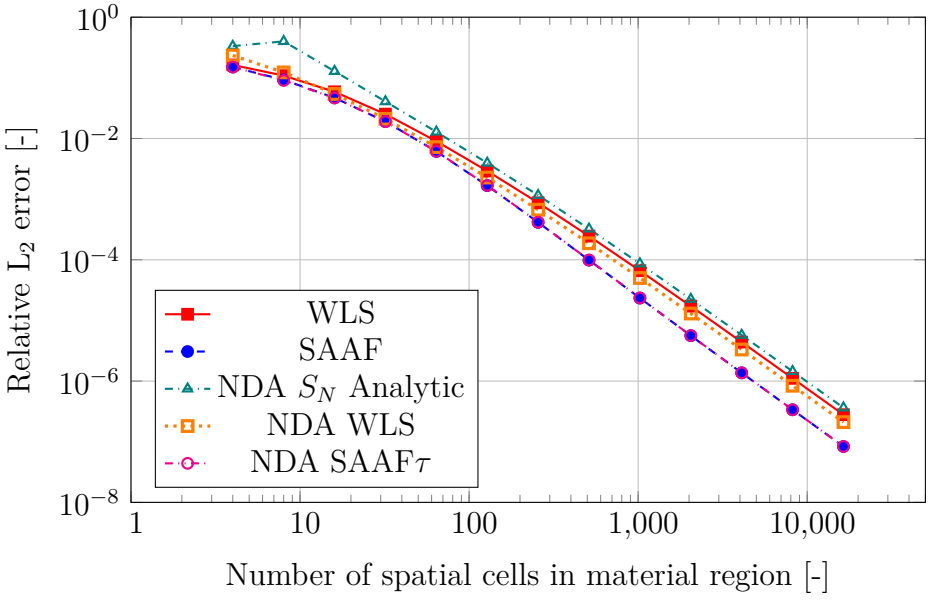

Figure 4.11 Convergence of the error for the two region problem for transport and NDA solutions with constant 8 cells in the void region and mesh refinement in the material region.

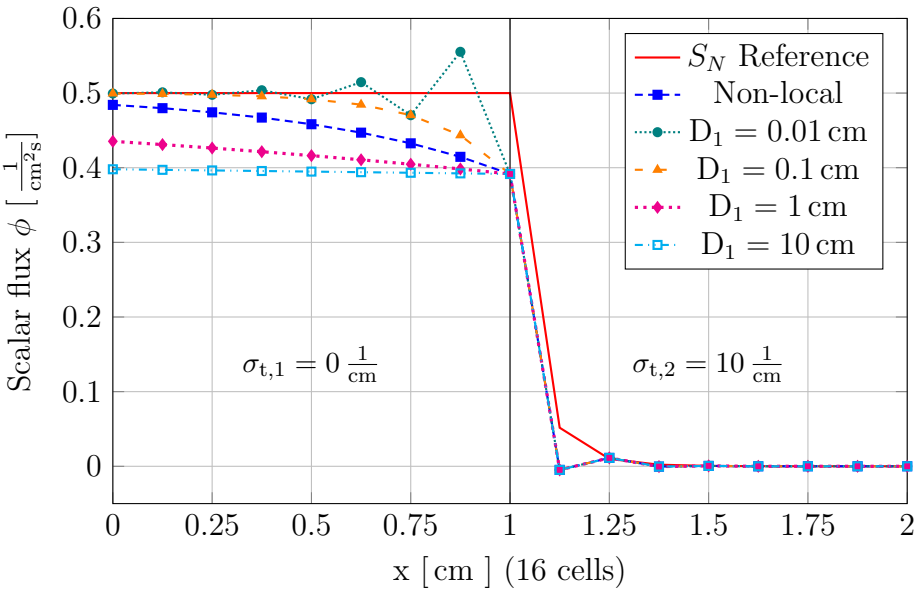

Figure 4.12 Results for the NDA WLS scheme using different diffusion coefficients in the void region.

interface propagated into the void. Improving the error in the material regions hence also improves the error in the void region.

4.2.3 Accuracy of the diffusion coefficient

The influence of the non-local diffusion coefficient is also of interest. Since this problem is a purely absorbing problem, the diffusion coefficient is a free parameter. In problems with scattering, a poor choice for the diffusion coefficient can reduce the iterative convergence of the NDA scheme or make it unstable (Chapter 3). Nevertheless we studied the effect of this parameter on solution of our scheme, especially since the NDA WLS scheme is non-consistent and it is not guaranteed that the diffusion terms cancel.

We used the local diffusion coefficient with several constant values in the void region and compared the results to the non-local diffusion coefficient in Fig. 4.12.

For the NDA WLS the choice of the diffusion coefficient has a large impact on the scalar flux in the void region. The scheme is not consistent for small σ_t, hence small differences between the transport and NDA solution arise. If the diffusion coefficient is too large, these differences will be magnified and lead to a wrong result in the void region ($D \geq 10\,cm$). For small diffusion coefficients the result started to oscillate in the void region. The non-local diffusion coefficient $D_{nl} \approx 0.25\,cm$ is in this case of the right magnitude. However, it is not the optimal choice to minimize the error. The NDA SAAFτ is consistent and therefore not affected by the choice of the diffusion coefficient as shown in Fig. 4.13.

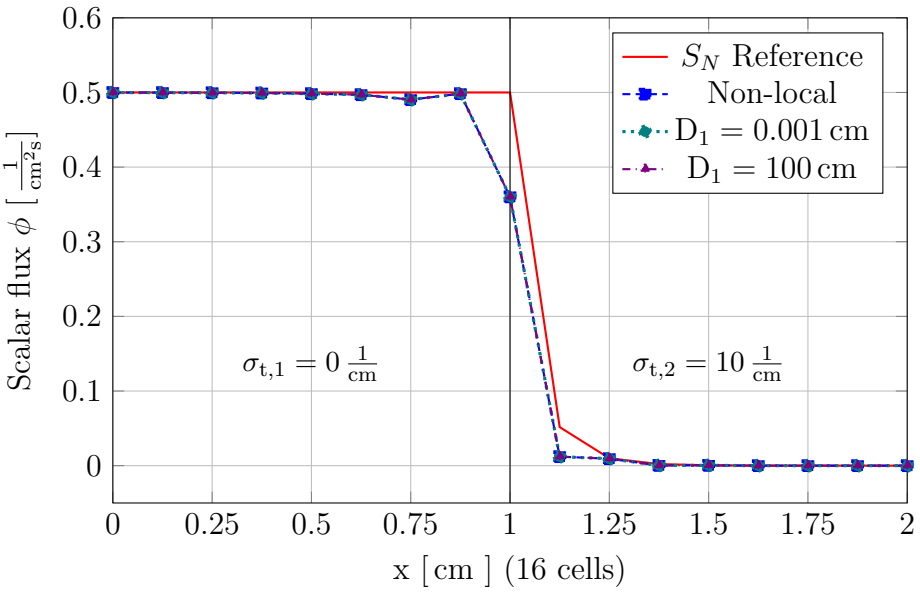

Figure 4.13 Results for the NDA SAAFτ scheme using different diffusion coefficients in the void region.

The next question is, how accurate the non-local diffusion coefficient should be. Non-local diffusion coefficient were calculated with different refinements from 8 to 256

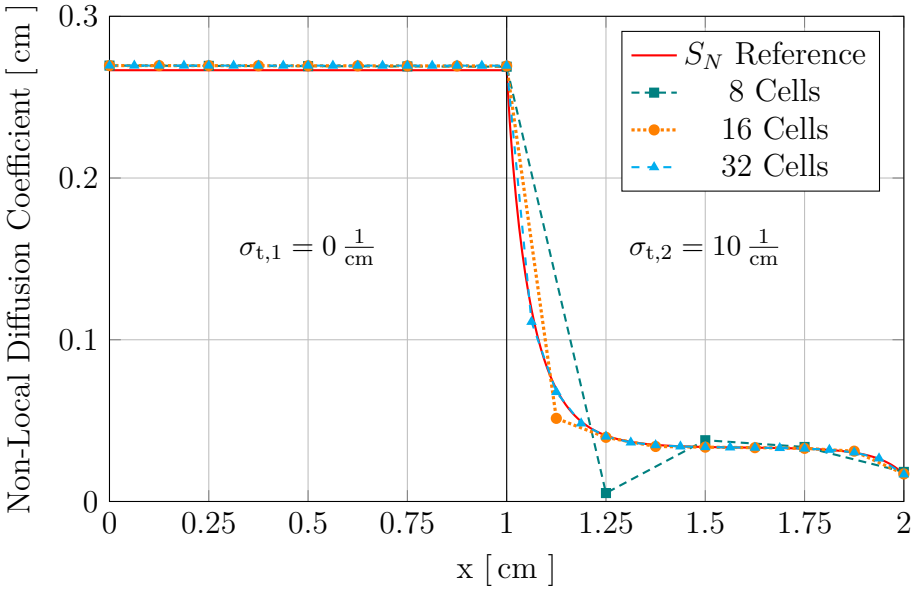

Figure 4.14 Nonlocal diffusion coefficients calculated on different meshes for the two region problem.

cells as shown inFig. 4.14. These were then used to calculate the NDA solution on a 8 cell mesh (Fig. 4.15). The accuracy of the non-local diffusion coefficient does not have any influence on the results, no matter if we used a diffusion coefficient calculated on a coarse mesh with 8 cells or on a fine mesh with 256 cell. Additionally, no difference could be observed between numerically obtained diffusion coefficients and analytically calculated ones (Eq. (B.19)). The diffusion coefficients showed large differences in the material region as shown in Fig. 4.14, however the NDA WLS scheme is consistent for sufficient large cross sections σ_t. Therefore the diffusion terms cancel. In the void the diffusion coefficients were almost exactly the same, no matter the mesh they were calculated on. Also no difference in the error convergence could be seen as shown in Fig. 4.16.

These results indicate, that for the consistent schemes the diffusion coefficient

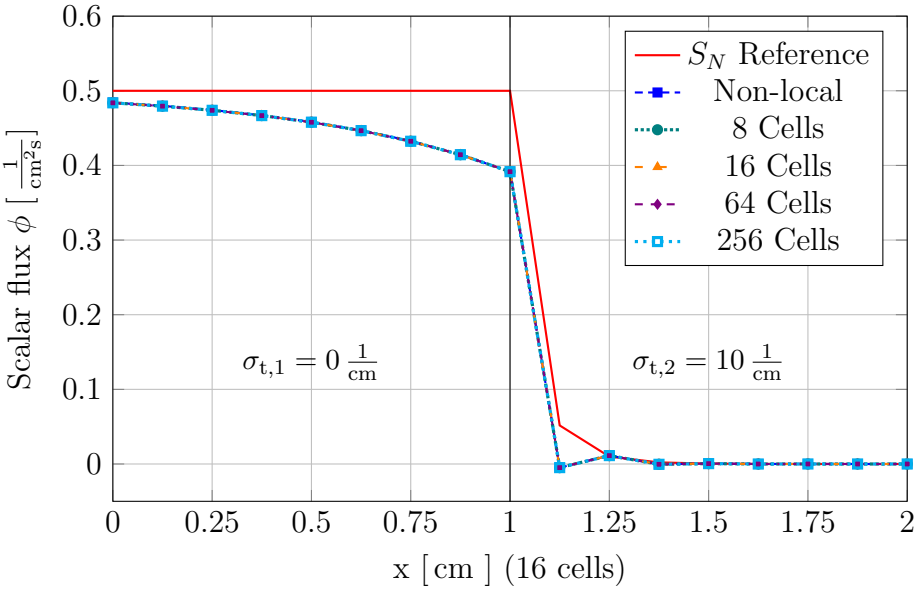

Figure 4.15 Results for the NDA WLS scheme using non-local diffusion coefficients, which were calculated on different meshes (non-local diffusion coefficient's computation mesh size given).

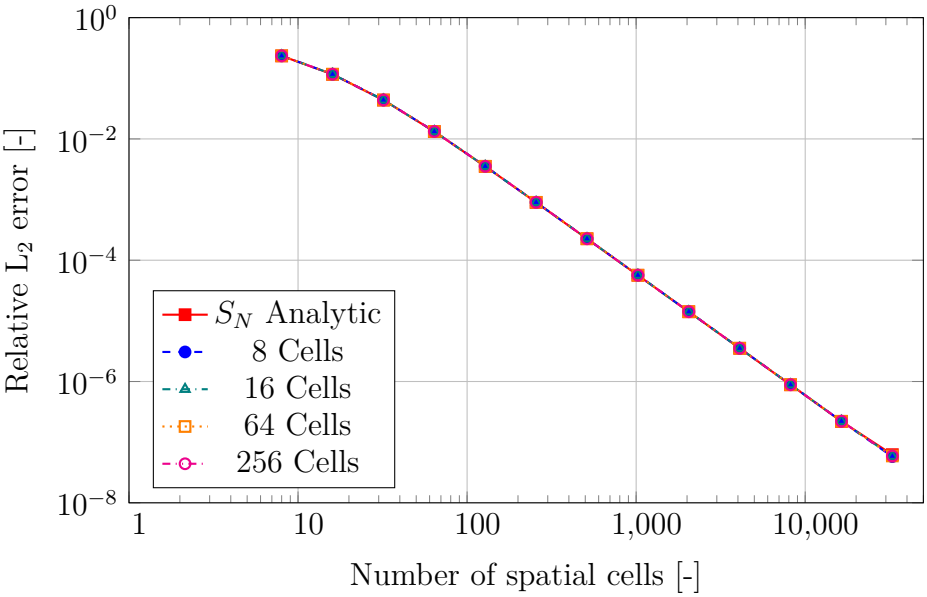

Figure 4.16 Error convergence for NDA WLS with non-local diffusion coefficients, which were calculated on different meshes (non-local diffusion coefficient's computation mesh size given).

does not impact the results but only the convergence. Hence it should be chosen to minimize the spectral radius. For the NDA WLS scheme, voided regions are not consistent. Hence the diffusion coefficient impacts the result. The nonlinear diffusion coefficient gives reasonable results, but a smaller diffusion coefficient reduced the error in the void. However this diffusion coefficient might have a negative effect on the iterative convergence for cases with scattering.

4.2.4 Causality across the material interface

The results for the NDA WLS were non-constant in the void. As showed earlier, this solution is part of the solution space of the drift-diffusion equation (Eq. (4.4)). The exponential solution is caused by the interface value between the material and void region. The material is optical thick, thus an unresolved boundary layer is formed. This error is then propagated back into the void region. The underlaying issue is the causality. The problem is highly directional, with particles streaming only from left to right. The second order drift equation however is propagating information backwards, from right to left. In this section we will study several methods to ameliorate the inaccuracies, however these are only additional, short proof of concepts without the detailed approach we performed for the method developed so far.

The non-constant scalar flux in the void can be ameliorated by restoring causality. A simple test was performed separating the low order solve into two, while using a single solve for the high order equation. Using two separated calculations for the two regions showed in Fig. 4.17 that the result for the void region is in fact constant for the WLS and S_N analytic drift vector. Separating the two regions restored causality across the material interface. The SAAFτ now shows the worst result since the corresponding drift vector was not constant. In the material region the scalar flux at $x = 1$ showed large deviations to the analytic solution. As mentioned above, this is

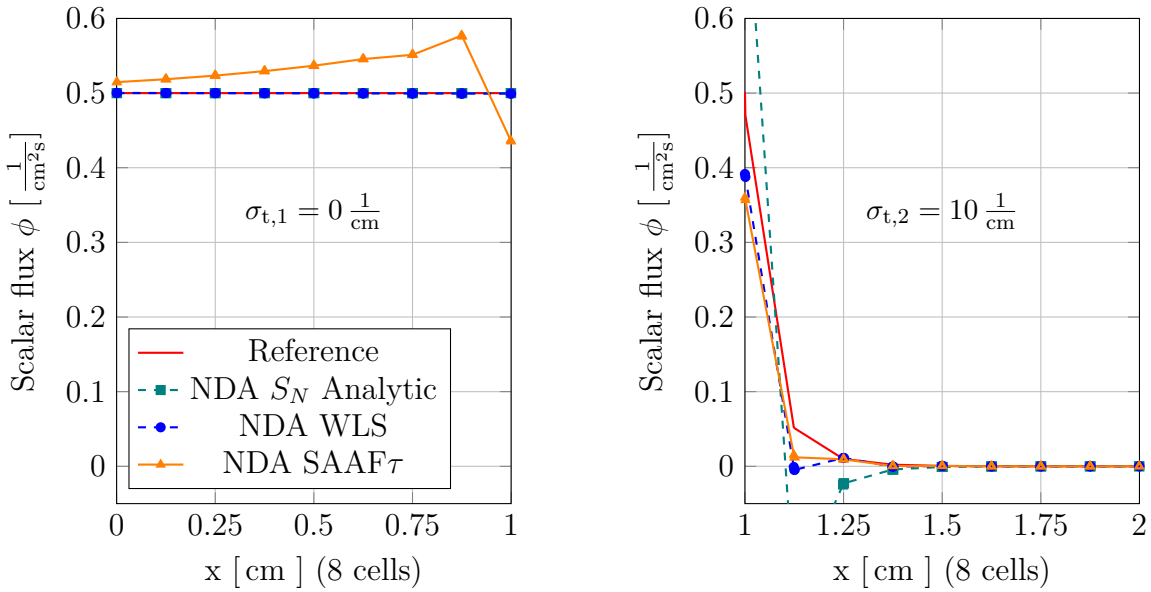

(a) Void region

(b) Absorber region

Figure 4.17 Results for separated solve of the two region problem with NDA using drift vectors from a not-separated transport solve.

due to an unresolved boundary layer.

Performing separate calculations for the drift-diffusion is only possible if the directionality of the problem is simple and known. For complex geometries separation is easily achieved. We will study three approaches to restore or improve causality for the drift-diffusion equation. The first one is an upwind scheme, the second one is an artificial diffusion coefficient, the last one a DFEM scheme.

First lets consider the upwind scheme. For this we use the balance equation Eq. (3.1) and modify it to

$$\frac{\partial}{\partial x}\left[\tilde{J}^{k+\frac{1}{2}}\phi^{k+1}\right] + \sigma_{\text{t}}\phi^{k+1} = 0 \tag{4.6a}$$

with the boundary conditions

$$J^{k+1}\left(x_{\mathrm{L}}\right)=\hat{j}^{\mathrm{in}}\left(x_{\mathrm{L}}\right)-\frac{\kappa^{i+\frac{1}{2}}\left(x_{\mathrm{L}}\right)}{4}\phi^{k+1}\left(x_{\mathrm{L}}\right) \tag{4.6b}$$

$$J^{k+1}\left(x_{\mathrm{R}}\right)=\frac{\kappa^{i+\frac{1}{2}}\left(x_{\mathrm{R}}\right)}{4}\phi^{k+1}\left(x_{\mathrm{R}}\right) \tag{4.6c}$$

with the current factor

$$\tilde{J}^{k+\frac{1}{2}}=\frac{J^{k+\frac{1}{2}}}{\phi^{k+\frac{1}{2}}} \tag{4.7}$$

The current is then upwinded. Depending on the sign of the current factor, the derivative is calculated on the left or right side of the central node

$$\left(\tilde{J}\phi,\vec{\nabla}\phi^{*}\right)_{\mathcal{D}}=\begin{cases}\tilde{J}\left(\phi_{i-\frac{1}{2}}-\phi_{i+\frac{1}{2}}\right) & \tilde{J}\geq 0\\ \tilde{J}\left(\phi_{i+\frac{1}{2}}-\phi_{i+\frac{3}{2}}\right) & \tilde{J}<0\end{cases} \tag{4.8}$$

Note that we have two boundary conditions, but only one is used in this case by the scheme due to the upwinding.

The result are show in Fig. 4.18. In most of the void regions the scalar flux is constant for the NDA using the WLS and S_N analytic current factor. Only the last cell before the material regions is decreasing towards the interface. The NDA SAAFτ shows an earlier decrease. The upwind scheme eliminates the propagation of the error from the interface into the void region. Nevertheless it is not able to eliminate the error in the last cell due to the interface node value, since the solution must be continuous. The main weakness of the upwind scheme is the first order convergence as shown in Fig. 4.19.

The effect of upwinding can also be achieved by an artificial diffusion method [11]. This method introduces an artificial diffusion term to change the CFEM first order derivative to an upwind derivative. We already showed in Section 4.2.3 that a smaller

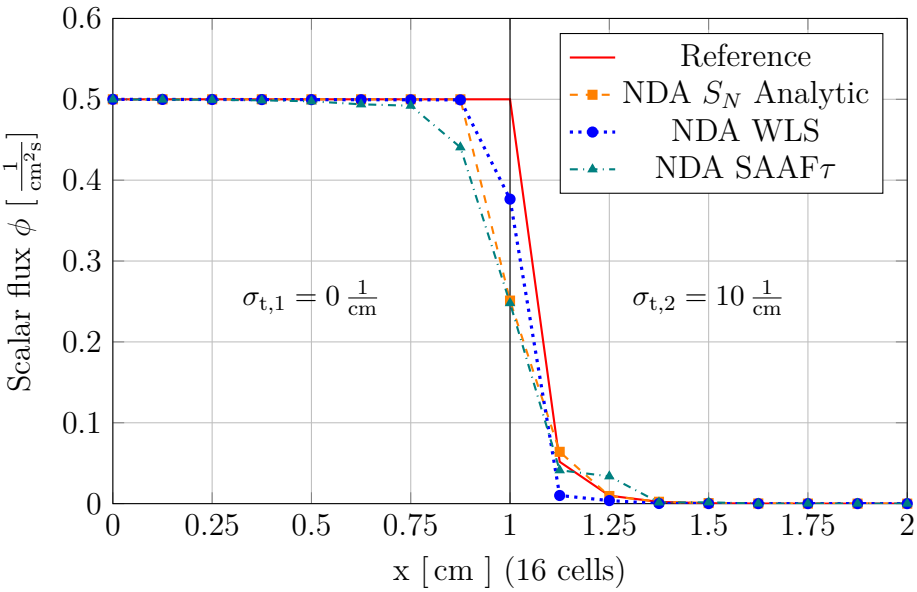

Figure 4.18 Results for the low-order equation using the upwind scheme with different drift vectors.

diffusion coefficient gives somewhat better results until the solution starts oscillating. Using this method, we can find this optimal diffusion coefficient. Consider the weak form of an advection equation on a mesh with cell size h and the velocity $u > 0$. The resulting one-dimensional CFEM discretization is

$$-\left(u\phi, \vec{\nabla}\phi^*\right)_{\mathcal{D}} = \frac{u}{2}\left(\phi_{i+\frac{3}{2}} - \phi_{i-\frac{1}{2}}\right) \tag{4.9}$$

which is, as already mentioned, not a stable discretization. With the right amount of diffusion added to Eq. (4.9), the discretization changes to upwind. The necessary amount of artificial diffusion is

$$\epsilon \equiv \frac{uh}{2} \tag{4.10}$$

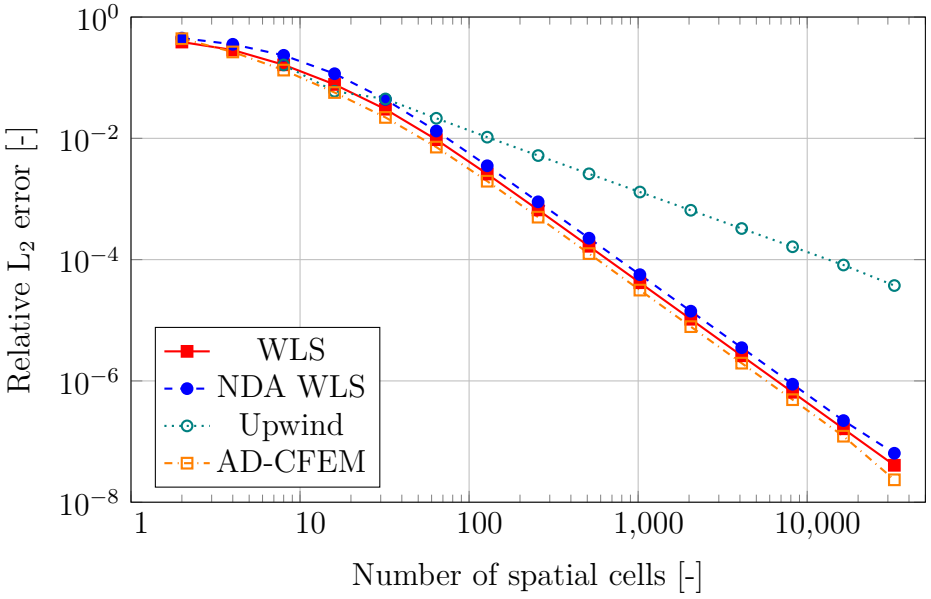

Figure 4.19 Convergence of the upwind and artificial diffusion scheme (AD-CFEM) for the two region problem in comparison to the WLS transport and standard CFEM NDA WLS scheme.

and this changes the advection-diffusion equation to

$$\begin{aligned} -\left(u\phi, \vec{\nabla}\phi^*\right)_{\mathcal{D}} - \left(\epsilon\vec{\nabla}\phi, \vec{\nabla}\phi^*\right)_{\mathcal{D}} &= \frac{u}{2}\left(\phi_{i+\frac{3}{2}} - \phi_{i-\frac{1}{2}}\right) - \frac{\epsilon}{h}\left(2\phi_{i+\frac{1}{2}} - \phi_{i-\frac{1}{2}} - \phi_{i+\frac{3}{2}}\right) \\ &= u\left(\phi_{i+\frac{1}{2}} - \phi_{i-\frac{1}{2}}\right). \end{aligned} \tag{4.11}$$

The one-dimensional drift-diffusion Eq. (4.3) in voids is an advection-diffusion equation with $u = \tilde{J}$, because the slope of the scalar flux is zero in the void and the diffusion term in the drift vector vanishes. Hence the artificial diffusion coefficient is

$$\mathrm{D}_\epsilon \equiv \frac{\tilde{J}h}{2} \tag{4.12}$$

with the current factor $\tilde{J}$ defined in Eq. (4.7). This diffusion coefficient is then used

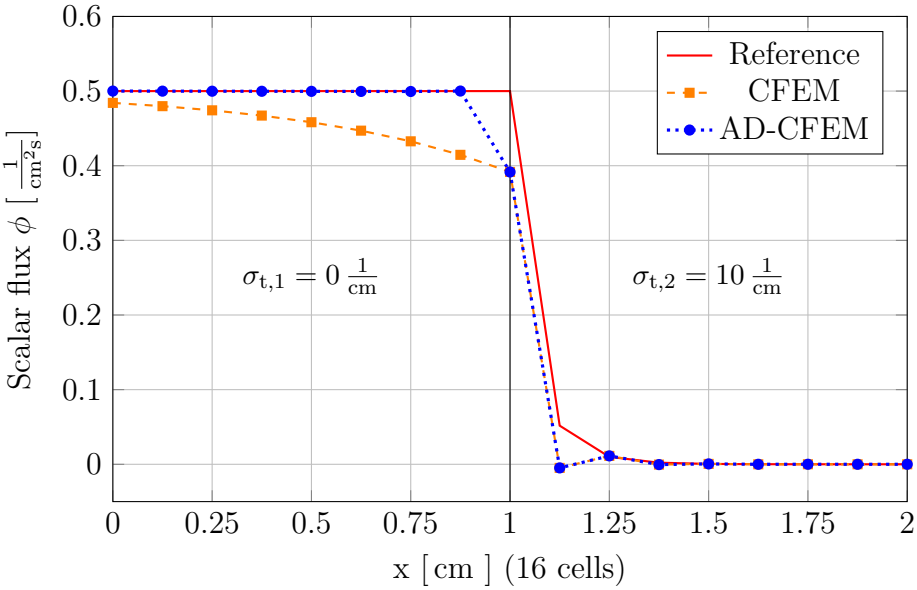

Figure 4.20 Results for the low-order equation using the artificial diffusion scheme (AD-CFEM) in comparison to the NDA WLS scheme using a non-local diffusion coefficient.

in the standard drift-diffusion Eq. (3.28d) without any further modifications. Since the diffusion term only vanishes in the void region, the scheme in the material region is not changed to upwind.

The result is similar to the upwind scheme as shown in Fig. 4.20. However, for these we did not change the low-order discretization but only the diffusion coefficient. Since the diffusion coefficient was chosen to achieve upwinding in the void, it limits this effect to the void. So this scheme is effectively upwinding only in the void region, and using the standard discretization in the material region. It is clearly that the diffusion coefficient defined in Eq. (4.10) is the optimal diffusion coefficient to Fig. 4.12. In contrast to the upwind solution, the error of the artificial diffusion scheme converges second order as shown in Fig. 4.19, because the upwind is limited to the void region of the problem. Surprisingly, the artificial diffusion scheme has even a

slightly smaller error the WLS transport equation. However, the artificial diffusion coefficient is dependent on $\tilde{J}$, which makes its effect on the iterative convergence problematic.

The last approach allows a discontinuous solution. If we decouple the solution at the interface and force causality across the interface the problem should be solved. There are two choices. The first is to only allow a discontinuity at the interface and use CFEM for the remaining parts. This solution is similar to what Zheng proposed for the LS equation [80], however we would use it only for the low order equation. This method requires the user to identify and treat all problematic interfaces. For complex geometries this would mean a major task. The second possibility is the use of a DFEM drift-diffusion scheme. Using a DFEM scheme eliminates the necessity of identifying problematic interfaces. In this dissertation we chose the second option, however the developed scheme is easily adapted for larger CFEM regions.

The used DFEM drift-diffusion equation was first proposed by Schunert et al. [60] for the NDA using first order transport. The drift-diffusion equation used the internal penalty method [71]

$$\sum_{\tau\in\mathcal{D}}\left(\mathrm{D}\vec{\nabla}\phi,\vec{\nabla}\phi^*\right)_\tau+\sum_{\tau\in\mathcal{D}}\left(\hat{\alpha}\phi,\vec{\nabla}\phi^*\right)_\tau+\sum_{\tau\in\mathcal{D}}\left(\sigma_\mathrm{a}\phi,\phi^*\right)_\tau+\sum_{\tau\in\mathcal{D}}\left\langle\kappa\phi-\hat{j}^{\,\mathrm{in}},\phi^*\right\rangle_{\partial\mathcal{D}_{V,\tau}}$$
$$+\sum_{\tau\in\mathcal{D}}\langle[\![\hat{\gamma}\phi]\!],[\![\phi^*]\!]\rangle_{\Gamma_\tau}+\sum_{\tau\in\mathcal{D}}\langle\hat{\kappa}[\![\phi]\!],[\![\phi^*]\!]\rangle_{\Gamma_\tau}+\sum_{\tau\in\mathcal{D}}\left\langle\{\!\{\vec{n}\cdot\mathrm{D}\vec{\nabla}\phi\}\!\},[\![\phi^*]\!]\right\rangle_{\Gamma_\tau}$$
$$=\sum_{\tau\in\mathcal{D}}\left(q,\phi^*\right)_\tau \quad (4.13)$$

where τ is a cell of the mesh and Γ_τ its interior interfaces with the global normal $\vec{n}$. The notation $[\![f]\!]=f^+-f^-$ denotes the jump across an interface, with upwind and downwind sides defined by the $\vec{n}$ (vector normal points from - to +) and $\{\!\{f\}\!\}=$

$\frac{1}{2}\left(f^{+}+f^{-}\right)$ the mean value. The penalty factor is

$$\hat{\kappa}=\max\left(\frac{1}{4},\frac{\mathrm{D}^{+}}{h^{+}}+\frac{\mathrm{D}^{-}}{h^{-}}\right) \tag{4.14}$$

The correction terms for the volumetric part ($\hat{\alpha}$) and the boundary condition (κ) are already known from the CFEM scheme Eq. (3.28). As mentioned above, this equation is also valid if τ is a larger region of the multiple mesh cells since the volume integrals are identical to the CFEM equation.

The last remaining part is the correction term for the internal interfaces. It is based on the SYW closure in the reference

$$\hat{\gamma}^{+}=\frac{\hat{\jmath}^{-}}{\phi}-\frac{1}{2}\frac{\vec{n}\cdot\left[\mathrm{D}\vec{\nabla}\phi\right]^{+}}{\phi}-\hat{\kappa} \tag{4.15a}$$

$$\hat{\gamma}^{-}=\frac{\hat{\jmath}^{+}}{\phi}+\frac{1}{2}\frac{\vec{n}\cdot\left[\mathrm{D}\vec{\nabla}\phi\right]^{-}}{\phi}-\hat{\kappa} \tag{4.15b}$$

Note that for the positive factor the partial current goes in the negative direction. The scalar flux is continuous on the high-order system, but not the derivate. The closure cancels the stability and consistency terms in the case of convergence between the high-order and low-order equation, only the current across the interface remains

$$\begin{aligned}\sum_{\tau\in\mathcal{D}}\left\langle\vec{n}\cdot\vec{J},[\![\phi^{*}]\!]\right\rangle_{\Gamma_{\tau}}=&\sum_{\tau\in\mathcal{D}}\langle[\![\hat{\gamma}\phi]\!],[\![\phi^{*}]\!]\rangle_{\Gamma_{\tau}}\\&+\sum_{\tau\in\mathcal{D}}\langle\hat{\kappa}[\![\phi]\!],[\![\phi^{*}]\!]\rangle_{\Gamma_{\tau}}+\sum_{\tau\in\mathcal{D}}\left\langle\{\!\{\vec{n}\cdot\mathrm{D}\vec{\nabla}\phi\}\!\},[\![\phi^{*}]\!]\right\rangle_{\Gamma_{\tau}}\end{aligned} \tag{4.16}$$

The results for the two region problem are shown in Fig. 4.21. Clearly, the solution of the DFEM scheme is almost constant in the void. Across the interface a large jumps in the scalar flux occurs and in the material regions the scalar flux has almost

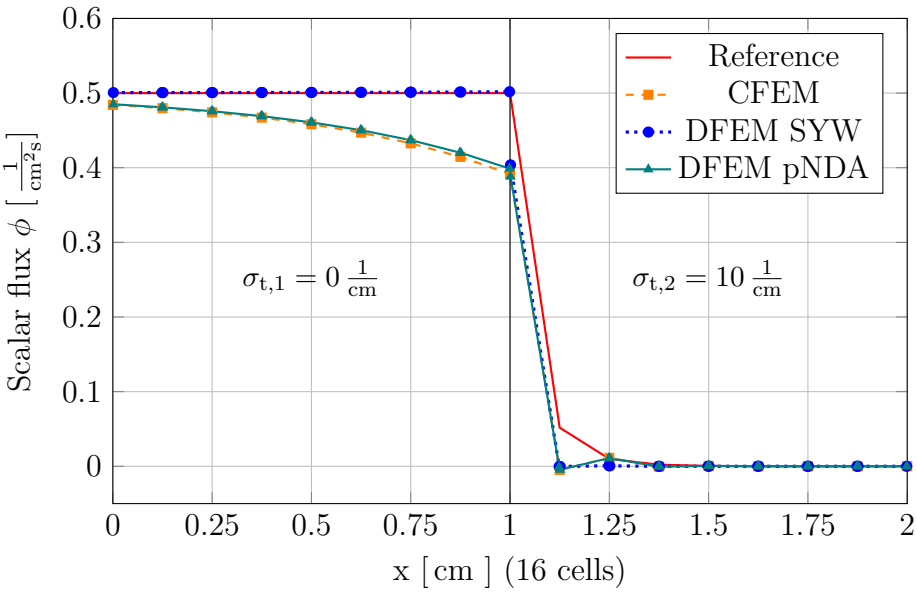

Figure 4.21 Results for the low-order equation using the DFEM scheme with the SYW and pNDA face closures and comparison against the standard CFEM NDA WLS scheme.

the same value as the CFEM results on the interface. Further in the material regions the DFEM scheme however underestimates the scalar flux. However, these results prove that a discontinuity at the material-void interface can improve the accuracy significantly. Since the low-order system is computational much cheaper than the transport solve, the added complexity by the DFEM scheme does not affect the overall cost much.

The convergence of the used SYW closure Eq. (4.15) is only first order as shown in Fig. 4.22. However, the results also showed that for coarse meshes, here with up to 32 cells, the DFEM SYW scheme shows a significantly reduced error compared to the CFEM scheme and even to the WLS transport scheme. A second closure, a modified

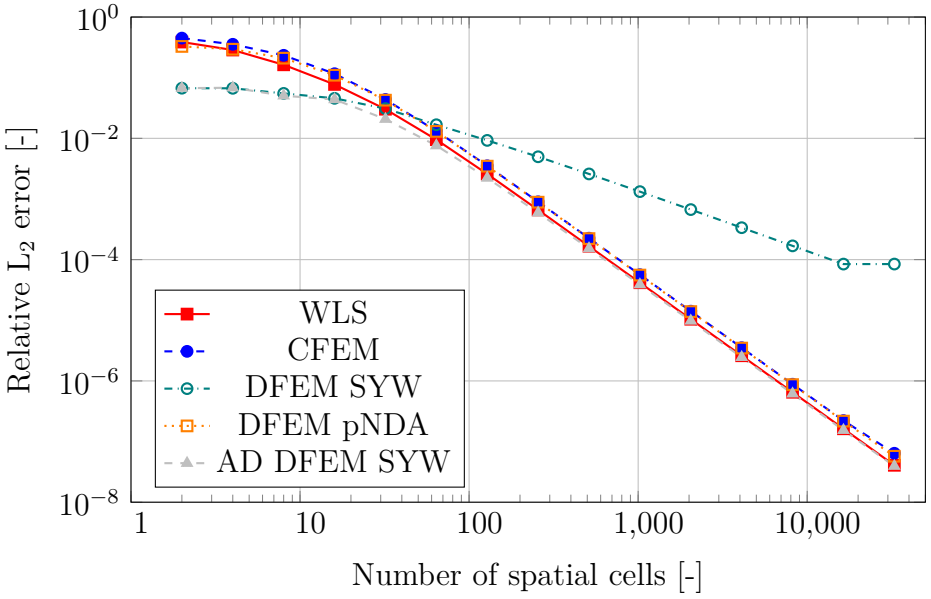

Figure 4.22 Convergence of the DFEM error for the two region problem for transport and NDA solutions in comparison to the standard CFEM NDA WLS scheme and WLS transport solutions.

version of the pNDA closure

$$\hat{\gamma}^+ = \frac{\hat{j}^-}{\phi} + \frac{1}{4} - \frac{1}{2}\frac{[\![\vec{n}\cdot \mathrm{D}\vec{\nabla}\phi]\!]}{\phi} - \frac{1}{2}\hat{\kappa} \tag{4.17a}$$

$$\hat{\gamma}^- = \frac{\hat{j}^+}{\phi} + \frac{1}{4} + \frac{1}{2}\frac{[\![\vec{n}\cdot \mathrm{D}\vec{\nabla}\phi]\!]}{\phi} - \frac{1}{2}\hat{\kappa} \tag{4.17b}$$

gives second order convergence, however no reduced error for coarse meshes is seen. Interestingly, if we combine use the artificial diffusion coefficient Eq. (4.10) with the DFEM SYW scheme Eq. (4.15), we obtain a scheme that has a significantly reduced error for coarse meshes, and second order convergence for fine meshes.

Again, all additional discretization schemes studied in this sections are only preliminary proof of concepts. Since the test problem does not have scattering we

cannot make any statement about the iterative behavior of these methods. Considering the large influence of the diffusion coefficient on the spectral radius, especially the artificial diffusion method might not converge for scattering ratios close to unity. The Fourier analysis is however not trivial since the diffusion coefficient is dependent on the actual high order solution. Therefore we will continue our work with the scheme we proved to work and accept the inaccuracies in voids.

4.3 C5G7 reactor physics benchmark

The C5G7 MOX benchmark problem is a challenging test for modern deterministic transport codes. We focused on the two dimensional version of the benchmark, which already requires large amounts of computational resources. The twenty sets of results that were initially submitted to the benchmark committee can be found in a special issue of Progress in Nuclear Energy [66]. More recent calculations of the benchmark with a spatial and angular convergence study were presented by McGraw [42] and Wang [73]. These calculations were used as a reference solution to validate the LS implementation in Rattlesnake.

The mesh is generated using the 2D mesh generator Triangle [64] with a geometry file which is created by a Rattlesnake mesh generator. The quality of the mesh ensures that no triangle has an interior angle less than 20 degrees. In order to limit the number of elements in the mesh, the surrounding reflector region is divided into three separate regions as shown in Fig. 4.23 employing a coarser mesh far away from the fuel region, while the same maximum triangle area is applied to all fuel assemblies.

Three different meshes, with 8, 16 and 32 equal sides approximating the circumference of the fuel pins, were generated. All meshes conserve the volume of each fuel pin and hence the mass of fissile material. More details about the meshes can be found in the original paper [73].

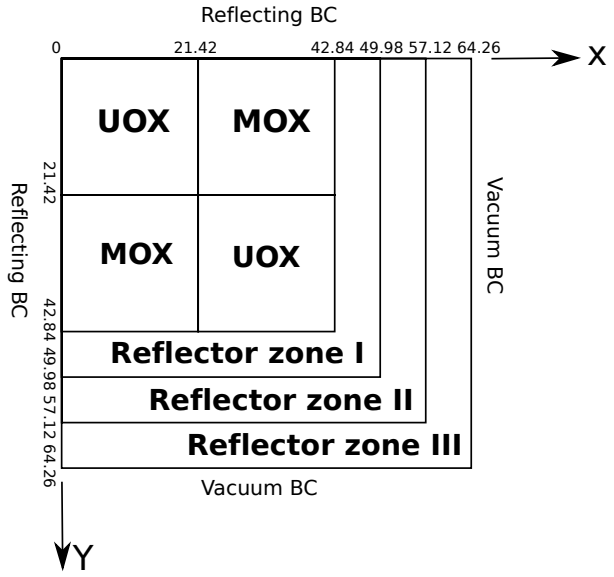

Figure 4.23 Zone layout of the C5G7 benchmark geometry. Reprinted from Wang et. al. [73].

4.3.1 Implementation in Rattlesnake

The high-order low-order system is represented by two sets of equation systems in Rattlesnake. The low-order diffusion equation is solved with the PJFNK solver [51] preconditioned with Hypre BoomerAMG [25]. BoomerAMG is not specifically designed for the non-symmetric Jacobian of this system. Currently there is a study in progress to replace it with an AMG solver for anisotropic diffusion [13, 40], which is better suited for non-axis aligned problems. Nevertheless, for now BommerAMG is an effective preconditioner. Before the actual solve Rattlesnake performs several free power iteration. The power iteration ensure that the initial guess for the Newton solve is close to the largest eigenvalue. All consecutive solves use Picard iterations. Each Picard iterations consists of the steps corresponding to Eq. (3.28) or Eq. (3.26). First the low-order equation is solved using a nonlinear eigenvalue solver [28] to obtain an initial guess for the scalar flux. The scalar flux is transfered to the high-order

system. The left hand side of the transport equation, the streaming and collision part, is inverted. Finally, the drift vector and boundary coefficients are updated using the angular fluxes. The convergence of this scheme is checked with both criteria Eqs. (3.26e) and (3.28e) to allow the reuse of code for WLS and SAAFτ implementations.

Given a specific mesh and an angular quadrature, the operator left hand side of both WLS and SAAFτ equation are fixed, and therefore the matrix can be assembled during the initial setup. Since the low order and high-order system use the same mesh, the spatial quadrature points are identical. All coefficients and drift vectors are only evaluated on the quadrature points and then transfered to the low-order system. The low-order system uses the same code for both high-order schemes. Code duplications were also avoided for the boundary coefficient and transfer routines, only the evaluation of the drift vector is different between WLS and SAAF.

Rattlesnake provides routines to calculate the non-local diffusion coefficient. Two options are available, the on-the-fly calculation and the prepared calculation. The on-the-fly calculation provides the non-local diffusion tensor on every quadrature point in the domain. The auxiliary transport system is solved separately from the main solve and any scheme provided by Rattlesnake can be used. The system for the diffusion tensor is automatically set up and solved prior to the main solve. This method provides the highest accuracy, however it requires the auxiliary system to be solved during every run. This is extremely expensive for real world problems.

The second method generated the non-local diffusion tensors in a completely separated calculation and writes the resulting diffusion tensors into the cross section file. This method eliminates the need to recalculate the diffusion tensor for every run. The limitation of this methods is, that the information are only available per homogenized region, so with far less detail than the on-the-fly calculations.

Nevertheless we chose to use this method. The reduction in computational time and the reduced amount of memory necessary to perform the calculations allowed us to actual run the problem without an excessive amount of computational resources. The other reason is, that the accuracy of the non-local diffusion coefficient has only a limited influence on the result, as shown in Section 4.2.3.

4.3.2 Numerical results for the original benchmark

For the first calculations NDA with the unweighted LS method and boundary condition Eq. (2.26) were used. The void NDA modifications were not needed for this benchmark. All reported errors for the eigenvalue, and pin power distributions were calculated with respect to the reference solution reported by McGraw [42]. The purpose of these calculations is a verification of the LS implementation in Rattlesnake. Therefore we perform spatial and angular refinements to ensure a correct implementation. First, convergence as a function of the number of polar angles was studied for a Bickley3-Optimized quadrature [79]. Table 4.1 shows the results for the coarsest mesh (Mesh 08) and 32 azimuthal angles ($N_A = 32$). It shows clearly, that for 4 polar angles, the polar discretization error for the eigenvalue is converged to below 1 pcm and the pin power errors below 0.001 %. Therefore, the contribution of the polar errors are insignificant in comparison to the other discretization errors. Hence, for the reminder of this study, we fix the number of polar angles to 4. The SAAF convergence study found the same number of polar angles, hence we can compare the azimuthal results to the SAAF results.

Further calculations were performed to study the convergence with spatial mesh refinement and increasing number of azimuthal directions. The errors with respect to the reference are shown in Table 4.2. The table shows the error in the eigenvalue compared to the reference PDT solution, the average pin power error (AVG) and the

Table 4.1 Error convergence of the C5G7 benchmark with refinement of the polar quadrature on the coarsest mesh and 32 azimuthal angles for the eigenvalue error and average (AVG), root-mean-square (RMS) and mean relative error (MRE) of pin power errors.

Number of polar angles	k_{eff} error [pcm]	AVG [%]	RMS [%]	MRE [%]
2	52.350	0.395	0.016	0.515
3	45.816	0.352	0.014	0.449
4	44.589	0.350	0.014	0.445
5	44.386	0.350	0.014	0.445

corresponding root-mean square (RMS) and mean relative errors (MRE) for the pin powers. Column PP1 shows the relative error for the maximal pin power and PP2 the error for the minimal power. Additionally the relative error for all four assembly powers is shown.

We compared the results from our calculations using NDA LS with the results obtained by NDA SAAF [73]. The direct comparison for the eigenvalue is shown in Fig. 4.24a. While the errors are slightly better for this benchmark using NDA LS, it demonstrates, that the two methods are comparable, and that the NDA LS method is capable of solving complex, reactor type problems. Also the pin power results support this, showing LS errors of the same order of magnitude as the NDA SAAF errors method as can be seen in Figs. 4.24b and 4.24c.

We subsequently performed calculations to compare the transport and the NDA schemes. These calculations were performed with Gauss-Chebychev quadrature with 4 polar and 32 azimuthal angles. The calculations were performed two years after the initial convergence study, the use of a different quadrature and different input settings explain the small deviations in the results that are shown in Table 4.3 to the earlier results. For the transport solution a relative tolerance to the initial solution

Table 4.2 Errors associated with various parameters of the refinement study. The fuel assembly relative errors are ordered: (i) Center UOX, (ii) right MOX, (iii) top MOX and (iv) UOX adjacent to the reflector.

Mesh	N_A	k_{eff} [pcm]	AVG [%]	RMS [%]	MRE [%]	PP1 [%]	PP2 [%]	Fuel assemblies i [%]	ii [%]	iii [%]	iv [%]
8	8	50.449	0.356	0.014	0.455	0.410	1.688	0.246	0.308	0.286	0.032
8	16	44.641	0.350	0.014	0.445	0.400	1.685	0.237	0.299	0.277	0.035
8	24	44.585	0.350	0.014	0.445	0.400	1.685	0.237	0.298	0.277	0.036
8	32	44.589	0.350	0.014	0.445	0.400	1.685	0.237	0.298	0.277	0.035
8	48	44.592	0.350	0.014	0.445	0.400	1.685	0.237	0.298	0.277	0.035
8	64	44.592	0.350	0.014	0.445	0.400	1.685	0.237	0.298	0.277	0.035
16	8	61.160	0.205	0.008	0.272	0.241	0.767	0.164	0.188	0.194	0.000
16	16	42.243	0.184	0.007	0.240	0.207	0.773	0.138	0.161	0.167	0.011
16	24	40.474	0.182	0.007	0.238	0.204	0.775	0.136	0.159	0.165	0.012
16	32	40.223	0.182	0.007	0.237	0.203	0.775	0.136	0.159	0.165	0.012
16	48	40.178	0.182	0.007	0.237	0.203	0.775	0.136	0.159	0.165	0.012
16	64	40.178	0.182	0.007	0.237	0.203	0.775	0.136	0.159	0.165	0.012
32	8	68.508	0.126	0.005	0.171	0.146	0.372	0.111	0.123	0.127	0.012
32	16	42.329	0.097	0.004	0.128	0.098	0.389	0.075	0.088	0.091	0.005
32	24	38.060	0.094	0.004	0.123	0.092	0.390	0.071	0.083	0.087	0.007
32	32	37.030	0.093	0.004	0.121	0.091	0.391	0.070	0.082	0.086	0.007
32	48	36.695	0.093	0.004	0.121	0.090	0.391	0.070	0.082	0.085	0.007
32	64	36.674	0.093	0.004	0.121	0.090	0.391	0.070	0.082	0.085	0.007

of 10^{-8} was used. The NDA calculations used the difference between the scalar flux solutions of 10^{-8} with a high order relative tolerance of 10^{-4}. These tolerances were used for all following calculations.

The non-conservative LS transport formulation showed large deviations in all errors, no matter which boundary condition was used (LS 1 uses Eq. (2.27) and LS 2 uses Eq. (2.26). This demonstrates how important the use of a conservative scheme for criticality calculations is. The WLS 2 transport solution was exactly the same as the SAAF solution. This is yet another indicator that the WLS and SAAF are closely related, even with the use of the optional boundary condition Eq. (2.26). The WLS 1 solutions showed significantly larger errors than the WLS 2 solutions, which is interesting, since the boundary condition Eq. (2.27) showed better results

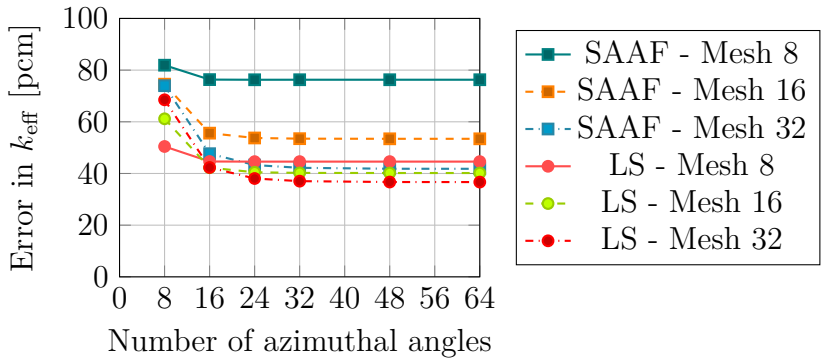

(a) Error in k_{eff}

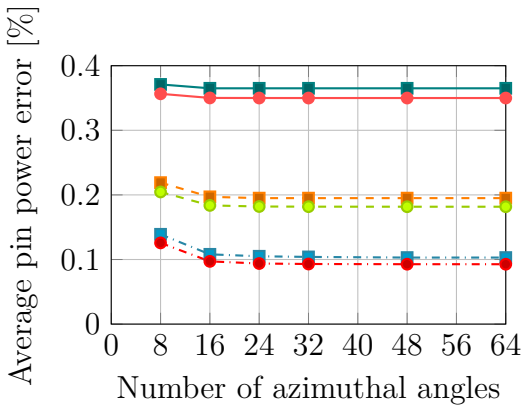

(b) Average pin power error

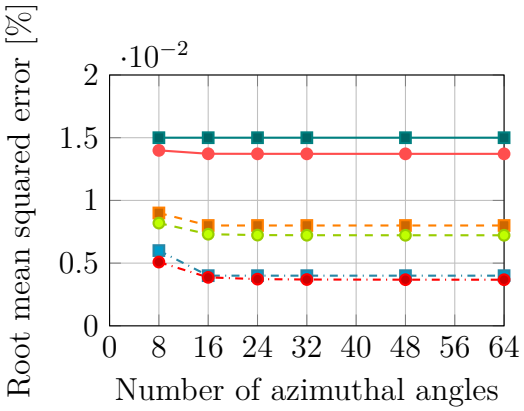

(c) Root mean squared error

Figure 4.24 Comparison of the results for the C5G7 benchmark for the LS and SAAF calculations.

for the one dimensional problems. An explanation is, that this boundary condition is not conservative. The one dimensional problems were source problems and not as sensitive to conservation as eigenvalue problems. The best result for all errors gave the SAAFτ scheme with $\zeta = 0.5$, even though no voids are present in the original benchmark.

The results for the NDA schemes were shown in the second part of Table 4.3. The use of the conservative NDA with the non-conservative LS scheme showed that the

Table 4.3 Comparison of the eigenvalue error and the pin power errors for the transport and NDA schemes with 4 polar and 32 azimuthal angles and on the coarsest mesh.

Scheme	k_{eff} [pcm]	AVG [%]	RMS [%]	MRE [%]	MAX [%]	PP1 [%]	PP2 [%]
LS 1	15777.423	8.177	0.329	11.391	30.113	12.051	3.797
LS 2	15880.916	8.354	0.336	11.640	30.847	12.345	4.255
WLS 1	371.210	0.557	0.026	0.680	6.752	0.299	2.679
WLS 2	87.741	0.400	0.016	0.539	1.661	0.608	1.123
SAAF	87.741	0.400	0.016	0.539	1.661	0.608	1.123
SAAFτ	52.115	0.249	0.010	0.350	1.178	0.433	0.195
NDA LS 1	51.930	0.381	0.015	0.490	1.695	0.447	1.653
NDA LS 2	52.682	0.380	0.015	0.488	1.613	0.444	1.662
NDA WLS 1	84.170	0.398	0.016	0.537	1.618	0.579	1.099
NDA WLS 2	87.740	0.400	0.016	0.539	1.661	0.608	1.123
NDA SAAF	87.741	0.400	0.016	0.539	1.661	0.608	1.123
NDA SAAFτ	52.115	0.249	0.010	0.350	1.178	0.433	0.195

NDA ensures conservation. Both NDA LS results were within a reasonable range of error, with the error in the eigenvalue the lowest for all schemes for LS 1. The pin power results however were more comparable to the results of the NDA using SAAF and WLS than to the LS transport results. The NDA SAAFτ scheme gave the smallest errors for pin powers. Again SAAF and WLS 2, this time with NDA, gave the same results. The NDA results for WLS 2, SAAF and SAAFτ were consistent with the corresponding transport solves. The errors for NDA WLS 1 were below the errors of NDA WLS 2, another indicator that the boundary condition of WLS 1 are non-conservative and the NDA forces conservation.

The comparison of the runtime for all schemes and the number of NDA iterations are shown in Table 4.4. The transport solver employed a non-linear PJNFK solver [28] to find the eigenvalue and not the source iterations algorithm and hence no iteration

Table 4.4 Comparison of the transport and NDA calculation time and the number of NDA iterations for the original C5G7 benchmark.

Scheme	Transport	NDA	
	Time [h]	Time [h]	Iterations [-]
LS 1	5.1	4.4	12
LS 2	5.2	4.7	12
WLS 1	4.5	4.7	12
WLS 2	4.5	4.1	11
SAAF	4.2	5.7	15
SAAFτ	4.8	5.2	15

count can be given. All calculations were performed on 3 nodes of INL's HPC cluster Falcon [1] with 24 cores per node. The calculation times for transport and NDA were comparable. It is curious, that SAAF and SAAFτ required more NDA iterations than all LS schemes, especially since SAAF and WLS should be almost the same equation and gave exactly the same result as shown in Table 4.3.

4.3.3 Modified C5G7 benchmark for voids

We modified the C5G7 benchmark to test the modifications for voids. For that the moderator was changed to graphite, and all guide tubes and the central fission chamber of each fuel element was converted into a void. To quantify the effect of single changes, calculations were also run with graphite moderator but no voids further denoted by the graphite case. The case with voids will be referenced as void case. The result of both graphite and void case were compared against PDT calculations provided by McGraw.

First the effect of the nonlinear diffusion coefficient, which is necessary for the void calculations, on the accuracy of the results was studied. For that the graphite case was calculated with the local and the non-local diffusion coefficient. The non-local

Table 4.5 Comparison of the local and the non-local diffusion coefficient on the eigenvalue error and the average and maximal pin power error for the C5G7 graphite case.

Scheme	k_{eff} error [pcm]		Avg. error [%]		Max. error [%]	
	local	non-local	local	non-local	local	non-local
NDA LS 1	69.994	71.814	0.063	0.064	0.808	0.791
NDA LS 2	70.024	71.104	0.063	0.064	0.815	0.820
NDA WLS 1	68.901	69.693	0.068	0.068	0.849	0.828
NDA WLS 2	68.653	68.653	0.068	0.068	0.869	0.869
NDA SAAF	68.653	68.653	0.068	0.068	0.869	0.869
NDA SAAFτ	17.316	17.316	0.071	0.071	0.520	0.520

diffusion coefficient had to be calculated with a separate calculation and the results were averaged for every material. This was required because on the fly calculation in the current Rattlesnake implementation used too much memory. Table 4.5 shows the comparison for the errors in the eigenvalue and the average and maximal pin power errors. The use of the non-local diffusion coefficient only affected the result if the NDA scheme was not consistent (NDA schemes LS 1, LS 2 and WLS 1). The reason for this is, that high-order and low-order solution for these schemes are not exactly the same, consequently the diffusion terms in Eqs. (3.10) and (3.11) do not cancel. Nevertheless, the introduced error was approximately 1 pcm or less than 0.1 % for the pin powers. However this might not be the case in voids, since the difference between the transport and the drift-diffusion solution can be larger. The consistent schemes showed no difference between the calculations using the local coefficient and the ones using the non-local diffusion coefficient. The remaining errors had the same behavior and hence are not further discussed.

After we established that the non-local diffusion coefficient has only a minimal effect on the non-consistent LS schemes, we proceeded to the case containing voids.

The introduction of the voids instead of graphite in all guide tubes and the central rod of each fuel element had only a small influence on the eigenvalue of the problem. The reference solution showed a difference of 234 pcm between the two cases. All absolute eigenvalues can be found in Table C.1. The comparison of the errors to the PDT solution are shown in Tables 4.6 and 4.7. Table 4.6 shows the error in eigenvalue and the average and maximal pin power errors. The error in the eigenvalue for the non-conservative LS transport schemes is surprisingly small compared to the large errors seen in the original benchmark (Table 4.3). We have no other explanation than error cancellation. This theory is supported by the large average and maximal pin power errors. These were significantly larger than the errors for the other schemes.

The WLS 1 transport scheme showed the largest error in the eigenvalue for both graphite and void case. The WLS 2 scheme, which is conservative for cases with sufficient large cross sections had only half the error in the eigenvalue than the WLS 1 scheme. Again, this large difference came only from the boundary conditions. The error increased with the introduction of voids. In voids, both WLS 1 and WLS 2 are non-conservative, which explains the higher error in k_{eff}. The average pin power error for both schemes were comparable and the maximum error was significantly less for the WLS 1 transport scheme. The best transport scheme was SAAFτ. It also did not show a significant increase in errors when voids were introduced into the problem.

The NDA schemes for LS and WLS are conservative even with geometry containing voids. This can clearly seen in the results for the error in k_{eff}. The LS schemes error in the eigenvalue was larger than the pure transport but the pin power errors are now comparable with the WLS solution. Again we see error cancellation for void case in k_{eff} for the LS schemes. The average pin power errors increase significantly, which can be seen in Figs. C.1 and C.2. While for the graphite case the error was limited to the pins close to the reflector region, in the void case large errors occurred in the central

Table 4.6 Errors in k_{eff} and the average and maximal error in the pin powers for the graphite (graphite moderator and no voids) and the void case (graphite moderator and voids) of the modified C5G7 benchmark.

Scheme	k_{eff} error [pcm]		Avg. error [%]		Max. error [%]	
	graphite	void	graphite	void	graphite	void
LS 1	2.638	45.447	0.420	0.495	2.081	2.220
LS 2	18.348	61.775	0.372	0.444	1.978	2.118
WLS 1	143.832	155.156	0.068	0.088	0.577	0.728
WLS 2	68.653	84.537	0.068	0.097	0.869	1.043
SAAFτ	17.316	13.268	0.071	0.075	0.520	0.476
NDA LS 1	71.814	36.478	0.064	0.123	0.791	0.466
NDA LS 2	71.104	35.854	0.064	0.120	0.820	0.461
NDA WLS 1	69.693	56.809	0.068	0.092	0.828	0.660
NDA WLS 2	68.653	55.401	0.068	0.090	0.869	0.695
NDA SAAFτ	17.316	13.268	0.071	0.075	0.520	0.476

Table 4.7 Root-Mean-Square (RMS) of the pin power errors and error in the maximal (PP1) and minimal pin power (PP2) for the graphite (graphite moderator and no voids) and the void case (graphite moderator and voids) of the modified C5G7 benchmark.

Scheme	RMS [%]		PP1 [%]		PP2 [%]	
	graphite	void	graphite	void	graphite	void
LS 1	0.017	0.020	0.267	0.049	0.159	0.073
LS 2	0.016	0.019	0.527	0.306	0.114	0.117
WLS 1	0.003	0.004	0.394	0.481	0.193	0.140
WLS 2	0.003	0.004	0.593	0.689	0.219	0.125
SAAFτ	0.003	0.003	0.355	0.314	0.224	0.035
NDA LS 1	0.003	0.005	0.540	0.276	0.241	0.247
NDA LS 2	0.003	0.005	0.560	0.293	0.238	0.244
NDA WLS 1	0.003	0.004	0.565	0.435	0.231	0.135
NDA WLS 2	0.003	0.004	0.593	0.459	0.219	0.125
NDA SAAFτ	0.003	0.003	0.355	0.314	0.224	0.035

fuel element. Note that for the error plots the scale is limited to 0.25 % to show the distribution of the errors better, the error in single fuel pins can be larger than this. The plots have the same orientation as Fig. 4.23. The WLS NDA schemes were, in contrast to the transport schemes, almost identical. Also for these schemes the error in k_{eff} decreased but the average error in the pin power increased. Figures C.3 and C.4 show that for the graphite cases the error was located in the pins close to the graphite reflector. For the void case these errors stretch further towards the center of the core. Additionally fuel elements close to a void tube showed larger errors than for the graphite case. These increases were smaller than for the LS cases. The NDA WLS 2 in problems with void is not fully consistent anymore.

The SAAFτ NDA is consistent even in the void case. This scheme showed the lowest errors from all schemes. Figure C.5 shows that in the void case the errors close to the reflector continued further inwards, however no increase in the center of the core can be seen.

To demonstrate, that the non-conservative methods have a large error, we resubstituted water as moderator instead of graphite. Using again two cases, the water case, with guiding and central tubes filled with water and the void2 case, in which the guiding and central tubes were void. The differences of the water case to the original benchmark calculations were that the fission chambers were replaced by water, the use of the non-local diffusion coefficient and a PDT reference obtained with the same mesh size and angular quadrature as for the graphite and both void cases. The results in Tables 4.8 and 4.9 show the large errors of the non-conservative schemes. Even the WLS 2 schemes, which is no-conservative only in the voids and near-voids, showed a large error in the eigenvalue. The remaining results are similar to the results with graphite moderator.

Table 4.10 compares the runtime for transport and NDA calculations as well as

Table 4.8 Errors in k_{eff} and the average and maximal error in the pin powers for the water (water moderator and no voids) and the void2 case (water moderator and voids) of the modified C5G7 benchmark.

Scheme	k_{eff} error [pcm]		Avg. error [%]		Max. error [%]	
	water	void2	water	void2	water	void2
LS 1	15487.829	16599.864	8.294	8.463	31.023	32.334
LS 2	15589.399	16702.573	8.474	8.631	31.698	33.012
WLS 1	294.139	388.241	0.559	0.612	6.573	6.573
WLS 2	16.420	147.175	0.470	0.435	2.594	2.080
SAAFτ	101.149	60.980	0.307	0.306	1.752	1.718
NDA LS 1	39.069	6.536	0.469	0.544	2.767	2.968
NDA LS 2	38.233	5.631	0.467	0.543	2.765	2.844
NDA WLS 1	12.694	86.984	0.469	0.542	2.560	2.683
NDA WLS 2	16.420	89.650	0.470	0.551	2.594	2.773
NDA SAAFτ	101.149	60.980	0.307	0.306	1.752	1.718

Table 4.9 Root-Mean-Square (RMS) of the pin power errors and error in the maximal (PP1) and minimal pin power (PP2) for the water (water moderator and no voids) and the void2 case (water moderator and voids) of the modified C5G7 benchmark.

Scheme	RMS [%]		PP1 [%]		PP2 [%]	
	water	void2	water	void2	water	void2
LS 1	0.334	0.341	11.761	13.355	3.705	5.386
LS 2	0.341	0.348	12.062	13.635	4.174	5.810
WLS 1	0.026	0.027	0.365	0.506	2.313	2.881
WLS 2	0.019	0.018	0.548	0.258	0.743	1.577
SAAFτ	0.013	0.013	0.354	0.286	0.091	0.028
NDA LS 1	0.019	0.022	0.222	0.410	1.897	1.057
NDA LS 2	0.019	0.022	0.219	0.408	1.907	1.067
NDA WLS 1	0.019	0.023	0.516	0.507	0.715	0.585
NDA WLS 2	0.019	0.023	0.548	0.572	0.743	0.594
NDA SAAFτ	0.013	0.013	0.354	0.286	0.091	0.028

Table 4.10 Comparison of the transport and NDA calculation time and the number of NDA iterations for graphite (graphite moderator and no voids) the void (graphite moderator and voids) case of the modified C5G7 benchmark.

Scheme	Transport [h]		NDA [h]		NDA Iterations	
	Graphite	Void	Graphite	Void	Graphite	Void
LS 1	4.3	4.1	4.4	4.4	11	11
LS 2	3.9	4.1	4.2	4.2	11	11
WLS 1	4.0	4.4	4.8	12.9	11	11
WLS 2	3.8	4.0	3.5	12.3	9	11
SAAFτ	4.1	4.0	5.0	4.8	14	14

the iteration count for the NDA. The runtime for all schemes was comparable expect for the NDA WLS schemes. These took significantly longer than the NDA LS and even the NDA SAAFτ, which had more iterations. The explanation for this much larger runtime of the NDA WLS schemes is the time it took to solve the high order system. The system of the WLS scheme is worse conditioned because of the large values of the weight function, the calculation used a maximum weight $w_{\max} = 1000\,\text{cm}$. This caused the high order system to be more difficult to solve and hence the solver needed more time to reach the required tolerance. Table 4.11 shows the increase of the runtime with increasing $w_{\max}$. The number of required NDA iterations stayed constant. The transport WLS schemes did not show this large increase in runtime, because they required only one transport solve compared to 11 for the NDA, even though the tolerance for transport one was much tighter.

It is also shown in Table 4.11 that the accuracy in k_{eff} decreased with increasing $w_{\max}$, but the average pin power error improves. This is again a case of error cancellation for the eigenvalue as seen already above. The average pin power error did not improve much for $w_{\max} > 10\,\text{cm}$. The distribution of the pin power errors is shown in Fig. C.6. In the plots an improvement can be seen up to $w_{\max} = 100\,\text{cm}$.

Table 4.11 Comparison of the accuracy and runtime for increasing WLS weight function limit $w_{\max}$ of the NDA WLS 1 scheme for the void case (graphite moderator and voids).

$w_{\max}$ [-]	k_{eff} [pcm]	AVG [%]	MRE [%]	MAX [%]	Runtime [h]	Iterations [-]
1	36.478	0.123	0.122	0.466	4.4	11
10	46.382	0.096	0.096	0.591	4.8	11
100	55.717	0.090	0.091	0.661	5.1	11
500	56.685	0.092	0.093	0.660	6.4	11
1000	56.809	0.092	0.094	0.660	12.9	11

For this maximum weight the runtime is still comparable to the NDA SAAFτ scheme. Rattlesnake includes the reflective boundary conditions in the system matrix and hence the WLS matrix becomes unsymmetrical. This prevents the use of a more efficient solver at the moment, the main advantage of the LS and WLS scheme.

5. CONCLUSIONS

We derived a weighted LS transport equations and showed that we can make this equation equivalent to the SAAF equation by deploying the right weight function. However, to be able to handle voids, a modified weight function and optional boundary conditions were used, which renders the equations equal only for sufficient large cross sections and the correct choice for the optional boundary conditions. Even if the weight function does not completely guarantee causality for the WLS equation, the results improved significantly. The resulting discretization of the WLS scheme is, in contrast to the SAAFτ scheme, symmetric positive definite in problems with voids.

We analyzed the limit for the weight function to obtain an optimal result. Optimal means acceptable accuracy with the least amount of computational cost. We demonstrated that the weight function can be limited between 100 and 1000 without significant loss of accuracy. We further showed with the C5G7 benchmark, that the limit 100 is preferable, since higher limits increase the computational costs significantly without further improving the accuracy.

Based on the WLS equation, we modified the NDA algorithm to be well defined in geometries containing voids. To close the equations, a nonlocal diffusion coefficient and a combined formulation for the current were used. These modifications ensure that the NDA remained efficient for optically thick problems while allowing optically thin regions. Furthermore, the modifications lead to a NDA formulation that is unconditionally stable with a well resolved non-local diffusion coefficient. If the calculation for the non-local diffusion coefficient does not resolve the problem, the result could have oscillations which degrade the convergence or can make the scheme unstable. The calculation of the non-local diffusion coefficient is a pure absorber

problem, which might require increased refinement than a base problem with highly diffusive regions. For scattering ratios less than one the acceleration is efficient, while for a pure scatter the acceleration degrades for optical very thick cells. Feathering the mesh at the interface moves this increase of the spectral radius to even thicker cells. However physical problems always have absorption and hence this limit is only theoretical.

The NDA results for the WLS showed non-constant behavior in void regions for slab geometries. We showed that this scalar flux solution is conservative and within the solution space of the drift-diffusion equation. Improved accuracy of the drift vector does not ameliorate the error in the void region, since it is caused by the interface condition. We proved, that allowing a discontinuity at the interface eliminates the non-constant behavior. Appropriately introducing discontinuities in large and complicated geometries is extremely difficult and a topic for another study.

We performed a study on pure absorber problems even though no NDA iterations are required because the NDA scheme enforces conservation. For these problems the diffusion coefficient is a free parameter. Any value can be chosen and a solution can be obtained. In problems with scattering, where acceleration is required, it is not a free parameter, because it can make the iteration scheme unstable. The scalar flux solution in the void for the NDA WLS is affected by the diffusion coefficient. The artificial diffusion coefficient, which is equivalent to upwinding in the void region, gave the best solution. However, the iterative convergence properties of this diffusion coefficient were not tested. The solution for the non-local diffusion coefficient was close to the one of the artificial diffusion coefficient, making it an acceptable choice with proven good iterative properties.

The modified NDA scheme with non-local diffusion coefficient and the combined formulation of currents was fully implemented in Rattlesnake. A modified C5G7

benchmark was used to test the new NDA scheme on a more complicated problem with voided regions. The comparison to PDT and NDA SAAFτ showed, that the results are reasonable accurate. While the SAAFτ NDA scheme was comparable in some cases or slightly better in others, it lacks the symmetric-positive definite properties of the NDA WLS scheme. Thus the NDA WLS scheme can use the conjugate-gradient method, which requires the storage of only three solutions vectors. Compared to GMRES, which can require an arbitrary number of solutions vectors or a or restarts with degraded convergence properties, this gives the NDA WLS scheme an enormous advantage regarding memory. Sadly we could not exploit these advantages since Rattlesnake currently does not support SPD matrices.

5.1 Further work

Based on this work, we propose to continue testing the scheme with more complicated geometries. To do so, Rattlesnake must be adapted to take advantage of the symmetric-positive definite properties of the WLS discretization. This would allow to run larger and more refined benchmark problems.

REFERENCES

[1] *Idaho National Laboratory | TOP500 Supercomputer Sites*, https://www.top500.org/site/47650, March 2017.

[2] R. T. Ackroyd, *Least-squares derivation of extremum and weighted-residual methods for equations of reactor physics—I. The first-order Boltzmann equation and a first-order initial-value equation*, Annals of Nuclear Energy **10** (1983), no. 2, 65–99.

[3] R. T. Ackroyd, J. G. Issa, and N. S. Riyait, *Treatment of voids in finite element transport methods*, Progress in Nuclear Energy, Progress in Nuclear Energy (UK), vol. 18, 18-20 Sept. 1986, pp. 85–9.

[4] M. L. Adams, *Even-parity finite-element transport methods in the diffusion limit*, Progress in Nuclear Energy, Progress in Nuclear Energy (UK), vol. 25, 1991, pp. 159–98.

[5] Marvin L. Adams and Edward W. Larsen, *Fast iterative methods for discrete-ordinates particle transport calculations*, Progress in Nuclear Energy **40** (2002), no. 1, 3–159.

[6] Michael P. Adams, Marvin L. Adams, W. Daryl Hawkins, Timmie Smith, Lawrence Rauchwerger, Nancy M. Amato, Teresa S. Bailey, and Robert D. Falgout, *Provably optimal parallel transport sweeps on regular grids*, International Conference on Mathematics and Computational Methods Applied to Nuclear Science and Engineering, M and C 2013, vol. 4, American Nuclear Society, 5 - 9 May 2013, pp. 2535–2553.

[7] Michael P. Adams, Marvin L. Adams, Carolyn N. McGraw, Andrew T. Till, and Teresa S. Bailey, *Provably optimal parallel transport sweeps with non-contiguous partitions*, Mathematics and Computations, Supercomputing in Nuclear Applications and Monte Carlo International Conference, M and C+SNA+MC 2015, vol. 2, American Nuclear Society, 19 - 23 April 2015, pp. 1218–1236.

[8] R. E. Alcouffe, *Diffusion Synthetic Acceleration Methods for the Diamond-Differenced Discrete-Ordinates Equations*, Nuclear Science and Engineering **64** (1977), no. 2, 344–355.

[9] Dmitriy Y. Anistratov and Vladimir Ya. Gol'din, *Multilevel quasidiffusion methods for solving multigroup neutron transport k-eigenvalue problems in one-dimensional slab geometry*, Nuclear Science and Engineering **169** (2011), no. 2, 111–132.

[10] Yousry Azmy and Enrico Sartori, *Nuclear Computational Science*, Springer Netherlands, Dordrecht, 2010 (en).

[11] Alexander N. Brooks and Thomas J. R. Hughes, *Streamline upwind/Petrov-Galerkin formulations for convection dominated flows with particular emphasis on the incompressible Navier-Stokes equations*, Computer Methods in Applied Mechanics and Engineering **32** (1982), no. 1, 199–259.

[12] C. R. E. de Oliveira, M. D. Eaton, A. P. Umpleby, and C. C. Pain, *Finite element-spherical harmonics solutions of the 3D Kobayashi benchmarks with ray-tracing void treatment*, Progress in Nuclear Energy **39** (2001), no. 2, 243–61.

[13] H. De Sterck, T. Manteuffel, S. McCormick, K. Miller, J. Pearson, J. Ruge, and G. Sanders, *Smoothed Aggregation Multigrid for Markov Chains*, SIAM Journal on Scientific Computing **32** (2010), no. 1, 40–61.

[14] Mark D. DeHart, Javier Ortensi, Benjamin Baker, Frederick N. Gleicher, Yaqi Wang, and Sebastian Schunert, *Research in support of TREAT kinetics calculations using Rattlesnake/BISON coupling within MAMMOTH*, Physics of Reactors 2016: Unifying Theory and Experiments in the 21st Century, PHYSOR 2016, vol. 3, American Nuclear Society, 1-5 May 2016, pp. 1801–1814.

[15] Clif Drumm, Wesley Fan, Andrew Bielen, and Jeffrey Chenhall, *Least-squares finite-element algorithms in the SCEPTRE radiation transport code*, Ann Arbor **1001** (2011), 48109–2104.

[16] P. Feautrier, *Sur la resolution numerique de l'equation de transfert.*, Comptes Rendus Academie des Sciences (serie non specifiee) **258** (1964), 3189.

[17] Derek Gaston, Chris Newman, Glen Hansen, and Damien Lebrun-Grandie, *MOOSE: A parallel computational framework for coupled systems of nonlinear equations*, Nuclear Engineering and Design **239** (2009), no. 10, 1768–1778.

[18] E. M. Gelbard and L. A. Hageman, *The Synthetic Method as Applied to the* S_n *Equations*, Nuclear Science and Engineering **37** (1969), no. 2, 288–298.

[19] Christopher John Gesh, *Finite element methods for second order forms of the transport equation*, Ph.D. thesis, Texas A&M University, 1999.

[20] Samuel Glasstone, Milton C. Edlund, Clifford Beck, and Raymond L. Murray, *The Elements of Nuclear Reactor Theory*, American Journal of Physics **21** (1953), no. 5, 396–397.

[21] V. Ya. Gol'din, *A quasi-diffusion method of solving the kinetic equation*, USSR Computational Mathematics and Mathematical Physics **4** (1964), no. 6, 136–149 (en).

[22] Hai-tao Ju, Hong-chun Wu, Dong Yao, and Chun-yu Xian, *Least-squares finite-element SN method for solving three-dimensional transport equation*, Annals of Nuclear Energy **34** (2007), no. 6, 527–32.

[23] Jon Hansen, Jacob R. Peterson, Jim E. Morel, Jean C. Ragusa, and Yaqi Wang, *A least-squares transport equation compatible with voids*, Journal of Computational and Theoretical Transport **43** (2014), no. 1-7, 374–401.

[24] W. D. Hawkins, T. Smith, M. P. Adams, L. Rauchwerger, N. Amato, and M. L. Adams, *Efficient massively parallel transport sweeps*, ANS Annual Winter Meeting, Transactions of the American Nuclear Society (USA), vol. 107, American Nuclear Society, 11-15 Nov 2012, pp. 477–81.

[25] V. E. Henson and U. M. Yang, *BoomerAMG: A parallel algebraic multigrid solver and preconditioner*, Applied Numerical Mathematics **41** (2000), no. 1, 155–77.

[26] Eric Jones, Travis Oliphant, Pearu Peterson, and others, *SciPy.org*, https://scipy.org/, 2001 - 2017.

[27] Carl Klahr, *Limitations of Multigroup Calculations*, Nuclear Science and Engineering **1** (1956), no. 4, 253–267.

[28] D. A. Knoll, H. Park, and C. Newman, *Acceleration of* k*-Eigenvalue/Criticality Calculations Using the Jacobian-Free Newton-Krylov Method*, Nuclear Science and Engineering **167** (2011), no. 2, 133–140.

[29] H. J. Kopp, *Synthetic Method Solution of the Transport Equation*, Nuclear Science and Engineering **17** (1963), no. 1, 65–74.

[30] V. S. Anil Kumar, M. V. Marathe, S. Parthasarathy, A. Srinivasan, and S. Zust, *Provable Algorithms for Parallel Sweep Scheduling on Unstructured Meshes*, 19th

IEEE International Parallel and Distributed Processing Symposium, April 2005, pp. 26–26.

[31] Vincent M. Laboure, Yaqi Wang, and Mark D. DeHart, *Least-Squares PN Formulation of the transport equation using self-adjoint-angular-flux consistent boundary conditions*, Physics of Reactors 2016: Unifying Theory and Experiments in the 21st Century, PHYSOR 2016, vol. 5, American Nuclear Society, 1-5 May 2016, pp. 3376–3385.

[32] Vincent Matthieu Laboure, *Improved fully-implicit spherical harmonics methods for first and second order forms of the transport equation using Galerkin Finite Element*, Ph.D. thesis, Texas A&M University, 2016.

[33] Edward W Larsen, J. E Morel, and Warren F Miller Jr., *Asymptotic solutions of numerical transport problems in optically thick, diffusive regimes*, Journal of Computational Physics **69** (1987), no. 2, 283–324.

[34] Edward W. Larsen, Jim E. Morel, and Jijie Lou, *"Nonlocal" Diffusion Coefficients for Neutronic Systems Containing Voided Subregions*, M&C 2017 - International Conference on Mathematics & Computational Methods Applied to Nuclear Science & Engineering, 16-20 April 2017.

[35] Edward W. Larsen and Travis J. Trahan, *2-D anisotropic diffusion in optically thin channels*, 2009 ANS Annual Meeting and Embedded Topical Meetings: Risk Management and 2009 Young Professionals Congress, November 15, 2009 - November 19, 2009, Transactions of the American Nuclear Society, vol. 101, American Nuclear Society, 2009, pp. 387–389.

[36] K. D. Lathrop, *Ray Effects in Discrete Ordinates Equations*, Nuclear Science and Engineering **32** (1968), no. 3, 357–369.

[37] ———, *Remedies for Ray Effects*, Nuclear Science and Engineering **45** (1971), no. 3, 255–268.

[38] E. E. Lewis, *Much ado about nothing: Response matrices for void regions*, Annals of Nuclear Energy **31** (2004), no. 17, 2025–37.

[39] ———, *Fundamentals of nuclear reactor physics*, Academic Press, Amsterdam ; Boston, 2008, OCLC: ocn150330792.

[40] Thomas A. Manteuffel, Luke N. Olson, Jacob B. Schroder, and Ben S. Southworth, *A Root-Node Based Algebraic Multigrid Method*, arXiv:1610.03154 [math] (2016).

[41] G. I. Marchuk and Viacheslav Ivanovich Lebedev, *Numerical methods in the theory of neutron transport*, rev. 2nd ed ed., Harwood, Chur, Switzerland ; New York, 1986 (eng), OCLC: 13585064.

[42] Carolyn N. McGraw, Marvin L. Adams, W. Daryl Hawkins, Michael P. Adams, and Timmie Smith, *Accuracy of the linear discontinuous Galerkin method for 3D reactor analysis with resolved fuel pins*, Mathematics and Computations, Supercomputing in Nuclear Applications and Monte Carlo International Conference, M and C+SNA+MC 2015, vol. 4, American Nuclear Society, 19 - 23 April 2015, pp. 3155–3168.

[43] M. M. Miften and E. W. Larsen, *A symmetrized quasi-diffusion method for solving multidimensional transport problems*, 1992 Winter Meeting. International Conference on Fifty Years of Controlled Nuclear Chain Reaction: Past, Present and Future (Papers in Summary Form Only Received), 15-20 Nov. 1992, Trans. Am. Nucl. Soc. (USA), vol. 66, 1992, pp. 227–9.

[44] ———, *A symmetrized quasidiffusion method for solving transport problems in multidimensional geometries*, Proc. ANS Topical Meeting, Mathematical Methods and Supercomputing in Nuclear Applications, M&C + SNA (Karlsruhe, Germany), vol. 1, 1993, pp. 707–717 (English).

[45] W. F. Miller Jr. and Wm H. Reed, *Ray-Effect Mitigation Methods for Two-Dimensional Neutron Transport Theory*, Nuclear Science and Engineering **62** (1977), no. 3, 391–411.

[46] Warren F. Miller Jr., *Analysis of the finite differenced, even-parity, discrete ordinates equations in slab geometry*, Nuclear Science and Engineering **108** (1991), no. 3, 247–266.

[47] J. E. Morel and J. M. McGhee, *A self-adjoint angular flux equation*, Nuclear Science and Engineering **132** (1999), no. 3, 312–25.

[48] J. E. Morel, T. A. Wareing, R. B. Lowrie, and D. K. Parsons, *Analysis of Ray-Effect Mitigation Techniques*, Nuclear Science and Engineering **144** (2003), no. 1, 1–22.

[49] J. E. Morel, J. S. Warsa, and K. G. Budge, *Alternative Generation of Non-Local Diffusion Tensors*, Research memo, Texas A&M University, 2010.

[50] Jim E. Morel, *A Non-Local Diffusion Theroy*, Research Report LA-UR-07-5257, Los Alamos National Laboratory, NM, 2007.

[51] H. Park, D. A. Knoll, and C. K. Newman, *Nonlinear acceleration of transport criticality problems*, Nuclear Science and Engineering **172** (2012), no. 1, 52–65.

[52] Shawn D. Pautz, *An Algorithm for Parallel* S_n *Sweeps on Unstructured Meshes*, Nuclear Science and Engineering **140** (2002), no. 2, 111–136.

[53] Jacob R. Peterson, Hans R. Hammer, Jim E. Morel, Jean C. Ragusa, and Yaqi Wang, *Conservative nonlinear diffusion acceleration applied to the unweighted least-squares transport equation in MOOSE*, Mathematics and Computations, Supercomputing in Nuclear Applications and Monte Carlo International Conference, M and C+SNA+MC 2015, April 19, 2015 - April 23, 2015, vol. 1, American Nuclear Society, 2015, pp. 636–648.

[54] G. C. Pomraning and M. Clark, Jr., *The variational method applied to the monoenergetic boltzmann equation. Part II*, Nuclear Science and Engineering **16** (1963), no. 2, 155–164.

[55] W. H. Reed, *The Effectiveness of Acceleration Techniques for Iterative Methods in Transport Theory*, Nuclear Science and Engineering **45** (1971), no. 3, 245–254.

[56] Paul Reuss, *Neutron physics*, EDP Sciences, Les Ulis, France, 2008 (English), OCLC: 262519076.

[57] Yousef Saad, *Iterative Methods for Sparse Linear Systems, Second Edition*, 2 edition ed., Society for Industrial and Applied Mathematics, Philadelphia, April 2003 (English).

[58] Richard Sanchez, Cristian Rabiti, and Yaqi Wang, *Nonlinear acceleration of a continuous finite element discretization of the self-adjoint angular flux form of the transport equation*, Nuclear Science and Engineering **175** (2013), no. 3, 213–226.

[59] Sebastian Schunert, Hans R. Hammer, Jijie Lou, Yaqi Wang, Javier Ortensi, Frederick N. Gleicher, Benjamin Baker, Mark D. DeHart, and Richard C. Martineau, *Using Directional Diffusion Coefficients for Nonlinear Diffusion Acceleration of the First Order S_N Equations in Near-Void Regions*, ANS Winter Meeting (Las Vegas, NV), November 2016.

[60] Sebastian Schunert, Yaqi Wang, Frederick Gleicher, Javier Ortensi, Benjamin Baker, Vincent Laboure, Congjian Wang, Mark DeHart, and Richard Martineau, *A flexible nonlinear diffusion acceleration method for the SN transport equations discretized with discontinuous finite elements*, Journal of Computational Physics **338** (2017), 107–136.

[61] Sebastian Schunert, Yaqi Wang, Javier Ortensi, Frederick Gleicher, Benjamin Baker, Mark DeHart, and Richard Martineau, *A flexible nonlinear diffusion acceleration method for the first order eigenvalue SN equations discretized with discontinuous FEM*, Physics of Reactors 2016: Unifying Theory and Experiments in the 21st Century, PHYSOR 2016 (Sun Valley, ID), vol. 5, American Nuclear Society, 1-5 May 2016, pp. 3365–3375.

[62] Sebastian Schunert, Yaqi Wang, Javier Ortensi, Frederick N. Gleicher, Mark D. DeHart, and Richard C. Martineau, *A High-Order Nonlinear Diffusion Acceleration for the SN Equations Discretized with the Discontinuous FEM I: Theory and Numerical Results*, 2015 ANS WinterMeeting and Nuclear Techhnology Expo (Washington, DC), November 2015.

[63] ———, *A High-Order Nonlinear Diffusion Acceleration for the SN Equations Discretized with the Discontinuous FEM II: Fourier Analysis*, November 2015.

[64] Jonathan Richard Shewchuk, *Triangle: Engineering a 2D quality mesh generator and Delaunay triangulator*, Applied Computational Geometry towards Geometric Engineering, Springer, 1996, pp. 203–222.

[65] K. S. Smith, *Nodal method storage reduction by nonlinear iteration*, 1983 Annual Meeting of the American Nuclear Society, 12-16 June 1983, Trans. Am. Nucl. Soc. (USA), vol. 44, 1983, pp. 265–6.

[66] M. A. Smith, E. E. Lewis, and Byung-Chan Na, *Benchmark on deterministic 2-D MOX fuel assembly transport calculationswithout spatial homogenization*, Progress in Nuclear Energy **45** (2004), no. 2, 107–118.

[67] Weston M. Stacey, *Nuclear reactor physics*, 2nd completely revised and enlarged ed., Wiley-VCH, Weinheim, 2007.

[68] Travis J. Trahan and Edward W. Larsen, *3-D Anisotropic Neutron Diffusion in Optically Thick Media with Optically Thin Channels*, Proc. Intl. Conf. on Math. and Comput. Methods Applied to Nucl. Sci. Eng.(M&C 2011), Rio de Janeiro, Brazil, May 8, vol. 12, 2011.

[69] Todd James Urbatsch, *Iterative acceleration methods for Monte Carlo and deterministic criticality calculations*, Los Alamos National Laboratory (1995).

[70] V. S. Vladimirov, *Mathematical problems in the one-velocity theory of particle transport*, vol. 61, Atomic Energy of Canada Limited Chalk River„ Ontario, 1963.

[71] Yaqi Wang, *Adaptive mesh refinement solution techniques for the multigroup SN transport equation using a higher-order discontinuous finite element method*, Ph.D. thesis, Texas A&M University, 2009.

[72] ———, *Nonlinear diffusion acceleration for the multigroup transport equation discretized with SN and continuous FEM with Rattlesnake*, International Conference on Mathematics and Computational Methods Applied to Nuclear Science and Engineering, M and C 2013, vol. 4, American Nuclear Society, 5-9 May 2013, pp. 2649–2665.

[73] Yaqi Wang, Mark D. DeHart, Derek R. Gaston, Frederic N. Gleicher, Richard C. Martineau, Javier Ortensi, John W. Peterson, and Sebastian Schunert, *Convergence study of rattlesnake solutions for the two-dimensional C5G7 mox benchmark*,

Mathematics and Computations, Supercomputing in Nuclear Applications and Monte Carlo International Conference, M and C+SNA+MC 2015, vol. 4, American Nuclear Society, 19 - 23 April 2015, pp. 2881–2892.

[74] Yaqi Wang and Jean C. Ragusa, *A high-order discontinuous Galerkin method for the SN transport equations on 2D unstructured triangular meshes*, Annals of Nuclear Energy **36** (2009), no. 7, 931–939.

[75] Yaqi Wang, Sebastian Schunert, Mark DeHart, Richard Martineau, and Weixiong Zheng, *Hybrid with Lagrange multiplier and upwinding for the multiscale transport capability in Rattlesnake*, Progress in Nuclear Energy (2017).

[76] Yaqi Wang, Hongbin Zhang, and Richard C. Martineau, *Diffusion Acceleration Schemes for Self-Adjoint Angular Flux Formulation with a Void Treatment*, Nuclear Science and Engineering **176** (2014), no. 2, 201–225.

[77] Jeffrey Willen, H. Park, and William Taitano, *Applying nonlinear diffusion acceleration to the neutron transport k-eigenvalue problem with anisotropic scattering*, Nuclear Science and Engineering **181** (2015), no. 3, 351–360.

[78] Jeffrey Willert, H. Park, and William Taitano, *Applying nonlinear diffusion acceleration to fixed-source problems with anisotropic scattering*, 18th Topical Meeting of the Radiation Protection and Shielding Division of ANS, RPSD 2014 (Knoxville), American Nuclear Society, 2014, September 14 - 18, pp. 196–199.

[79] Akio Yamamoto, Masato Tabuchi, Naoki Sugimura, Tadashi Ushio, and Masaaki Mori, *Derivation of Optimum Polar Angle Quadrature Set for the Method of Characteristics Based on Approximation Error for the Bickley Function*, Journal of Nuclear Science and Technology **44** (2007), no. 2, 129–136.

[80] Weixiong Zheng, *Least-Squares and other Residual Based Techniques for Radiation Transport Calculations*, Dissertation, Texas A&M University, College Station, TX, December 2016.

APPENDIX A

HETEROGENEOUS FOURIER ANALYSIS RESULTS

A.1 Local Diffusion Coefficient

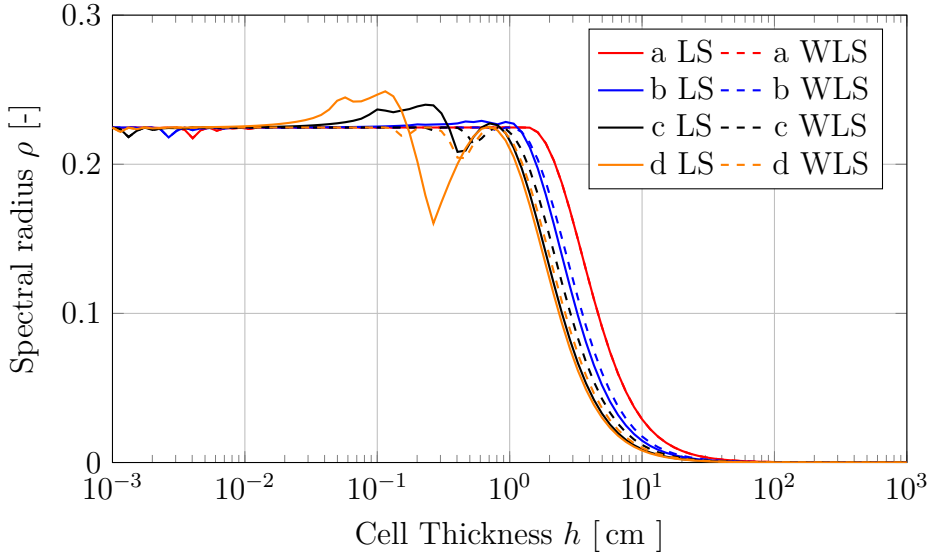

(a) Eddington drift vector

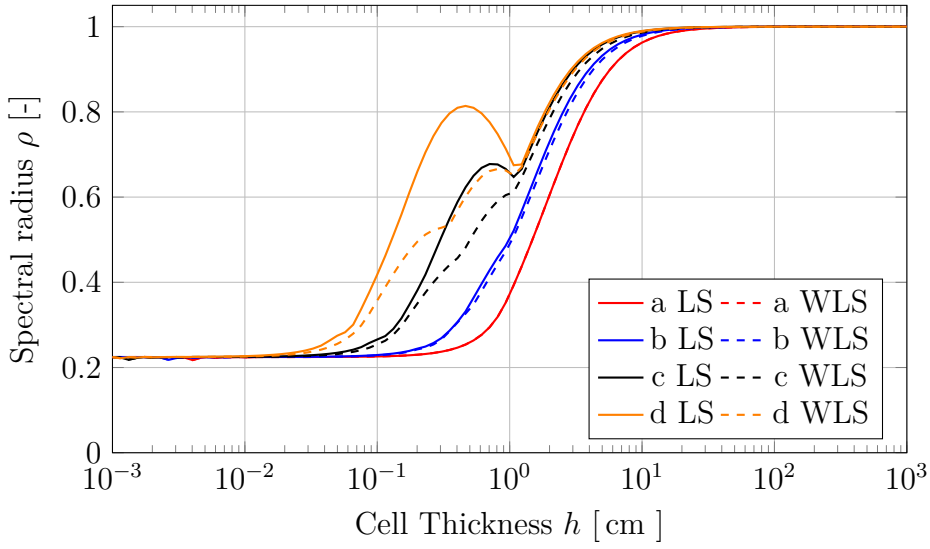

(b) Current drift vector

Figure A.1 Spectral radii for test cases 1 (Table 3.1) for the different NDA schemes with LS and WLS high order transport equation using the local diffusion coefficient.

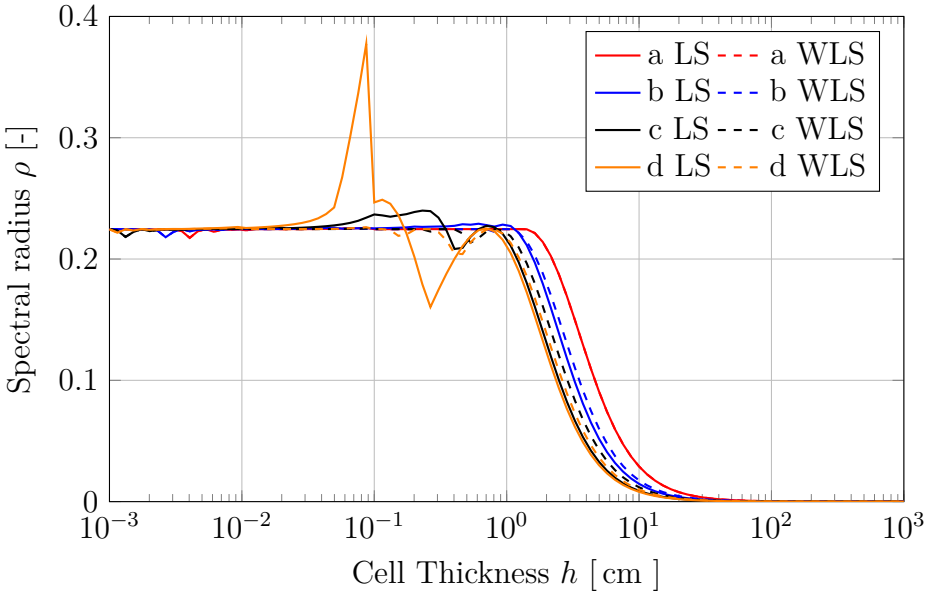

(c) Combined drift vector

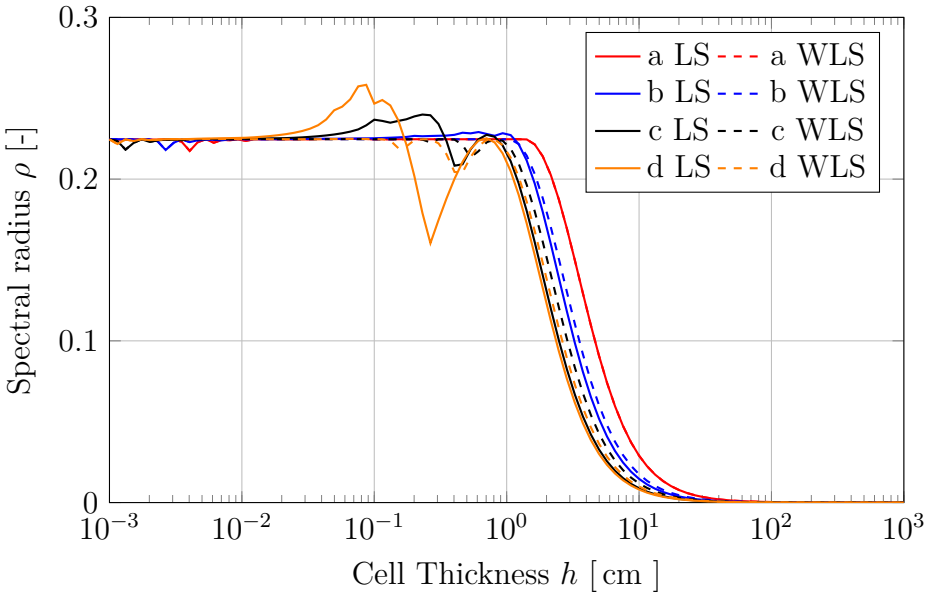

(d) τ drift vector

Figure A.1 Continued.

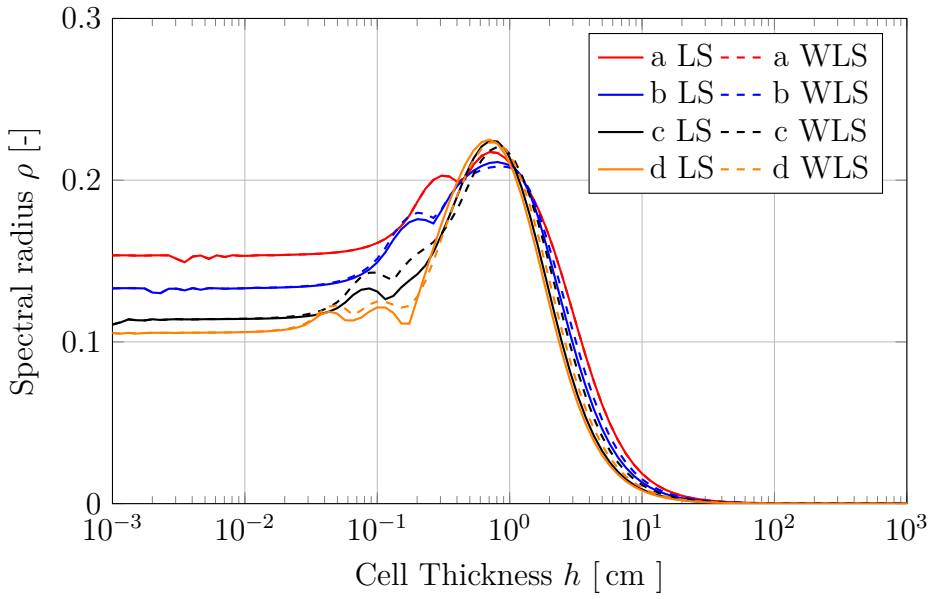

(a) Eddington drift vector

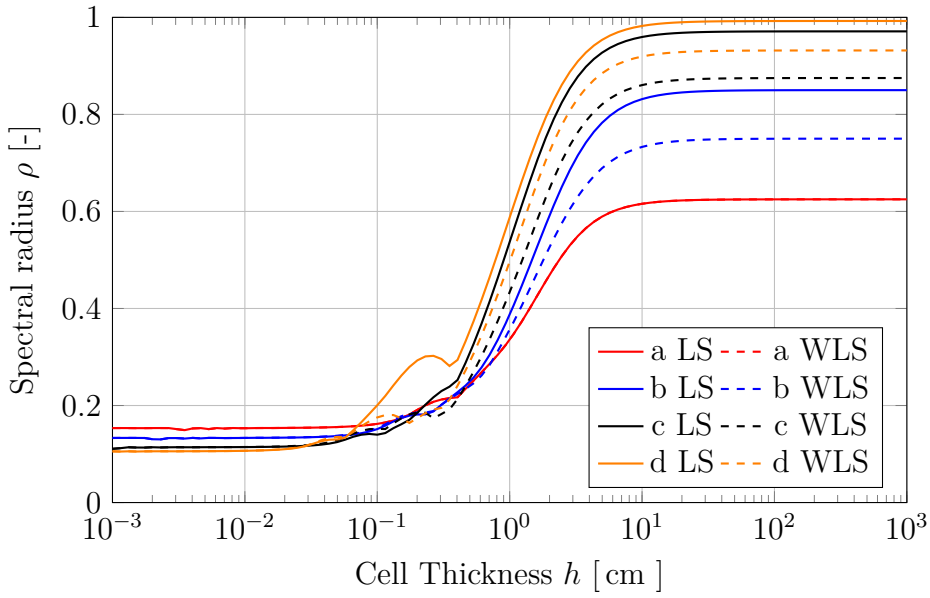

(b) Current drift vector

Figure A.2 Spectral radii for test cases 2 (Table 3.2) for the different NDA schemes with LS and WLS high order transport equation using the local diffusion coefficient.

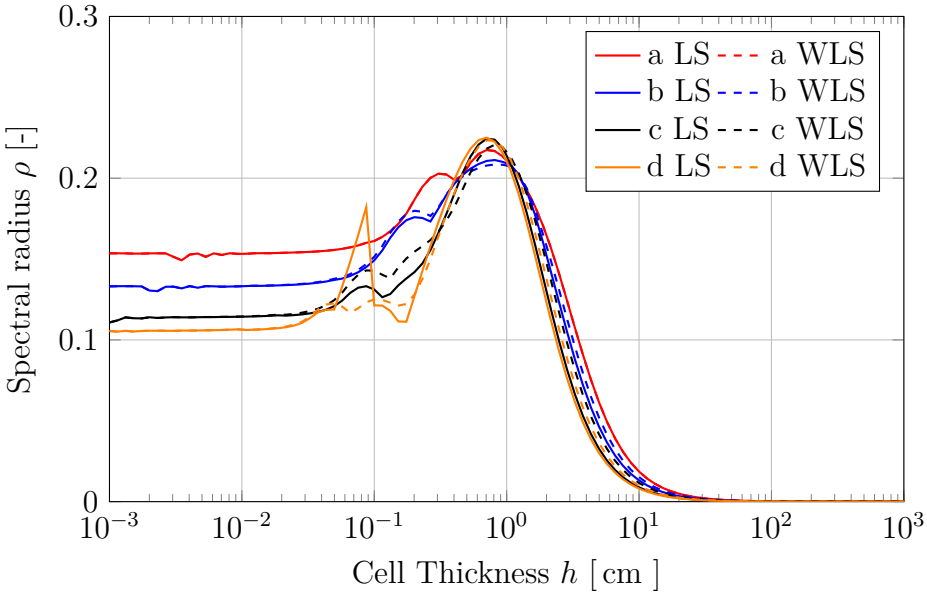

(c) Combined drift vector

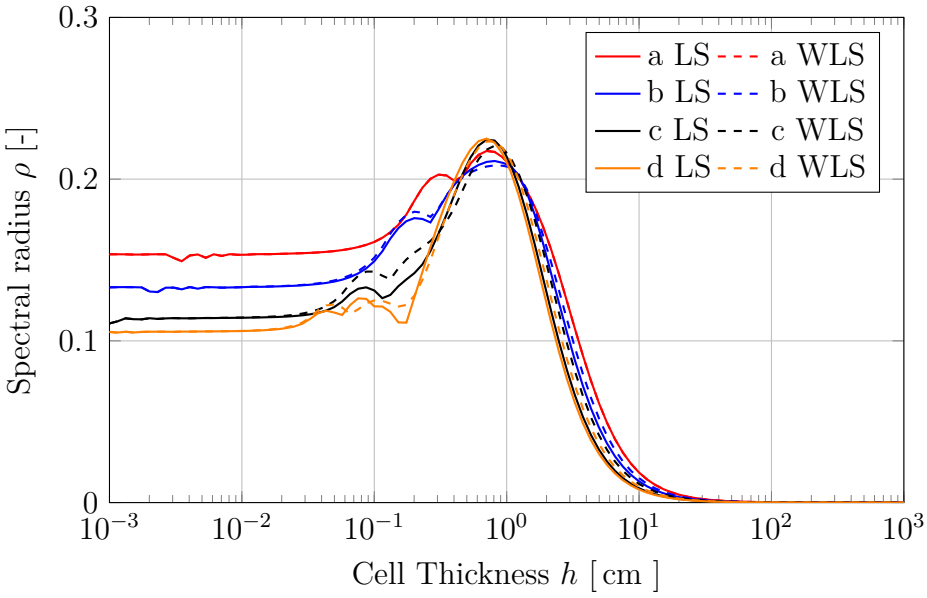

(d) τ drift vector

Figure A.2 Continued.

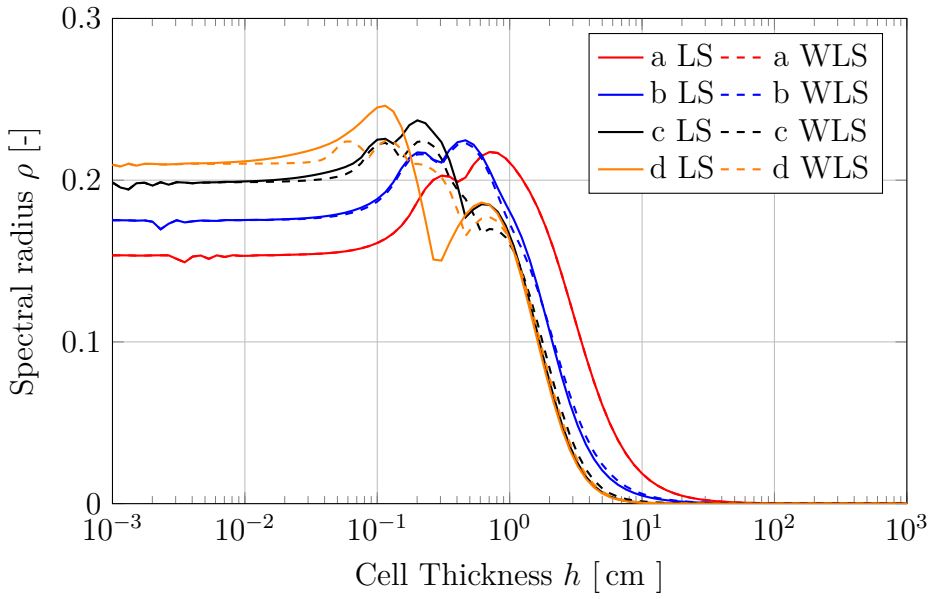

(a) Eddington drift vector

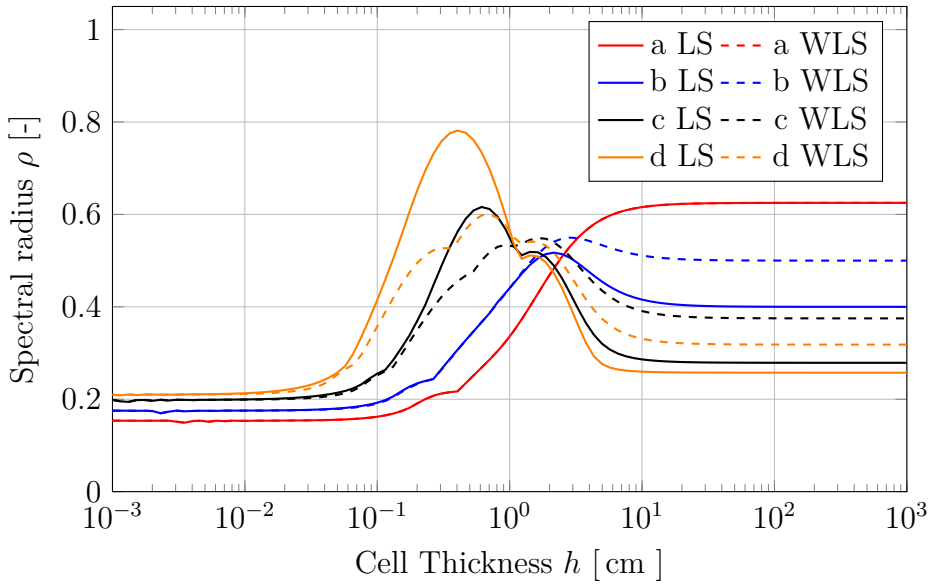

(b) Current drift vector

Figure A.3 Spectral radii for test cases 3 (Table 3.3) for the different NDA schemes with LS and WLS high order equation transport using the local diffusion coefficient.

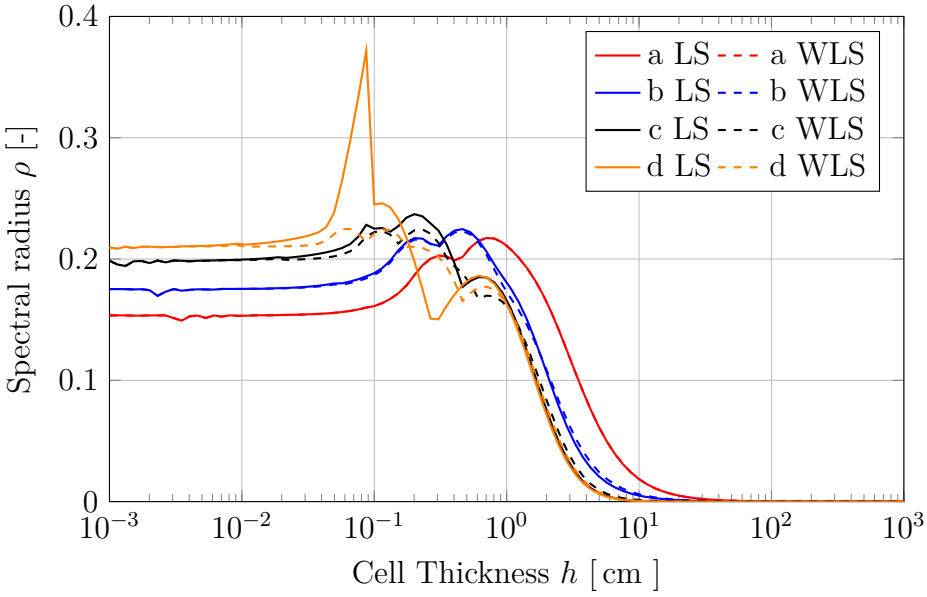

(c) Combined drift vector

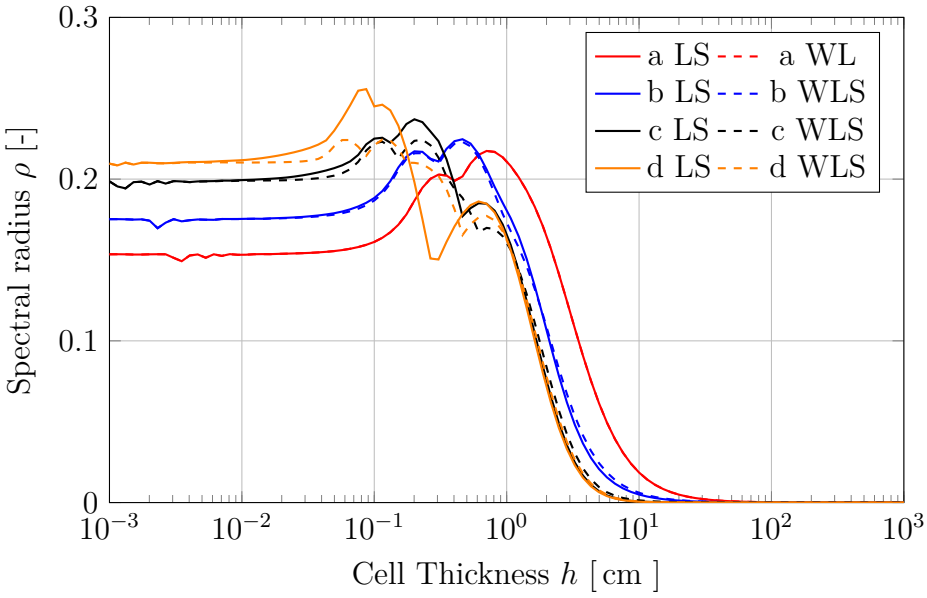

(d) τ drift vector

Figure A.3 Continued.

A.2 Non-local Diffusion Coefficient

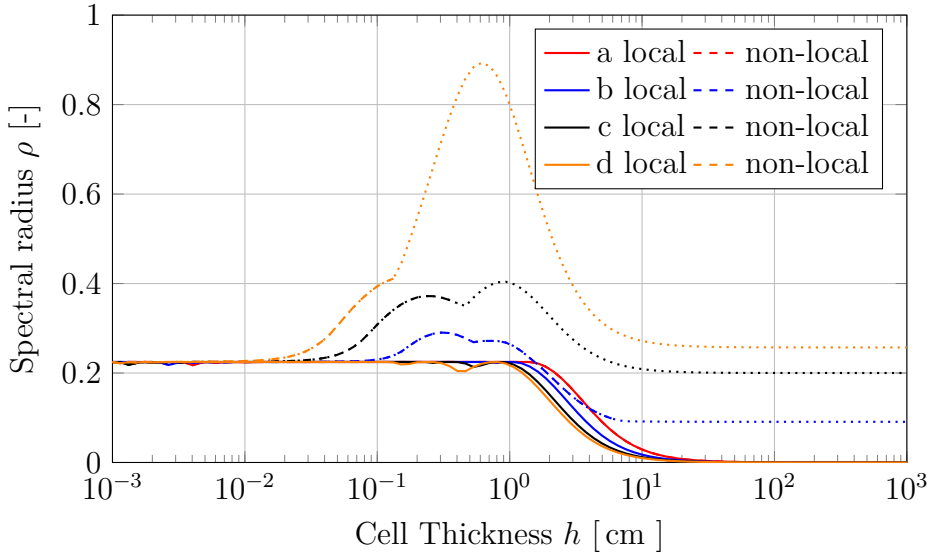

(a) Eddington drift vector

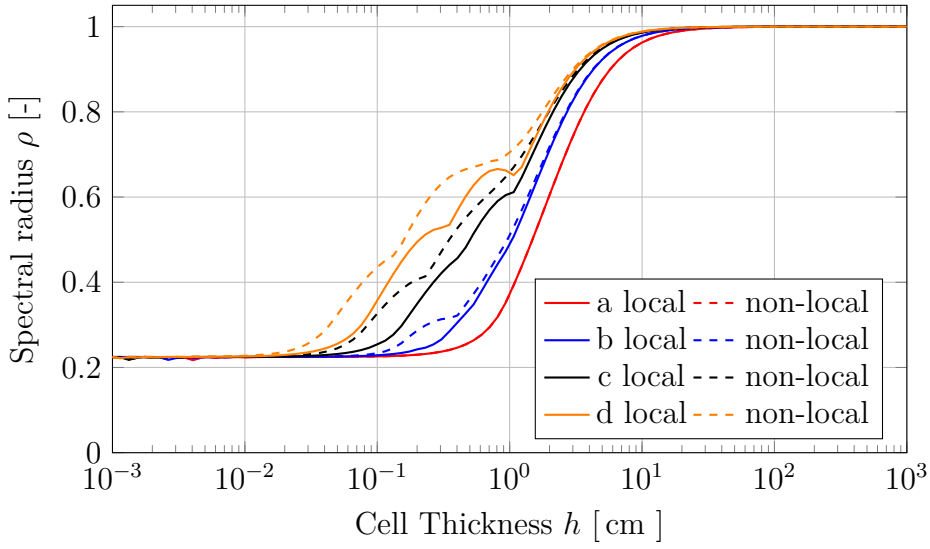

(b) Current drift vector

Figure A.4 Spectral radii for test cases 1 (Table 3.1) for the different NDA schemes with WLS high order equation using the local and non-local diffusion coefficient.

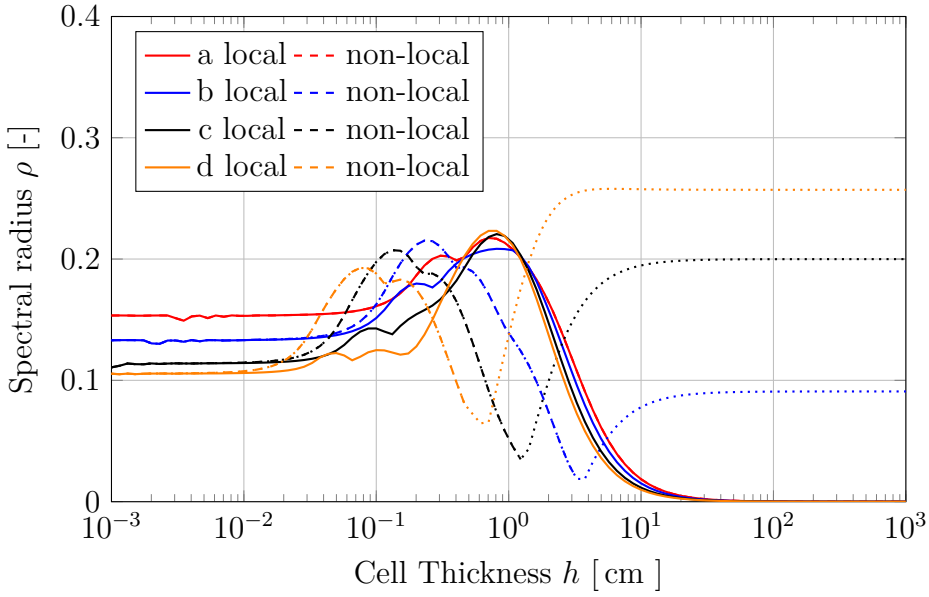

(a) Eddington drift vector

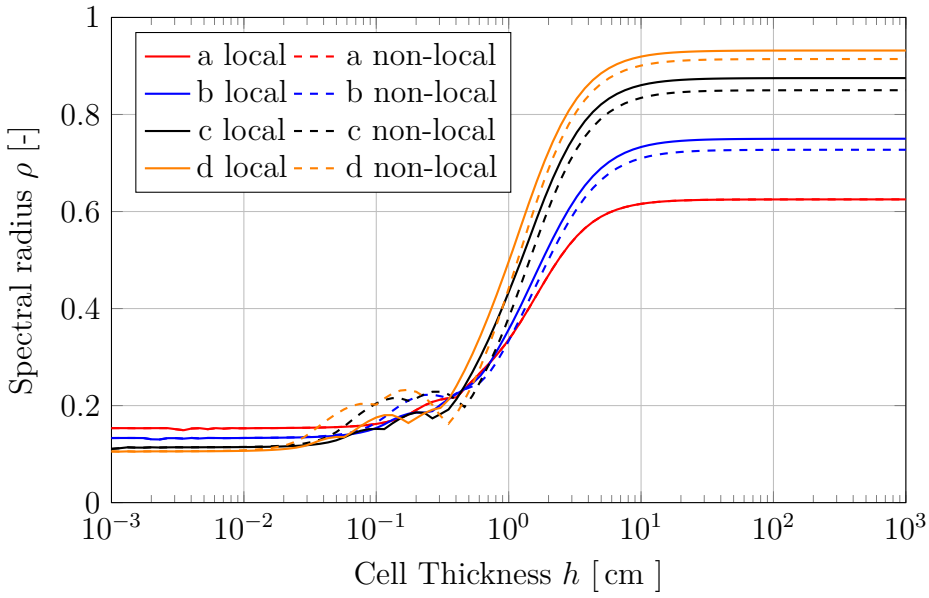

(b) Current drift vector

Figure A.5 Spectral radii for test cases 2 (Table 3.2) for the different NDA schemes with WLS high order equation using the local and non-local diffusion coefficient.

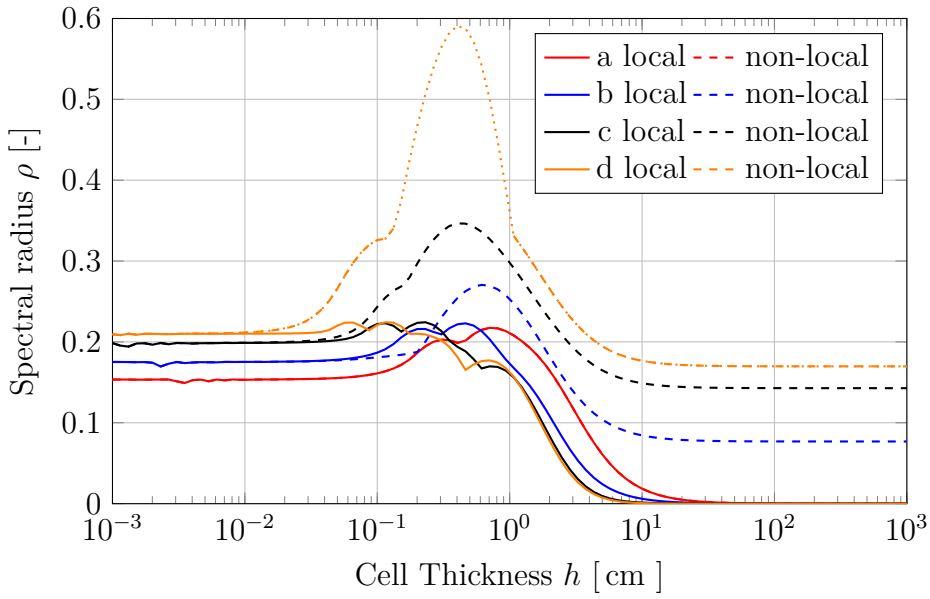

(a) Eddington drift vector

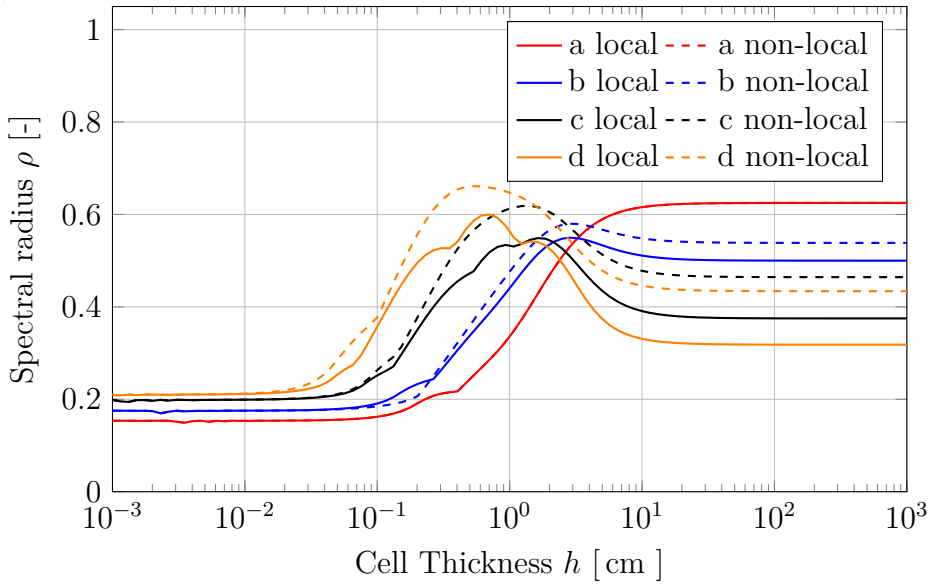

(b) Current drift vector

Figure A.6 Spectral radii for test cases 3 (Table 3.3) for the different NDA schemes with WLS high order equation using the local and non-local diffusion coefficient.

A.3 Joined Non-local Diffusion coefficient

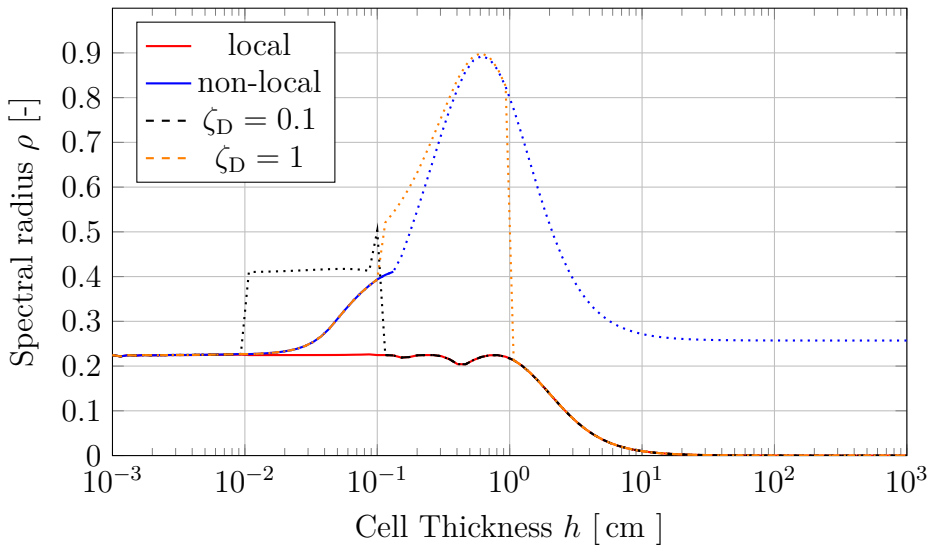

(a) Test case 1d

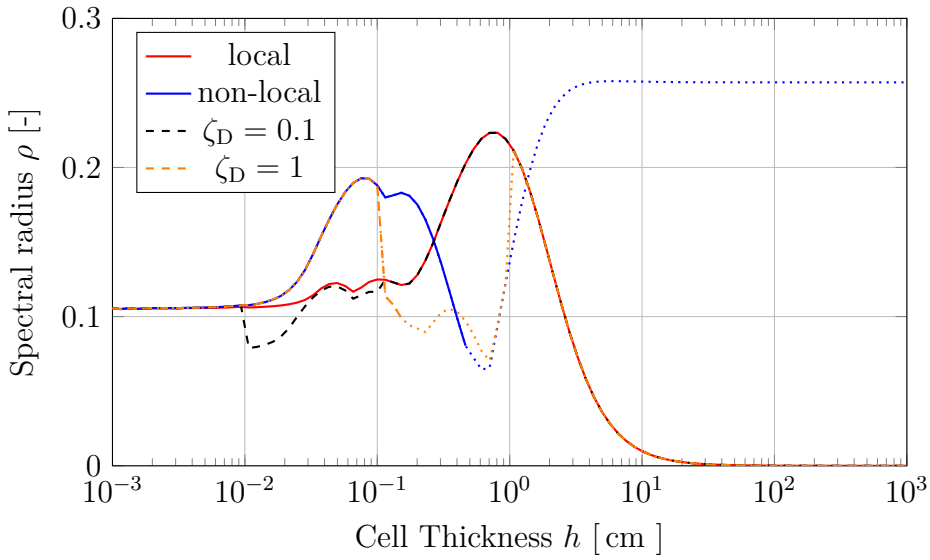

(b) Test case 2d

Figure A.7 Spectral radii for the joined diffusion coefficient Eq. (3.109) compared to the local and non-local definition (dotted line indicated negative eigenvalues).

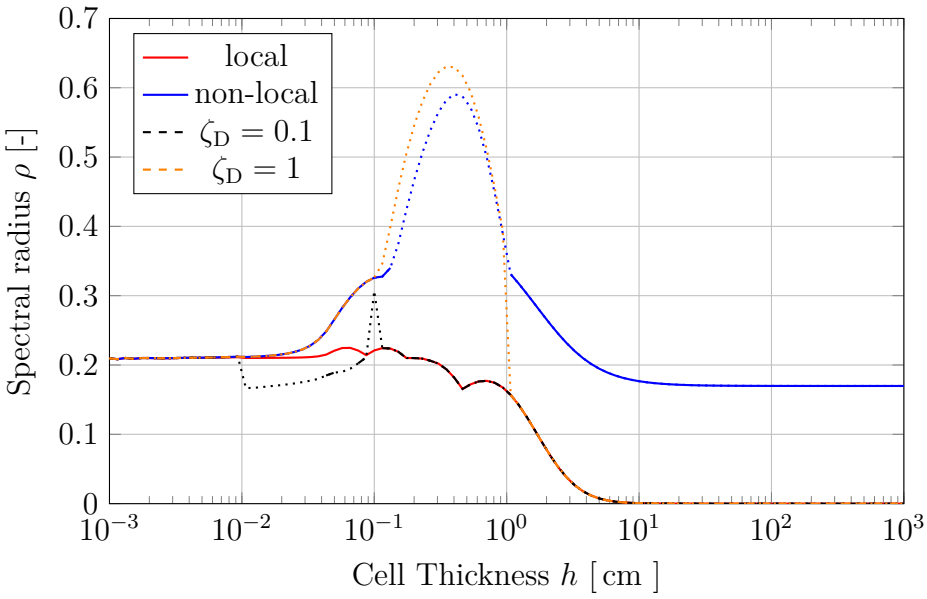

(c) Test case 3d

Figure A.7 Continued.

A.4 Void Problems

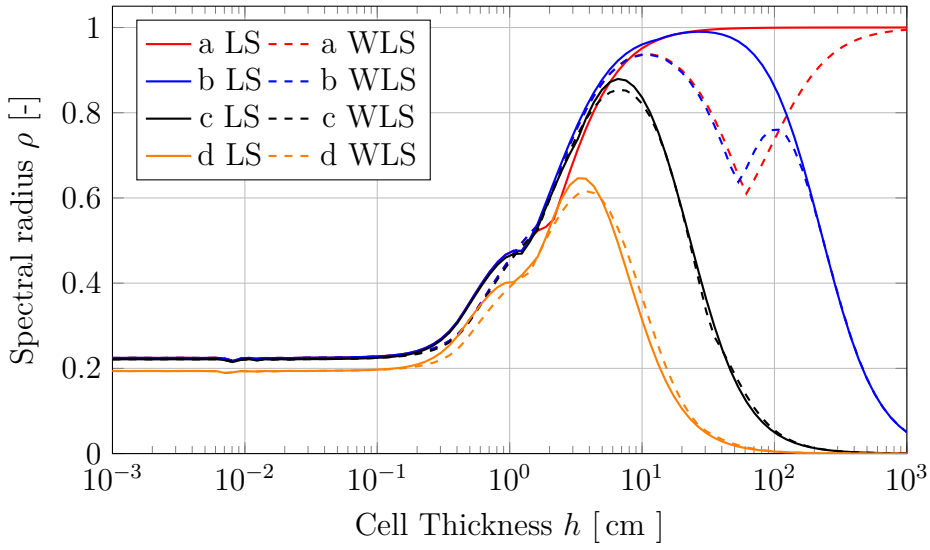

(a) Current drift vector

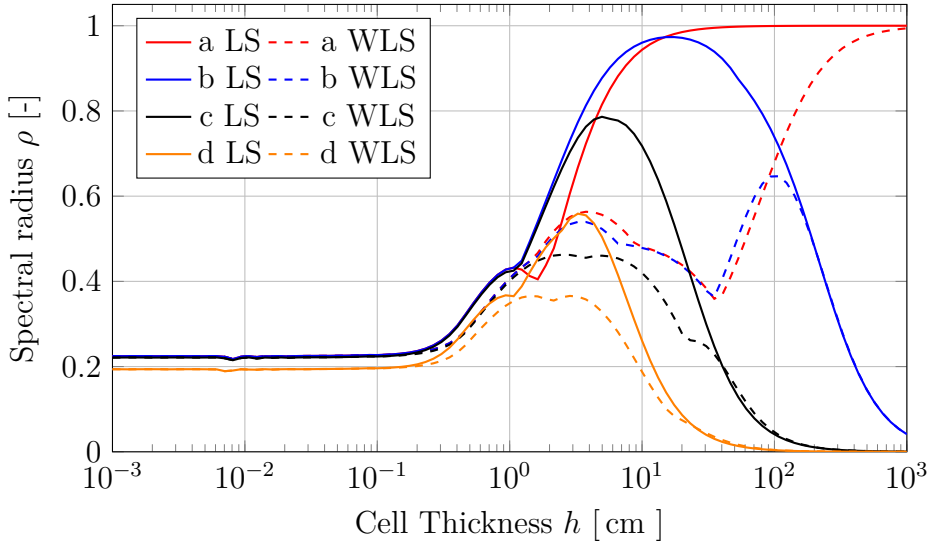

(b) Combined drift vector

Figure A.8 Spectral radii for the void test cases (Table 3.4) using the non-local diffusion coefficient for the NDA schemes using LS and WLS high order solutions.

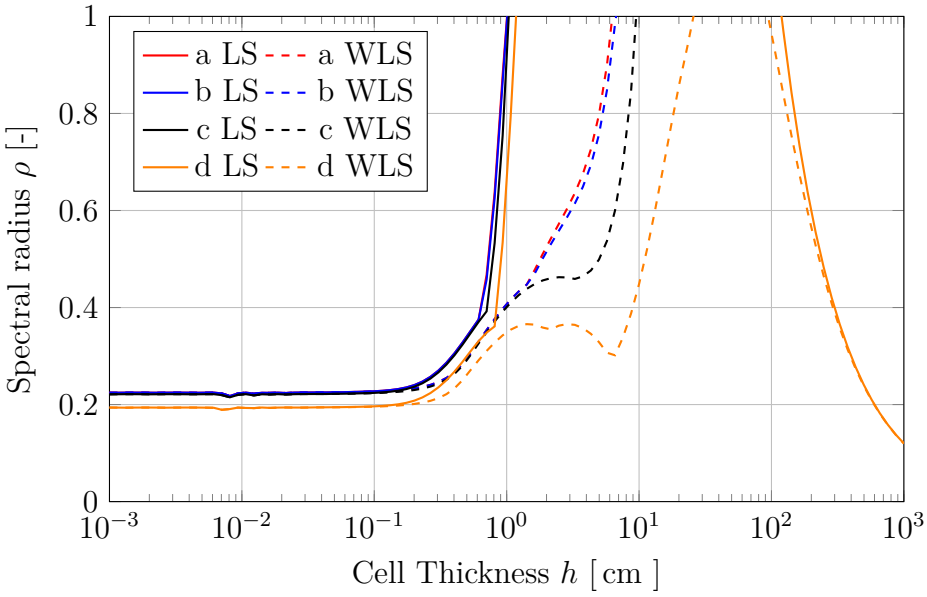

(c) τ drift vector

Figure A.8 Continued.

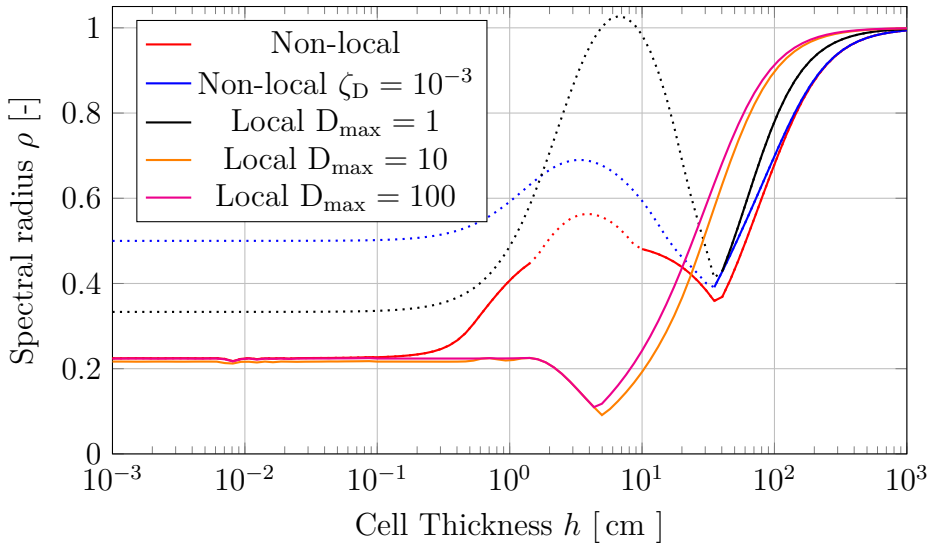

(a) Case 4a: $c = 1.0$

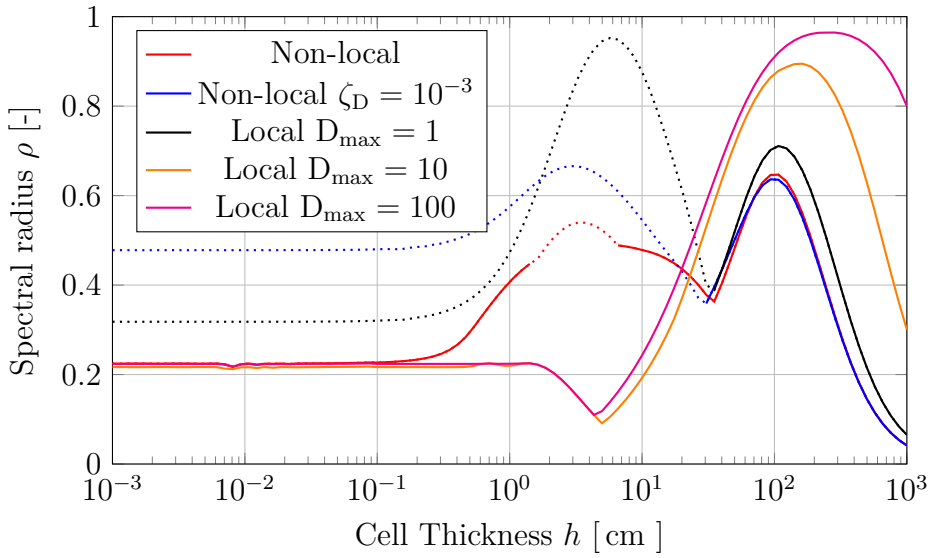

(b) Case 4b: $c = 0.9999$

Figure A.9 Comparison of spectral radii for different void diffusion coefficients for the void test cases (Table 3.4) using the WLS combined scheme (dotted line indicated negative eigenvalues).

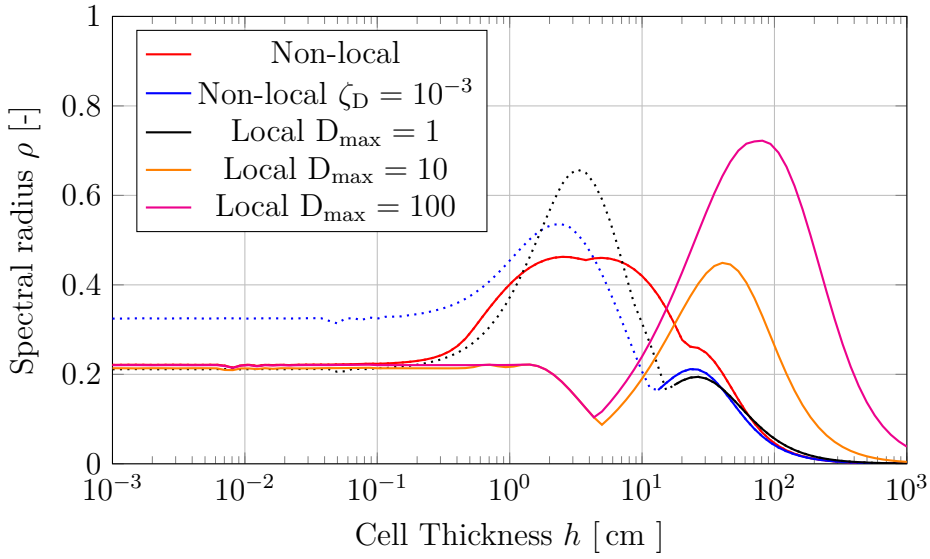

(c) Case 4c: $c = 0.99$

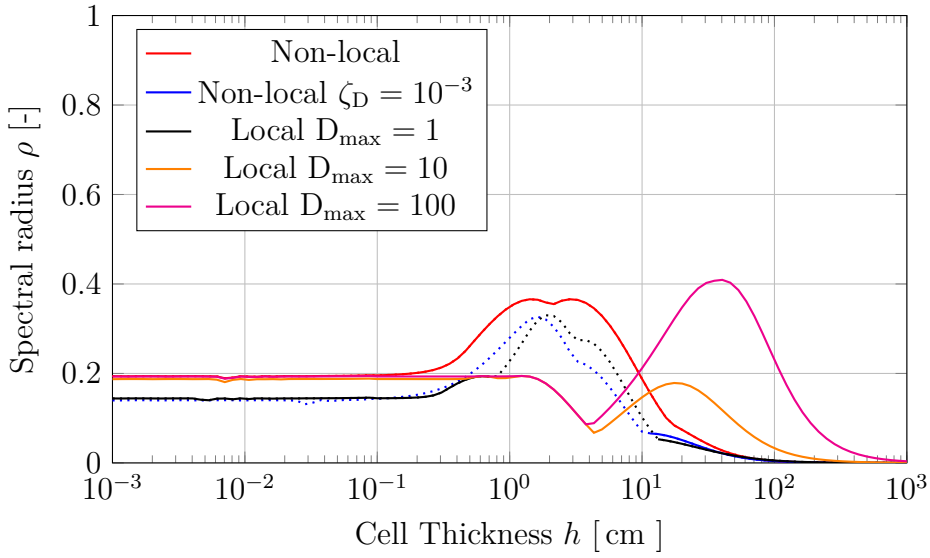

(d) Case 4d: $c = 0.9$

Figure A.9 Continued.

APPENDIX B

ANALYTIC ANALYSIS OF THE TWO REGION PROBLEM

The problem is an one dimensional two absorber problem. The left half of the problem contains a void ($\sigma_{\mathrm{t},1} = 0\,\frac{1}{\mathrm{cm}}$), while the right side contains a strong absorber ($\sigma_{\mathrm{t},2} = 10\,\frac{1}{\mathrm{cm}}$). On the left boundary is an incident isotropic flux $\phi_{\mathrm{B}} = 1.0\,\frac{1}{\mathrm{cm}^2\mathrm{s}}$. The problem is 2 cm wide with x_{L} the left boundary, x_{R} the right boundary and $x_{\mathrm{I}} = 1\,\mathrm{cm}$ the interface between the void and the absorber.

B.1 Analytic Solution

The solution for the angular flux for a given direction μ is for the void region

$$\psi_1(x,\mu) = \begin{cases} \frac{\phi^{\mathrm{inc}}}{2} & \mu > 0 \\ 0 & \mu < 0 \end{cases} \tag{B.1a}$$

and in the absorber region

$$\psi_2(x,\mu) = \begin{cases} \frac{\phi^{\mathrm{inc}}}{2} \mathrm{e}^{-\frac{\sigma_{\mathrm{t}}}{\mu}(x-x_{\mathrm{I}})} & \mu > 0 \\ 0 & \mu < 0 \end{cases} \tag{B.1b}$$

Integrating Eq. (B.1) over all angles gives the scalar flux in the void region

$$\phi_1(x) = \frac{\phi^{\mathrm{inc}}}{2} \tag{B.2a}$$

and in the absorber region

$$\phi_2(x) = \frac{\phi^{\mathrm{inc}}}{2} \mathrm{E}_2(\sigma_{\mathrm{t}}(x - x_{\mathrm{I}})) \tag{B.2b}$$

with the exponential-integral function

$$\mathrm{E}_n(x) \equiv \int_1^\infty \frac{\mathrm{e}^{-xt}}{t^n}\, dt \tag{B.3}$$

The first derivatives are

$$\frac{\partial}{\partial x}\phi_1(x) = 0 \tag{B.4a}$$
$$\frac{\partial}{\partial x}\phi_2(x) = -\frac{\phi^{\mathrm{inc}}}{2}\sigma_{\mathrm{t}}\mathrm{E}_1(\sigma_{\mathrm{t}}(x - x_{\mathrm{I}})) \tag{B.4b}$$

and the second ones

$$\frac{\partial^2}{\partial x^2}\phi_1(x) = 0 \tag{B.5a}$$
$$\frac{\partial^2}{\partial x^2}\phi_2(x) = \frac{\phi^{\mathrm{inc}}}{2}\sigma_{\mathrm{t}}^2\mathrm{E}_0(\sigma_{\mathrm{t}}(x - x_{\mathrm{I}})) \tag{B.5b}$$

The current can be found to

$$J_1(x) = \frac{\phi^{\mathrm{inc}}}{4} \tag{B.6a}$$
$$J_2(x) = \frac{\phi^{\mathrm{inc}}}{4}\mathrm{E}_3(\sigma_{\mathrm{t}}(x - x_{\mathrm{I}})) \tag{B.6b}$$

B.1.1 Drift Vector

The drift vector Eq. (3.77) becomes in one dimension

$$\hat{\alpha}(x) \equiv \frac{1}{\phi(x)}\left(-J(x) - \mathrm{D}(x)\frac{\partial}{\partial x}\phi(x)\right) \tag{B.7}$$

This gives for the void region

$$\begin{aligned}\hat{\alpha}_1(x) &= -\frac{1}{\phi_1(x)} J_1(x) \\ &= -\frac{1}{2}\end{aligned} \tag{B.8a}$$

and the absorber region

$$\begin{aligned}\hat{\alpha}_2(x) &= \frac{1}{\phi_1(x)}\left(-J_2(x) - \mathrm{D}_2(x)\frac{\partial}{\partial x}\phi_2(x)\right) \\ &= -\frac{1}{\mathrm{E}_2(\sigma_\mathrm{t}(x-x_\mathrm{I}))}\left(\left[\frac{1}{2}\mathrm{E}_3(\sigma_\mathrm{t}(x-x_\mathrm{I}))\right] - \mathrm{D}_2(x)\left[\mathrm{E}_1(\sigma_\mathrm{t}(x-x_\mathrm{I}))\right]\right)\end{aligned} \tag{B.8b}$$

B.1.2 Analytic S_N solution

For the convergence study with S_N calculations, it is necessary to use a semi-analytic reference solution that uses the same angular discretization. Given the Gauss-quadrature $\{\omega_m, \mu_m\}$ the analytic solution for one direction is given by:

$$\psi_{m,1}(x) = \begin{cases} \frac{\phi^\mathrm{inc}}{2} & \mu_m > 0 \\ 0 & \mu_m < 0 \end{cases} \tag{B.9a}$$

and in the absorber region

$$\psi_{m,2} = \begin{cases} \frac{\phi^\mathrm{inc}}{2}\mathrm{e}^{-\frac{\sigma_\mathrm{t}}{\mu_m}(x-x_\mathrm{I})} & \mu_m > 0 \\ 0 & \mu_m < 0 \end{cases} \tag{B.9b}$$

The scalar flux is then

$$\phi(x) = \sum_{m=1}^{M} \omega_m \psi_m(x) \tag{B.10}$$

We only have angular flux in the positive direction, therefore the integration becomes

$$\phi_1(x) = \frac{\phi^{\text{inc}}}{2} \sum_{m=\frac{M}{2}+1}^{M} \omega_m \tag{B.11a}$$

$$\phi_2(x) = \frac{\phi^{\text{inc}}}{2} \sum_{m=\frac{M}{2}+1}^{M} \omega_m \mathrm{e}^{-\frac{\sigma_t}{\mu_m}(x-x_I)} \tag{B.11b}$$

We also use a semi-analytic input for the drift vector to study the effect of the angular discretization on the spatial convergence. The current becomes

$$J(x) = \sum_{m=1}^{M} \omega_m \mu_m \psi_m(x) \tag{B.12}$$

Again, we only have nonzero values for the positive direction, rendering the integrals to half range integrals

$$J_1(x) = \frac{\phi^{\text{inc}}}{2} \sum_{m=\frac{M}{2}+1}^{M} \omega_m \mu_m \tag{B.13a}$$

$$J_2(x) = \frac{\phi^{\text{inc}}}{2} \sum_{m=\frac{M}{2}+1}^{M} \omega_m \mu_m \mathrm{e}^{-\frac{\sigma_t}{\mu_m}(x-x_I)} \tag{B.13b}$$

With the definition of the drift vector Eq. (B.7) we get

$$\hat{\alpha}_1 = \frac{1}{\sum_{m=\frac{M}{2}+1}^{M} \omega_m} \left[- \sum_{m=\frac{M}{2}+1}^{M} \omega_m \mu_m \right] \tag{B.14a}$$

and

$$\hat{\alpha}_1 = \frac{1}{\sum\limits_{m=\frac{M}{2}+1}^{M} \omega_m \mathrm{e}^{-\frac{\sigma_\mathrm{t}}{\mu_m}(x-x_\mathrm{I})}} \left[- \sum_{m=\frac{M}{2}+1}^{M} \omega_m \mu_m \mathrm{e}^{-\frac{\sigma_\mathrm{t}}{\mu_m}(x-x_\mathrm{I})} - \sum_{m=\frac{M}{2}+1}^{M} \omega_m \frac{\sigma_\mathrm{t}}{\mu_m} \mathrm{e}^{-\frac{\sigma_\mathrm{t}}{\mu_m}(x-x_\mathrm{I})} \right] \tag{B.14b}$$

B.2 Analytic Nonlocal Diffusion Coefficient

The nonlocal diffusion coefficient Eq. (3.74) becomes in one dimension

$$\mathrm{D}\left(x\right) \equiv \int_{-1}^{1} \mu^2 f\left(x,\mu\right) \, d\mu \tag{B.15}$$

with the auxiliary system

$$\mu \frac{\partial}{\partial x} f + \sigma_\mathrm{t} f = \frac{1}{2} \tag{B.16a}$$

and the boundary condition

$$f\left(x_\mathrm{L},\mu\right) = 0 \qquad \mu > 0 \tag{B.16b}$$

$$f\left(x_\mathrm{R},\mu\right) = 0 \qquad \mu < 0 \tag{B.16c}$$

The solution to Eq. (B.16) for the void region is

$$f_1\left(x,\mu\right) = \begin{cases} \frac{x-x_\mathrm{L}}{2\mu}, & \mu > 0 \\ \frac{x-x_\mathrm{I}}{2\mu} + f(x_\mathrm{I},\mu), & \mu < 0 \end{cases} \tag{B.17}$$

and the solution for the absorber region is

$$f_2(x,\mu) = \begin{cases} \frac{1}{2\sigma_t}\left(1 - e^{-\frac{\sigma_t}{\mu}(x-x_I)}\right) + f(x_I,\mu)e^{-\frac{\sigma_t}{\mu}(x-x_I)}, & \mu > 0 \\ \frac{1}{2\sigma_t}\left(1 - e^{-\frac{\sigma_t}{\mu}(x-x_R)}\right), & \mu < 0 \end{cases} \tag{B.18}$$

We use this solution to calculate the diffusion coefficient with Eq. (B.15). The coefficient for the void region is constant in space

$$\begin{aligned} D_1(x) &= \int_{-1}^{1} \mu^2 f_1(x,\mu)\, d\mu \\ &= \int_{-1}^{0} \mu^2 \left(\frac{x - x_I}{2\mu} + \frac{1}{2\sigma_t}\left(1 - e^{-\frac{\sigma_t}{\mu}(x_I - x_R)}\right)\right) d\mu + \int_{0}^{1} \mu^2 \frac{x - x_L}{2\mu}\, d\mu \\ &= \frac{x_I - x_L}{2} + \frac{1}{2\sigma_t}\left(\frac{1}{3} - E_4(\sigma_t(x_R - x_I))\right) \end{aligned} \tag{B.19a}$$

and only dependent on the width of the void plus the boundary inflows. For the absorber region the coefficient is the classical diffusion coefficient with a correction for boundary effects

$$\begin{aligned} D_2(x) &= \int_{-1}^{1} \mu^2 f_2(x,\mu)\, d\mu \\ &= \int_{-1}^{0} \mu^2 \frac{1}{2\sigma_t}\left(1 - e^{-\frac{\sigma_t}{\mu}(x-x_R)}\right) d\mu \\ &\quad + \int_{0}^{1} \mu^2 \left(\frac{1}{2\sigma_t}\left(1 - e^{-\frac{\sigma_t}{\mu}(x-x_I)}\right) + \frac{x_I - x_L}{\mu} e^{-\frac{\sigma_t}{2\mu}(x-x_I)}\right) d\mu \\ &= \frac{1}{3\sigma_t} - \frac{1}{2\sigma_t}\Big(E_4(\sigma_t(x_R - x)) + E_4(\sigma_t(x - x_I))\Big) + \frac{x_I - x_L}{2} E_3(\sigma_t(x - x_I)) \end{aligned} \tag{B.19b}$$

The thicker the region gets, the closer the coefficient goes to the classical diffusion coefficient in the middle of the region.

APPENDIX C

RESULTS FOR THE MODIFIED C5G7 BENCHMARK

C.1 Eigenvalues

Table C.1 Eigenvalues for all C5G7 calculations: Original (original benchmark geometry) Graphite (graphite moderator), void (graphite moderator and voids), Water (water moderator), Void2 (water moderator and voids).

Scheme	Original	Graphite	Void	Water	Void2
PDT	1.18646	0.65639	0.65405	1.19862	1.17829
LS 1	1.34423	0.65642	0.65450	1.35350	1.34429
LS 2	1.34527	0.65657	0.65466	1.35451	1.34532
WLS 1	1.18274	0.65495	0.65250	1.19568	1.17441
WLS 2	1.18558	0.65570	0.65320	1.19845	1.17682
SAAF	1.18558	0.65570	-	1.19845	-
SAAFτ	1.18698	0.65622	0.65391	1.19963	1.17890
NDA LS 1	1.18594	0.65567	0.65368	1.19901	1.17836
NDA LS 2	1.18593	0.65568	0.65369	1.19900	1.17835
NDA WLS 1	1.18561	0.65569	0.65348	1.19849	1.17742
NDA WLS 2	1.18558	0.65570	0.65349	1.19845	1.17740
NDA SAAF	1.18558	0.65570	-	1.19845	-
NDA SAAFτ	1.18698	0.65622	0.65391	1.19963	1.17890

C.2 Graphical comparisons for graphite and void case

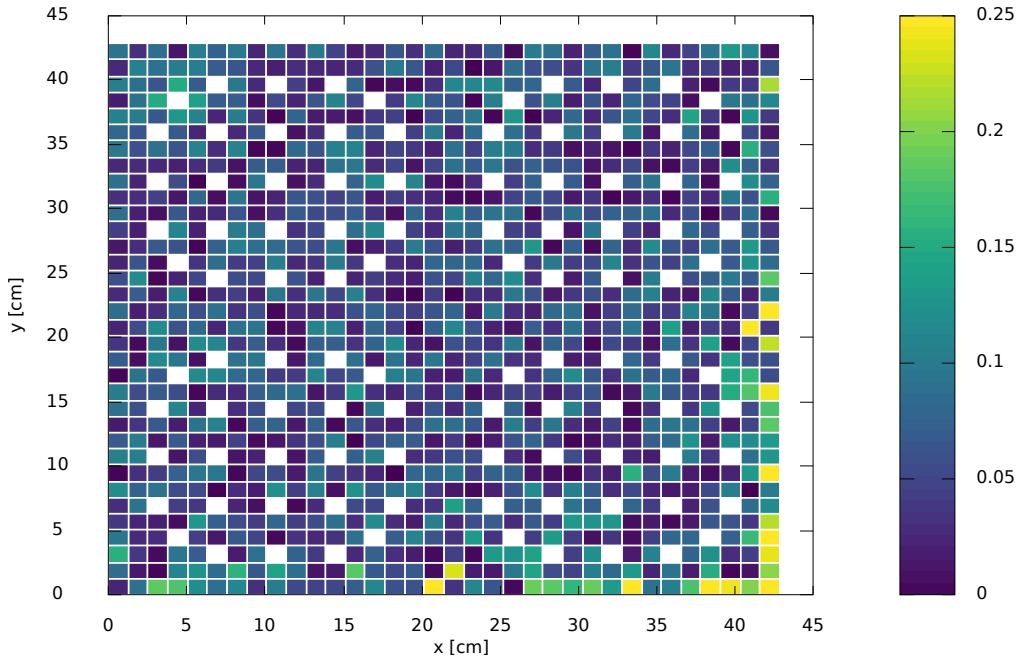

(a) Graphite case

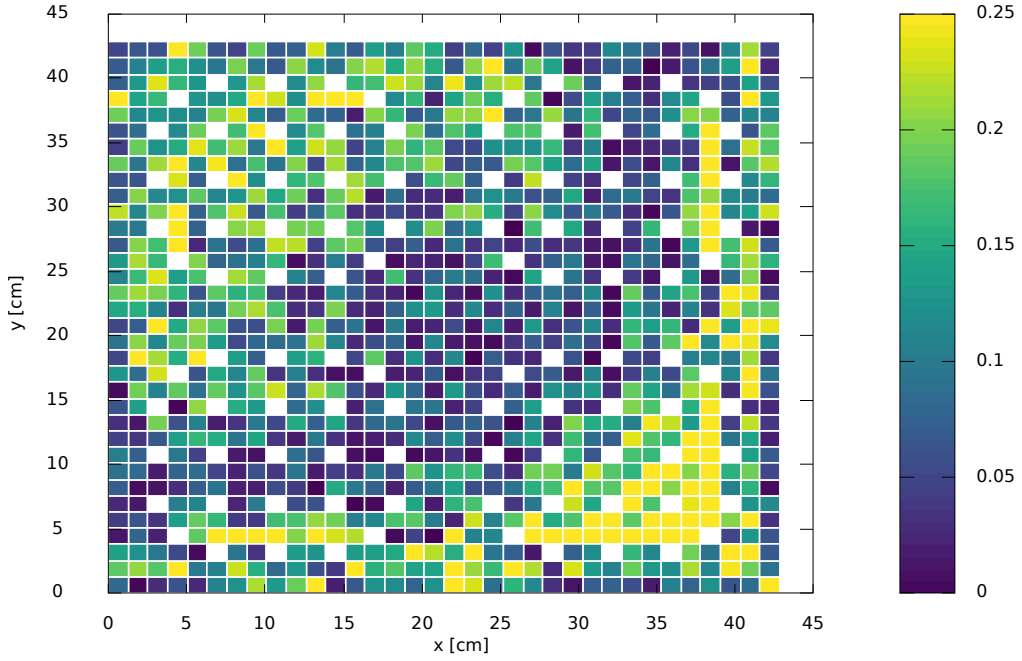

(b) Void case

Figure C.1 Distribution of the pin power errors in percent for the NDA LS 1 scheme, scale limited to 0.25 %.

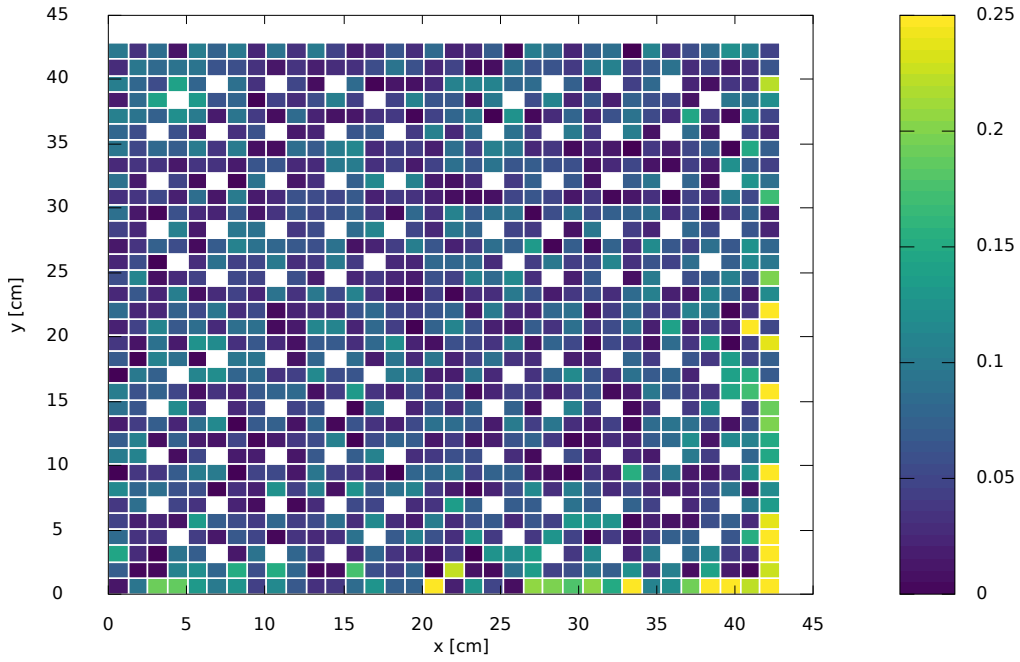

(a) Graphite case

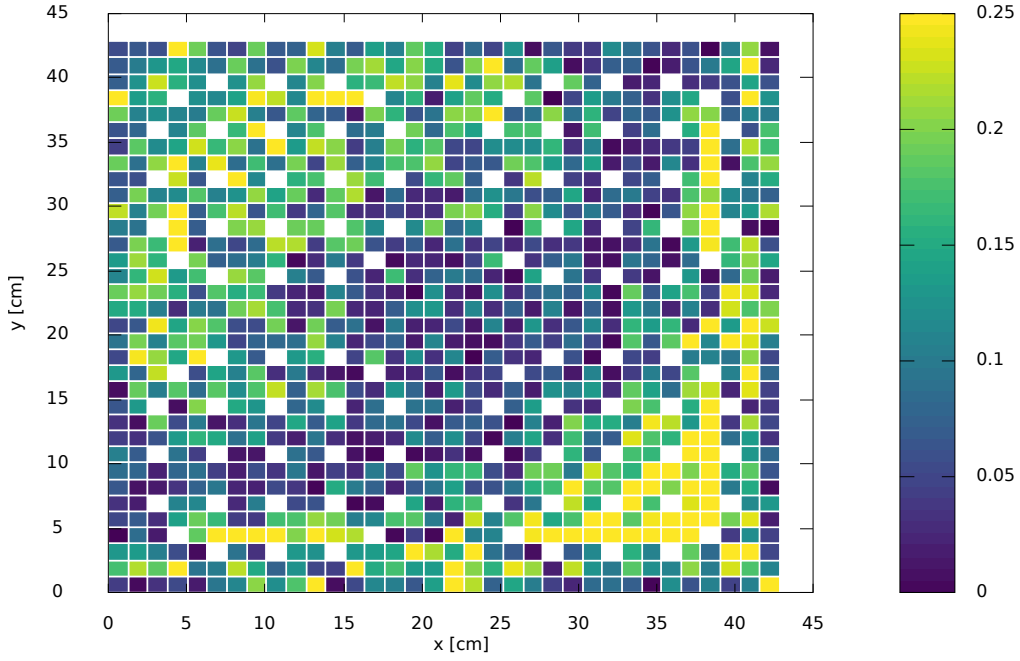

(b) Void case

Figure C.2 Distribution of the pin power errors in percent for the NDA LS 2 scheme, scale limited to 0.25 %.

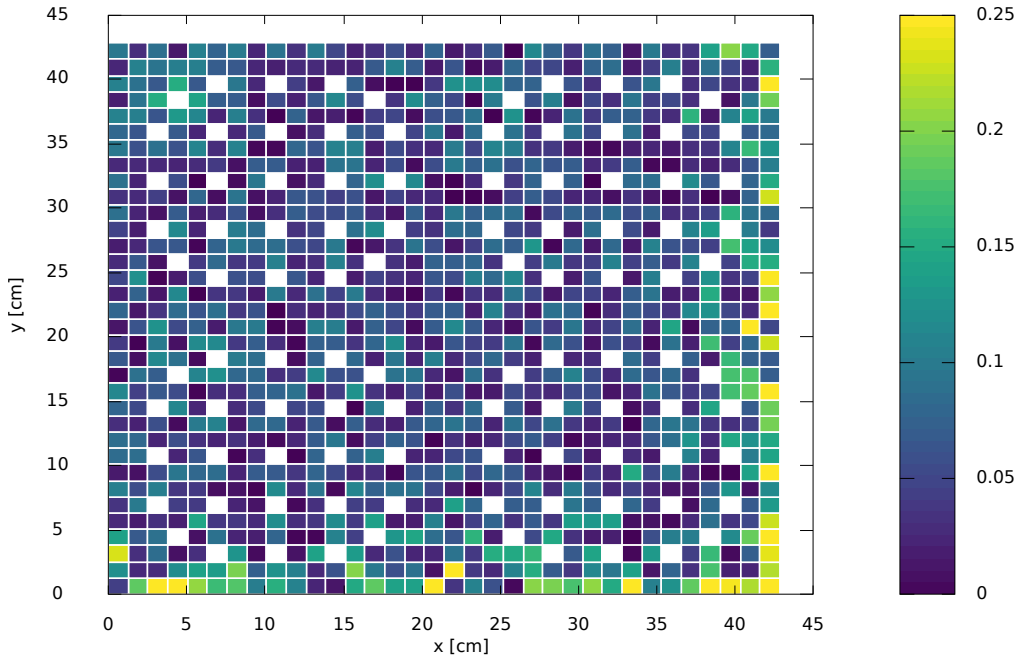

(a) Graphite case

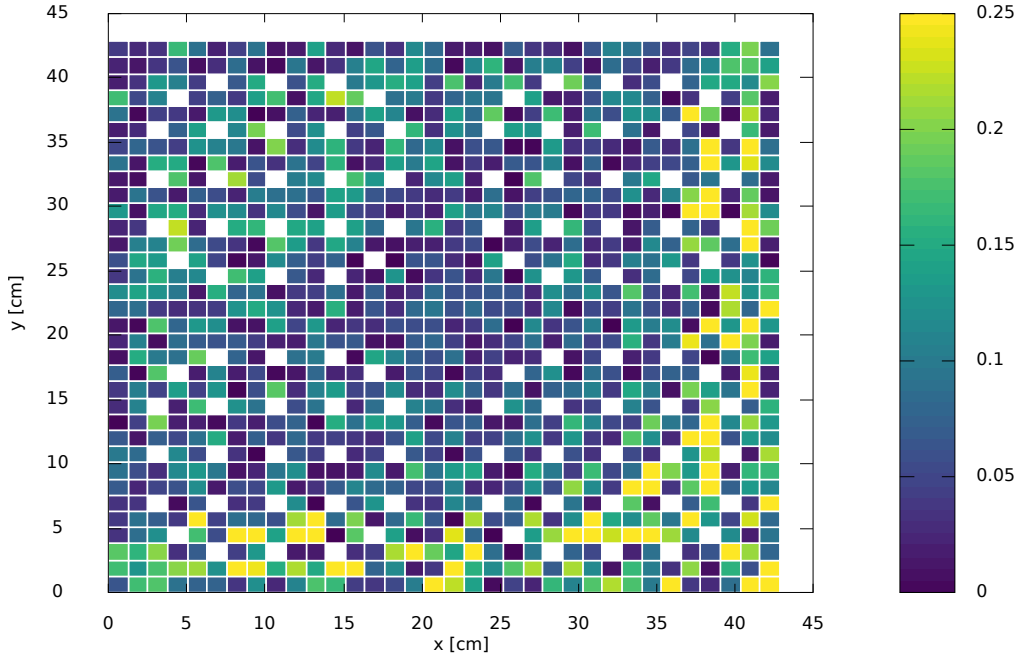

(b) Void case

Figure C.3 Distribution of the pin power errors in percent for the NDA WLS 1 scheme, scale limited to 0.25 %.

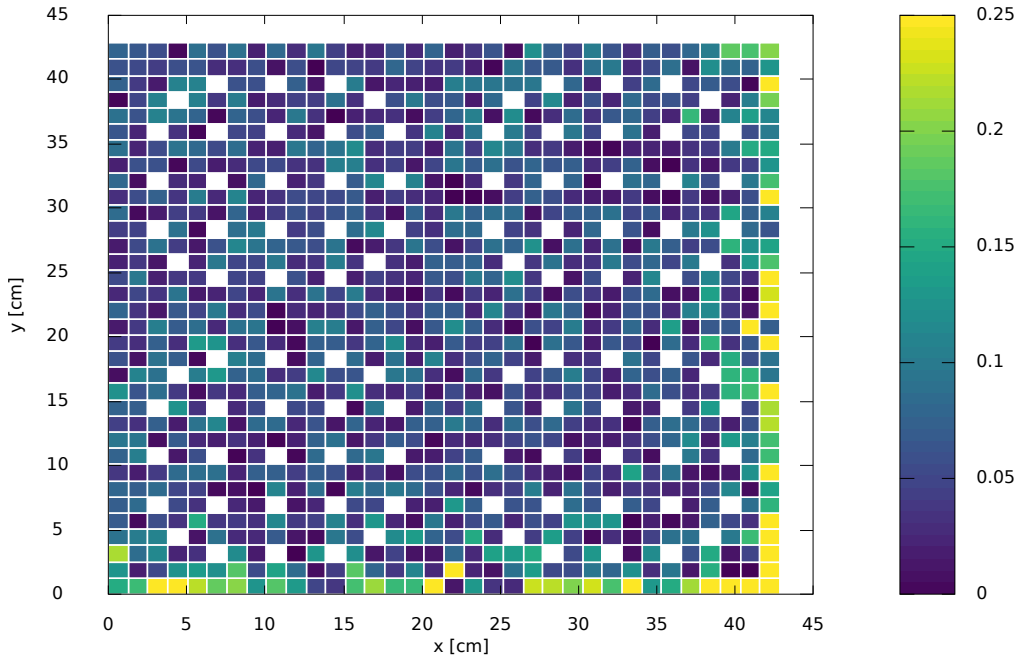

(a) Graphite case

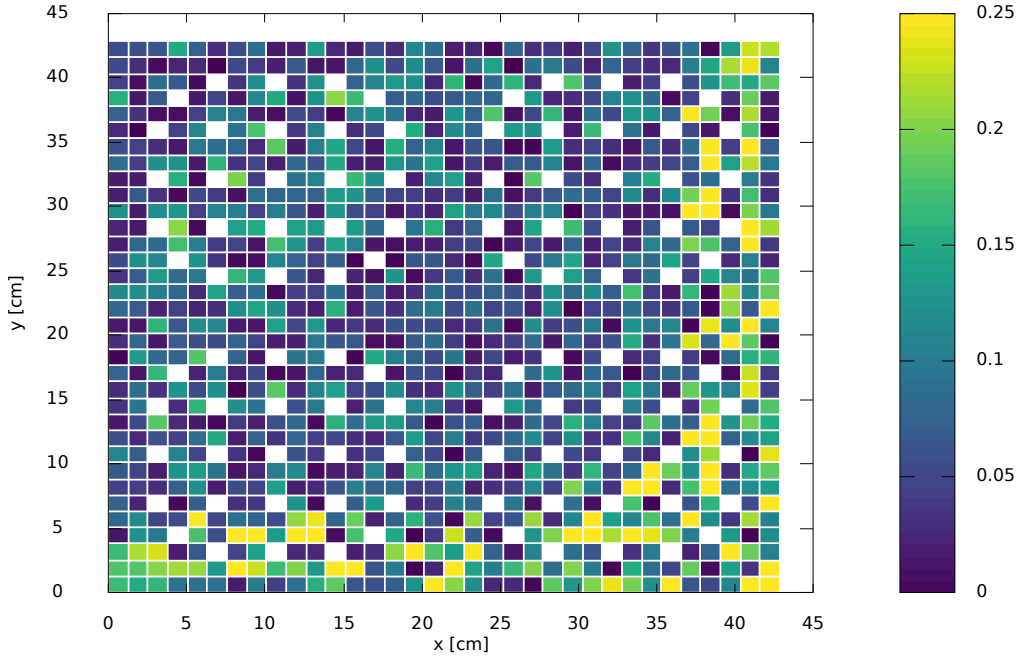

(b) Void case

Figure C.4 Distribution of the pin power errors in percent for the NDA WLS 2 scheme, scale limited to 0.25 %.

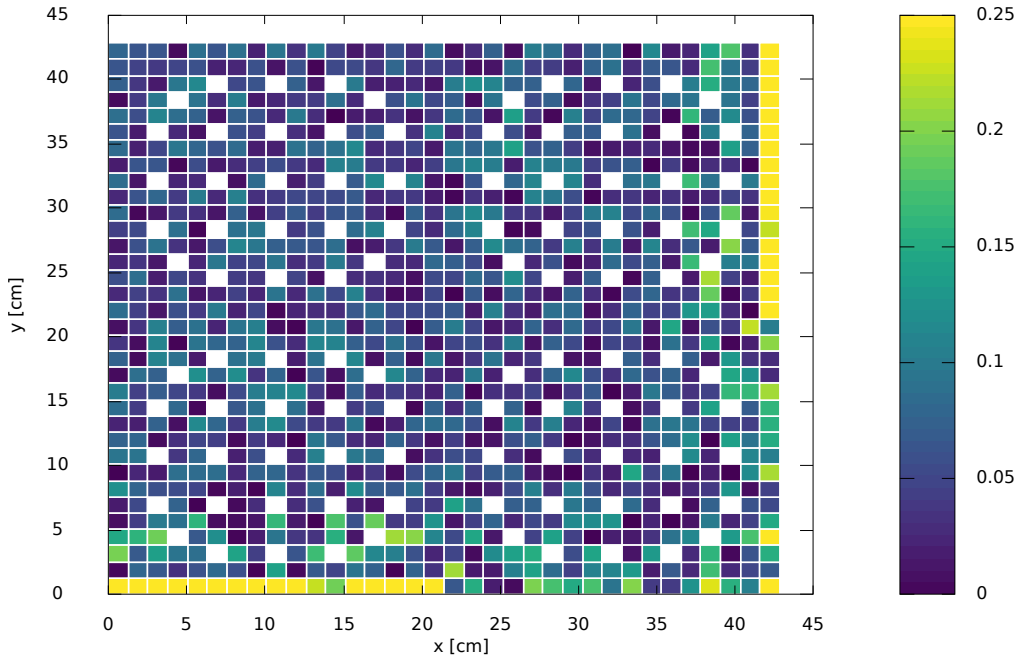

(a) Graphite case

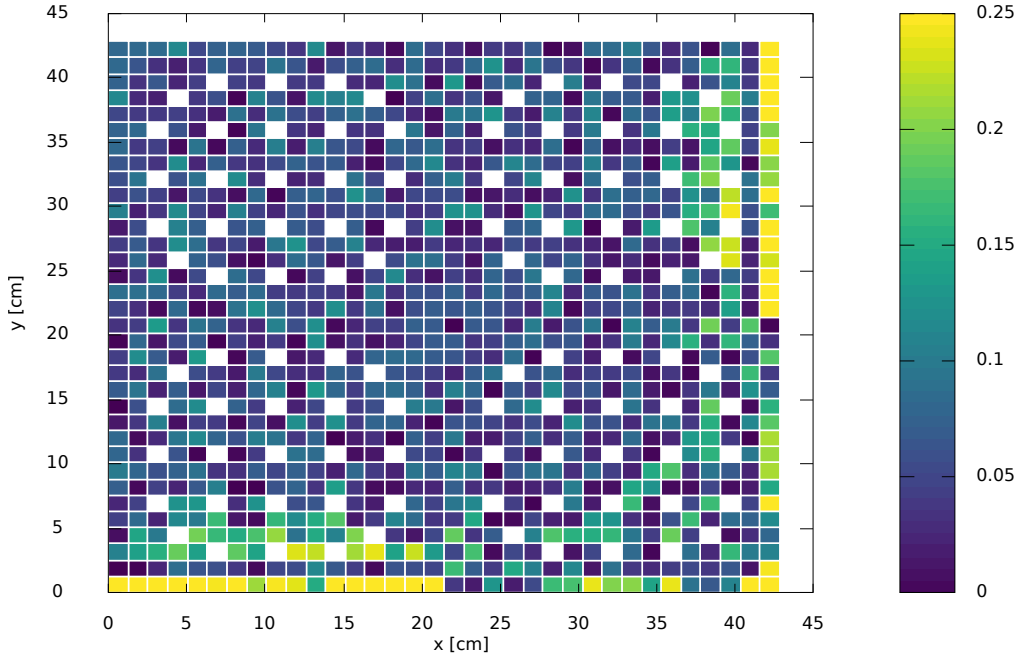

(b) Void case

Figure C.5 Distribution of the pin power errors in percent for the NDA SAAFτ scheme, scale limited to 0.25 %.

C.3 WLS weight function limit

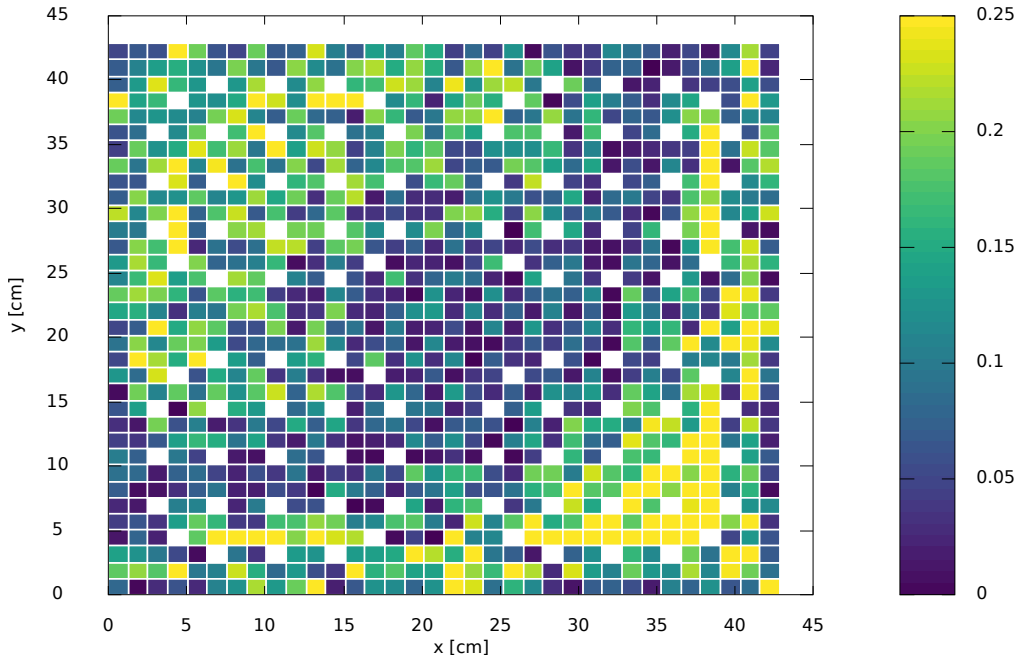

(a) $w_{\max} = 1$

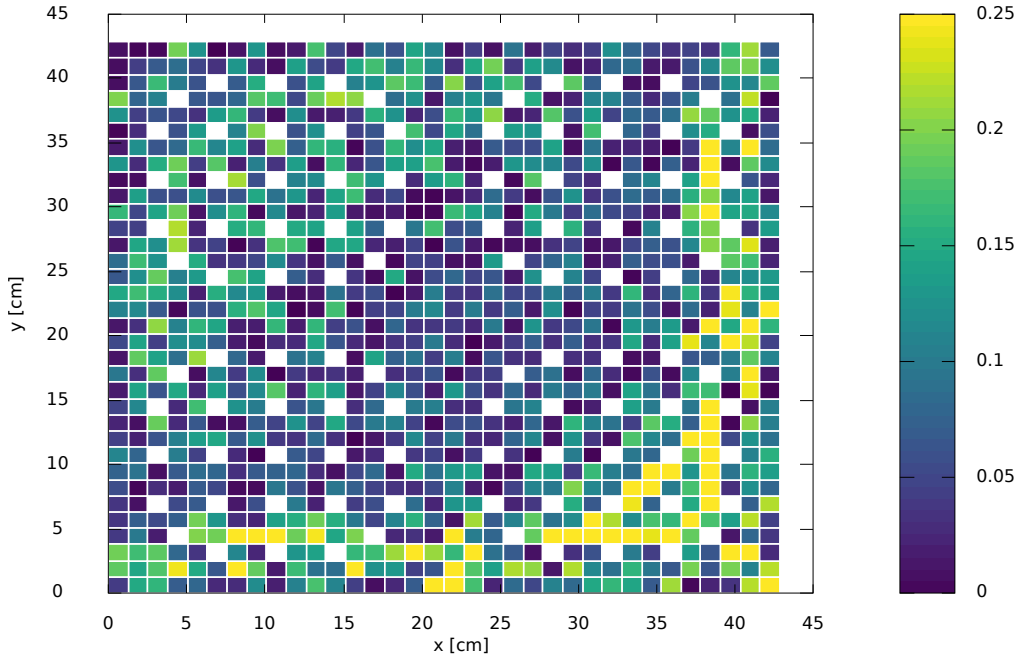

(b) $w_{\max} = 10$

Figure C.6 Distribution of the pin power errors in percent for the NDA WLS 1 scheme with varying $w_{\max}$, scale limited to 0.25 %.

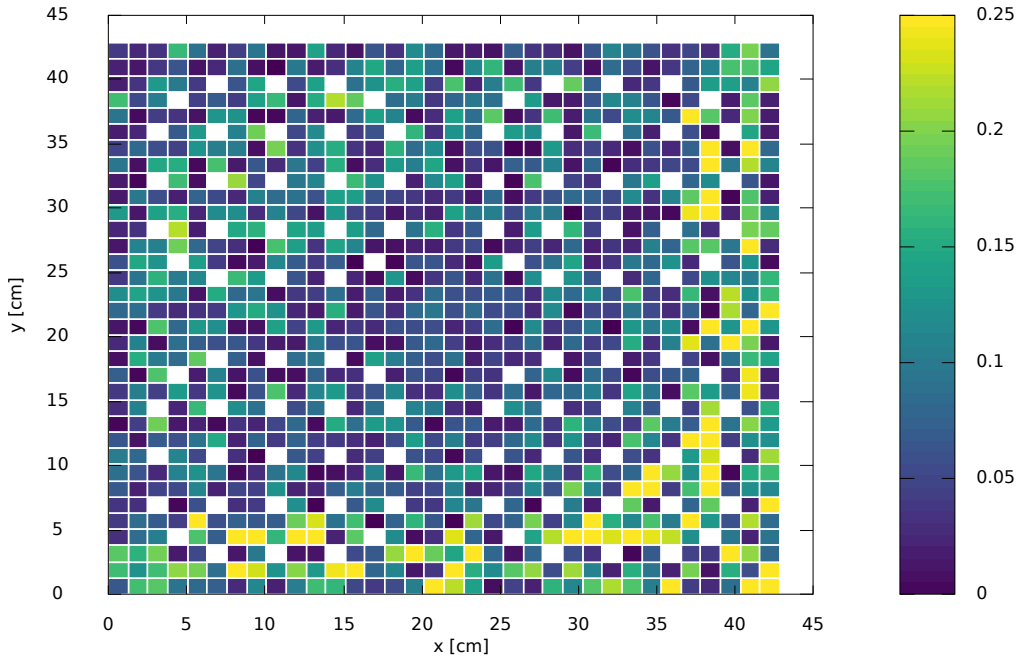

(c) $w_{\max} = 100$

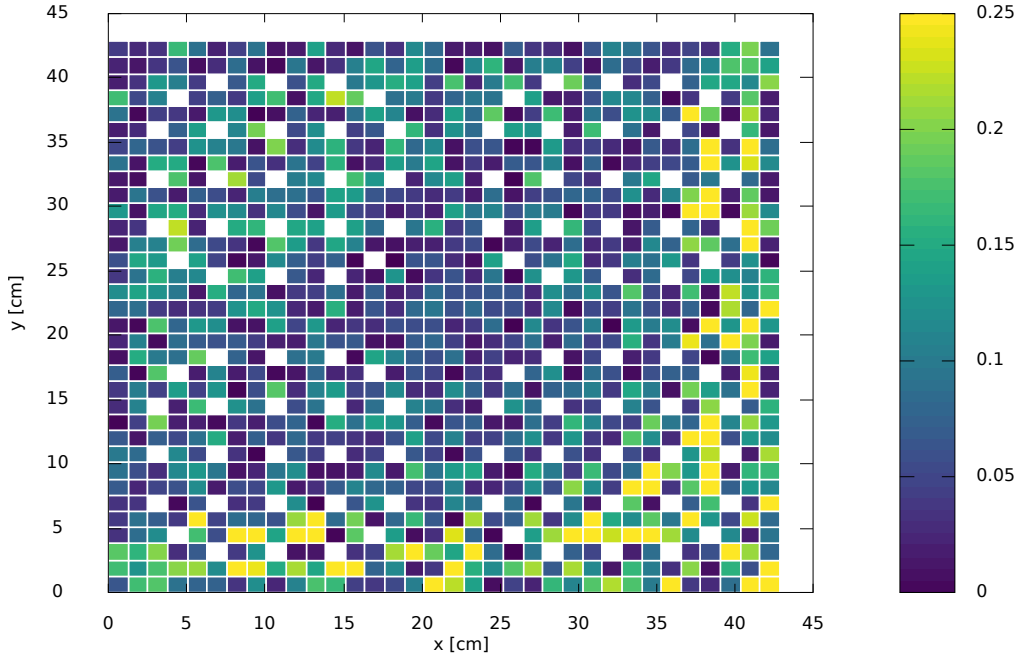

(d) $w_{\max} = 500$

Figure C.6 Continued.

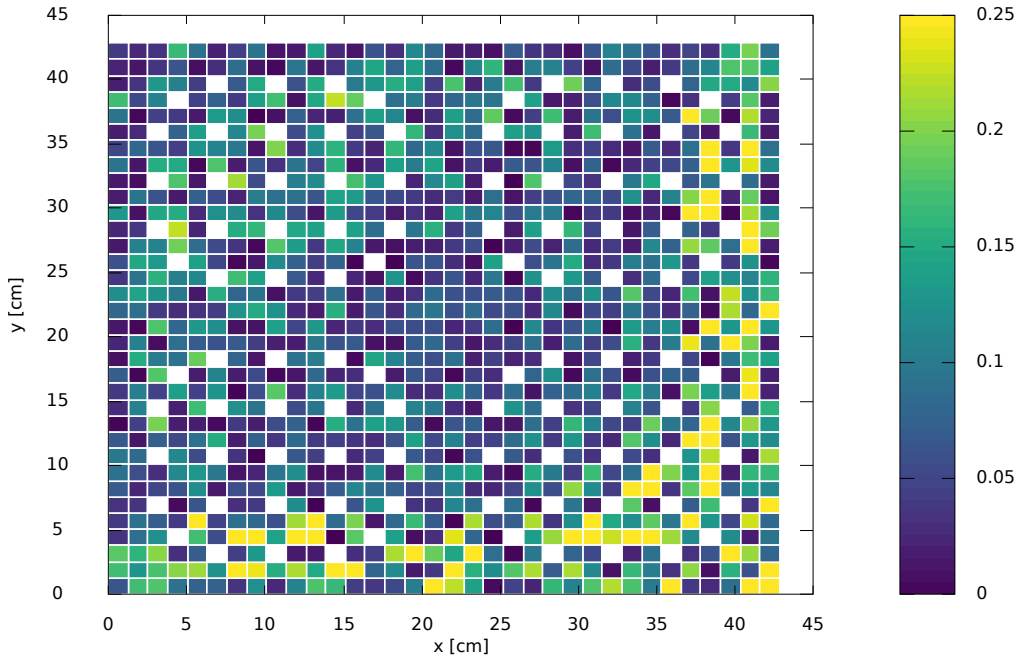

(e) $w_{\max} = 1000$

Figure C.6 Continued.